



5-2020

## **A Compact Neutron Scatter Camera Using Optical Coded-Aperture Imaging**

Micah Folsom

*University of Tennessee*, [mfolsom@vols.utk.edu](mailto:mfolsom@vols.utk.edu)

Follow this and additional works at: [https://trace.tennessee.edu/utk\\_graddiss](https://trace.tennessee.edu/utk_graddiss)

---

### **Recommended Citation**

Folsom, Micah, "A Compact Neutron Scatter Camera Using Optical Coded-Aperture Imaging. " PhD diss., University of Tennessee, 2020.  
[https://trace.tennessee.edu/utk\\_graddiss/5803](https://trace.tennessee.edu/utk_graddiss/5803)

This Dissertation is brought to you for free and open access by the Graduate School at TRACE: Tennessee Research and Creative Exchange. It has been accepted for inclusion in Doctoral Dissertations by an authorized administrator of TRACE: Tennessee Research and Creative Exchange. For more information, please contact [trace@utk.edu](mailto:trace@utk.edu).

To the Graduate Council:

I am submitting herewith a dissertation written by Micah Folsom entitled "A Compact Neutron Scatter Camera Using Optical Coded-Aperture Imaging." I have examined the final electronic copy of this dissertation for form and content and recommend that it be accepted in partial fulfillment of the requirements for the degree of Doctor of Philosophy, with a major in Nuclear Engineering.

Jason Hayward, Major Professor

We have read this dissertation and recommend its acceptance:

Klaus Ziock, Lawrence Heilbronn, Eric Lukosi

Accepted for the Council:

Dixie L. Thompson

Vice Provost and Dean of the Graduate School

(Original signatures are on file with official student records.)

# **A Compact Neutron Scatter Camera Using Optical Coded-Aperture Imaging**

A Dissertation Presented for the

Doctor of Philosophy

Degree

The University of Tennessee, Knoxville

Micah John Folsom

May 2020

Copyright © 2020 by Micah John Folsom

All rights reserved.

## ACKNOWLEDGEMENTS

An old African proverb states, “It takes a village to raise a child,” and the same is true of a dissertation. This work would not have been possible without the dedicated support of a community of scientists, engineers, friends, and family. First, I thank my advisor, Dr. Hayward, without whom, I would not have come to Tennessee at all. Despite an embarrassingly low undergraduate GPA, Dr. Hayward believed in my ability and passion for scientific research, giving me the opportunity to become a successful graduate student. He always listened and took time out of his busy schedule to see to my needs, above and beyond the call of duty.

I would also like to thank Dr. Ziock, whose unending knowledge, curiosity, and attention to detail greatly improved the quality of my work and helped shape me as a researcher. From the beginning of my master’s work to the end of my PhD, he spent countless hours with me at the white board and staring at my computer monitor, spit-balling ideas for detector designs, exploring the nuances of complex topics, and making sure that I was successful. There were many times where I struggled to grasp a concept, and he exhibited exceptional patience in guiding me to understanding.

Dr. Hausladen was absolutely instrumental in the completion of this dissertation; his insights into physics, detector design, and how the world works were invaluable. Whenever I hit a seemingly insurmountable roadblock, Dr. Hausladen was there to show me a way around, or through it. We had many candid hallway conversations that evolved into major breakthroughs in this work, and he always made me feel like just another scientist instead of a subordinate.

I am extremely thankful for a number of other scientists at ORNL who lent me their ears, their brains, and their valuable time, without obligation: Dr. Blackston, Dr. Newby, Dr. Fabris, and Dr. Nattress especially. I would also like to thank others in our group at ORNL, and the other members of this collaboration for their feedback and support.

Thank you to the GEM Fellowship that helped fund my studies and gave me the opportunity to learn from and encourage other aspiring minority scientists.

Finally, thank you to my friends and family, without whom, I would be lost. Over the last six years, they believed in me and encouraged me, to no end, and I could not have done it without them.

## **ABSTRACT**

The detection and localization of fast neutron resources is an important capability for a number of nuclear security areas such as emergency response and arms control treaty verification. Neutron scatter cameras are one technology that can be used to accomplish this task, but current instruments tend to be large (meter scale) and not portable. Using optical coded-aperture imaging, fast plastic scintillator, and fast photodetectors that were sensitive to single photons, a portable neutron scatter camera was designed and simulated. The design was optimized, an experimental prototype was constructed, and neutron imaging was demonstrated with a tagged  $^{252}\text{Cf}$  source in the lab.

# TABLE OF CONTENTS

1	Introduction.....	1
1.1	Neutron Scatter Cameras .....	2
1.2	Fast Plastic Scintillators.....	6
1.3	Multi-anode Photodetectors.....	10
1.3.1	Photomultiplier Tubes.....	11
1.3.2	Silicon Photomultipliers.....	12
1.3.3	Microchannel Plate Photomultiplier Tubes .....	13
1.4	Fast Digitizers .....	14
1.4.1	CAEN V1742.....	15
1.4.2	Struck SIS3305 .....	15
1.5	Localization in Bulk Scintillators .....	15
1.6	Coded-Aperture Imaging .....	17
1.6.1	Background and Theory.....	17
1.6.2	Anti-aliasing.....	21
1.7	Retroreflectors.....	23
2	Previous Work and System Concepts .....	25
2.1	Two-Plane and Multi-Volume NSC Geometries.....	25



2.2	Overview of Proposed Compact NSC Geometries .....	27
2.2.1	Design Goals .....	27
2.2.2	Monolithic Design .....	28
2.2.3	Optically Segmented Design.....	30
2.2.4	Optical Coded Aperture .....	32
2.3	Original Contributions .....	33
3	Initial Design Studies .....	35
3.1	Coded-Aperture Counting Statistics Study .....	35
3.1.1	Introduction.....	35
3.1.2	Coded-Aperture Imaging .....	36
3.1.3	Analytical Expression .....	41
3.1.4	Equation Validation .....	45
3.1.5	Simulation Geometry .....	46
3.1.6	Data Analysis .....	48
3.1.7	Results.....	49
3.1.8	Discussion.....	53
3.1.9	Conclusions.....	55
3.2	Initial Designs .....	55
3.2.1	Design A: Monolithic, one-sided readout, 2-D mask .....	57

3.2.2	Design B: Monolithic, two-sided readout, orthogonal 1-D masks .....	58
3.2.3	Design C: Two equal volumes, two-sided readout, 2-D mask in center.....	58
3.2.4	Design D: Segmented slabs with 1-D mask along length.....	60
3.2.5	Simulation Results and Down-Selection .....	60
4	OCA Slab Design Study .....	67
4.1	Full Physics Simulations.....	67
4.2	Event Reconstruction Methods .....	72
4.2.1	Construction of Detector Response Table .....	73
4.2.2	Triggering .....	74
4.2.3	Energy Determination.....	75
4.2.4	Time Determination .....	75
4.2.5	Localization: Cross-correlation Method .....	75
4.2.6	Study of Centroiding for Cross-correlation Method.....	78
4.2.7	Localization: Maximum Likelihood Method.....	82
4.2.8	Localization: $\chi^2$ Method.....	84
4.2.9	Localization: Log-likelihood Method.....	85
4.3	OCA Slab Parameter Study .....	87
4.3.1	OCA Slab Reference Design .....	88
4.3.2	No Coded Mask .....	90

4.3.3	Detector Height.....	91
4.3.4	Inter-slab Air Gaps.....	92
4.3.5	Inter-slab Reflectors.....	93
4.3.6	Retroreflector .....	94
4.3.7	Narrow-edge Air Gap .....	95
4.3.8	Narrow-edge Reflector.....	95
4.3.9	Gap Light Guide Thickness .....	96
4.3.10	Focal Length .....	97
4.3.11	EJ-232Q Scintillator Material .....	98
4.3.12	Detector Pixel Size.....	99
4.3.13	Parameter Study Summary .....	100
4.4	OCA Slab Prototype Simulation.....	102
4.4.1	Overall Performance .....	102
4.4.2	Neutron Backprojection .....	104
4.4.3	Optical Crosstalk.....	105
5	Experimental Work.....	107
5.1	Prototype Mechanical Design.....	107
5.1.1	Slab Fabrication .....	107
5.1.2	3-D Printed Enclosure.....	108

5.1.3	Slab Assembly .....	112
5.1.4	MAPMT Breakout Board and 3-Slab Signal Summation .....	118
5.2	Photodetector .....	121
5.2.1	Photodetector Calibration .....	121
5.3	Data Acquisition System.....	127
5.4	Retroreflector Characterization.....	129
5.4.1	Introduction.....	129
5.4.2	Theory .....	131
5.4.3	Methods.....	132
5.4.4	Laser Measurement.....	137
5.4.5	Scintillator Measurement .....	140
5.4.6	Spatial Alignment .....	141
5.4.7	Gain Calibration.....	141
5.4.8	Event Localization .....	142
5.4.9	Laser Measurement Results .....	142
5.4.10	Scintillator Measurement Results .....	149
5.4.11	Discussion.....	158
5.4.12	Conclusions.....	160
5.5	Prototype Characterization.....	161

5.5.1	Data Acquisition and Response Table .....	161
5.5.2	Energy Calibration .....	165
5.5.3	Response Event Selection .....	170
5.5.4	Response Validation .....	172
5.5.5	Timing Performance .....	181
5.6	Prototype Measurements.....	183
5.6.1	Experimental Setup and Event Selection Cuts.....	183
5.6.2	Example Double Scatter Event .....	189
5.6.3	Backprojected Neutron Images .....	191
5.6.4	Backprojected Compton Images .....	197
6	Summary and Conclusions .....	201
6.1	Future Work .....	204
	List of References .....	206
	Vita.....	212

## LIST OF TABLES

Table 1.1. List of relevant scintillator characteristics for a selection of reference materials and candidate plastic scintillators. ....	7
Table 3.1. Alignment of $\mathbf{D}$ and $\mathbf{G}$ when the correct basis direction is used. Columns highlighted with gray are open mask pixels that align with detector pixels in $\mathbf{D}$ with one count. ....	42
Table 3.2. Example ideal hit pattern $\mathbf{D}$ and decoder $\mathbf{G}$ when assuming the wrong basis direction. Gray shading shows when an open mask pixel and hit detector pixel align whereas black shading indicates a count in the detector behind a closed mask pixel. ....	42
Table 3.3. List of ranks, total numbers of pixels, and numbers of open pixels and open fractions for the simulated 1-D and 2-D MURA coded-mask patterns. ....	48
Table 4.1: Summary of X position resolutions for each method. The FWHM is calculated via linear interpolation on the histogram. Errors are calculated assuming Poisson statistics. ....	80
Table 4.2. Performance comparison of the different localization algorithms for the OCA Slab Reference Design. The values are the standard deviations of Gaussian fits to the difference distributions, described in more detail in Section 4.3. ....	87
Table 4.3. Comparison of performance between the reference design and the same detector with no coded mask pattern. ....	91
Table 4.4. Comparison of performance for different detector heights. The number of reconstructed events was the number of detected neutron scatters with two or more interactions. Approximately the same number of source particles were emitted. ....	92

Table 4.5. Comparison of reference design performance, with and without the inter-slab air gaps. ....	93
Table 4.6. Comparison of reference design performance, with and without the inter-slab reflectors. ....	94
Table 4.7. Comparison of the reference design performance with and without the retroreflector. ....	94
Table 4.8. Comparison of the reference design performance with and without an air gap at the narrow edges. ....	95
Table 4.9. Comparison of the reference design performance with and without a reflector at the narrow edges. ....	96
Table 4.10. Comparison of the reference design performance for different thicknesses of gap light guide.....	97
Table 4.11. Comparison of the reference design performance for different focal lengths. ....	98
Table 4.12. Comparison of the reference design performance to the same design using EJ-232Q. ....	99
Table 4.13. Performance of an OCA compact NSC with a 3 mm element size. ....	99
Table 4.14. Full summary of parameter study results based on simulated data. ....	100
Table 5.1. List of manufacturers and part names for the tapes investigated in this study. ....	133
Table 5.2. Light collection efficiency, relative to the best performer, as a function of the surface treatment. Data are from the central beam position shown in Figure 5.28 and Figure 5.29. ....	151

Table 5.3. Intrinsic $X$ spatial resolution versus top surface treatment. A beam spot size of 1.6 mm was subtracted in quadrature. ....	153
Table 5.4. Contributions to the overall width and relative light collection efficiencies for each surface treatment. Data are from the center beam location. The beam spot width was subtracted in quadrature.....	158
Table 5.5. Summary of off-grid beam reconstruction performance. The assumed beam spot size was 5.5 mm FWHM.....	180



## LIST OF FIGURES

Figure 1.1. Schematic of traditional two-plane NSC geometry. An incident neutron with energy $E_n$ is scattered by angle $\theta$ as it transfers $E_p$ to a proton. The scattered neutron with energy $E_n'$ interacts again in the back plane a few nanoseconds later. ....	4
Figure 1.2. Reproduced from [24]. Energy equivalent light output of BC-420, equivalent to EJ-212, as a function of energy deposited, relative to electrons.....	9
Figure 1.3. Reproduced from [25]. Proton light yield relative to the electron light yield for EJ-204. Note that the ordinate axis is in light yield, which is different than the energy equivalent MeVee units shown in Figure 1.2. ....	10
Figure 1.4. Reproduced from [36]. Schematic diagram of a coded aperture system, showing the shadow pattern projected on a pixelated detector by the mask. ....	18
Figure 1.5. Demonstration of software focusing using a coded-aperture system with a 5 mm focal length. Top left: 2-D rank 17 MURA pattern used. Top right: hit map of over 10,000 detected counts. Bottom left: peak counts as a function of assumed source distance, showing a peak at the true location. Bottom right: final reconstructed image. ....	20
Figure 1.6. Left: hit pattern obtained by observing an infinitely far away (parallel beam) source. Right: decoded images, where black is single sampled and red is anti-aliased. The pattern is a 1-D rank 17 MURA. ....	22
Figure 1.7. Schematic depiction of common types of reflection. Solid lines highlight the trajectories of emitted light and dashed lines represent reflected light.....	23
Figure 1.8. Diagram of a) spherical bead retroreflection and b) corner cube retroreflection. Optically transmissive material is shown as blue and specular reflector is shown as gray. ....	24

Figure 2.1. Reproduced from [7]. Picture of the two-plane NSC developed by Sandia National Labs. Two planes of scintillators are visible, along with a source-moving structure on the right. ....	26
Figure 2.2. Reproduced from [14]. Picture of MINER, the compact NSC using liquid scintillator cells. ....	27
Figure 2.3. Reproduced from [26]. Schematic of a neutron scatter event in a monolithic volume.....	29
Figure 2.4. Reproduced from [53]. Model of the optically segmented compact NSC design. ....	31
Figure 2.5. Reproduced from [55]. Schematic diagram of the gamma-ray OCA detector system. ....	33
Figure 3.1. Left: hit patterns with 1, 2, 3, 20, or 500 detected counts (from top to bottom). Right: Corresponding images reconstructed using cross-correlation. ....	39
Figure 3.2. Rank-17 MURA mask pattern used for demonstration; black pixels are transparent and white pixels are opaque. ....	40
Figure 3.3. Comparison of values computed using Eq. 3 (open circles) and directly (open squares). ....	46
Figure 3.4. Schematic diagram of the simulation geometry. ....	47
Figure 3.5. Probability of obtaining the correct source location as a function of the number of detected photons, shown for a range of MURA coded-mask ranks. a) 1-D mask patterns. b) 2-D mask patterns.....	50
Figure 3.6. Comparison of P values produced using Eq. 3, the direct calculation, and the Monte Carlo result. ....	51

Figure 3.7. Average number of photons required to obtain the correct location as a function of the number of mask pixels. Solid lines are computed from the Monte Carlo data and dashed lines are computed using Eq. 3.....	52
Figure 3.8. Schematics of all four initial designs: a) Design A, b) Design B, c) Design C, d) Design D. Blue regions are scintillator, green regions are light guides, gray indicates photodetector, yellow areas are retroreflectors, and dashed black lines show the mask planes.....	56
Figure 3.9. Peak counts (weighted average of the two sides) as a function of distance from the mask (depth). The emission point was truly at 4.5 cm, where a 1 MeV energy deposition released about 1680 photons. ....	61
Figure 3.10. Peak counts (weighted average of the two sides) as a function of distance from the mask (depth). The emission point was truly at 1.5 cm, where a 200 keV energy deposition released about 275 photons. ....	62
Figure 3.11. Peak counts and reconstructed X image for two 20 MeV depositions in Design B. The locations were at the same XY position and separated by 4 cm in Z.	64
Figure 3.12. Peak counts and reconstructed X image for two 20 MeV depositions in Design B. The locations were at the same Z position and separated by 5 cm in X...	64
Figure 3.13. Comparison of X and Z localization performance for Designs B (red) and D (black). Solid lines were produced using the cross-correlation, and dashed lines were produced by taking the center of mass of the hit maps for comparison. Each plot contains about 30,000 events. ....	65
Figure 4.1. Screen capture of the Geant4 simulation geometry for the OCA Slab Prototype. Open mask elements are shown in yellow and magenta indicates closed elements. The retroreflector is shown in gray and ESR is shown in red. The green track coming from the top and exiting the bottom is the incident neutron, and the other tracks are optical photons. ....	69

Figure 4.2. Screen capture of an event where a neutron was incident from the bottom, scattered once in the lower slab, then scattered again in the upper slab. Green lines indicate neutron and optical photon tracks, and red dots indicate when a track hits or crosses a volumetric boundary.....	70
Figure 4.3. The same neutron scatter event as in Figure 4.2, but from an orthogonal view. ....	71
Figure 4.4. Absolute photodetection efficiency as a function of position in a single slab of the OCA Slab Reference Design.....	74
Figure 4.5. Transit time of photons from emission point to detection in the MAPMT. There was 3 cm of light guide between the bottom of the scintillator and the phototubes, resulting in the 300 ps offset. ....	74
Figure 4.6. Detected hit map (black) and expected hit map from the response table (red), using the true scatter location. ....	77
Figure 4.7. Annotated plots of the software focusing (top) and final decoded image (bottom). The reconstructed positions are shown (truth: (2.20, -1.66) cm).....	78
Figure 4.8 Log-scale $\Delta X$ distributions using the COM on the whole image (black), fitting with a Gaussian (red), and using the COM on only the peak bin and its nearest neighbors (blue). ....	80
Figure 4.9: X resolution as a function of detector pixel size and number of peak bins used in the COM calculation. Solid lines are produced using aliased images whereas dashed lines use anti-aliased images.....	82
Figure 4.10. Heat map of probabilities for a single event using the ML approach. Locations were identically zero when a pixel behind a mask element detected a photon. The red dot indicates the true interaction location.....	84
Figure 4.11. Heat map of inverted $\chi^2$ values for the example event. ....	85

Figure 4.12. Heat map of inverted, negated log-likelihood values. The true source position is shown as a red dot. ....	86
Figure 4.13. Schematic diagrams (not to scale) of the reference detector geometry. Left: side view. Middle: another side view. Top right: top view. Bottom right: CAD drawing, with the scintillator shown as turquoise, the light guides shown as green, and the mask plane shown as purple. ....	89
Figure 4.14. Performance of the OCA Slab Reference Design. The distributions are fit with a Gaussian superposed with a linear offset. The means and standard deviations are shown in the top right. ....	90
Figure 4.15. Simulated spatial, timing, and energy performance of the OCA Slab Prototype Design. These are comparisons of reconstructed and true values for neutron scatter interactions in which at least two slabs triggered (at least 10 photons detected). ....	103
Figure 4.16. Left: backprojected image using reconstructed neutron scatter information. Right: backprojected image using the truth information. There are 6086 events in the images. ....	105
Figure 4.17. Simulation of optical crosstalk in the prototype detector. Roughly 10% of the light goes to each neighbor. ....	106
Figure 5.1. Picture of a single bare slab. The closest end in the image is the side viewed by the MAPMT. Small, thin lines appear at the edges where slab pieces were joined together. The mask pattern seen on the side closest to the viewer is an optical illusion of the mask projected through the light guide. ....	108
Figure 5.2. Pictures of the 3-D printed enclosure with a single slab placed inside, showing how the slabs sit when placed. ....	109

Figure 5.3. 3-D printed enclosure for the slab modules and MAPMTs. The breakout board sits in place on top and the side plate is below. ....	111
Figure 5.4. Breakout board to provide MCX connectors for 192 anodes and 3 dynodes from the MAPMTs. The bottom hosts rows of pins for the MAPMTs to plug into. ....	112
Figure 5.5. Image of the slab assembly, clamped, with inter-gap layers in place. ....	113
Figure 5.6. Glued surface after allowing it to dry and peeling off the parchment paper. ....	115
Figure 5.7. Picture of the finished slab assembly. Minor defects are visible due to bubbles in the glue, along with some wicking into the gaps. ....	116
Figure 5.8. Top left: finished slab assembly. Top right: slab assembly coupled to the phototubes with grease. Bottom left: the enclosure as it was slipped over the assembly. Bottom right: assembly fully in the enclosure with two sheets of ESR covering the side, with the side plate removed. ....	117
Figure 5.9. Front and back views of the completed prototype detector assembly. The three high voltage cables from the three H12700s are visible, along with 192 MCX anode outputs and 3 dynode outputs. ....	118
Figure 5.10. Picture of the fully wired prototype mounted inside the dark box before the box was extended. 192 anode cables are connected to the prototype, with 72 connected to the summation board. High voltage cables are gray and connected to a common source. ....	120
Figure 5.11. Picture of the pegboard used to hold the optical fiber up to the MAPMT anodes. ....	122
Figure 5.12. Image of the gain calibration setup inside the dark box. The MAPMT was mounted in an aluminum chassis. The laser fired from the left, was diffused, then was piped into the optical fiber, which plugged into the pegboard. ....	122

Figure 5.13. Pulse integral spectrum for a representative anode, fit with Eq. 5.1. ....	124
Figure 5.14. Individually normalized gain-QE heat maps measured using the optical fiber experiment.....	125
Figure 5.15. Measured gain-QE heat maps normalized to the highest-gain anode out of all three.....	125
Figure 5.16. Schematic of the readout and data acquisition system for the experimental prototype. ....	127
Figure 5.17. Diagram of a block of scintillator with black side walls, a photosensor on the bottom, and a reflector on top. Three different types of reflections are shown, with solid lines indicating emitted photons and dashed lines indicating reflected photons. ....	130
Figure 5.18. Schematic diagrams of a) microsphere retroreflectors and b) microprism retroreflectors. Reflective material is shown in gray. Retroreflective sheets are made by closely arraying these microstructures on a flat surface. ....	130
Figure 5.19. Photo of the five tapes studied. The polygonal features are 3-4 mm and the tapes are attached to 3-D-printed slides. ....	134
Figure 5.20. Microscope images of the reflective tapes. All five images are the same scale.....	136
Figure 5.21. Zoomed-in optical microscope images, taking the central 500×500 pixels region of the pictures in Fig. 4. Microprisms are evident in the top left, top right, and bottom right images, whereas microspheres are shown on the other two: top middle and bottom left. ....	136
Figure 5.22. Closeup of the beamsplitter, photodiode, rotation stage, sample holder, and camera. A beam spot produced by a red laser during alignment is also visible at the center of the sample. ....	138

Figure 5.23. Camera images with the beam incident normal to the tapes. The directly transmitted beam spot is seen in the bottom images (solid circle), while the partial reflection off the tape (dashed circle) is visible in two of the images. ....	144
Figure 5.24. Camera images with the beam incident $5^\circ$ relative to normal.....	145
Figure 5.25. Camera images with the beam incident $25^\circ$ relative to normal.....	146
Figure 5.26. Camera images with the beam incident $40^\circ$ relative to normal.....	147
Figure 5.27. Relative retroreflected intensity as a function of incident beam angle. ....	148
Figure 5.28. $^{133}\text{Ba}$ spectra from the central beam location for every surface treatment. All eight distributions have the same number of counts. ....	150
Figure 5.29. $^{133}\text{Ba}$ spectra, zoomed-in on the Compton edge. Fits with the error function are shown. ....	150
Figure 5.30. Solid: reconstructed $X$ positions for two beam locations and four surface treatments: Oralite tape (blue), air (brown), Teflon (green), and black paint (black). Dashed lines show fits using a Gaussian with a linear baseline. ....	152
Figure 5.31. Measured intrinsic spatial resolution as a function of lateral position in the detector. A beam spot size of 1.6 mm FWHM was subtracted in quadrature. ....	154
Figure 5.32. $X$ -projection of 30,000 anode hit maps from the middle beam location, integrated across the two central $Y$ rows of anodes. Events are selected from the Compton edge region.....	156
Figure 5.33. Hit maps from Figure 5.32 with the black paint hit map subtracted from the others.....	156
Figure 5.34. Picture of the experimental calibration setup. ....	162



Figure 5.35. Count rate as a function of beam position. The phototubes were at the top of the image. Count rates are shown for 37 X positions and 12 Z positions with 5 mm separation in both dimensions.....	162
Figure 5.36. Example pulses from a single scatter event. The incident gamma ray deposited about 150 keV into slab 1.....	164
Figure 5.37. Waveforms from a ~300 keV energy deposition in one of the hardware summed slabs. There is an electronic reflection, caused by an impedance mismatch in the summation circuit board, around 20 ns after the real pulse. ....	165
Figure 5.38. Hit map generated from the pulses pictured in Figure 5.36. About 150 keV was deposited in the slab at $Y = -9$ mm. Light seen in the slab below was likely due to optical crosstalk. ....	165
Figure 5.39. $^{133}\text{Ba}$ energy spectra from all five fully instrumented slabs for a central beam location, after calibration. ....	166
Figure 5.40. Simulated energy spectrum for a $^{133}\text{Ba}$ point source placed in the center of a slab. ....	167
Figure 5.41. Heat map of $1/\chi^2$ values from fitting the spectrum for a single slab from a central beam location. A maximum (the best fit) is visible at (3.8, 0.16).....	169
Figure 5.42. Overlaid simulated and experimental spectra for the best-fitting blur and scale factors identified in Figure 5.41.....	169
Figure 5.43. Relative PDE as a function of interaction (beam) position. ....	170
Figure 5.44. Average, normalized hit maps for different levels of event selection cuts for interactions near the center of a slab. In general, better event selection resulted in relatively higher peaks and lower valleys in the distribution. ....	171

Figure 5.45. Normalized, average hit maps at three different beam positions. The green data are from the beam location closest to the MAPMTs, the red data are from the middle, and black data are from a far corner. ....	172
Figure 5.46. Hit map COM values as a function of beam position for a single slab. Each data point has between 500 and 5000 events, depending on location. ....	174
Figure 5.47. Hit map widths (standard deviations) as a function of beam position for a single slab. Each data point has between 500 and 5000 events, depending on location.....	174
Figure 5.48. Means of Gaussian fits of reconstructed $X$ positions at each beam location. The anomalous values were caused by poor fits.....	176
Figure 5.49. Standard deviations of Gaussian fits of reconstructed $X$ positions at each beam location. The anomalous values were caused by poor fits. ....	176
Figure 5.50. Means of Gaussian fits of reconstructed $Z$ positions at each beam location. The anomalous values were caused by failed or poor fits. ....	176
Figure 5.51. Standard deviations of Gaussian fits of reconstructed $Z$ positions at each beam location. The anomalous values were caused by poor fits. Interactions furthest from the phototubes (bottom row) tended to bunch up against the edge, causing the fit to fail.....	177
Figure 5.52. Reconstructed $X$ positions for the three off-grid beam locations. Gaussian fits of each are overlaid. The means of the fits were in good agreement with the true beam location, extracted from the 2-D stage encoder.....	178
Figure 5.53. Reconstructed $Z$ positions for the three off-grid beam locations. Gaussian fits of each are overlaid. The actual beam locations were extracted from the 2-D stage encoder. ....	178

Figure 5.54. Reconstructed interaction positions for the data set where the beam was pointed at the middle of the slabs. ....	179
Figure 5.55. Reconstructed energy spectra for all five fully instrumented slabs when a $^{137}\text{Cs}$ source was placed next to the detector. ....	181
Figure 5.56. Time difference between the fission chamber, extracted from the digitized CFD signal, and the assumed first gamma ray scatter, determined from a 50% CFD on the slab pulse.....	182
Figure 5.57. Schematic of the data acquisition setup for the $^{252}\text{Cf}$ fission chamber measurement. ....	183
Figure 5.58. Picture of the experimental setup. The prototype detector was inside the dark box on the right while the chamber was mounted outside the box and shielded with lead bricks. The chamber was not installed in this picture. ....	185
Figure 5.59. a) 500 overlaid waveforms of the leading edge of the fission chamber CFD signal. b) Spectrum of chamber trigger times, corresponding to the particle's time of flight.....	186
Figure 5.60. Deposited energy correlations between slabs with different levels of separation. 110,000 events from the first fission chamber location are shown. The left image shows the correlation for well separated slabs. The middle shows two slabs separated by a single slab. On the right is the energy correlation between two neighboring slabs, with the lines for threshold ceilings depicted in red. ....	188
Figure 5.61. Slab pulses for the demonstration neutron double scatter event. Vertical lines highlight the trigger times for the two slabs that triggered. Slab 0 was the closest fully instrumented slab to the source, while slab 4 was the furthest from the source. ....	190

Figure 5.62. Hit patterns for the example event. The very bottom and top two slabs ( $Y = -21, 15$ , and $21$ mm) were summed in hardware. The fission chamber was in the $-Y$ direction. ....	191
Figure 5.63. Backprojected images of neutron double scatters events for a source mimicking the experimental setup at the first source location. Left: reconstructed using realistic detector parameters, detailed in Section 4.1. Right: reconstructed using the scatter truth information (e.g. a perfect detector). The images contain 493 events. ....	192
Figure 5.64. Backprojected images of neutron double scatters events for a source mimicking the experimental setup at the second source location. Left: reconstructed using realistic detector parameters. Right: reconstructed using the scatter truth information (e.g. a perfect detector). The images contain 195 events. ....	192
Figure 5.65. Backprojected image of neutron double-scatter events at the first source location, 35 cm away. The true source location was approximately $(270^\circ, 90^\circ)$ . ..	194
Figure 5.66. Reconstructed incident neutron energy spectrum from the first source position. ....	194
Figure 5.67. Picture of the fission chamber at the second source position, which was closer to the floor. ....	195
Figure 5.68. Backprojected image of the fission chamber at the second source location, 76 cm away. ....	196
Figure 5.69. Incident neutron energy spectrum at the second source location. ....	197
Figure 5.70. Compton image of the $^{252}\text{Cf}$ source at the first source position. The image contains 2659 reconstructed events out of a total of 6 million triggers. ....	199
Figure 5.71. Compton image of the $^{252}\text{Cf}$ source at the second source position. The image contains 1621 reconstructed events out of a total of 998,000 triggers. ....	200

# 1 INTRODUCTION

Fission-energy neutrons provide a specific, low-background, and highly penetrating signal for a variety of nuclear security applications because there are very few naturally occurring sources of these neutrons. For some applications, simply counting neutrons or performing neutron spectroscopy is sufficient. Others require neutron imaging in order to better distinguish signal from background and to localize the emitting object when the general location is not known *a priori*. Several methods are available to image or directionally localize fast neutron sources, such as the use of collimators [1], coded-aperture imaging [2], and neutron kinematic imaging using neutron scatter cameras (NSC), also known as neutron time-of-flight (TOF) detectors [3]–[7]. The first two approaches suffer from relatively low sensitivity due to the attenuation of source particles and a large footprint as a consequence of the need for a large low-Z collimator and its required support structure. NSCs generate cones of possible incidence directions for each neutron, which add together to highlight the source location in the field of view. They (and imaging in general) benefit from improved background suppression since neutrons coming from outside the region of interest (ROI) result in cones that mostly do not overlap with those that originate within the ROI and thus do not contribute to the background in that direction. However, NSCs tend to be large ( $\sim\text{m}^3$ ) and have poor geometric detection efficiency. The goal of this work is to design, optimize, and construct a more efficient and more compact ( $\sim 10\text{ cm}^3$ ) NSC than the current state-of-the-art systems by utilizing fast plastic scintillators, multi-anode photodetectors, and coded-aperture imaging to spatially and temporally localize the origin of scintillation light within the active volume. To achieve comparable angular resolution and improved efficiency to current systems, a compact NSC must be able to localize scatters to a volume approximately  $1\text{ cm}^3$  in size with a temporal resolution of 1 ns.

This dissertation begins by describing the basic mechanics of NSCs and detailing the functions and operating theory of the different components of the proposed detector system, including the scintillator, photodetector, digitizer, and retroreflector (Chapter 1). Chapter 2 is an overview of current state-of-the-art NSC systems, how they perform, and

a description of the three compact designs being pursued by this collaboration, where design trade-offs and expected challenges are discussed. Chapter 3 continues by exploring the feasibility of coded-aperture imaging for this application and examines a set of proposed designs, leveraging optical transport simulations to select the most promising detector. The first half of Chapter 4 describes and compares different event localization methods for the selected design, and describes the Monte Carlo radiation transport simulations (performed with Geant4 [8]) developed to understand its performance characteristics. Based on these simulations, design parameters were studied for an experimental prototype, and Chapter 4 concludes by presenting the simulated performance of the prototype system. Chapter 5 covers the experimental work performed to characterize and calibrate system components in preparation for prototype construction, such as the photodetector and retroreflective tape. A working prototype was constructed, and images of fast neutron and gamma-ray sources are reported at the end of Chapter 5. Finally, this work concludes in Chapters 5.6 and 6.1 with comparisons of the simulation and experimental results, lessons learned, and future work.

## **1.1 Neutron Scatter Cameras**

NSCs use conservation of momentum and energy to kinematically constrain the incident direction and energy of a neutron that scatters sequentially off two protons in the detector volume. The recoiling proton directions are typically not known, so the incident neutron direction can only be limited to the surface of a cone whose opening angle is twice the scattering angle of the neutron. The cones are back-projected into 3-D space and many such double-scatter events generate many cones, whose overlaps create a hot spot, indicating the presence and direction to a fast neutron source.

Early NSCs were developed by astrophysicists in the mid-1960's to study very energetic (20 – 120 MeV) neutrons generated by solar cosmic rays [9]. The directional sensitivity of NSCs allows one to distinguish between neutrons coming from space and those coming from Earth. This development continued into the 1970's, 1980's, and beyond through experiments such as SONTRAC [10], [11]. NSCs were also used for fusion

plasma diagnostics [5] to detect 2.45 and 14.1 MeV neutrons resulting from deuterium-deuterium (D-D) and deuterium-tritium (D-T) fusion, respectively. The spatial distributions and energy spectra of these neutrons in the lab frame reveal information about the plasma conditions, so NSCs are a useful tool in this context. Over the last 20 years, there has been increased interest in using these instruments to identify and localize special nuclear material (SNM) that emits fission-energy neutrons [12], and it is for this purpose that this work is undertaken.

The example NSCs referenced above use a variety of detector geometries to detect neutron double-scatters. A typical approach is to have optically isolated cells of scintillator so that the light generated by each interaction is captured separately and is thus easier to analyze than the convolved distributions of light from both scatters in the same detector volume. This also means that detected scatters are necessarily separated by a significant distance, which affects the detection efficiency and imaging resolution. Modern systems employ many such scintillator cells to improve the overall geometric efficiency [13], [14]. Figure 1.1 illustrates the interaction geometry for the traditional two-plane NSC configuration.

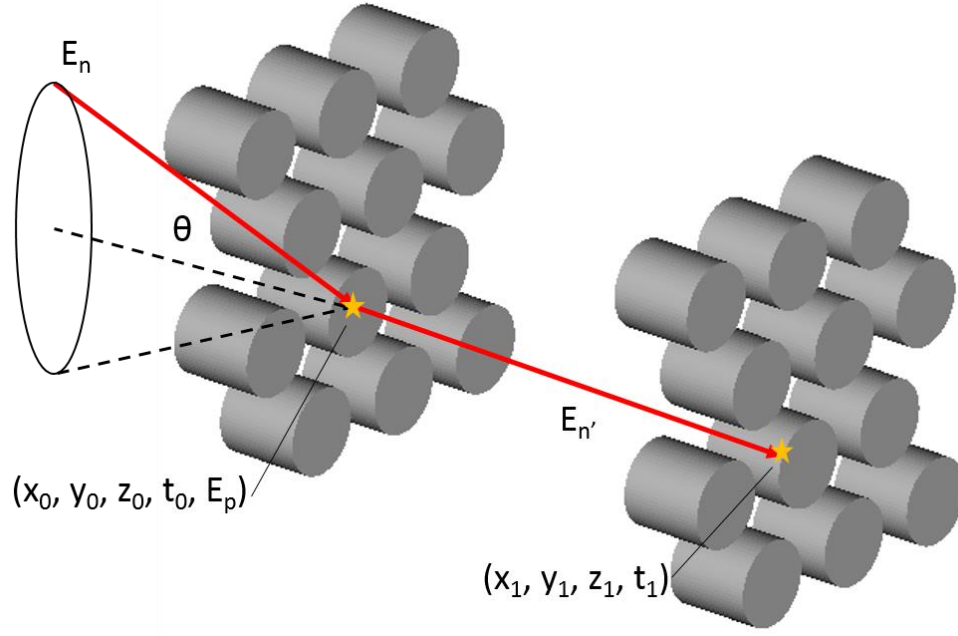


Figure 1.1. Schematic of traditional two-plane NSC geometry. An incident neutron with energy  $E_n$  is scattered by angle  $\theta$  as it transfers  $E_p$  to a proton. The scattered neutron with energy  $E_n'$  interacts again in the back plane a few nanoseconds later.

Suppose a neutron with kinetic energy  $E_n$  is incident on the detector volume and elastically scatters at least twice off of two or more different protons. If  $E_n'$  is the scattered neutron kinetic energy and  $E_p$  is the recoiling proton kinetic energy, then using conservation of energy, the incident neutron's kinetic energy is found from:

$$E_n = E_p + E_n' \quad (1.1)$$

$E_p$  is measured directly by observing the amount of scintillation light produced by the recoiling proton. If one assumes that the neutron is non-relativistic,  $E_n'$  is calculated by using the distance,  $d_{10}$ , and time,  $t_{10}$ , between the two scatters:



$$E_{n'} = \frac{1}{2} m_n \left( \frac{d_{10}}{t_{10}} \right)^2 \quad (1.2)$$

In this expression,  $m_n$  is the rest mass of the neutron. The scattering angle,  $\theta$ , of the deflected neutron can be found via conservation of momentum and algebraic manipulation. The momentum balance equation is:

$$\vec{p}_n = \vec{p}_p + \vec{p}_{n'} \quad (1.3)$$

Here,  $\vec{p}_n$ ,  $\vec{p}_{n'}$ , and  $\vec{p}_p$  are the incident neutron, scattered neutron, and recoil proton's momenta in the lab frame, respectively. Rearranging to isolate  $\vec{p}_p$ , squaring both sides, and expanding the terms, one obtains:

$$p_p^2 = p_n^2 + p_{n'}^2 - 2p_n p_{n'} \cos\theta \quad (1.4)$$

For a non-relativistic, massive particle, the momentum is simply  $p^2 = 2Em$  where  $E$  is the kinetic energy and  $m$  is the mass. Substituting into Equation 1.4,

$$E_p m_p = E_n m_n + E_{n'} m_n - 2\sqrt{E_n m_n E_{n'} m_n} \cos\theta \quad (1.5)$$

Now all that remains is to solve for  $\theta$ . To simplify the expression, neutron and proton masses are taken as equal (939.57 MeV/c<sup>2</sup> and 938.28 MeV/c<sup>2</sup>, respectively) and thus cancel out. Finally, one obtains the scattering angle,  $\theta$ , of the deflected neutron relative to its incident direction:

$$\theta = \cos^{-1} \sqrt{\frac{E_{n'}}{E_n}} \quad (1.6)$$

The traditional, two-plane implementation of the NSC involves planar arrays of cylindrical or cubic organic liquid or plastic scintillator cells that are each ~25 cm<sup>3</sup> (Figure 1.1). Incident neutrons scatter in the front plane and again in the back plane, allowing measurement of  $E_p$ ,  $d_{10}$ , and  $t_{10}$  and consequent calculation of the scattering angle  $\theta$ . Comparatively, for the compact NSC effort, the aim is to measure the same

quantities but generally with much higher resolution and in a much smaller active volume.

## **1.2 Fast Plastic Scintillators**

For more than a half century, scintillators have proven an effective medium to perform radiation spectrometry, particle identification, and imaging [15]–[17]. Scintillators commonly come in organic or inorganic forms, and depending on which, may be liquid, plastic, crystalline, glass, or ceramic. For the compact NSC, ultra-fast timing performance and fast neutron sensitivity are required, so plastic scintillators are a natural choice.

Organic scintillators tend to have very fast rise and decay times ( $\sim$ ns) and a high concentration of hydrogen atoms. Plastic scintillators are also cheaper and easier to shape and cut than crystalline scintillators. These benefits generally come at the cost of material density, and light output [18]–[21]. Table 1.1 lists common properties of interest for a selection of Eljen Corporation plastic scintillators (EJ-2xx), an organic liquid scintillator (EJ-301), and NaI(Tl) for reference.

Table 1.1. List of relevant scintillator characteristics for a selection of reference materials and candidate plastic scintillators.

<b>Material</b>	<b>Light Output (<math>\gamma</math>/MeVee)</b>	<b>10-90% Rise Time (ns)</b>	<b>Decay Constant (ns)</b>
NaI(Tl)	38,000	34	287
EJ-301	12,000	N/A	3.16, 32.3, 270*
EJ-200	10,000	0.9	2.1
EJ-204	10,400	0.7	1.8
EJ-208	9,200	1.0	3.3
EJ-212	10,000	0.9	2.4
EJ-232	8,400	0.35	1.6
EJ-232Q**	2,900	0.11	0.7

\* Has multiple, slower decay components to enhance pulse shape discrimination.

\*\* 0.5% benzophenone.

As charged particles traverse an organic scintillator and deposit energy, electrons are excited from the ground state ( $S_0$ ) into spin-0 singlet states, denoted  $S_1$ ,  $S_2$ , etc., for the first and second excited states, respectively. The charged particles could originate from an external source or could be recoil products from the interaction of indirectly ionizing radiation. Once excited, the electrons may quickly ( $\sim$ ns) decay back to the  $S_0$  state, emitting light via prompt fluorescence [22]. Alternatively, they may decay to an excited

triplet state (spin 1, denoted  $T_1$ ) via intersystem crossing, with a significantly longer half-life than the singlet states. From this state, there are two decay paths: to  $S_0$  (phosphorescence), or back to  $S_1$ , ultimately decaying back to  $S_0$  (delayed fluorescence). The excitation and decay pathways taken by energized electrons in the scintillator determine the time and wavelength profiles of the emitted scintillation light. The relative intensities of the different decay modes ultimately give way to pulse shape discrimination (PSD) capability, that is, the ability to discriminate between neutron and gamma-ray energy depositions. Scintillators exhibiting PSD tend to produce a higher fraction of triplet states and thus enhance the phosphorescence component of the scintillation light emission profile. The production of triplet states depends chiefly on the ionization density, which differs significantly between recoil electrons and protons. If one takes the ratio of light in the prompt vs. tail segments of the pulse, a bimodal distribution results, where one peak is associated with gamma rays and the other with neutrons [23].

While PSD is a desirable long-term quality of the compact NSC system, its demonstration is not necessary for the success of the prototype design. Differentiating between neutrons and gamma rays is possible using the time of flight between interactions, and in the lab, one can generate relatively isolated neutron signals by triggering in coincidence with a fission chamber or fast neutron generator, which is sufficient for testing the neutron imaging capability of the system. To this end, the fastest and brightest scintillator should be chosen, regardless of PSD capability. Out of the choices presented, EJ-232Q has the fastest timing profile, however the light output is very poor, and there are potentially complicating issues with absorption and re-emission that would compromise the spatial distribution of scintillation light. Therefore, EJ-204 was selected for most of the work presented in this document due to its optimal combination of light output and fast decay time among commercial fast-plastic scintillator offerings.

When this work started, the light output of scintillators with similar formulations to EJ-204 had been experimentally measured and were available in the literature [24]. Figure 1.2 shows the proton light yield relative to electrons in BC-420, equivalent in formulation

to EJ-212 (Table 1.1). We expected the light yield response as a function of energy to be nearly identical between EJ-204 and EJ-212 because of their very similar material properties.

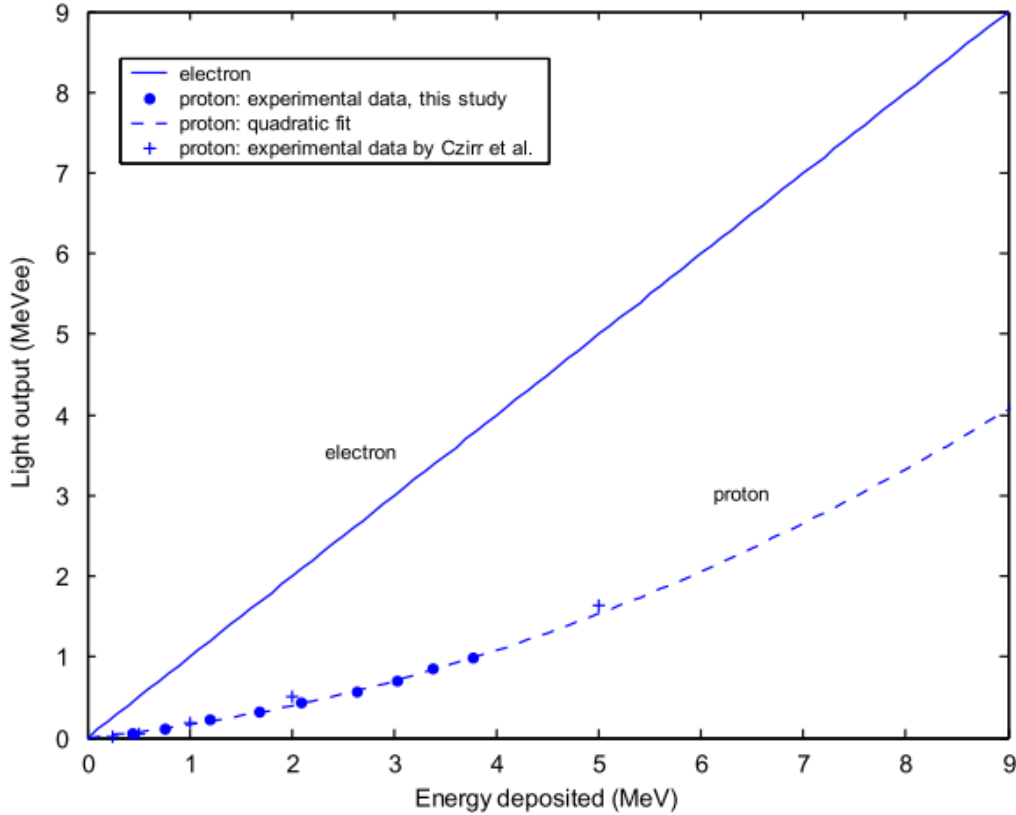


Figure 1.2. Reproduced from [24]. Energy equivalent light output of BC-420, equivalent to EJ-212, as a function of energy deposited, relative to electrons.

While this work was being performed, our collaborators at UC Berkeley measured the proton light yield of several scintillators including EJ-204 using a double time-of-flight experiment [25]. Figure 1.3 shows these values for comparison.

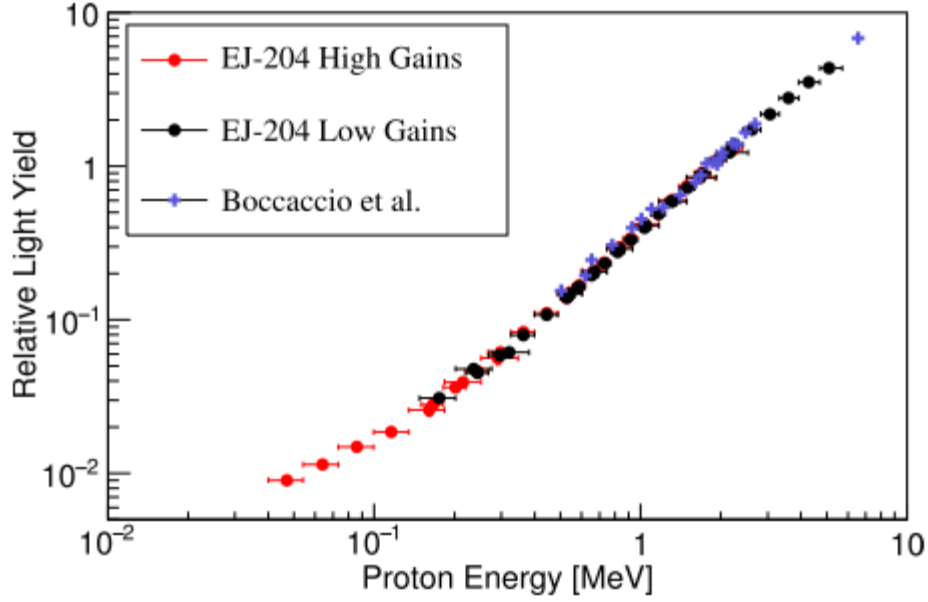


Figure 1.3. Reproduced from [25]. Proton light yield relative to the electron light yield for EJ-204. Note that the ordinate axis is in light yield, which is different than the energy equivalent MeVee units shown in Figure 1.2.

Since the new data did not come until later, the initial set of optical transport simulations, presented in Sections 3.2 and 3.2.5 utilize the relationship shown in Figure 1.2. The full physics simulations and experimental interpolation presented starting in Chapter 4 made use of the newer values measured by UC Berkeley [25].

### 1.3 Multi-anode Photodetectors

To capture the light emitted by the scintillator as a result of incident radiation depositing energy, one must use very sensitive photosensors that can resolve single photons. This is because, once the overall photodetection efficiency is considered, not many photons are expected to be detected in the compact NSC for a nominal energy deposition. Imagine,

for example, a neutron scattering off of a proton in EJ-204 and depositing 300 keV. Using the curve from Figure 1.1 and the light yield from Table 1.1, on average, 474 photons will be emitted. For a simple cubic geometry instrumented on every side with photodetectors such as the one proposed by [26], each one will observe 79 photons, reduced further by a typical quantum efficiency (QE) of e.g. 33%, bringing the total down to 26 photons detected per side. Spread across a photodetector surface made up of an 8×8-pixel array, the average occupancy is less than 1, which means single photon resolution is required.

In addition to single photon sensitivity, the compact NSC also demands photodetectors that are as fast as possible, which primarily means minimizing the rise time and transit time spread (TTS). There are three types of commercially available photodetectors that potentially meet both the photon detection sensitivity and timing requirements in the wavelength regime of interest. They are briefly described below.

### ***1.3.1 Photomultiplier Tubes***

Multi-anode photomultiplier tubes (MAPMT) are a promising option for the compact NSC due to high gains, fast timing, and acceptable fill factor. MAPMTs that would be appropriate for the compact NSC consist of arrays of pixels, with typically 8, 16, or 32 per side, with 6, 3, or 1.5 mm pixel sizes, respectively. Incident light passes through the entrance window (e.g. borosilicate glass) and then strikes a photocathode, liberating a photoelectron (a single low energy electron) that is electrically directed to the dynode amplification chain. At each step, electrons slam into the dynode, liberating even more electrons, that are then directed to the next dynode stage. Typical gain factors through the chain are on the order of  $10^6$ .

Prospective commercial MAPMTs for this effort include the series of offerings from Hamamatsu Photonics K.K. such as the H8500 and H12700. These phototubes have 8×8-pixel arrays with individual pixels that are 6×6 mm<sup>2</sup> in size and a TTS of 350 ps full width at half maximum (FWHM). The H12700 is the same as the H8500 but with a higher average QE across the sensitive wavelength range, 33% versus 25%, respectively.

Hamamatsu also offers the H9500/H13700, which are similar but instead have  $16 \times 16$  arrays of  $3 \times 3 \text{ mm}^2$  pixels. These MAPMTs have been used widely in nuclear physics and nuclear security and in general are well-characterized and understood.

One key drawback of using these devices is the presence of electronic crosstalk between pixels, that has multiple forms representing the possible sources [27]. One source crosstalk occurs when a photon strikes a pixel and some of the charge crosses into a neighboring pixel, where it is amplified and indistinguishable from a real photon hit in that pixel. The other most prominent source of crosstalk is due to capacitive coupling via the last dynode. This signal is bipolar, integrates nearly to zero, and appears everywhere in the phototube regardless of which pixel was struck. Both types of crosstalk have the effect of diminishing the ability to determine the number of photons that struck a given pixel due to additional variation on the signal amplitude. They also introduce complex correlations between pixels which can introduce biases in algorithms applied to the data.

Another drawback, particularly with the H12700, are reflections off of the photocathode causing photons to re-enter the scintillator, bounce around, then be detected later and possibly somewhere else. This has the advantage that a photon that otherwise may have been lost is instead detected, improving the effective QE. However, depending on the scintillator geometry, this can significantly distort the hit patterns observed by the MAPMT, degrading localization performance unless corrected. This issue is known but not well characterized in the available literature.

### ***1.3.2 Silicon Photomultipliers***

Silicon photomultipliers (SiPM) are a relatively recent addition to the field of pixelated photosensors. The SiPMs of interest for this work have 1.5-6 mm pixels and sensitivity to single photons. Like MAPMTs there is an entrance window, but instead of a photocathode, there is an array of silicon single photon avalanche diodes, each on the order of 10 microns in size. An incident photon photoelectrically liberates an electron in a microcell, which generates an avalanche in the reverse-biased p-n junction operated in Geiger mode. Each such microcell uses a quenching resistor to limit the discharge



Typical gains are similar to MAPMTs, around  $10^6$ , and QEs are around 25-50%, with higher QE values corresponding to devices that sacrifice elsewhere (e.g., the SiPM array has more nearest neighbor crosstalk).

Since each 1.5-6 mm SiPM pixel is effectively an independent device, the capacitive crosstalk seen with the MAPMTs is not observed with SiPMs. However, SiPMs are semiconductors with a narrow ( $\sim 1$  eV) band gap and therefore have high dark count rates ( $\sim 10^5/\text{mm}^2/\text{s}$  [28]), that are the result of a thermally excited electrons generating an avalanche in the diode. For comparison, MAPMTs have dark count rates on the order of  $10/\text{cm}^2/\text{s}$ , which is very unlikely to be observed in a typical  $\sim 10$  ns integration window. In SiPMs, such avalanches are indistinguishable from avalanches caused by electrons freed by scintillation photons. This means that SiPMs are also relatively sensitive to fluctuations in temperature – less impactful in the lab, but something to consider when imagining an instrument that is fieldable. In addition to dark counts, there is also afterpulsing, that is a byproduct of charges getting stuck in metastable traps and being released at a later time [29]. These afterpulses come  $\sim$ nanoseconds after the primary pulse and care would need to be taken to ensure they do not interfere with the expected neutron double-scatter signal (e.g., with digital signal processing, or cooling).

Another consideration is that the SiPM signals need to be amplified and shaped to have single photon sensitivity due to their high capacitance. This can quickly increase the power and cooling requirements of the system due to the high channel count, which is in direct contradiction to the goal of portability. Separate from the possible amplification requirements, SiPMs in general have a lower footprint than MAPMTs, which makes them an attractive choice, particularly as the technology continues to mature.

### ***1.3.3 Microchannel Plate Photomultiplier Tubes***

Microchannel plate multi-anode photomultiplier tubes (MCP-PMTs) are another candidate technology for observing photons produced by the scintillator in the compact NSC system. Like the aforementioned MAPMTs, MCP-PMTs use a photocathode to convert photons to electrons. Instead of a dynode chain, the electrons are directed to a

glass plate with millions of small channels ( $\sim 10\text{ }\mu\text{m}$  diameter). A high voltage bias is applied across the plate, and as electrons transit the capillaries and bounce off the internal walls, additional electrons are liberated, causing amplification. Due to the nature of the system, exceptional spatial and timing resolution is possible with MCP-PMTs; for example, the Photek MAPMT253 boasts a TTS of less than 40 ps root mean square (RMS).

While promising, MCP-PMT technology is not as mature as PMTs, and unlike SiPMs, does not mitigate their major drawbacks, most importantly electronic crosstalk. The MCP-PMT is one large device, so electrons generated by the photocathode in one area may miss a capillary and bounce across the plate, ultimately being detected in the wrong location at a later time [30]. This manifests as crosstalk and afterpulsing, which can confuse or obscure a real neutron scatter signal.

## **1.4 Fast Digitizers**

So far, fast plastic scintillators and fast photodetectors have been described. Naturally, the performance of these components drives the requirements of the digitizers used to record the signals. Taking advantage of the pulse speed requires a correspondingly fast digitizer to convert the electrical signals, produced by each anode of the photodetectors, to a digital signal that can be recorded to disk and analyzed later. As mentioned before, a typical neutron scatter separation time is on the order of 2 ns, while the resulting pulses have characteristic rise and decay times of a similar magnitude. To realistically capture this information and have the fidelity to reconstruct the individual scatter locations and times, one expects to need a digitizer with a bandwidth of around 500 MHz and a sampling rate over 1 GHz to record the pulse shape. While it is possible that a lower sampling frequency and bandwidth would be sufficient with refined and efficient algorithms, one would like as much information as possible from the prototype system so that the performance can be understood with a high level of detail.

Sufficiently low noise to resolve single photoelectron signals and sufficient dynamic range to capture more energetic events are needed for the compact NSC. Not only must

signals be sampled quickly and quietly, but the selected digitizer must also enable a high channel count. Every proposed compact NSC design requires a relatively high number of channels, from 64 at the low end to 384 at the high end for the prototypes, with more channels possible as the designs scale up.

Two commercial VME-based digitizer boards are available that meet the basic performance requirements for the compact NSC prototype. These are made by different manufacturers and are based on different fast sampling chip technologies. Both products are described below.

#### ***1.4.1 CAEN V1742***

The CAEN V1742 digitizer is based on the Domino Ring Sampler version 4 (DRS4) chip developed by the Paul Scherrer Institut [31]. This chip is a switched capacitor array, where each capacitor holds the value of one sample of the waveform. The array is periodically read out with available sampling frequencies between 750 MHz and 5 GHz and a bandwidth over 500 MHz. Each board has 32 signal channels and 2 trigger channels which are all digitized and have a dynamic range of 1 V peak-to-peak with 12-bit resolution.

#### ***1.4.2 Struck SIS3305***

The SIS3305 digitizer by Struck Innovative Systeme GmbH employs a different chip than the CAEN V1742, using a product by e2v Technologies. This product can sample at the desired 5 GHz, but only for two out of eight channels with 10-bit resolution. Due to the low channel density, this product is not feasible for the initial prototype since an impractical number of boards would be required.

### **1.5 Localization in Bulk Scintillators**

For a compact NSC to be realized that does not sacrifice efficiency or imaging resolution, excellent multi-hit spatial and temporal resolutions must be achieved in localizing the interactions. While limited work has been performed on localizing fast neutron scatters within bulk scintillator volumes, the problem has been heavily studied for gamma-ray

applications, such as positron emission tomography (PET) and Compton imaging [32], [33]. This work provides some information on the types of methods that can be used and the limits on achievable performance. Localizing neutron scatters functions exactly the same as gamma ray scatters, since recoil electrons (from gamma-ray scatters) and protons (from neutron scatters) both generate scintillation photons locally and isotropically and therefore produce the same distribution of light in the same geometry. The key difference is proton energy quenching, which results in significantly less light from a neutron scatter than an equivalent energy deposition by a gamma ray, up to about 1 MeV (Figure 1.2).

In general, when centroiding a population of detected hits, the ability to localize a single interaction  $\delta x$  is fundamentally limited by the width of the light spot  $w$  at the photosensor and the number of photons  $N$  contained therein [34]:

$$\delta x \approx \frac{w}{\sqrt{N}} \quad (1.7)$$

The exact dependence of the resolution on the width and number of detected counts will be a consequence of the detector systematics and reconstruction method used; however, in general, two things are always true:

1. Wider light distributions (from interactions further away) exhibit correspondingly worse localization performance than narrower light distributions.
2. Less intense distributions (from lower energy interactions) exhibit correspondingly worse localization performance than brighter distributions.

When designing a detector system with spatial sensitivity, there are two general approaches to maximizing the use of information contained in the light distribution. One option is to have an optically contiguous volume, then to use one's understanding of the light transport to estimate the interaction position from the observed light distributions. This could be as simple as finding the centroid or could involve building a detailed model of the optical transport in the system and fitting it to the observed data. Either way, the complexity and challenges with this method are in understanding and filtering the data and in building an accurate model of the system.

The second approach, adopted to some extent by the medical imaging industry for the most advanced PET detectors, is to use optical segmentation to force photons produced by interactions at a given locations to be optically confined to a small area or volume, minimizing  $w$  in Eq. 1.7. In the case of detectors for PET, the scintillator is segmented into pillars, piping the light down to the photosensors in a way that it remains densely distributed. The depth information is generally lost since the light is not allowed to spread out, however the lateral position information is efficiently preserved. By using highly reflective materials to coat the internal walls of the pillars, the number of detected counts (corresponding to the energy resolution) is also maximized.

Both approaches are being explored by the collaborative effort to develop the compact NSC. This work will examine a hybrid concept, where optical segmentation is used in one spatial dimension, and coded-aperture imaging combined with a detailed response model of the detector is used to localize in the other two spatial dimensions.

## 1.6 Coded-Aperture Imaging

### 1.6.1 Background and Theory

Coded-aperture imaging is a technique that allows one to localize emissive particle sources [35], [36]. This capability is very powerful in situations where the particles of interest cannot be easily focused, as can be done with optical light. It was first developed to image astronomical x-rays and gamma rays, which are very difficult or impossible to focus with lens or mirror systems. Pinhole systems can be used, but at a very steep cost in detection efficiency. To overcome this shortcoming, multi-pinhole apertures were developed, eventually evolving into the coded apertures we use today.

In coded-aperture imaging, the incident particle flux is modulated using an aperture or coded mask pattern (Figure 1.4), where the feature size limits the achievable spatial resolution of the imaging system. The patterns can be produced a number of ways, such as randomly, pseudo-randomly, or with a specific set of features [37], [38]. This work examines the uniformly redundant array (URA) mask pattern and its sibling the modified

URA (MURA) [39], [40] pattern, which have ideal imaging characteristics and were demonstrated to be effective in previous work [33]. The mechanics and limits of these patterns are explained and reported in Section 3.1.

One way to understand the coded-aperture concept is to think of it as a hardware convolution between the source and mask distributions, the product of which is detected by a pixelated sensor. Reconstructing an image of the source is therefore an exercise in deconvolving the measured pattern using the aperture as a kernel.

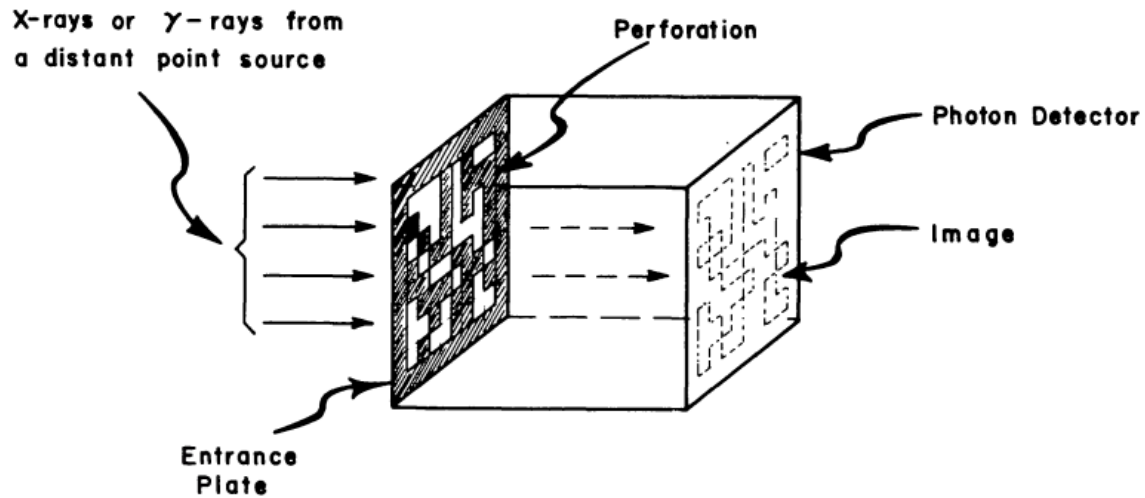


Figure 1.4. Reproduced from [36]. Schematic diagram of a coded aperture system, showing the shadow pattern projected on a pixelated detector by the mask.

As its development suggests, another way to conceptualize coded-aperture imaging is to imagine the coded mask as an array of pinholes. An image of the source is projected

through every pinhole, inverted and magnified depending on its distance from the pinhole and the distance from the pinhole to detector array (commonly known as the focal length). The ability to localize a source depends on the highest spatial frequency (pinhole size) present in the mask, explaining why the mask pixel size drives the achievable spatial resolution.

Mathematically, coded-aperture imaging can be represented by the following equation [39]:

$$\mathbf{I} = \mathbf{G} * \mathbf{D} \quad (1.8)$$

Where  $\mathbf{I}$  is a matrix representing the reconstructed image,  $\mathbf{D}$  is the detected hit pattern,  $*$  is the convolution operator, and  $\mathbf{G}$  is the decoding matrix.  $\mathbf{G}$  is essentially the mask pattern kernel and has a value of +1 for open elements and -1 for closed elements. Elements of  $\mathbf{I}$  are therefore maximized when large numbers of detected counts in  $\mathbf{D}$  overlap with open elements in  $\mathbf{G}$ , indicating the presence of a source. Section 3.1 contains a detailed mathematical explanation of how the coded-aperture image reconstruction is performed, with examples.

An important difference between the current application and astronomical observations is that, in the latter, sources are very far away, so the effective magnification is very close to 1. Conversely, in the near field, focal lengths may be on the same order as the distance between the mask and source. This means that the magnification may change significantly in the field of view (FOV). Fortunately, this creates an opportunity: with a fixed focal length, one can perform reconstruction assuming different source distances, then choose the best one (“software focusing”), yielding another spatial dimension of sensitivity [34]. An example is shown in Figure 1.5 for a simulated coded-aperture imaging scenario. A 2-D mask (top left) modulated a point source, producing the hit pattern in the top right. The hit pattern was decoded at a range of source distances in 1 mm steps and the source peak intensity plotted on the bottom right. The peak is clearly

visible at the true location, 3.5 cm from the mask. The bottom right image shows the 2-D reconstructed coded-aperture image using the extracted source distance.

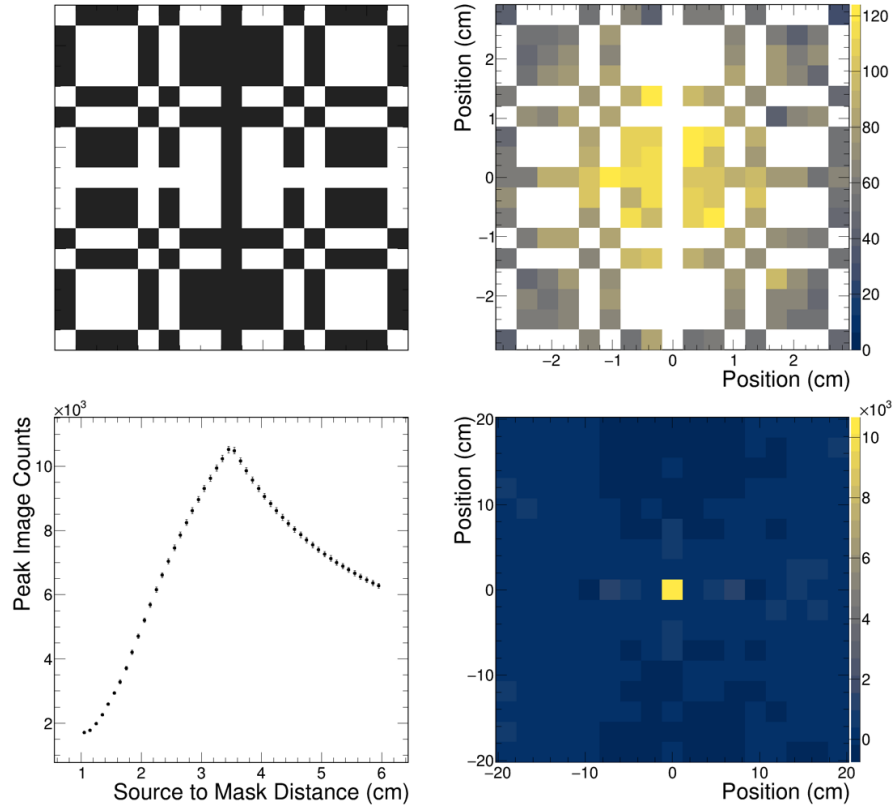


Figure 1.5. Demonstration of software focusing using a coded-aperture system with a 5 mm focal length. Top left: 2-D rank 17 MURA pattern used. Top right: hit map of over 10,000 detected counts. Bottom left: peak counts as a function of assumed source distance, showing a peak at the true location. Bottom right: final reconstructed image.



Coded-aperture imaging in the near field was employed for the spiritual predecessor to this work [33] and was demonstrated to perform as expected. It has also been studied for use in medical imaging [41] and, as a result of this track record, was determined to be suitable for this application.

As shown with the gamma-ray system, the mask pattern can be repeated due to the cyclic nature of the aperture. Instead of requiring a large rank pattern to cover the entire area of the photodetectors, a lower rank pattern was repeated instead. While the projection of light will be most intense behind the cycle of the mask where the interaction occurred, counts under the other cycles can simply be added and utilized. In practice, this was accomplished by first centroiding the hit pattern to find which mask cycle the event occurred over, adding all detected counts (with the correct offset) to the primary region, then decoding.

### ***1.6.2 Anti-aliasing***

In images, aliasing is pixilation of the items in the image, particularly noticeable at the edges of shapes, due to the output image resolution being too low. The video game and movie industries have developed a number of sophisticated techniques, known as anti-aliasing, to address this problem and improve the visual quality of scenes rendered on-screen. One of the simplest ways help mitigate aliasing is called full-scene anti-aliasing (FSAA) [42]. FSAA works by producing the image at a higher resolution than the display, then down-sampling it, producing a smoother image since neighboring pixels are averaged together. To give a simple example, if there are two pixels that lie on a sharp transition from white to black when rendering at the target resolution, an anti-aliased image may instead have light and dark gray pixels, making the transition appear smoother.

In the coded-aperture imaging context, anti-aliasing is a useful tool to smooth out the reconstructed image. Smoothing the distribution makes the centroiding algorithm that is used to calculate the final position more reliable since there are fewer sharp transitions between adjacent pixels. In this work, anti-aliasing is emulated by oversampling the

magnified, detected hit pattern in software by a factor of two before performing the cross-correlation. This is subtly different than what is traditionally done, which is to physically oversample the mask pattern by choosing detectors with sufficiently small pixels compared to the mask pixel size [43]. In both cases, the result is a smoother-looking decoded image with twice as many pixels as the aliased image, as shown in Figure 1.6 for an infinitely far away point source and perfectly absorptive rank 17 1-D MURA mask pattern.

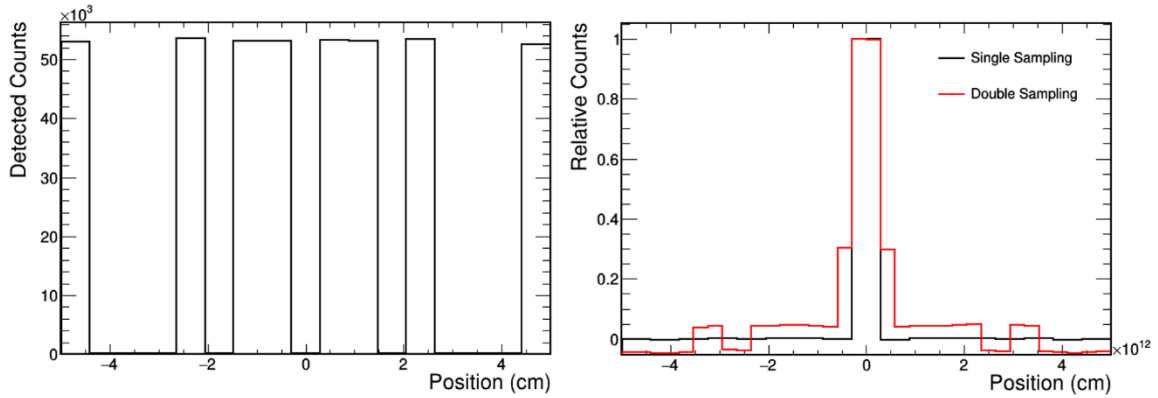


Figure 1.6. Left: hit pattern obtained by observing an infinitely far away (parallel beam) source. Right: decoded images, where black is single sampled and red is anti-aliased. The pattern is a 1-D rank 17 MURA.

As shown, a centroiding algorithm that considers the peak pixel and its two nearest neighbors would include the baseline pixels in the single sampled image (black). In the near field, these pixels may be artificially high or low due to solid angle artifacts, so this results in a biased value. Comparatively, when double sampled, the peak counts are spread across the core pixels, providing a smoother peak for the centroiding algorithm.

## 1.7 Retroreflectors

For many applications involving scintillators, the exposed (not occupied by photosensors) surface(s) of the active volume are covered with reflective material to redirect the light towards the photosensor, increasing light collection efficiency. Common materials include Teflon tape or white paint for diffuse reflection and Enhanced Specular Reflector (ESR) for specular reflection [44]. Figure 1.7 shows schematic drawings of the different types of reflection.

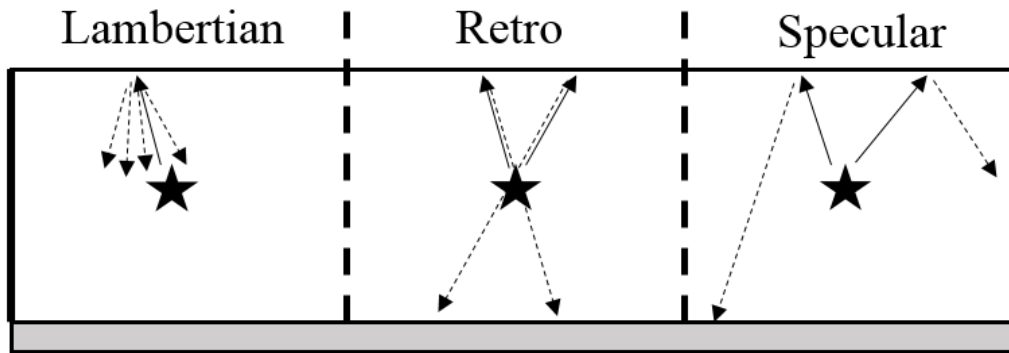


Figure 1.7. Schematic depiction of common types of reflection. Solid lines highlight the trajectories of emitted light and dashed lines represent reflected light.

A retroreflective surface is another type of reflective surface that redirects the light back along its incident direction, which in this case is back through the interaction site. In practice, this is typically accomplished with either spherical beads or corner cube structures (Figure 1.8); in both cases, the light is redirected  $180^\circ$  back along its incident direction, with a small offset that depends on the size of the microstructure.

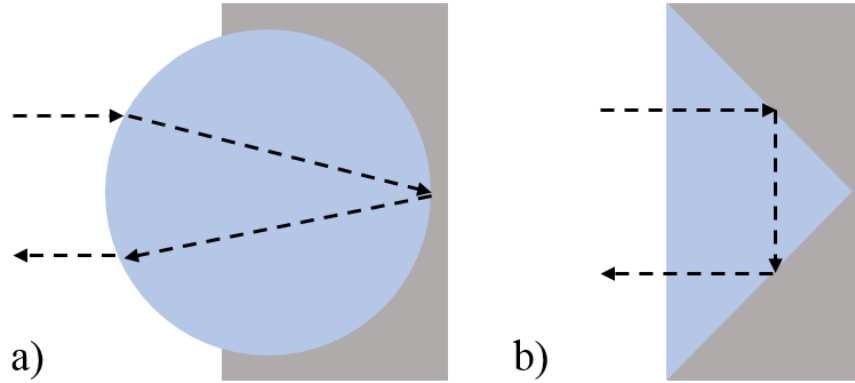


Figure 1.8. Diagram of a) spherical bead retroreflection and b) corner cube retroreflection. Optically transmissive material is shown as blue and specular reflector is shown as gray.

Retroreflectors are most commonly used to improve the visibility of road markings and words on road signage, causing light emitted by headlights to be reflected back to the driver. For this type of application, the retroreflector is typically in tape form, which is usually composed of many small corner cube structures. Bicycle reflectors and the Lunar Laser Ranging Experiment [45] are other examples of arrayed corner-cube retroreflectors, but with larger corner cube sizes. Examples of the spherical type of retroreflector are cat's and spider's eyes, which appear shiny ("eyeshine") in certain lighting conditions. The retroreflection is made possible by a reflective layer of tissue behind the eye called tapetum lucidum that aids night vision [46] and that is not found in humans.

Compared to the other types of reflections, retroreflections have additional potential to improve localization in bulk scintillators by both improving the counting statistics and narrowing the width of the light that arrives at the photosensors (Eq. 1.7). The magnitude of the added improvement depends on the scintillator geometry and the spatial

distribution of the radiation hits. For bulk volumes, retroreflectors work best for wide, thin crystals, since in this arrangement, the light reflected off the face opposite the photosensors is a significant fraction of the signal. As the scintillator gets taller, interactions can occur further from the photosensor, giving the light more room to spread; the width of the direct, un-reflected light spot therefore dominates the resolution. Using a retroreflector improves the counting statistics, benefitting the spatial resolution, while minimizing the spread of the reflected light.

Following a similar trend as event localization in bulk scintillators, information on the use of retroreflectors with scintillators is most abundant within the medical imaging community. This is because some of the detector types used for medical imaging, for example Anger cameras [47], stand to benefit significantly from improved optical conditions leading to higher quantities of light arriving at the photosensors with less dispersion. Making the surface of the scintillator retroreflective is accomplished by use of either a commercial tape [48], [49] or by embedding cubic structures into the scintillator itself and backing them with reflective material [50]–[52]. In all but one of these examples, retroreflectors were demonstrated to improve the localization performance. The one exception is [48], which did not realize an improvement over Teflon because the scintillator pixels were taller than they were wide. As explained previously, with this type of geometry, one does not expect to benefit from using retroreflectors.

## **2 PREVIOUS WORK AND SYSTEM CONCEPTS**

### **2.1 Two-Plane and Multi-Volume NSC Geometries**

As stated, a traditional approach to NSCs is to build two planar arrays of cylindrical liquid scintillator cells and backproject neutrons that scatter once in each plane. Figure 2.1 shows one such instrument designed by Sandia National Labs [7]. It had four 5-inch diameter, 2-inch thick scintillator elements in the front plane and 5-inch diameter and 5-inch thick cells in the back plane. The liquid scintillator was EJ-301.

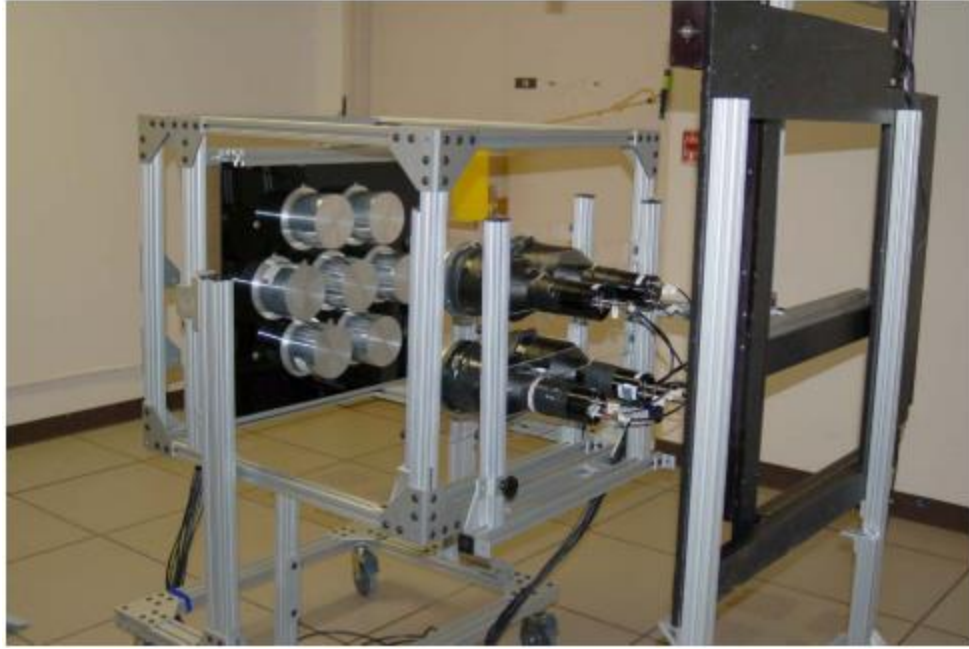


Figure 2.1. Reproduced from [7]. Picture of the two-plane NSC developed by Sandia National Labs. Two planes of scintillators are visible, along with a source-moving structure on the right.

This design was successful because neutrons could be effectively identified and backprojected due to the relatively large ( $\sim 10$ s of ns) travel time between planes, combined with the necessarily large lever arm ( $d_{10}$  in Figure 1.1 and Eq. 1.2). While the cells were somewhat large, what matters is that they were small relative to the size of the lever arm.

Using a similar principle, a more compact design was developed, also by Sandia National Labs (Figure 2.2) [14]. This too utilized liquid scintillator, this time EJ-309, in cells that were 3 inches in diameter and 3 inches thick. The smaller form factor allowed this device to be man-portable and battery operated. Compared to the current compact NSC effort,

this was still relatively large, with each cell having approximately the same volume as the prospective NSC designs.



Figure 2.2. Reproduced from [14]. Picture of MINER, the compact NSC using liquid scintillator cells.

## 2.2 Overview of Proposed Compact NSC Geometries

### 2.2.1 *Design Goals*

Three design concepts for a compact NSC are being concurrently developed under the umbrella of the Single Volume Scatter Camera (SVSC) collaboration. While there are commonalities in the detector readout, each takes a fundamentally different approach to

the problem of localizing double neutron scatters within a few centimeters and nanoseconds of each other in a compact volume. These different detector geometries each have their own benefits and pose their own challenges.

The first approach, referred to as the *monolithic* approach, employs a contiguous cube of fast plastic scintillator with pixelated photosensors on each side. A maximum likelihood-based algorithm is used to reconstruct the neutron interaction information [26]. The second, named the *optically segmented* approach, divides the scintillator volume into  $5 \times 5 \times 200 \text{ mm}^3$  (nominally) bars wrapped with reflective material and instrumented on the two square ends with pixelated photodetectors that match the bar pixel size [53], [54]. The final design, and the focus of this work, is the *optical coded aperture*, or OCA, approach, which uses coded-aperture imaging to spatially localize the scintillation light in a monolithic or partially-segmented volume [33], [55].

Regardless of detector geometry, each detector system aims to measure the three quantities required to determine the scattering angle and energy of the incident neutron:  $E_p$ ,  $d_{10}$ , and  $t_{10}$  (Eq. 1.1, 1.2, and 1.6). The fidelity with which these quantities can be measured is reflected by, and can be calculated from, the energy, spatial, and timing resolutions of the composite detector system. To achieve comparable imaging resolution as the current state-of-the-art systems, the compact NSC must (to first order) achieve spatial and timing performance that are better, proportional to the decrease in scatter separation distance and time. That is, the two-plane NSC constructed by Sandia National Lab [7] achieved approximately  $10 \times 10 \times 10 \text{ cm}^3$  spatial resolution with  $d_{10} \sim 50 \text{ cm}$ , and 2 ns timing resolution with  $t_{10} \sim 30 \text{ ns}$ . For a compact system, expected neutron scatter separations would be  $d_{10} \sim 2 \text{ cm}$  and  $t_{10} \sim 2 \text{ ns}$ , so a comparable, compact system should ideally achieve around  $1 \text{ cm}^3$  spatial resolution and 200 ps timing resolution.

### 2.2.2 *Monolithic Design*

The monolithic approach uses a contiguous cube of fast plastic scintillator instrumented on every side with pixelated photodetectors (Figure 2.3) [26]. The times and locations of optical photons are recorded as they arrive at the photodetectors and these observations



are provided to a binned maximum-likelihood event reconstruction algorithm that incorporates the physics of neutron energy depositions and optical photon transport in the detector system. From the recorded event data, the algorithm produces the times, locations, and relative intensities of the assumed number of neutron scatters, which can then be backprojected.

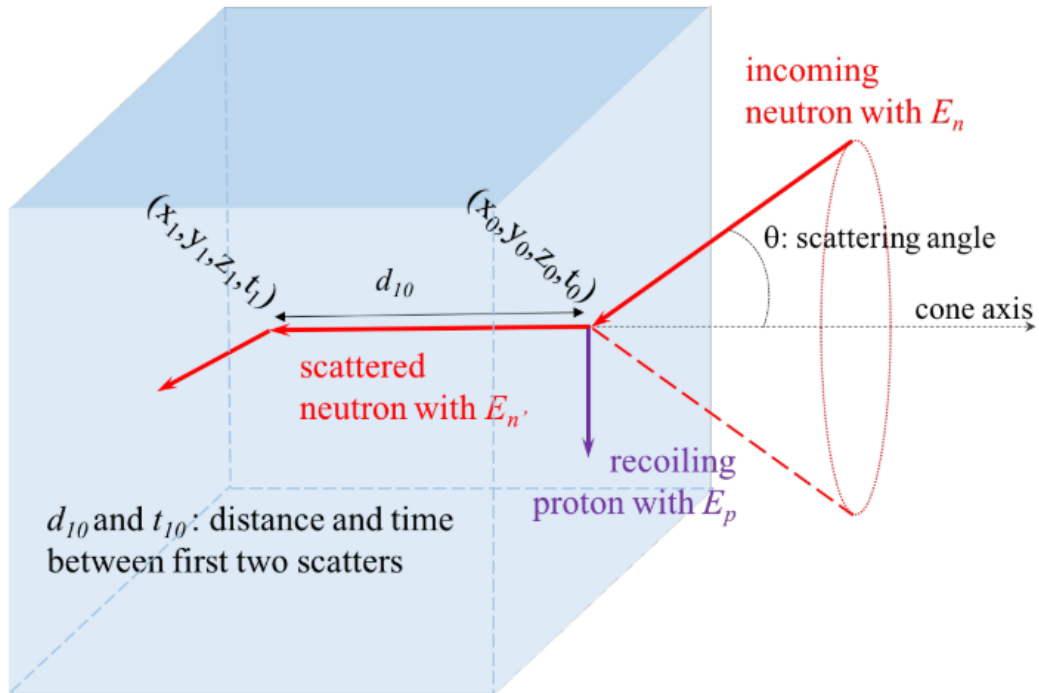


Figure 2.3. Reproduced from [26]. Schematic of a neutron scatter event in a monolithic volume.

Compared to the other two approaches, the physical geometry of the system is the simplest, requiring only six pixelated photodetectors and a block of plastic scintillator. However, the trade-off is a much more complex and computationally intensive reconstruction process and a higher channel count. While the computational demands are difficult to compare between designs, particularly since the prototypes are still being developed, a few metrics for comparison are channel count per unit active volume, and channel scaling with increased active volume. The first monolithic prototype is a  $5 \times 5 \times 5$  cm<sup>3</sup> cube with 64 channels on each side, resulting in a total of 384 readout channels and 3.072 channels/cm<sup>3</sup>. The full detector design is a  $10 \times 10 \times 10$  cm<sup>3</sup> scintillator cube with 256 channels per side, for a total of 1536 channels, yielding 1.536 channels/cm<sup>3</sup>. While the channels per unit volume becomes much more favorable with a larger volume, the total channel count is not feasible to implement without, for example, employing application-specific integrated circuits (ASICs), and the overall channel count is several times larger than the other compact NSC designs.

### ***2.2.3 Optically Segmented Design***

The optically-segmented compact NSC prototype design is composed of an  $8 \times 8$  array of closely-packed  $0.5 \times 0.5 \times 20$  cm<sup>3</sup> bars with matching arrays of silicon photomultipliers (SiPM) on either end [53]. The bars are wrapped in Teflon or ESR to maximize light collection and the interaction position along the length of the bar is determined from a combination of the relative intensities and arrival times of the light at either end of the bars. The bar position determines the other two spatial dimensions, and the total light collected can be used to determine  $E_p$ . The system triggers on coincidence between two or more bars; scatters within the same bar are not resolved. An alternative version of this system was recently demonstrated in simulation space using Stilbene instead of fast plastic [56].

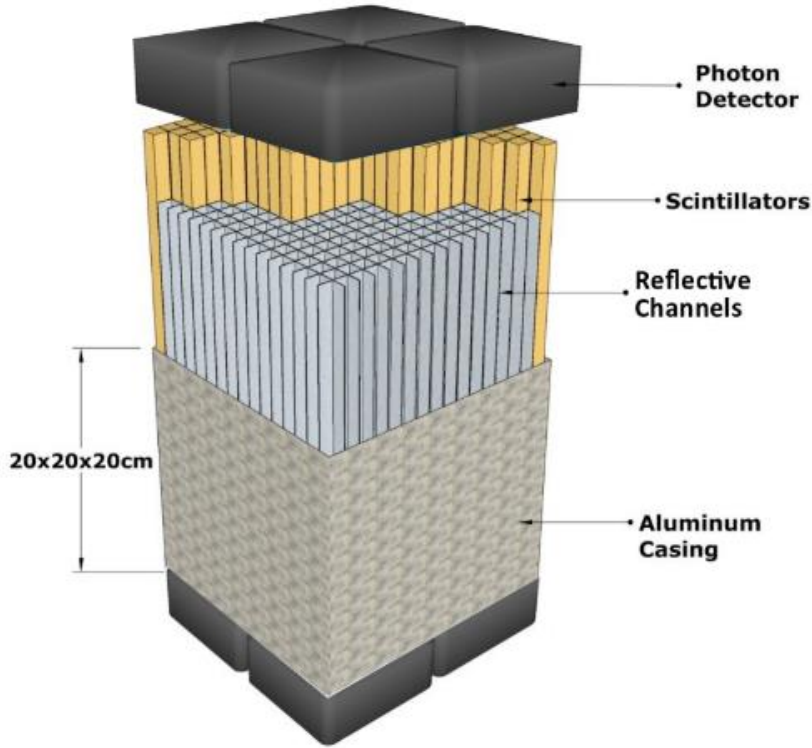


Figure 2.4. Reproduced from [53]. Model of the optically segmented compact NSC design.

In contrast with the monolithic design, much of the system's complexity is in hardware rather than in the reconstruction process. While there will be some optical and electronic crosstalk, the light is largely contained within the wrapped bars and therefore a clear, concentrated signal is generated by a neutron scatter. Since the signal is piped into two pixels per scatter, instead of distributed across 384 channels, single photon-level sensitivity is not required, easing the data requirements and complexity of instrumenting the SiPMs. Because the complexity is in the hardware, however, the quality of assembly becomes very important. Single bars have been characterized in detail [54] but there is significant variation in the performance between bars due to imperfections in the

production process. These performance degrading factors include quality of bar surfaces due to machining/polishing, quality of Teflon wrapping, optical mating of the bars to SiPM pixels, and others.

The channel count per unit active volume is very favorable compared to the monolithic design. The initial optically segmented prototype is 320 cm<sup>3</sup> and 128 channels, for a ratio of 0.4 channels/cm<sup>3</sup> compared to 3.07 channels/cm<sup>3</sup> for the monolithic. However, as noted earlier, the channel density improves as the monolithic block size increases while the channel density is constant for the optically segmented design regardless of array size (given a fixed bar size). To achieve a comparable channel density, the monolithic design would need to be more than 30×30×30 cm<sup>3</sup> and have almost 14,000 channels, which is not practical with modern hardware.

#### ***2.2.4 Optical Coded Aperture***

The optical coded aperture (OCA) design for the compact NSC leverages a previously demonstrated design for Compton imaging gamma rays [26], [33], [55] and will be the primary subject of this dissertation. The detector system utilized coded-aperture imaging, described in Section 1.6, to image the scintillation light. In a fully monolithic volume, 3-D localization was possible with this method due to significant differences in magnification for objects at different distances in the near field. This approach is analogous to software focusing in a lens-based system; the focal length is fixed and the assumed source to mask (object to lens) distance is iteratively varied until a sharp image is found. It is the logical inverse of how a photographic camera works, in which case the object of interest is at a fixed distance, and the focal length is adjusted until a sharp image appears.

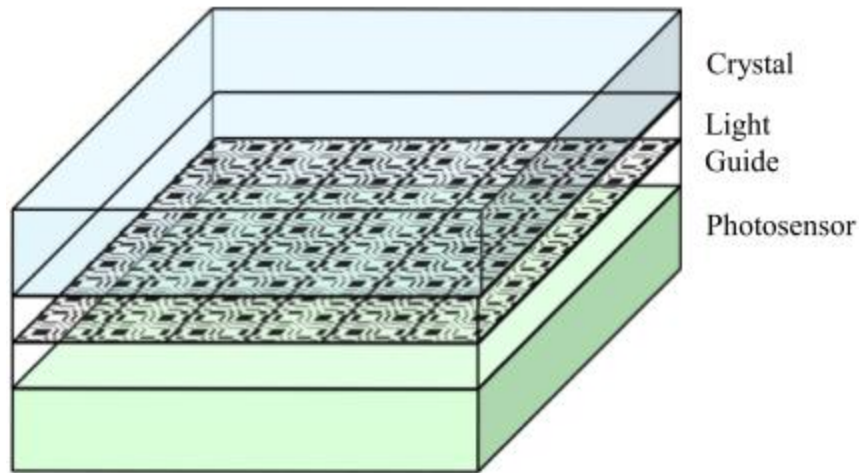


Figure 2.5. Reproduced from [55]. Schematic diagram of the gamma-ray OCA detector system.

A prototype of the gamma-ray OCA-based detector was built, demonstrating the concept for a thin crystal emulating a thick crystal – a thin crystal was exposed to a collimated gamma-ray beam with different thicknesses of light guide between the active volume and mask, mimicking a thick detector. Single site localization was shown with  $\sim 2$  mm resolution in each spatial dimension at the  $^{137}\text{Cs}$  photopeak energy of 662 keV. This work picks up where the prior detector system left off; the concept has been demonstrated, and the next step was to find a way to localize multiple-site scatters.

### 2.3 Original Contributions

Unless otherwise specified, all work presented henceforth was completed by the author. The original contributions are summarized thusly:

1. Demonstration of the feasibility of coded-aperture imaging in the expected counting statistics regime (Section 3.1).

2. Conception and simulation of potential coded-aperture-based designs for the compact NSC (Sections 3.2-3.4).
3. Development and demonstration of event localization techniques including the typical cross-correlation used with coded-aperture systems as well as a detector-response-based approach (Chapter 4).
4. Simulation parameter study of the novel compact NSC design and simulated performance demonstration with the planned prototype (Sections 4.4-4.5).
5. Experimental characterization of retroreflective tapes using a laser and a scintillator (Section 5.4).
6. Construction, characterization, and demonstration of neutron and gamma-ray imaging capability of the compact NSC prototype (Sections 5.4-5.6).

## 3 INITIAL DESIGN STUDIES

### 3.1 Coded-Aperture Counting Statistics Study

#### 3.1.1 Introduction

Recently, there has been renewed interest in neutron scatter cameras (NSCs) that infer the direction of incident neutrons (up to a cone) via the kinematics of neutrons that have two or more scatters off hydrogen in the detector. In the past [13], [57], individual neutron scatters had to be in separate detectors. More recently, novel approaches have been devised to make NSCs that are both smaller and more efficient by resolving multiple interactions in a compact detector. One approach [26] uses a single, monolithic volume of fast organic scintillator (e.g., EJ-232Q) and the information contained in the arrival times and locations of scintillation photons at the outer surface of the detector to infer the locations of neutron interactions within it. To achieve the desired imaging efficiency, neutron–proton elastic scatters must be spatially localized to approximately 1 cm and temporally localized to approximately 1 ns within the monolithic volume. Another approach [53], [54] to a compact NSC uses volumes of scintillators that are optically segmented into light pipes to achieve position sensitivity in two dimensions and the number and arrival times of photons at the ends of these light pipes to determine the third dimension, energy, and time.

The present work relates to a third approach, where the positions of interactions within a volume of scintillator are determined by means of an optical coded mask. In this design, an optical coded mask is placed between the scintillator volume, an index-matched, transparent volume, and a position-sensitive photodetector (PSPD). In this arrangement, the size of the optical shadow pattern projected onto the PSPD depends on the distance of the neutron interaction from the mask, which allows the 3-D location of the interaction to be estimated [33]. Achieving a high efficiency depends on localizing low-energy ( $\sim 300$  keV) depositions from neutron scatter interactions, in which case only about 120 optical photons might be emitted from EJ-232Q, meaning a PSPD that observes one face of the

detector might detect as few as five scintillation photons. In this regime, the number of detected counts is on the order of the number of pixels in the coded mask.

To this end, Monte Carlo simulations of optical photon transport were conducted to investigate coded-aperture imaging in this counting statistics-limited regime. An analytical expression was derived to relate the average number of detected counts required to localize a distant point source with some probability, depending on the number of mask elements. The expression was validated by performing a direct calculation and by comparing it to the Monte Carlo data. Although the simulations used optical photons, the results apply generally to coded-aperture imaging of any particle type, with consideration of systematic factors affecting specific detector systems such as those described in Section 4.

### ***3.1.2 Coded-Aperture Imaging***

Coded-aperture imaging is used in a wide array of different applications, including x-ray astronomy and nuclear security [58], [59]. This imaging method is generally feasible where the particles of interest can be attenuated by a relatively small thickness (less than the mask pixel width) of material and is most beneficial for cases in which other modalities tend to falter (such as lenses for x-ray imaging). Coded-aperture imaging operates by detecting the shadow pattern cast onto a position-sensitive sensor by an emissive object. The mask is constructed by employing a procedure such as the one described in [39] to create a pattern with desirable imaging characteristics. For this work, image reconstruction was performed using the cross-correlation method [39]. In many systems, the mask is twice the extent of the sensor, with the base mask pattern and sensor center-aligned. The mask patterns of interest for this work are uniformly redundant arrays (URA) and modified uniformly redundant arrays (MURA), which differ slightly in the sequence length and decoder function construction but operate and perform the same. 2-D MURA patterns are square, having  $r \times r$  pixels, whereas URAs are rectangular, having  $r \times (r-2)$  pixels, where  $r$  is the mask rank, a prime number used to generate the mask pattern.



An image of a single point source,  $\mathbf{I}$ , is obtained by taking the correlation (\*) between the recorded data,  $\mathbf{D}$ , and the mask decoder function,  $\mathbf{G}$  (with values  $\pm 1$  depending on whether the mask pixel is transparent (1) or opaque (-1)):

$$\mathbf{I} = \mathbf{G} * \mathbf{D} \quad (3.1)$$

The vector equation is solved by summing all elements of the product of  $\mathbf{G}$  and  $\mathbf{D}$ , shifting  $\mathbf{D}$  by one element, then multiplying and summing again, until  $\mathbf{D}$  has shifted across every element of  $\mathbf{G}$ . The equation representing this process is Eq. 3.1. Each shifted location of  $\mathbf{D}$  represents a different basis vector and the value of the sum is the reconstructed value using that basis direction. The decoding process therefore involves reconstructing the hit pattern using every orthogonal basis vector in the field of view (FOV).

$$I(k, l) = \sum_i^r \sum_j^{r_2} D(i, j) G(i + k, j + l) \quad (3.2)$$

where  $r$  is the mask rank, and  $r_2$  is equal to 1) 0 for a 1-D pattern ( $l=j=0$ ), 2)  $r$  for a 2-D MURA pattern, and 3)  $r-2$  for a 2-D URA pattern.

Obtaining a meaningful image and selecting the correct source location relies on detecting multiple particles at the detector. For instance, if only a single count is detected, then the reconstructed image is merely a shifted reproduction of the mask pattern (with values of  $\pm 1$ ), and the shift depends on the location of the observed count in the PSPD. If two counts are detected in different pixels, then the reconstructed image will contain values of  $\pm 2$  and 0 (i.e., the superposition of two images produced by two single counts), demonstrated by Figure 3.1. In these cases, the source location is ambiguous because it could be any maximum-value pixel; assuming 50% open fraction, in the first case, half the pixels have the peak value of +1, and in the second case, a quarter of the pixels have the maximum peak value of +2. In the limit of a nearly infinite number of detected counts  $n$  from a single source location and no noise or background, the resulting image will have

a single pixel (corresponding to the correct basis vector) with a value of  $n$  and all other pixels will fluctuate about 0 with amplitude  $\sqrt{n}$ . This image unambiguously determines the source location. For a smaller number of detected counts  $n$ , the reconstructed image may not unambiguously determine the source location. Therefore, for a specified mask with  $R$  total pixels and detected counts  $n$ , there exists a probability,  $P$ , that one selects the correct source location, which has the following behavior: as  $n$  approaches zero,  $P$  approaches  $1/R$  (all image pixels are equal in value and thus equally likely to be correct), and conversely as  $n$  increases toward infinity,  $P$  approaches and reaches 1 at the discrete value of  $n = N_{open}/2 + 1$ . The quantity  $N_{open}$  is the number of open pixels in the pattern; for the MURA masks shown in this work,  $N_{open} = (R - 1)/2$ .

Figure 3.1 demonstrates this concept graphically using a rank-17 2-D MURA [40] mask pattern. On the left in Figure 3.1 are the detected hit patterns and on the right are the decoded images. Figure 3.2 shows the coded-aperture pattern used. As the number of detected counts increases, the number of possible source locations decreases until only a single pixel remains. Note that the central pixel, reconstructed using the correct basis vector, has exactly the total number of detected counts whereas the pixels reconstructed with the incorrect basis directions – every other pixel – fluctuate about 0 with amplitude  $\sqrt{n}$ .

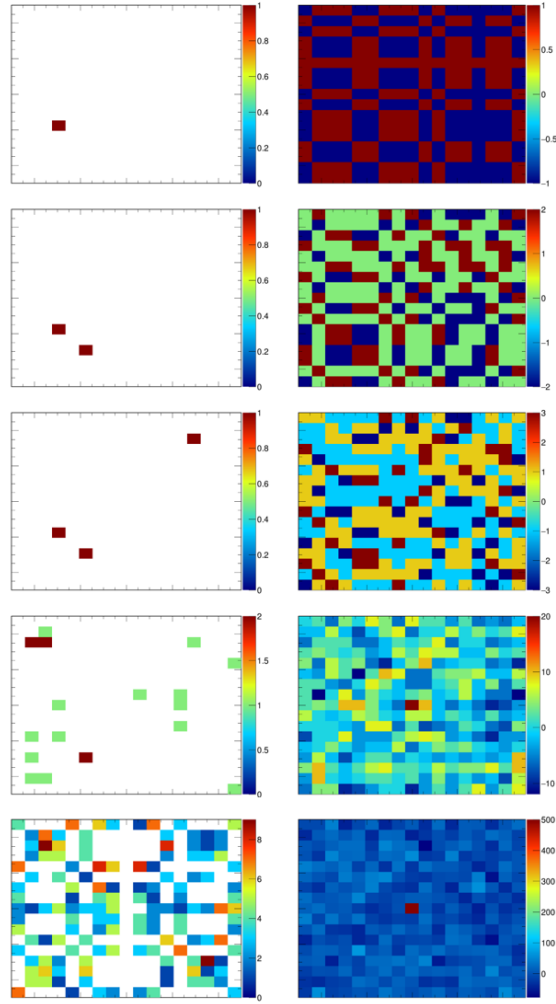


Figure 3.1. Left: hit patterns with 1, 2, 3, 20, or 500 detected counts (from top to bottom). Right: Corresponding images reconstructed using cross-correlation.

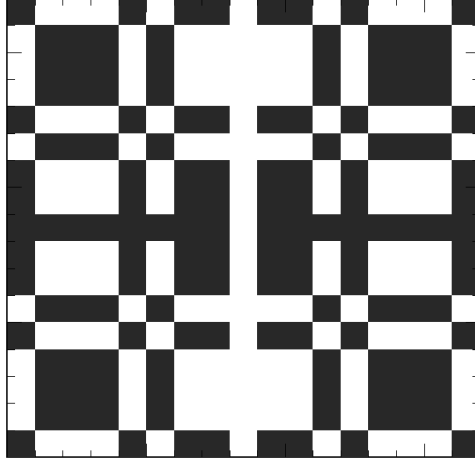


Figure 3.2. Rank-17 MURA mask pattern used for demonstration; black pixels are transparent and white pixels are opaque.

For the application discussed previously, the question is, for a particular number of detected counts and mask rank, what is the probability of selecting the correct source location? To answer this, an analytical expression is necessary to relate the number of detected counts to the probability of identifying the correct source location for a specified mask rank. This study is subtly different from the analysis of the signal-to-noise ratio (SNR) in coded-aperture imaging [60] because the goal is to find the threshold at which the imaging mode will likely fail to produce a unique source location. Comparatively, the SNR estimates the confidence in the intensity of the source location that is found. To address this question, an analytical expression was developed and empirically validated using direct calculations and Monte Carlo optical photon simulations of different mask arrangements.

### 3.1.3 Analytical Expression

Based on the number of open mask pixels, an expression relating the average number of detected photons required to correctly identify the source location with some probability can be derived. We illustrate the derivation with a rank-13 1-D MURA, but the expression holds for any rank 1-D or 2-D URA or MURA and a point source anywhere in the FOV. We assume an isotropic point source of visible photons at the center of the FOV and infinitely far away from a perfectly opaque mask. Photons are therefore only detected under mask openings and nowhere else. Only one photon may be detected per pixel. For this example, the mask is a rank-13 1-D MURA pattern with  $N_{open} = 6$  open pixels and 7 closed pixels. Represented as an array where “0” indicates no hits (the detector pixel is behind a closed mask pixel) and “1” represents a hit (the detector pixel is behind an open mask pixel), the ideal hit pattern  $\mathbf{D}$  is:

$$\mathbf{D} = [0 \ 0 \ 1 \ 1 \ 0 \ 1 \ 0 \ 1 \ 0 \ 1 \ 1 \ 0 \ 0].$$

The corresponding decoder for this mask pattern is:

$$\mathbf{G} = [1 \ -1 \ 1 \ 1 \ 1 \ -1 \ -1 \ -1 \ -1 \ 1 \ 1 \ 1 \ -1 \ 1 \ 1 \ 1 \ -1 \ -1 \ -1 \ -1 \ 1 \ 1 \ -1 \ 1].$$

The hit pattern  $\mathbf{D}$  has length  $R$  while the decoder has length  $2R-1$ ;  $\mathbf{G}$  is created from the same decoder sequence repeating twice (minus 1 element) to enable reconstruction with every basis vector. In other words,  $\mathbf{G}$  is extended so as to appear circular when cross-correlated with  $\mathbf{D}$ . Since the source is at the center of the FOV, the ideal hit pattern  $\mathbf{D}$  is just a replication of the mask pattern  $\mathbf{M}$  with a single hit in each open pixel. If we reconstruct this hit pattern with the correct basis direction – the 7th basis vector, the portion of the decoder that is used is from  $G(7)$  to  $G(19)$  (1-indexed), then the decoded value is (using Eq. 3.2 with  $j=l=0$ ):

$$\begin{aligned} I(7) &= 0(-1) + 0(-1) + 1(1) + 1(1) + 0(-1) + 1(1) + 0(1) + 1(1) + 0(-1) + 1(1) \\ &\quad + 1(1) + 0(-1) + 0(-1) = 6. \end{aligned}$$

Reconstruction by the (correct) 7th basis vector is illustrated in Table 3.1.

Table 3.1. Alignment of  $D$  and  $G$  when the correct basis direction is used. Columns highlighted with gray are open mask pixels that align with detector pixels in  $D$  with one count.

$D$	0	0	1	1	0	1	0	1	0	1	1	0	0	SUM
$G$	-1	-1	1	1	-1	1	1	1	-1	1	1	-1	-1	
*	0	0	1	1	0	1	0	1	0	1	1	0	0	6

Note that when the correct basis direction is used, all of the hits contribute +1. In contrast, if one reconstructs with an incorrect basis direction, for instance, the first basis vector, then the portion of the decoder that is used is from  $G(1)$  to  $G(13)$ , and the decoded value is:

$$I(1) = 0(1) + 0(-1) + 1(1) + 1(1) + 0(-1) + 1(-1) + 0(-1) + 1(-1) + 0(1) + 1(1) + 1(-1) + 0(1) + 0(1) = 0.$$

Reconstruction by the (incorrect) 1st basis vector is illustrated in Table 3.2.

Table 3.2. Example ideal hit pattern  $D$  and decoder  $G$  when assuming the wrong basis direction. Gray shading shows when an open mask pixel and hit detector pixel align whereas black shading indicates a count in the detector behind a closed mask pixel.

$D$	0	0	1	1	0	1	0	1	0	1	1	0	0	SUM
$G$	1	-1	1	1	-1	-1	-1	-1	1	1	-1	1	1	
*	0	0	1	1	0	-1	0	-1	0	1	-1	0	0	0

Note that when the incorrect basis direction is assumed, half the hits contribute -1, and half the hits contribute +1, resulting in a net of 0, as expected for the orthogonality of the two basis vectors. In this scenario, reconstructing with the correct basis direction will always result in a value equal to the total number of detected hits. However, with sparse photon hits, it is sometimes possible to reconstruct the total hits with the wrong basis vector. What is required to produce an image with a unique source location is a sufficient number of hits to differentiate every incorrect basis direction from the correct one; this requires an open pixel in  $\mathbf{M}$  corresponding to a -1 value in the decoder  $\mathbf{G}$  for every incorrect basis vector to be hit, reducing its reconstructed value below the maximum. For example, imagine that only the 1st, 2nd, and 5th open pixels (refer to the gray columns in Table 3.1) were hit; both the wrong basis direction (Table 3.2) and the correct direction (Table 3.1) would reconstruct with a value of 3, leaving the source location ambiguous. For any given combination of 3 hits, there will be incorrect basis directions that reconstruct to the same value as the correct one. Therefore, 4 distinct hits, or  $N_{open}/2 + 1$  hits, are required to guarantee uniqueness, as every incorrect basis direction will have at least one pixel contributing -1 to the sum whereas the correct one will have none.

The next step is to take this trend and translate it into a probability by calculating what fraction of the time the wrong basis vectors reconstruct to the maximum, depending on the number of distinct open pixels hit:

1. For 0 hits, all basis vectors produce the same value, 0, and thus the source is equally likely to be in any pixel.
2. For 1 hit, there are 6 open pixels, but only 3 correspond to +1 in  $\mathbf{G}$  and will reconstruct to the maximum (the other 3 will contribute -1). There are  $\binom{6}{1} = 6$  ways to hit 1 of 6 open pixels and only  $\binom{3}{1} = 3$  ways to hit a pixel that reconstructs to the maximum so  $3/6=1/2$  of basis vectors will reconstruct to the maximum.
3. For 2 hits, there are  $\binom{6}{2} = \frac{6!}{4!2!} = 15$  ways to hit 2 of 6 pixels, but only  $\binom{3}{2} = \frac{3!}{2!1!} = 3$  ways to hit a pair of pixels that will reconstruct to the maximum. Therefore,  $3/15 = 1/5$  of basis vectors will reconstruct to the maximum.

4. For 3 pixels hit, there are  $\binom{6}{3} = \frac{6!}{3!3!} = 20$  ways to hit 3 of 6 pixels, but only  $\binom{3}{3} = 1$  way to hit 3 pixels that will reconstruct to the maximum. As a result, 1/20 of basis vectors will reconstruct to the maximum.
5. For 4 or more hits, there is no way for the incorrect basis vectors to reconstruct to the maximum – all will have at least one pixel contributing -1. Following the previous logic, there are  $\binom{3}{4} = 0$  ways to hit 4 pixels that will reconstruct to the maximum using the wrong basis direction. A unique source location is therefore guaranteed.

For the rank-13 1-D MURA pattern, there are 13 total basis vectors, with one correct and 12 incorrect directions, so the number of times one selects the incorrect source location is 12 times the fraction of wrong basis vectors that reconstruct to the maximum value. This fraction is the number of ways to hit incorrect basis vectors that reconstruct to the maximum divided by the number of ways to hit the open pixels. In general, for a pattern with  $R$  pixels, the number of wrong basis vectors when hitting  $n$  distinct pixels is:

$$N_{mistakes} = \begin{cases} (R - 1) \frac{\binom{N_{open}/2}{n}}{\binom{N_{open}}{n}}, & n \leq \frac{N_{open}}{2} \\ 0, & n > \frac{N_{open}}{2} \end{cases} \quad (3.3)$$

The probability of getting the correct answer is then the number of ways to reconstruct to the correct maximum divided by the total number of ways to get an answer that reconstructs to the maximum. That is,

$$P_{correct} = \frac{1}{1 + (R - 1) \frac{\binom{\frac{N_{open}}{2}}{n}}{\binom{N_{open}}{n}}} \quad (3.4)$$

When expanded, the combinatorial term is:



$$(R - 1) \frac{\binom{\frac{N_{open}}{2}}{n}}{\binom{N_{open}}{n}} = (R - 1) \frac{\left(\frac{N_{open}}{2}\right)! (N_{open} - n)!}{N_{open}! \left(\frac{N_{open}}{2} - n\right)!} \quad (3.5)$$

Because the factorial is only defined for integer hits  $n$ , it is desirable to interpolate and infer the average number of (non-integer) hits to reach a specified probability of finding the true source location, such as 90%. To this end one may substitute the gamma function  $\Gamma$ :

$$(R - 1) \frac{\Gamma\left(\frac{N_{open}}{2} + 1\right)}{\Gamma(N_{open} + 1)} \frac{\Gamma(N_{open} - n + 1)}{\Gamma\left(\frac{N_{open}}{2} - n + 1\right)} \quad (3.6)$$

Eq 3.4 assumes that each hit  $n$  is in a different pixel; in more realistic scenarios, the same open pixel may be hit multiple times. The additional count does not help distinguish between the correct and incorrect basis vectors since that pixel already added or subtracted 1. Therefore, in more realistic scenarios, the required  $n$  will be increased by a value representing the probability of hitting the same pixel twice for a given source and detector arrangement.

### 3.1.4 Equation Validation

Eq. 3.4 was validated directly calculating the probability of obtaining the correct source location for a select mask rank and number of hits detected in distinct pixels. This brute-force calculation is done by performing, for each mask rank, the cross-correlation on every possible hit pattern for each number of detected hits, then finding the fraction of image pixels with the maximum value. For each pattern only one pixel will be correct, so the probability of finding the correct one is the inverse of the number of pixels reconstructed with the maximum value.

For a coded mask with  $N_{open}$  open mask pixels there are  $2N_{open}-1$  possible unique hit patterns comprising all combinations of integer numbers of distinct hits from 0 to  $N_{open}$ .

Using the same notation as in Section 3.1.3, the hit patterns – the values of  $\mathbf{D}$  behind open pixels – are equivalent to the set of binary sequences representing unsigned integers from 0 to  $2N_{open}-1$ . These sequences were calculated and used to populate  $\mathbf{D}$ , which was then reconstructed using the cross-correlation. Figure 3.3 shows the comparison between the values produced by Eq. 3.4 and this direct calculation for three different-rank masks. The direct calculation and Eq. 3.4 match exactly.

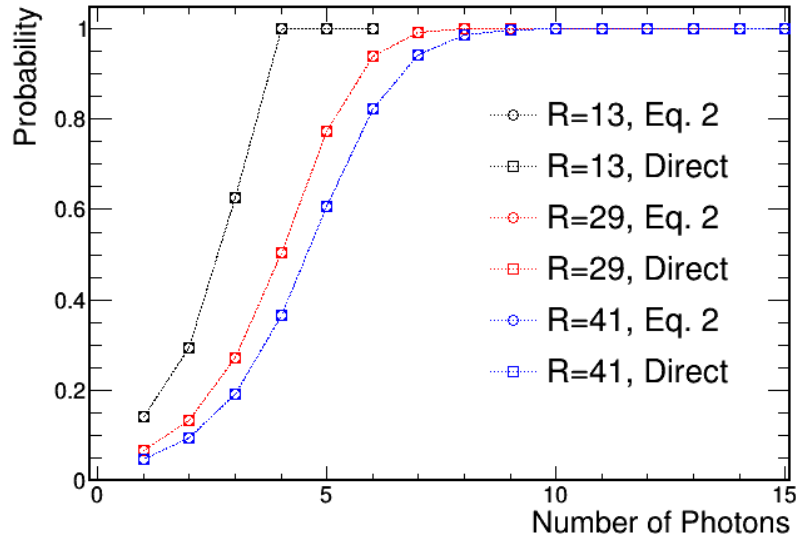


Figure 3.3. Comparison of values computed using Eq. 3 (open circles) and directly (open squares).

### 3.1.5 Simulation Geometry

To validate Eq. 3.4, Geant4.10.05 [8] was used to model a coded-aperture system comprising a point source for optical photons, an absorptive coded mask, and a PSPD. All transport media had the same index of refraction and had no optical absorption or scattering. The simulation results were analyzed with the ROOT library [61]. The

simulations (Figure 3.4) use a  $10 \times 10 \text{ cm}^2$  parallel beam of monochromatic (405 nm) optical photons originating 1 m from a perfectly absorptive  $10 \times 10 \times 0.01 \text{ cm}^3$  MURA coded mask uniformly illuminating it. A  $10 \times 10 \text{ cm}^2$  PSPD with unity quantum efficiency and perfect spatial resolution is placed 1 mm behind the mask, allowing the source to cast a shadow of the pattern onto the PSPD. The space between the source and photodetector is composed of air. This arrangement represents a coded-aperture system with a magnification factor of 1 viewing a point source that is infinitely far away (equivalent to a parallel beam source for the viewer).

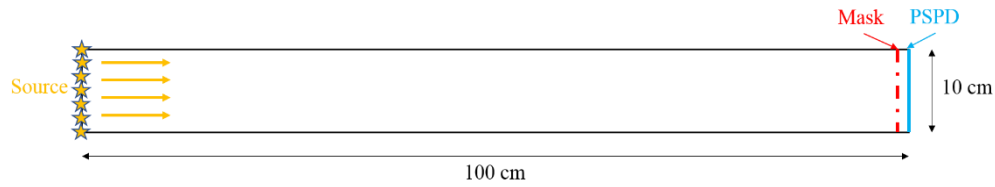


Figure 3.4. Schematic diagram of the simulation geometry.

A range of mask ranks for 1-D and 2-D MURA patterns were simulated to understand the expected ability of each to localize the point source. Although the mask ranks were varied, the pixel sizes were also changed to maintain a fixed total pattern size. Table 3.3 details the ranks of the patterns used. Ten million optical photons were generated for each mask rank, resulting in approximately five million detected counts in the PSPD. Roughly half are lost to absorption by the mask patterns, which have open fractions near 50%.

Table 3.3. List of ranks, total numbers of pixels, and numbers of open pixels and open fractions for the simulated 1-D and 2-D MURA coded-mask patterns.

<b>1-D MURA Rank</b>	<b>Total Pixels</b>	<b>Open Pixels</b>	<b>Open Fraction</b>
5	5	2	0.46
13	13	6	0.47
17	17	8	0.48
29	29	14	0.49
37	37	18	0.49
41	41	20	0.49
53	53	26	0.49
61	61	30	0.49
73	73	36	0.49
<b>2-D MURA Rank</b>	<b>Total Pixels</b>	<b>Open Pixels</b>	<b>Open Fraction</b>
3	9	4	0.44
7	49	24	0.49
11	121	60	0.50
17	289	144	0.50
29	841	420	0.50
43	1849	924	0.50

### 3.1.6 Data Analysis

The probability of obtaining the correct source location as it relates to the average number of detected particles for each mask configuration is determined statistically with the following multi-step analysis process:

1. Randomly and uniformly sample  $n$  detected photons (with replacement) from the data set, where  $n$  is an integer from 1 to 25.
2. Perform the cross-correlation image reconstruction on the detected hit pattern to produce a decoded image.
3. Count the number of reconstructed image pixels with intensity equal to the total number of detected counts.
4. Repeat steps 1–3 for every mask configuration for 50,000 trials.

For each mask rank and specified number of detected counts, this process allows the probability of obtaining the correct source location in the reconstructed image to be determined. Note that because there is no background or noise, if a unique source location is found in this arrangement, it is guaranteed to be the correct location.

### **3.1.7 Results**

As predicted by Eq. 3.4, one expects that the distributions of  $P$  vs.  $n$  will shift to the right as the mask rank increases. That is, as the number of open mask elements goes up, the required number of photons to obtain the correct source location also goes up (recall that  $N_{open}/2 + 1$  distinct hit(s) are required to guarantee it). Figure 3.5 shows these distributions for 1-D and 2-D MURA mask patterns produced using the Monte Carlo data.

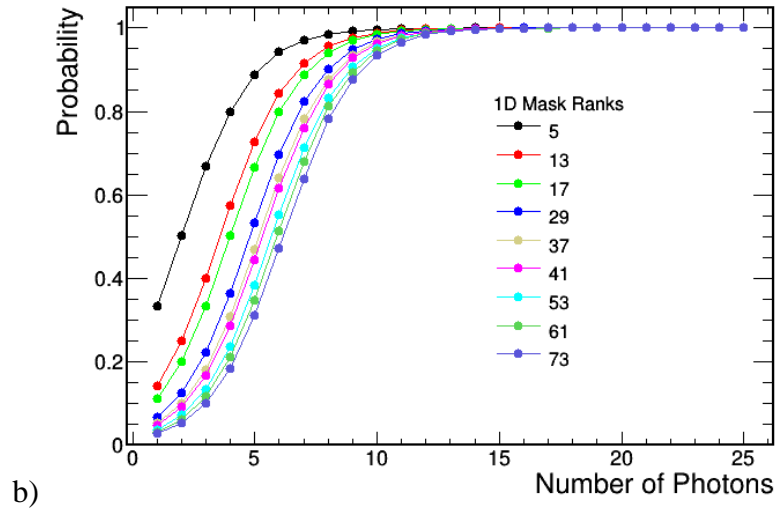
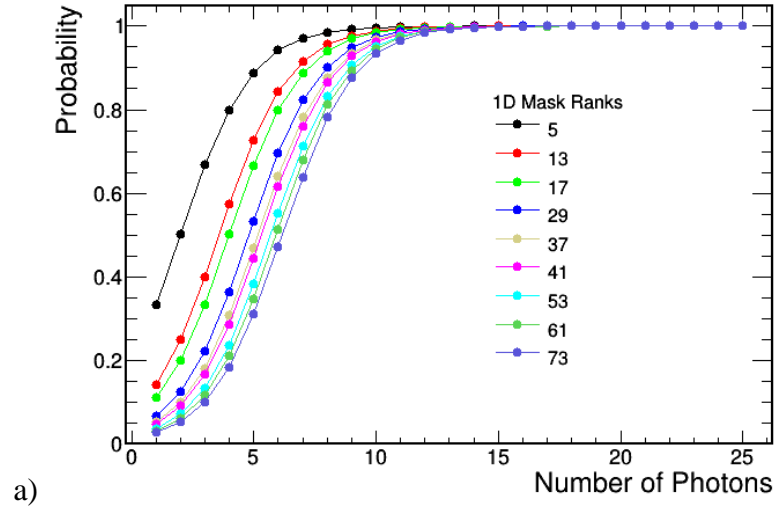


Figure 3.5. Probability of obtaining the correct source location as a function of the number of detected photons, shown for a range of MURA coded-mask ranks. a) 1-D mask patterns. b) 2-D mask patterns.

On the far left of the top plot in Figure 3.5a is the rank-5 1-D pattern (black), which has a roughly 90% probability of obtaining the correct source location with only five photons. Comparatively, the rank 29 pattern (dark blue) does not reach this point until about 10 detected photons. The same trends hold for the 2-D mask patterns.

Figure 3.6 extends Figure 3.5 by showing the comparison between  $P$  values calculated from Eq. 3.4, using the brute force calculation, and those extracted from the Monte Carlo data. The curves from the Monte Carlo data are shifted toward higher  $n$  due to the possibility of multiple counts hitting the same detector pixel.

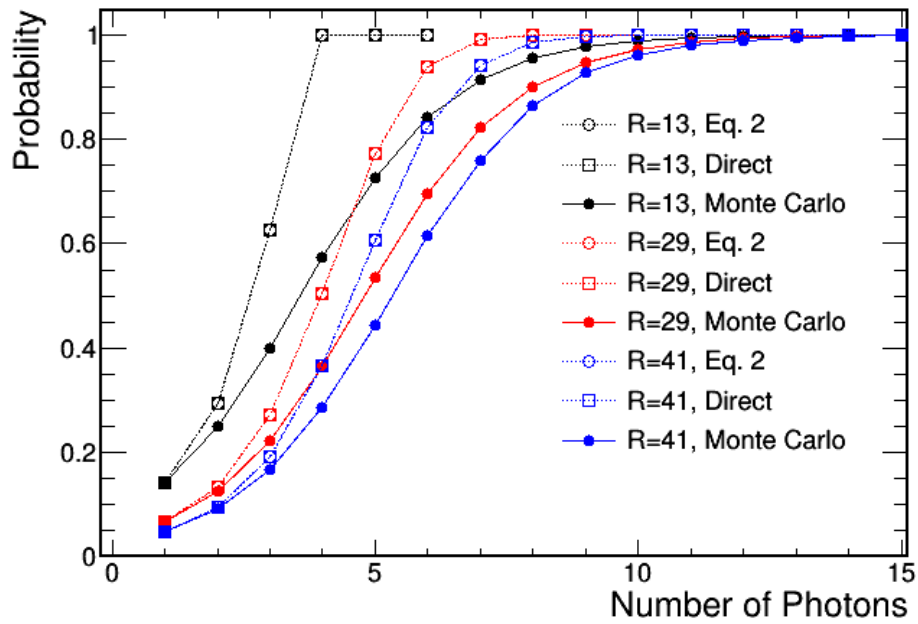


Figure 3.6. Comparison of  $P$  values produced using Eq. 3, the direct calculation, and the Monte Carlo result.

Another way to look at these data is to ask the following question: On average, for a desired probability of localizing the source to the correct pixel, how many photons must be detected? These values are the points where a horizontal line at a given probability intersects the curves in Figure 3.5 and Figure 3.6. These values can be determined by interpolating on the curves using a cubic spline. The results of this analysis are shown in Figure 3.7.

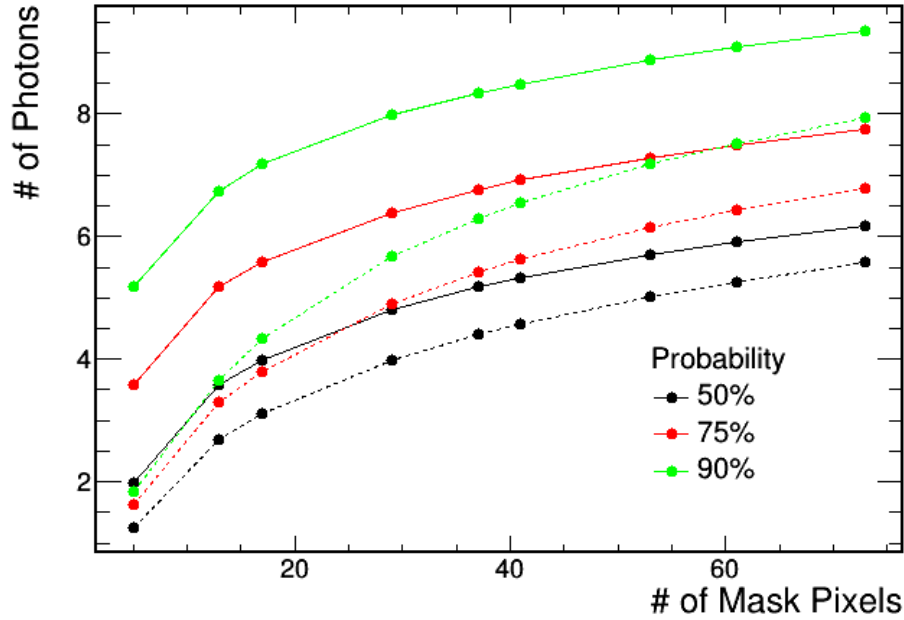


Figure 3.7. Average number of photons required to obtain the correct location as a function of the number of mask pixels. Solid lines are computed from the Monte Carlo data and dashed lines are computed using Eq. 3.



Figure 3.7 shows that the derived analytical expression Eq. 3.4 produces results that match the shape of those produced by the Monte Carlo data, with a vertical shift (increased  $n$ ) caused by multiple photons hitting the same pixel. At low numbers of pixels, Eq. 3.4 predicts decreasingly less hits required compared to the Monte Carlo result because of the increasing probability of hitting the same pixel as the number of pixels diminishes. Figure 3.6 and Figure 3.7 show that coded-aperture imaging can still be expected to correctly localize a distant point source with more than 90% probability for a low mask rank and fewer than 10 detected photons. Whether or not the mask is 1-D or 2-D is irrelevant; the relationship depends only on the total number of mask pixels.

### **3.1.8 Discussion**

The results show that coded-aperture imaging is expected to be feasible in the counting statistics-limited regime expected for the aforementioned NSC application. In that application, the number of photons required to localize the scatter interaction in the scintillator volume effectively sets a lower energy threshold on observable proton recoils.

However, the foregoing provides only a theoretical floor on how few quanta are required and does not include various perturbative effects that will occur in a real system. Such issues include variation in the number of detected counts in each pixel (i.e., due to electronic noise), dark counts, near-field effects, background, and transmission through the mask. The first two cannot be completely mitigated in any system, and consequently all issues listed may increase the number of required photons while simultaneously reducing the SNR. Another limitation of this study is the perfect registration between the source and the mask/detector pixels. In a real implementation, sources will appear at different locations in the field of view, splitting the peak counts and thereby increasing the number of photons required to produce the correct answer.

Moreover, variation in the number of detected counts in a given pixel can result in several negative outcomes when the image is reconstructed. If fewer particles are detected than really hit the pixel, for example due to electronic noise, then the SNR is reduced

compared to the true value, but the ability to find the true source location is not affected, except for the case where no particles are detected when one or more was truly incident.

In contrast, if multiple particles are detected in a pixel where only one particle was truly incident, only the SNR is impacted. If one or more counts were detected in a pixel where no particle was truly present, the overall number of particles required to produce the correct source location for that configuration would increase, particularly if the hit occurs behind a closed mask element when reconstructing with the correct basis vector, because a -1 would be added for the reasons explained in Section 3.1.3. An example source of this type of error is dark counts, which are temporally random, detected hits in pixels that do not correspond to real particle hits. For the NSC application, these tend to be uniformly distributed across the PSPD, and assuming the dark count rate does not overwhelm the signal, dark counts raise the floor on the number of required photons to find the correct source location.

Near-field artifacts become an issue when the coded-aperture magnification is significantly greater than 1, which is the case for the proposed NSC design. There are two components to the artifacts: those introduced by not knowing the correct magnification and those introduced by the difference in intensity at the detector due to the solid angle. Unfortunately for this detector design, the mask cannot be rotated, so the mask/anti-mask approach to correcting the intensity-induced artifacts is not feasible [41]. Preliminary efforts indicate that obtaining a coarse estimation of the source location before performing the coded-aperture reconstruction may allow a solid angle correction to be used to alleviate a component of the intensity-driven near-field effects. One expects that the near-field artifacts also have the consequence of slightly increasing the required number of detected photons unless completely corrected for, in which case one expects this analysis to remain true.

The foregoing issues highlight the fact that Eq. 3.4 provides only a theoretical minimum count required. To fully understand the performance of a coded aperture in a particular instrument requires detailed simulations and measurements that include these and other

effects that will, inevitably, somewhat raise the threshold of required counts for reliable imaging.

Finally, it is possible that alternative methods of coded-aperture image reconstruction, such as the use of maximum likelihood-based approaches, could allow for a lower floor on the number of hits required to find the source. These methods may be able to use additional information, such as the photon arrival times at the PSPD, to estimate the source position in the cases where the cross-correlation would produce multiple locations. These and other methods are currently being explored for the coded-aperture-based NSC detector design.

### **3.1.9 Conclusions**

An analytical expression relating the number of coded-mask elements, the number of detected particles, and the probability of correctly localizing an emissive source is reported. This equation is supported by Monte Carlo simulations of optical photons in a typical coded-aperture imaging system. According to Eq. 3.4, the average number of required photons to produce a given probability of finding the true source location depends combinatorically on the number of open mask elements. The equation presented, assuming the cross-correlation reconstruction is used, reflects a lower bound on the number of counts required, which is increased by the systematic factors outlined above. These factors will change depending on the application; for example, transmission through the mask is a larger problem when imaging neutrons compared to optical photons. Similarly, for the proposed NSC design, the system will be housed in a light-tight enclosure, so compared to gamma-ray imaging systems that inevitably detect background counts from every direction, stray particle backgrounds practically do not exist.

## **3.2 Initial Designs**

Four designs were conceived that employed optical coded-aperture imaging for the NSC application. The first, Design A, was essentially the same as the geometry demonstrated in [33], [55] with the inorganic scintillator replaced by fast plastic and a retroreflector

added to the side opposite to the photodetectors. Design B was inspired by double-sided strip semiconductor detectors and utilizes orthogonal 1-D coded masks on either side of the active volume. Each side localizes one dimension, then the third is obtained by employing software focusing from both sides. The third, Design C, has a 2-D mask in the middle of the active volume with MAPMTs on either side. Finally, Design D, which was chosen as the OCA Slab Prototype Design, utilizes 1-D coded masks and optically separated slabs of the active volume in an effort to simplify the multi-scatter reconstruction process. These four designs are shown schematically in Figure 3.8.

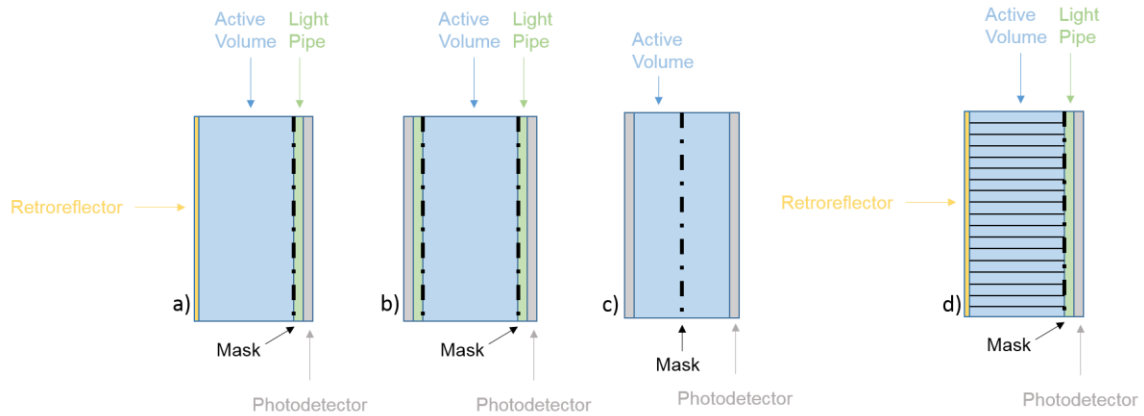


Figure 3.8. Schematics of all four initial designs: a) Design A, b) Design B, c) Design C, d) Design D. Blue regions are scintillator, green regions are light guides, gray indicates photodetector, yellow areas are retroreflectors, and dashed black lines show the mask planes.

In Section 3.1, it was shown that coded-aperture imaging is potentially viable at very low numbers of detected counts ( $\sim 10$ ). The next step was to examine the single event localization performance, motivated by the idea that if the design did not perform well for single-site energy depositions, then reconstructing multiple scatters would likely be infeasible. In fact, multi-site localization proved to be the most challenging component of the detector design due to the complexity of unfolding overlapping light distributions.

For all of the work reported in this section, a common set of photodetector, reflector, and light guide properties were used. The assumed photodetector had the properties of a Hamamatsu Photonics H9500 MAPMT, which has a  $16 \times 16$  array of 3 mm pixels, a typical QE of 24%, a rise time (10-90% time) of 800 ps, a transit time of 6 ns, and a transit time spread (TTS) of 400 ps FWHM. The MAPMT entrance window was not included. The retroreflector was perfectly efficient and introduced no angular deviation; that is, every incident photon was backscattered by exactly  $180^\circ$ . Light guides were modeled as non-scintillating plastic which had the same refractive index as EJ-204. The coded masks were perfectly absorptive, and the mask holes had the same refractive index as the scintillator and light guides. The mask pixel size was the same as the detector pixel size in all cases. These design parameters were chosen as reasonable for the first attempt at modeling the detector mechanics and were not intended to be comprehensive.

Additionally, where applicable, the detector volume was made much larger than it would be in a real prototype to minimize edge effects. To the same end, events were only simulated in the central region of the volume, as far away from the edges as possible. For Designs A, B, and C, the active volume was  $50 \times 50 \times 5 \text{ cm}^3$ , and for Design D, the slab was 50 cm long in the X (mask pattern) dimension.

### ***3.2.1 Design A: Monolithic, one-sided readout, 2-D mask***

Design A (Figure 3.8a) took the design from the previous gamma-ray system [33], [55] and modified it for the NSC application. This meant changing NaI or CsI scintillators to fast plastic such as EJ-204. Due to the reduced photon counting statistics compared to the gamma-ray system, a retroreflector was added to the surface opposite from the mask to

improve the light collection efficiency. The reduced counting statistics also suggests that one should use as low a mask rank as possible so that low-energy depositions have the maximal chance to be correctly reconstructed. To this end, Design A employed a 2-D rank-5 MURA coded mask pattern with 3 mm pixels.

### ***3.2.2 Design B: Monolithic, two-sided readout, orthogonal 1-D masks***

This design (Figure 3.8b) takes a similar approach to event localization as double-sided strip detectors. Orthogonal 1-D coded mask patterns were placed on opposing sides of the scintillator volume, with each allowing determination of different lateral dimensions, and both used to determine the Z (depth) dimension via software focusing, described in Section 1.6. A key benefit over Design A is that, since a 1-D mask pattern is used, the photon counting statistics requirements are lower. The depth resolution also improves because of the combined information from both sides. A feature of near-field coded-aperture imaging is that the depth resolution gets worse as the source moves further away from the mask, thus reducing the change in magnification as a function of distance. With the two-sided arrangement, as the interaction location moves away from one side, thus decreasing its depth localization performance, it gets closer to the other side, improving it.

### ***3.2.3 Design C: Two equal volumes, two-sided readout, 2-D mask in center***

The third design (Figure 3.8c) has a 2-D coded mask in the depth-center of the active volume with two MAPMTs on either side. As a result, for a given interaction, one photodetector observes the light directly while the other observes it through the mask pattern. Compared to Designs A and B, light collection efficiency is better because the mask is only attenuating the light in one direction instead of both (note that, in Design A, retroreflected light is still modulated by the mask). Photon counting statistics could be further improved by making the mask out of retroreflective material so the MAPMT that directly views the interaction would also have a reflected component that is modulated by the mask pattern. However, this also significantly increases the complexity of the reconstruction routine.

This design benefits from the removal of most of the light guide compared to the other three geometries, which means less inactive material for incident neutrons to scatter off of, reducing background. In practice, a thin light guide between the scintillator and MAPMT is desirable so light from interactions very close to the MAPMT has a chance to spread out. Unfortunately, these potential benefits are offset by several undesirable features of this system. Due to the complexity of the detector response as a function of the interaction position, particularly for two or more scatters, a sophisticated reconstruction algorithm would be required.

Another drawback of this design relates to the region in the depth-center of the detector, e.g., very close to the mask. This region exhibits a few interesting qualities. One can imagine a neutron scatter in or near an open element, in which case it is possible that *none* of the light is modulated by the mask. Similarly, if the event is directly behind a closed element from the perspective of one MAPMT, then that photodetector might observe zero photons from an energetic deposition. When using the cross-correlation for localization, the region near the mask in  $Z$  ( $< 5$  mm or so) was overmagnified such that the source image did not fit within the FOV of the MAPMT. These events therefore could not be reconstructed using the cross-correlation technique, and a more sophisticated method is required. The end result of the combination of these effects is that, even though the light guide has been eliminated, there are significant regions in the active volume where interactions will be difficult or impossible to accurately reconstruct.

So far, the focus has been on spatial performance, however energy reconstruction with this design is also very challenging. This is because of the numerous and complicated optical pathways a photon can take from the interaction site to the MAPMT, including reflections off of the mask, the side walls, and the MAPMT. The result is that the photodetection efficiency will change significantly and possibly abruptly over small changes in interaction location.

### ***3.2.4 Design D: Segmented slabs with 1-D mask along length***

Design D (Figure 3.8d) was the last one conceived and thus incorporated many of the lessons learned from developing the other designs. Beyond single-site localization, the single largest challenge for the other three designs was the jump from single to multiple-site interaction localization due to the added complexity required of the reconstruction algorithm. This design mitigates that challenge by optically segmenting the scintillator volume in one dimension, then utilizes a 1-D coded mask to localize in the other two. In some sense, the detector is a combination of the optically segmented, monolithic, and coded aperture-based designs, attempting to leverage the strengths of each where possible.

The detector volume is segmented into slabs where the pitch matches the photodetector pixel size, the height is nominally 5 cm, and the length and number of slabs are determined by the number of available MAPMTs that can be tiled together. In between the slabs, there is a sandwich of air, ESR, absorber (aluminum), ESR, and air, which acts as an optical reflector to reduce optical crosstalk and pipe the light down to the photodetector. While ESR is an effective reflector, the photons tend to bounce on the order of a dozen times while traversing the slab, so even a 1.5% chance to transmit becomes significant, motivating the absorber in between ESR layers. At the top is a retroreflector and below the active volume is a light guide to spread the light, the coded mask, then another light guide to provide the focal length. The light guide has the same refractive index as the scintillator; it is the same plastic material but without the scintillating components.

### ***3.2.5 Simulation Results and Down-Selection***

While developing the simulation and analysis codes for them was a valuable learning experience, Designs A and C were ultimately not benchmarked in great detail. The 2-D mask pattern required by Design A meant an unacceptably, and unnecessarily, high counting statistics requirement. Single-site localization with Design C was going to be especially complex, so it was reasoned that two-site localization would be impractical.



Design B still required solving the multiple-site challenge, but the relative simplicity of single-site localization gave hope.

The multiple-site problem is best demonstrated with an example. Figure 3.9 shows the peak counts as a function of depth for a simulated event in Design B. This was the total peak counts from decoding hit patterns on both sides of the detector. The light emitted was equivalent to a neutron elastically scattering off a proton and depositing 1 MeV, so this was a relatively energetic deposition. The peak is clearly visible at 4.5 cm.

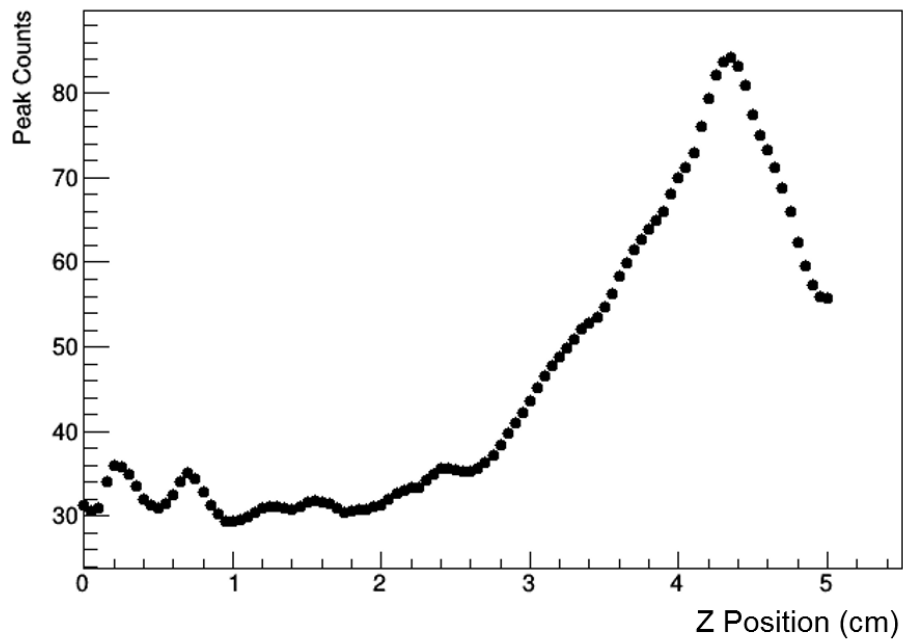


Figure 3.9. Peak counts (weighted average of the two sides) as a function of distance from the mask (depth). The emission point was truly at 4.5 cm, where a 1 MeV energy deposition released about 1680 photons.

Figure 3.10 shows the same plot, but for a single 200 keV deposition that released much less light at the same location. Using this information alone, it would be difficult or impossible to determine that there was only one interaction. This demonstrates the challenge of reconstructing low-energy depositions, which constitute the majority of multiple-site interactions.

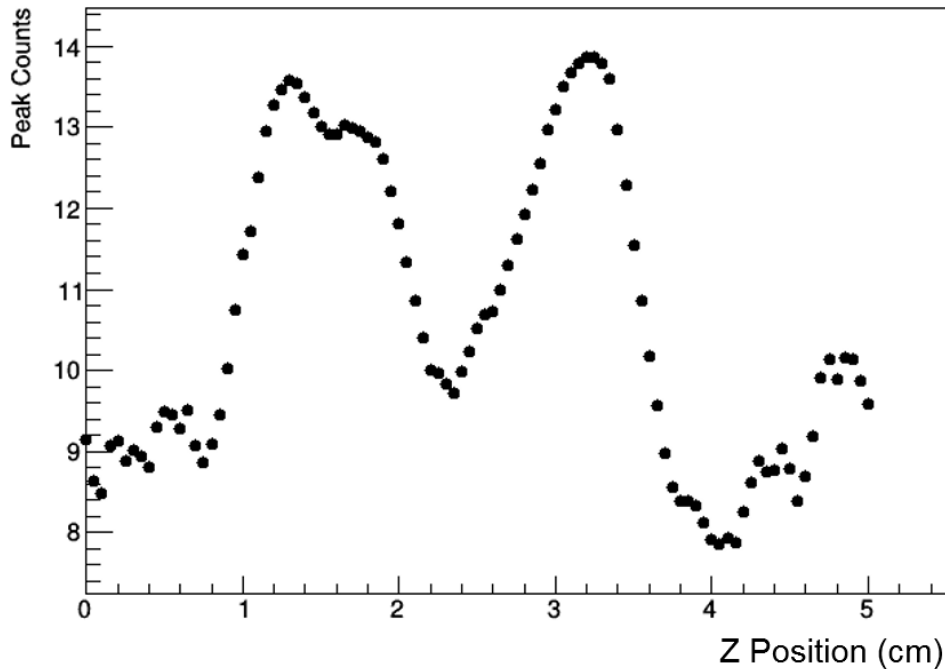


Figure 3.10. Peak counts (weighted average of the two sides) as a function of distance from the mask (depth). The emission point was truly at 1.5 cm, where a 200 keV energy deposition released about 275 photons.

To complicate things further, recall that the  $Z$  position, obtained from software focusing, is required to decode the image and calculate the  $X$  and  $Y$  positions. So, any effort to select one of the peaks in Figure 3.10 would likely require reconstructing the  $XY$  position at both locations, then choosing one based on another piece of information. This quickly becomes an arduous and computationally intensive process.

Figure 3.11 and Figure 3.12 provide two more examples. In the former, an unrealistically large amount of energy (20 MeV) was deposited at the same  $XY$  locations (the mask plane dimension), separated by 4 cm in  $Z$  (orthogonal to the mask plane). This is the ideal case: the separation is apparent in  $Z$ , but only a single peak is visible in  $X$ . Since the  $Z$  dimension must be determined first, and two peaks are identifiable, this event is reconstructable. However, in the latter figure, the same energies were deposited at locations separated by 5 cm in  $X$ , but at the same  $Z$  position. Reconstructing this event is difficult since multiple steps through the process are required to determine that there were two interactions. At low statistics, it is even more challenging since multiple peaks (due to artifacts and statistical fluctuations) may be present even with one interaction, as shown in Figure 3.10.

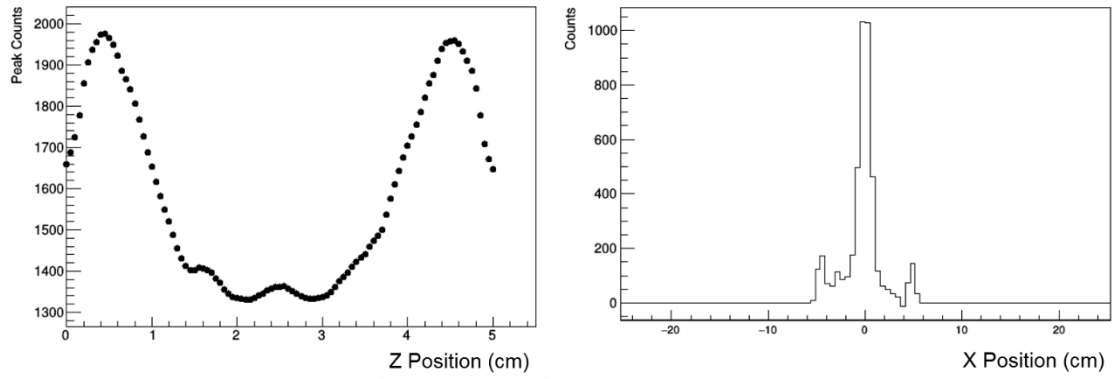


Figure 3.11. Peak counts and reconstructed  $X$  image for two 20 MeV depositions in Design B. The locations were at the same  $XY$  position and separated by 4 cm in  $Z$ .

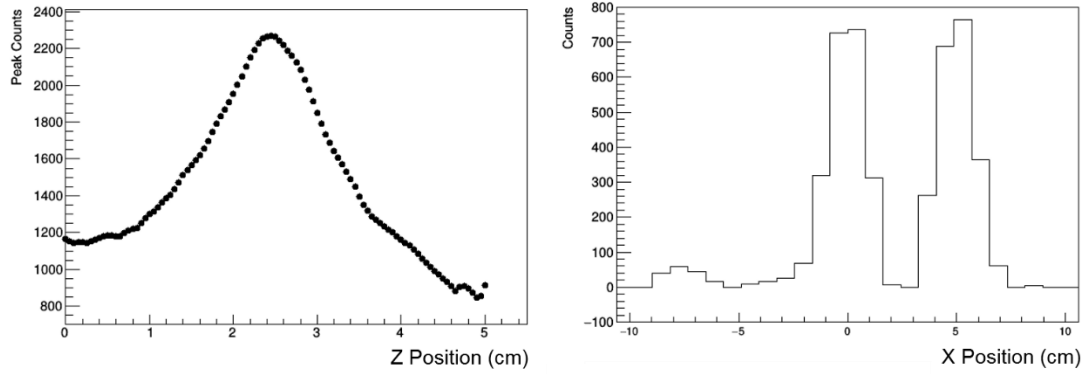


Figure 3.12. Peak counts and reconstructed  $X$  image for two 20 MeV depositions in Design B. The locations were at the same  $Z$  position and separated by 5 cm in  $X$ .

Viewing these distributions, the challenge quickly becomes apparent – disentangling the overlapping peak counts and overlapping  $XY$  peaks at the same time is very difficult. Doing so would likely require a much more sophisticated algorithm than the cross-correlation employed here. While it is possible Design B may ultimately perform better

than Design D, the practical implementation of Design D is much easier. For these reasons, Design D, the slab detector geometry with 1-D coded mask patterns, was selected.

Despite Design B not being selected, it was considered the best alternative to Design D, and the single-site performance of both Designs B and D were benchmarked (Figure 3.13). The simulations randomly chose single site interaction locations from the central  $5 \times 5 \times 5 \text{ cm}^3$  volume of the full  $50 \times 50 \times 5 \text{ cm}^3$  detector (or  $5 \times 5 \times 0.3 \text{ cm}^3$  in the central slab for Design D), far away from the edges. Every event simulated 300 keV deposited by a neutron scatter, emitting about 424 photons, Poisson-distributed. The mask pattern was a 1-D rank 17 MURA with 1.4 mm pixels and a 5 mm focal length in both cases. The photodetector had 3 mm pixels with a 25% QE.

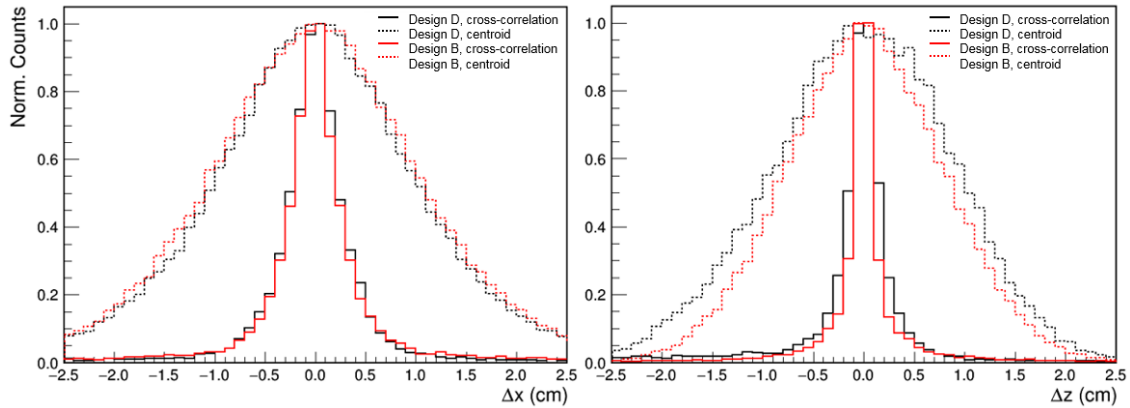


Figure 3.13. Comparison of X and Z localization performance for Designs B (red) and D (black). Solid lines were produced using the cross-correlation, and dashed lines were produced by taking the center of mass of the hit maps for comparison. Each plot contains about 30,000 events.

For comparison, dashed lines show the result when the centroid and width of the light spot were used for localizing in  $X$  and  $Z$ , respectively. The FWHM reported was calculated by interpolating on the histogram. The performance in both cases was very good, but the exact resolution should be taken lightly. As stated previously, the simulation idealized many factors; the goal was to understand if the designs were feasible and to gain insight into how they behaved. The next chapter dives much deeper into aspects of realizable hardware, utilizing a full physics simulation to model and benchmark Design D in detail.

## 4 OCA SLAB DESIGN STUDY

### 4.1 Full Physics Simulations

As discussed, the initial design studies (Chapter 3) demonstrated the feasibility of the OCA Slab design utilizing a custom but idealized optical transport code using Geant4 [8]. A full physics simulation, also using Geant4 and based on existing code written by our collaborators at Sandia National Lab (SNL), was developed next. The new simulation included collaborative upgrades to the SNL code to enable rapid prototyping and modification of detector designs without recompilation, had an improved user interface, was multithreaded, and generally was more modular. The need for these features was driven by the fact that the code would be used by multiple researchers developing the different designs outlined in Section 2.2.

Practically speaking, it was impossible to include every physical effect in the Monte Carlo simulation. As a result, the most important systematic effects were included while others were treated as behaving ideally. The simulation code included common neutron and gamma-ray sources with a variety of geometries and emission distributions to choose from. It modeled the transport for these particles, from emission to final energy deposition (or escape from the simulation world). For particles that deposited energy in the active scintillator volume, scintillation photons were produced according to the light yield and wavelength distributions reported by the manufacturer and a bi-exponential time profile. The rise time and decay times used were the values reported in Table 1.1. The proton light yields measured by [25] for EJ-204 were used, and the ion light yield was assumed to be linear and equal to 1.7% of the electron light yield [62] for an equivalent energy deposition.

For the optical transport in the full physics simulations, optically coupled surfaces were all perfectly polished. The attenuation length and material composition of the scintillator reported by the manufacturer were used. The refractive indices of the scintillator (and light guides), and the borosilicate glass MAPMT entrance window were 1.58 and 1.49, respectively. The entrance window was 1.5 mm thick, allowing the light to spread out

and induce optical crosstalk in neighboring slabs. The mask pattern was 100  $\mu\text{m}$  thick, perfectly absorptive, and the openings had the same refractive index as the plastic. The retroreflector was kept perfectly efficient and introduced no angular dispersion. The ESR was 98.5% efficient and the aluminum in between was 100% absorptive.

The simulation code recorded the times of, and energies deposited by neutron scatters (truth information), as well as the times and locations of scintillation photons as they struck the back of the MAPMT entrance window. Further processing applied a typical QE of 33% by randomly eliminating 67% of detected photons. A Gaussian-distributed TTS was also applied with a FWHM of 350 ps, reflecting the reported TTS of the H12700 MAPMT. Photon arrival locations were binned into a uniform array of  $8 \times 8$  pixels  $6 \times 6 \text{ mm}^2$  in extent each to account for the finite resolution of the phototubes.

A pencil beam of 2.5 MeV monoenergetic beam of neutrons was directed at the detector for demonstration purposes. Figure 4.1 shows a screen capture of the OCA Slab Prototype detector geometry with a single neutron scatter event, visualized using the Geant4 Qt interface. In the image, the blue axis is Z, the red axis is X, and the green axis is Y. As shown, the scintillation light generated by the recoiling proton was ultimately piped down the slab towards the photodetectors.



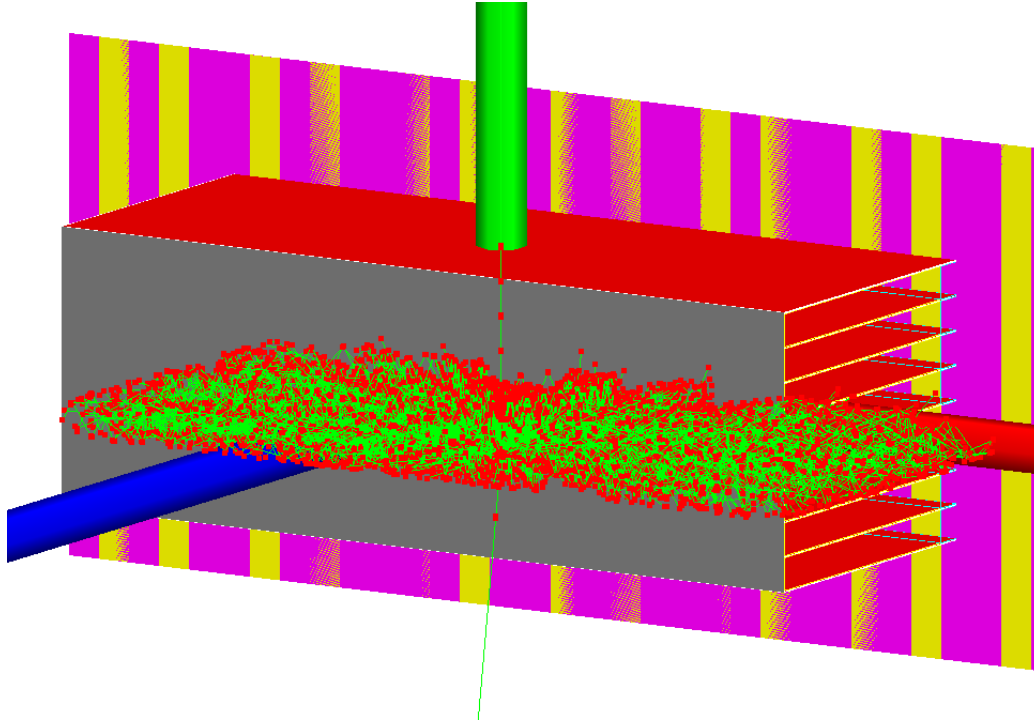


Figure 4.1. Screen capture of the Geant4 simulation geometry for the OCA Slab Prototype. Open mask elements are shown in yellow and magenta indicates closed elements. The retroreflector is shown in gray and ESR is shown in red. The green track coming from the top and exiting the bottom is the incident neutron, and the other tracks are optical photons.

Figure 4.2 and Figure 4.3 show a neutron double-scatter event across two slabs from two viewing angles. The neutron is again incident from the top, scatters once in the second slab, then again in the last slab before exiting down to the right. As with Figure 4.1, the optical isolation between slabs is clearly visible. If one looks carefully, the top left of Figure 4.2 contains an example of a photon that crossed slab boundaries at the mask plane, where there was no optical segmentation in the simulation. This was a very rare occurrence since the mask was 100  $\mu\text{m}$  thick.

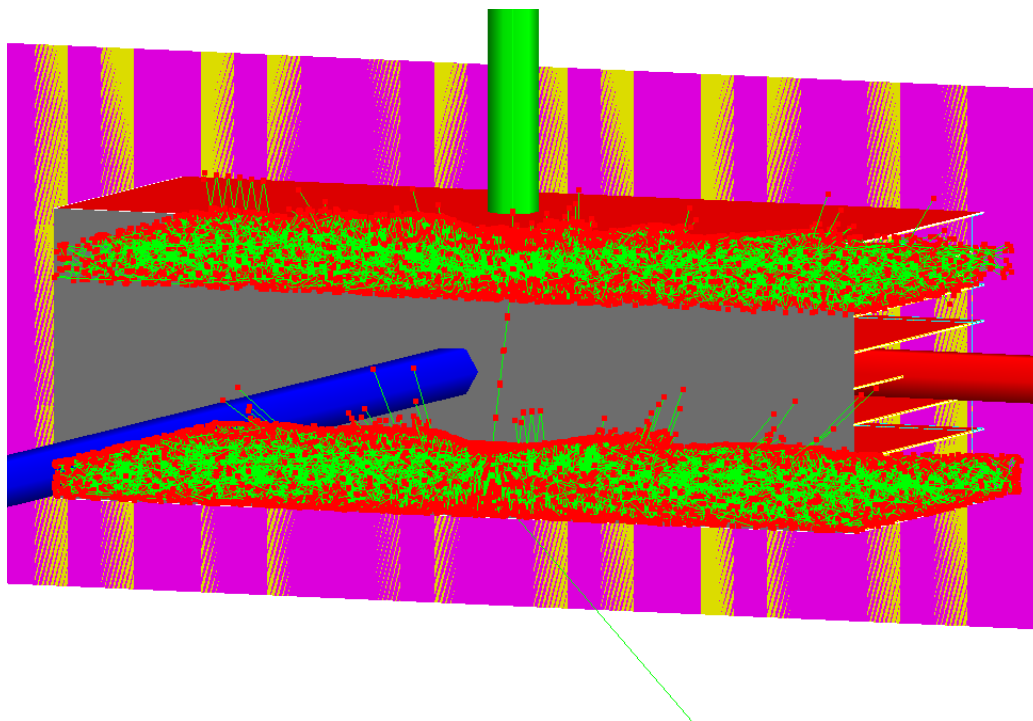


Figure 4.2. Screen capture of an event where a neutron was incident from the bottom, scattered once in the lower slab, then scattered again in the upper slab. Green lines indicate neutron and optical photon tracks, and red dots indicate when a track hits or crosses a volumetric boundary.

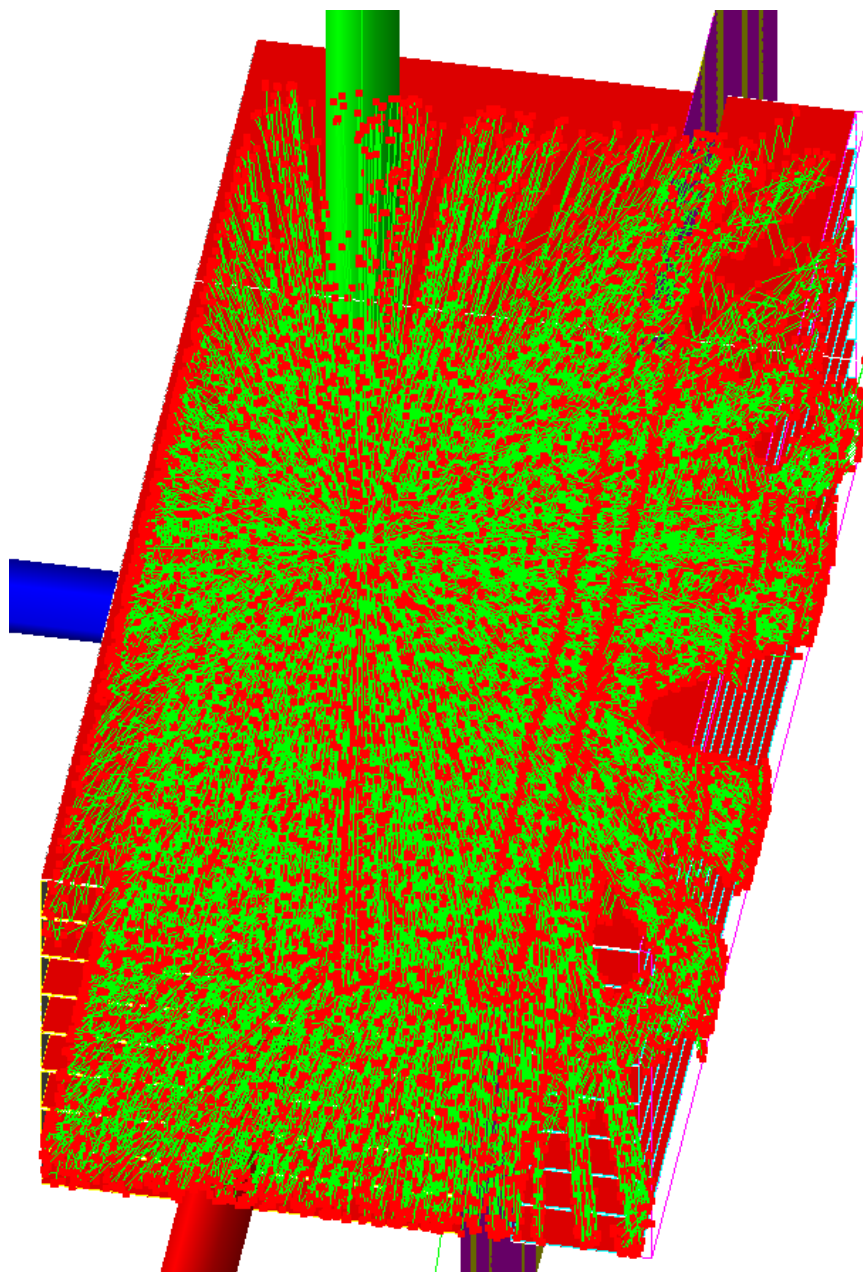


Figure 4.3. The same neutron scatter event as in Figure 4.2, but from an orthogonal view.

The attenuation of the scintillation light by the coded mask before it reaches the phototubes is also very clear. The boundaries between scintillator and light guide are also apparent as lines of red dots, which indicate tracks crossing volumetric boundaries.

## 4.2 Event Reconstruction Methods

A simulated event is comprised of a neutron double scatter that deposits energy at two locations in the detector volume. The event reconstruction process involves determining where, when, and how much energy was deposited by each interaction. It also includes triggering: the act of determining that there was an event in the first place. All of these steps will be detailed in this section, starting with the most involved task, scatter localization. While the triggering occurs first in the analysis chain, localization is required for the energy and timing determinations since they are dependent on the interaction positions.

So far, we have only discussed reconstructing interaction locations by performing the cross-correlation iteratively at a set of interaction distances and identifying the most in-focus location. Alternatively, one can calculate [26] or empirically determine the detector response, then fit the measured data from an event to the expected signal from interactions at different locations throughout the detector volume. The best-fitting location is then chosen as the correct interaction position. To this end, a number of different goodness-of-fit metrics were tested. One of the benefits of the fitting approach is that systematic effects that are difficult to describe analytically can be incorporated into the system response. This capability was required to successfully conduct the parameter study, since certain detector features (e.g. reflectors placed on the narrow side walls of the slab) break the assumptions inherent to the cross-correlation reconstruction. As will be shown, the fit-based techniques perform better, not only because of the aforementioned inclusion of geometric effects, but because the fits explicitly include the uncertainties as well.

Both the cross-correlation and response-fitting methods were evaluated based on their ability to localize a set of simulated neutron double-scatter events. Before comparing

these methods, the process for building the detector response using simulated data and the details of the fitting procedures are described below.

#### ***4.2.1 Construction of Detector Response Table***

The simulated response table was built by placing an optical photon point source in a  $45 \times 15$  array of locations in the  $Y$  centers of a slab with points 3.2 mm and 3.3 mm apart in the  $X$  and  $Z$  dimensions, respectively. The grid spacing was selected as roughly half the mask pixel size, motivated by Nyquist-Shannon sampling theorem [63]; it was empirically determined that finer spacing yielded minimal to no gains in resolution. The grid (in the  $XZ$  plane) therefore covered the entire active volume of a slab. The point source emitted one million optical photons with wavelengths and a bi-exponential time profile characteristic to EJ-204. The hit maps, photodetection efficiencies (PDE), and relative timings, determined using a 30% constant fraction discriminator (CFD), were recorded for each grid location. The timing was recorded to include the fact that events at different locations have different light transit times to reach the photodetector. In EJ-204, for optical photons, the speed of light is approximately 20 cm/ns, so a photon emitted furthest away from the MAPMTs took about 250 ps longer to reach them than one emitted near the light guide. Photons were very likely to bounce multiple times on the way to the phototube, extending their path beyond the expectation from the speed of light and the detector height alone. Figure 4.4 shows the PDE distribution and Figure 4.5 shows the transit time distribution in one slab of the OCA Reference Design (Section 4.3.1), determined using the method described above.

Note that for the algorithms described in Sections 4.2.7, 4.2.8, and 4.2.9, the expected hit maps had to be normalized to unity. In the case of the likelihood-based approaches, this was necessary to account for the diminishing probability of observing a photon as the distance to the photosensor increased. For the  $\chi^2$  method, the normalization accounted for the fact that the table was constructed by emitting a large number of photons, but event-by-event, the numbers of detected counts varied significantly, depending on the amount of energy deposited.

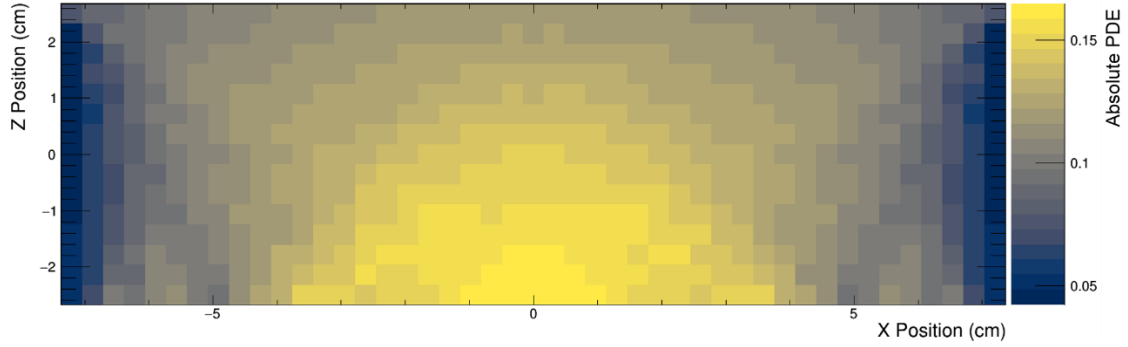


Figure 4.4. Absolute photodetection efficiency as a function of position in a single slab of the OCA Slab Reference Design.

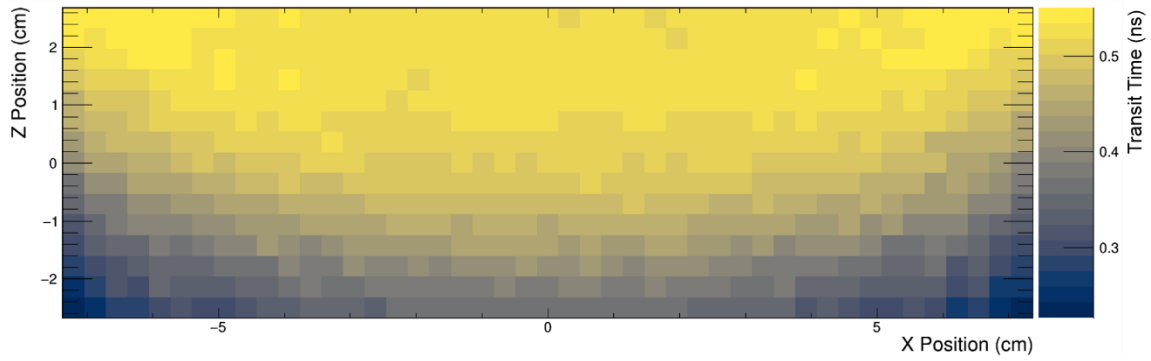


Figure 4.5. Transit time of photons from emission point to detection in the MAPMT. There was 3 cm of light guide between the bottom of the scintillator and the phototubes, resulting in the 300 ps offset.

#### 4.2.2 Triggering

During event reconstruction, a slab was considered triggered when 10 or more photons were detected. Depending on the interaction location within the slab, this corresponds to a proton recoil low-energy threshold between 150 and 450 keV. There was no logic included to detect slabs that triggered due to optical crosstalk. While there are events in this category, they were not found to be a significant source of error, constituting less

than 5% of the reconstructed neutron double-scatter events. As will be shown in Section 4.5.1, we expect about 10% of the detected light from one slab to be detected by the anodes under each neighboring slab, for a total loss of 20%. With a threshold of 10 photons, an interaction would need to generate enough photons that 100 were detected in the primary slab, corresponding to neutron scatters that deposited more than 1.5 MeV.

#### ***4.2.3 Energy Determination***

The proton recoil energy was calculated by first localizing the event, then determining the number of emitted photons by accounting for the QE and photodetection efficiency (Figure 4.4). The proton light yield table used for the simulations was then interpolated with a cubic spline to obtain the energy deposited.

#### ***4.2.4 Time Determination***

The timing was determined by applying a leading-edge discriminator (LED) with a threshold of one photon. An LED was used instead of a CFD due to the limited photon counting statistics. Since the events were simulated, there was no noise, dark counts, or other mechanism to detect a false count in a slab besides optical crosstalk. The time was then adjusted using the tabulated transit times from the look-up-table, depending on the interaction location.

#### ***4.2.5 Localization: Cross-correlation Method***

The cross-correlation event reconstruction method was a direct implementation of the concepts outlined in Section 1.6 and shown in Figure 1.5. To decrease the computational load, the cross-correlation decoding algorithm used a look-up-table (LUT) instead of calculating the cross-correlation directly. The decoded images corresponding to every detector pixel and source distance combination were calculated in advance, effectively creating a map between one count in a given MAPMT pixel and the image produced by decoding that count. This had the benefit of being computationally much faster (factor of  $\sim 10$ ) and made it easier to incorporate necessary normalizations. Proper normalizations were critical in determining the depth; since as the magnification changed, the number of pixels projected onto the detector did as well. Even though it used a LUT, the basic

approach was the same as described in Section 1.6. After identifying a slab that was above threshold, images were made for a range of source distances. The source distance that produced the image with the highest peak counts was chosen as the source distance. The centroid of this image was then determined to find the lateral location along the slab by taking the center of mass of the peak bins.

The previous gamma-ray system [33] corrected for the distortion of the light spot due to the index change [64], but it should be noted that the change occurred at a fundamentally different point in the coded-mask system compared to this system. In the prior work, the index change was between the scintillator and the light guides, between the source and the mask; whereas here, the change is between the mask and the phototubes. The index change is also much less in this system (1.8 to 1.5 in the prior work, compared to 1.58 to 1.5 here). Some attempts were made to introduce a correction factor, but it proved to not be worth pursuing because the fit-based approaches were more effective. The result of the index change was a bias in the  $Z$  reconstruction, which itself caused a smaller bias in the  $X$  reconstruction (see Figure 4.7).

To demonstrate the different localization methods, it is helpful to show an example. For this purpose, a true single site neutron scatter event was selected from the set of reconstructed events for the OCA Reference Design (Section 4.3.1). The neutron scattered off of a proton at (2.20, 2.19, -1.66) cm, depositing 433 keV. Figure 4.6 plots the detected photon hit map together with the hit map expected from the true interaction location, taken from the response table.



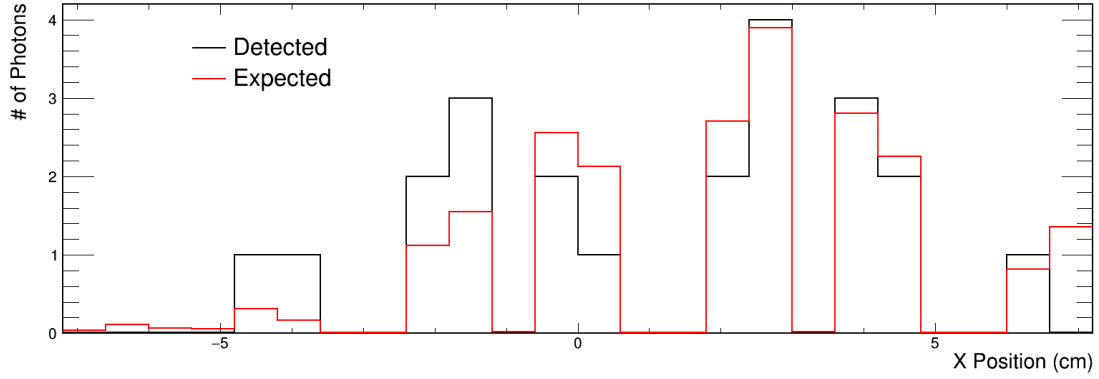


Figure 4.6. Detected hit map (black) and expected hit map from the response table (red), using the true scatter location.

The result of applying the cross-correlation algorithm to find the interaction location is shown in Figure 4.7. It shows the peak image counts as a function of depth to find the  $Z$  position (top) and the final decoded image (bottom), used to find the  $X$  position. In the bottom image, most of the FOV is empty because the mask pattern was repeated. Due to the periodic nature, counts from the repeated projected patterns further from the interaction location were added to the primary location to improve statistics.

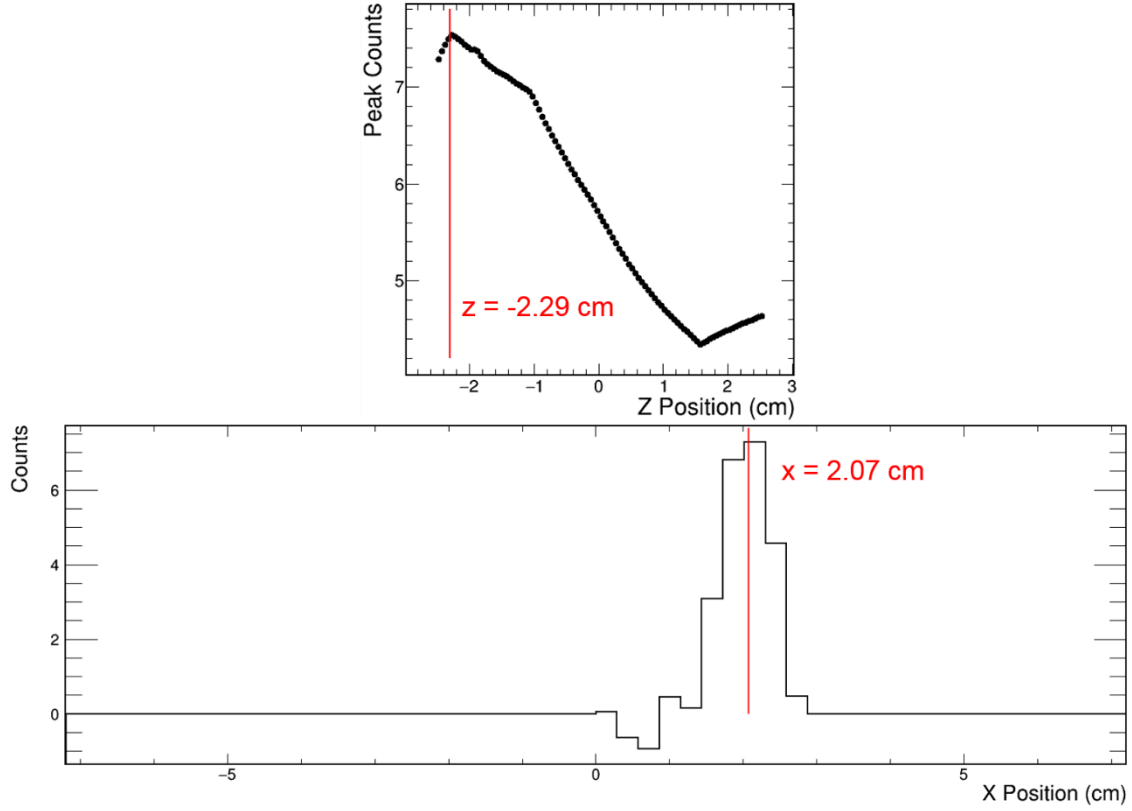


Figure 4.7. Annotated plots of the software focusing (top) and final decoded image (bottom). The reconstructed positions are shown (truth: (2.20, -1.66) cm).

#### 4.2.6 Study of Centroiding for Cross-correlation Method

Three methods were examined to find the final  $X$  position from the reconstructed images: center of mass on the whole image, a Gaussian fit on the reconstructed image, and center of mass (COM) on only the peak pixels. Since the reconstructed image bins can have negative values, and the baseline does not generally average to zero due to near-field artifacts (in the far field, the intensity is relatively uniform, whereas in the near field, the solid angle causes a significant fall-off), taking the center of mass of the whole image

works very poorly. Figure 4.7 (bottom) shows an example of a reconstructed image. Using a Gaussian fit performs better than finding the COM of the whole image, with  $X$  resolution comparable to the peak-only centroiding, but the  $\Delta X$  distribution has tails that result in overall poorer energy and timing performance. Figure 4.8 shows the  $\Delta X = X_{recon} - X_{true}$  distributions for all three methods using roughly 30,000 reconstructed double-scatter events in the OCA Slab Reference Design. Table 4.1 summarizes the performance results.

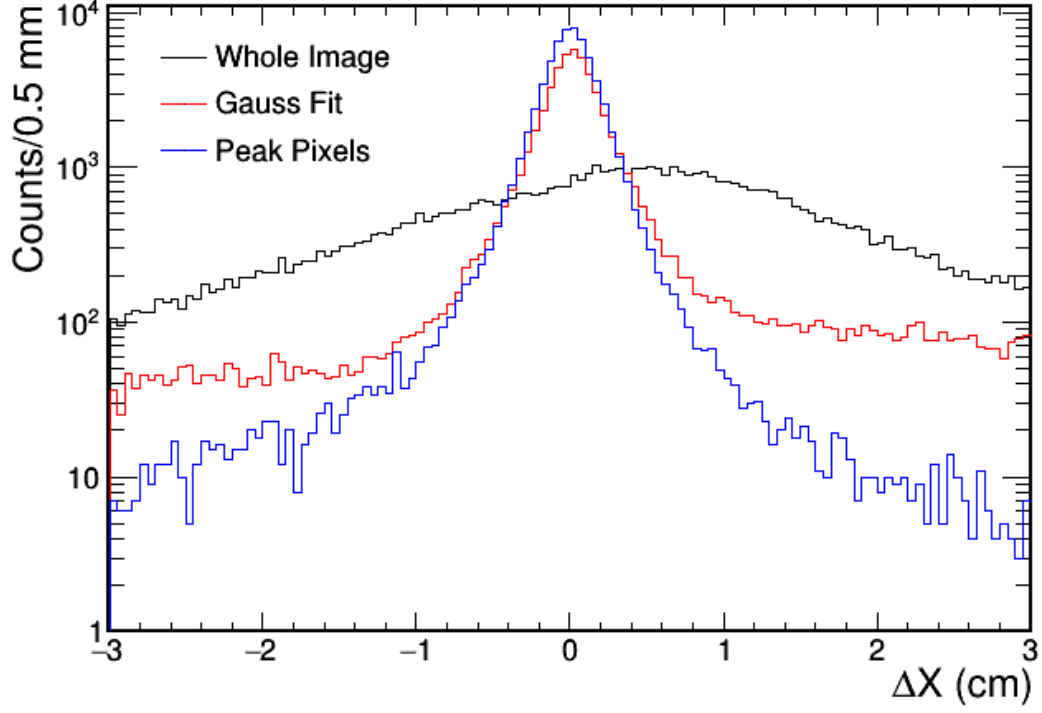


Figure 4.8 Log-scale  $\Delta X$  distributions using the COM on the whole image (black), fitting with a Gaussian (red), and using the COM on only the peak bin and its nearest neighbors (blue).

Table 4.1: Summary of X position resolutions for each method. The FWHM is calculated via linear interpolation on the histogram. Errors are calculated assuming Poisson statistics.

Method	FWHM (cm)
Whole Image COM	$2.299 \pm 0.007$
Gaussian Fit	$0.315 \pm 0.001$
Peak-Only COM (3 Pixels)	$0.292 \pm 0.001$

It was initially unclear whether the number of peak bins over which to apply the COM depends on the mask pixel size, the source distance, and whether or not the image is anti-aliased. In the ideal case, a point source should have all of its counts concentrated in a single peak bin. By empirically comparing the distributions of the  $X$  resolution for each of the six detector pixel sizes and aliasing arrangements of interest — three detector resolutions (1.5, 3, and 6 mm) with two variations each (aliased and anti-aliased) — the optimum number of bins was determined to be one on either side of the peak bin (three total). The results of this study are shown in Figure 4.9. In all cases, an optimum was found at three bins; one bin (just the peak) provided no additional information, while including more than three bins meant integrating the baseline, which included near-field artifacts.

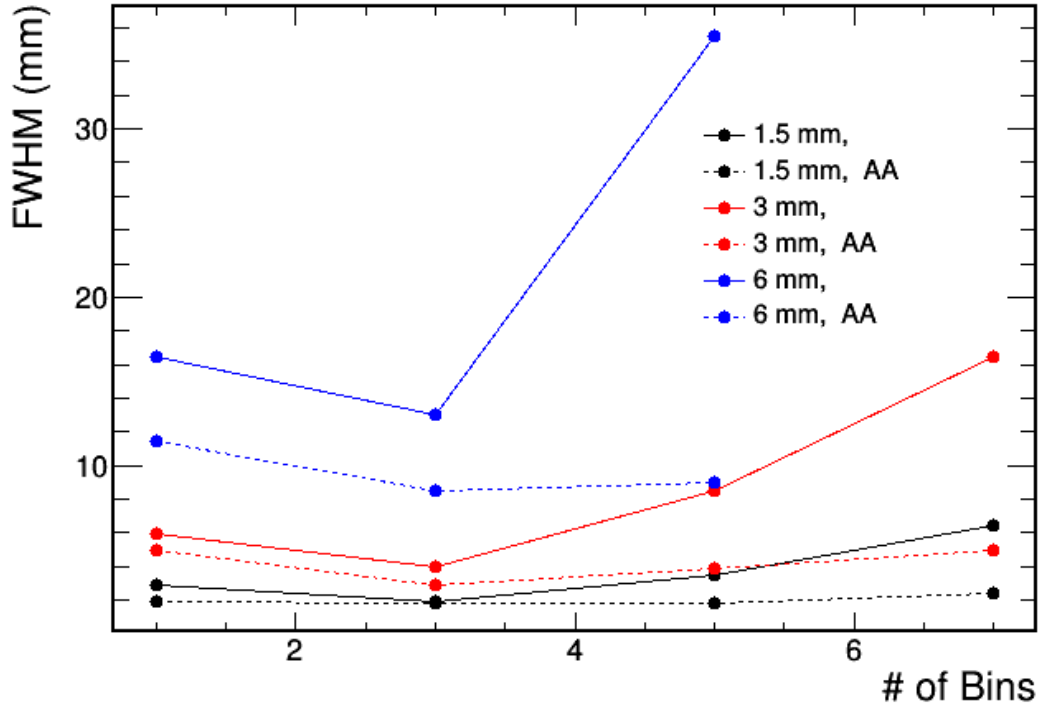


Figure 4.9: X resolution as a function of detector pixel size and number of peak bins used in the COM calculation. Solid lines are produced using aliased images whereas dashed lines use anti-aliased images.

#### 4.2.7 Localization: Maximum Likelihood Method

For a given event, the maximum likelihood (ML) approach used the hit maps from the response table to find the interaction location that was most likely [65]. Using the known number of photons emitted from each interaction location in the response table, an absolute probability of detecting a photon in a given detector pixel from any interaction location was calculated directly. As was the case for some of the other methods, the relative confidence in the number of photons in the observed data was not considered. The likelihood of the observed 1-D hit pattern  $d$ , where  $d_i$  is the number of photons

observed in a pixel, being generated from location  $(x, z)$  with probability distribution  $p$  is expressed as (where  $p_i$  is the probability of observing a photon from this location in pixel  $i$ ):

$$L(x, z) = \prod_{i=1}^{N_{pixels}} d_i p_i(x, z), \text{ for pixels where } d_i \neq 0 \quad (4.1)$$

The simplest approach to maximize the likelihood is to iterate over every  $(x, z)$  location, calculate  $L$ , then determine the global maximum. More sophisticated methods exist that do not require testing every location, however the total number of locations was typically only  $45 \times 15 = 675$ , which is on the order of the minimum number of calculations that e.g. a minimizer would perform anyway, so the brute force method was used since it was guaranteed to find the global maximum. Note that  $p_i(x, z)$  could be zero since there were no sources of accidental photons in this simulation. Because the slabs were identical, the response for only a single slab was constructed. If one pixel that had probability ( $p_i$ ) of zero observed a photon, then the entire quantity  $L$  goes to zero, making these pixels very important for this method. By contrast, methods that utilize the uncertainties would instead treat these pixels with low importance due to their high relative uncertainties.

Once the 2-D distribution of ML values were calculated, the center of mass of this distribution was used to determine the final  $(x, z)$  interaction position. This is distinct from, but similar in results to, interpolating on the hit maps themselves when doing the comparison on simulated data, which was done with the experimental data.

Figure 4.10 shows the likelihood heat map from the example event from Section 4.2.5. As mentioned, likelihood values could be exactly zero if a photon was detected behind a closed mask element, since the response for that pixel was zero at that interaction location.

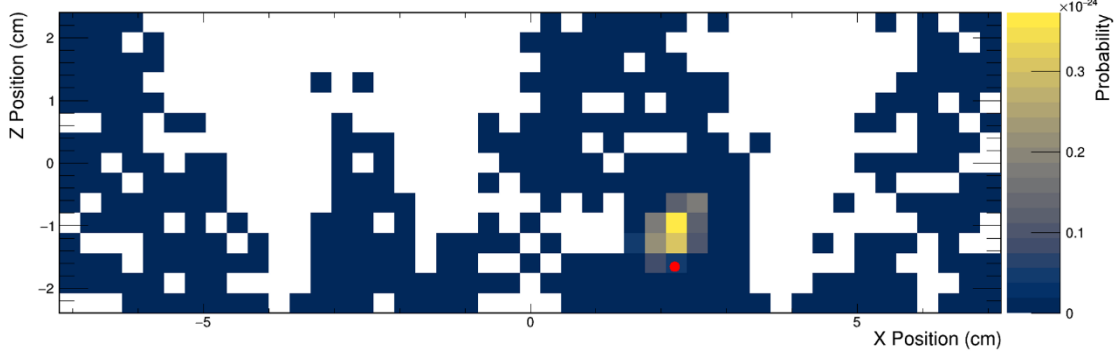


Figure 4.10. Heat map of probabilities for a single event using the ML approach. Locations were identically zero when a pixel behind a mask element detected a photon. The red dot indicates the true interaction location.

#### 4.2.8 Localization: $\chi^2$ Method

$\chi^2$  minimization is a common technique of comparing a function or set of data to another [65]. The metric is the sum of the squares of the differences between the two items at every data point of interest, weighted by the confidence in that value, assumed to be normally distributed. Like with the ML technique, finding the interaction location involved iterating over the response table and finding the entry that best matches the observed data (maximizes  $1/\chi^2$ ):

$$\chi^2 = \sum_{i=1}^{N_{pixels}} \left( \frac{d_i - p_i(x, z)}{\sigma_i} \right)^2 \quad (4.2)$$

Here,  $\sigma_i$  is the standard deviation of the observed value  $d_i$ , assumed to be equal to  $\sqrt{d_i}$ . In cases where zero photons were detected in a pixel,  $\sigma_i = 1$  was used to avoid dividing by zero. Figure 4.11 shows the inverted  $\chi^2$  heat map for the demonstration event. While the



peak is not as sharp as the ML method shown above, the centroid of the distribution is closer to the true source location.

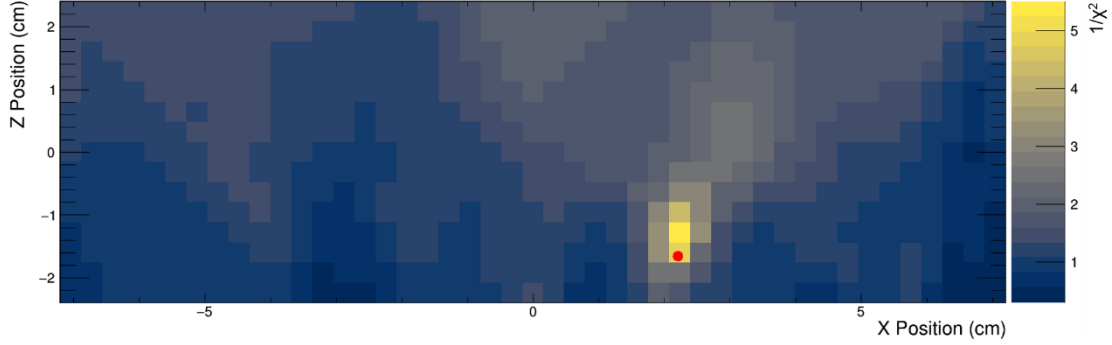


Figure 4.11. Heat map of inverted  $\chi^2$  values for the example event.

#### 4.2.9 Localization: Log-likelihood Method

The log-likelihood is conceptually similar to the ML approach, except uncertainties are assumed Poissonian and incorporated into the comparison. This yields better localization performance at the cost of computational time, since the logarithm is an expensive operation. Using the same definitions as the previous two approaches, the comparison equation is [65]:

$$L = \sum_{i=1}^{N_{pixels}} p_i(x, z) - (d_i \log(p_i(x, z))) \quad (4.3)$$

The same normalizations were applied here as the ML approach. This method was expected to perform the best based on its theoretical formulation, and this was found to be true empirically. Using the same example event shown in the last two sections, Figure

4.12 shows the heat map of log-likelihood values, inverted and negated for presentation purposes.

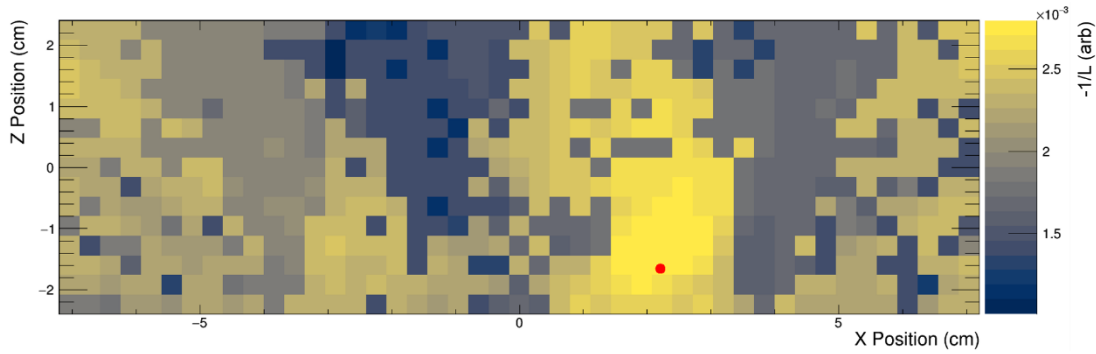


Figure 4.12. Heat map of inverted, negated log-likelihood values. The true source position is shown as a red dot.

As with the other response-based localization methods, contours tended to align with shadows from the mask pattern. Overall, the cross-correlation performed the worst because it did not explicitly consider the photon counting statistics. Refractive index changes, such as at the MAPMT entrance window, were also not treated, as described in 4.2.5.

The challenges faced by the cross-correlation method would be exacerbated in an experimental prototype because additional factors, such as the gaps between MAPMTs, would need to be incorporated. There will likely also be photon pathways that break the assumptions of the decoding procedure that will harm performance. Beyond this method, the straight-forward maximum likelihood had the lowest resolution of the response-based methods. This was primarily because the approach did not consider counting statistics. The log-likelihood method yielded the best performance, summarized in Table 4.2, so it was used for the parameter study, prototype simulation, and experimental work.

Table 4.2. Performance comparison of the different localization algorithms for the OCA Slab Reference Design. The values are the standard deviations of Gaussian fits to the difference distributions, described in more detail in Section 4.3.

Method	$\sigma_{\Delta X}$ (mm)	$\sigma_{\Delta Z}$ (mm)
<b>Cross-correlation</b>	$6.651 \pm 0.002$	$7.046 \pm 0.003^*$
<b>Maximum likelihood</b>	$4.122 \pm 0.002$	$5.090 \pm 0.002$
$\chi^2$	$2.768 \pm 0.001$	$4.018 \pm 0.002$
<b>Log-likelihood</b>	$2.407 \pm 0.001$	$3.388 \pm 0.001$

\* There was also an offset of about -6.5 mm due to the refractive index change.

### 4.3 OCA Slab Parameter Study

A simulation parameter study was conducted to understand the quantitative impact of varying the most important parameters with respect to the system performance. The goal was to use this information to decide what parameters to use for the prototype detector. First, the performance of a reference design chosen based on the foregoing work will be reported. While not optimal, the characteristics of that design were expected to yield a reasonable result. Each parameter of interest was then varied independently, and the same analysis was performed.

In every configuration for this study, the detector was exposed to a simulated cone beam of neutrons produced by  $^{252}\text{Cf}$  point source positioned at (57.7, 57.7, 57.7) cm, 1 meter from the detector center. Approximately 7.5 million neutrons were directed at the detector, resulting in ~500,000 reconstructable neutron double-scatter events. The log-

likelihood reconstruction described in Section 4.2.9 was used to localize scatter locations in all cases. Except for the case with 3 mm pixels, the response table consisted of 45×15 points. For 3 mm pixels, a response table with twice as many points, to account for the smaller pixel size, was used. Each section below describes what each parameter means, as well as how and why it impacted the performance.

In the tables of results that follow, each column is the standard deviation of the respective distribution fit with a Gaussian with a linear offset:

$$f(x) = ae^{-\frac{1}{2}\left(\frac{x-x_0}{\sigma}\right)^2} + bx + c \quad (4.1)$$

reflecting the relative performance. This function was chosen because it provided a consistent measure of the width of the distributions. Each entry in the tables consist of 100,000 or more reconstructed two-scatter events, for a total of more than 200,000 interactions. The statistical errors were therefore expected to be much smaller than systematic errors due to differences between the fit function and the measured distributions, e.g., see Figure 4.14, and are not reported.

#### ***4.3.1 OCA Slab Reference Design***

The reference design (Figure 4.13) had 8 slabs that were 5.7 mm wide, 50 mm high, 142 mm long, separated by 300 μm gaps containing a sandwich of air/ESR/aluminum/ESR/air. The narrow side walls were black and there was a perfect retroreflector on the side opposite the MAPMTs. The focal length was 1 cm and the gap light guide, positioned between the scintillator and mask, was 2 cm. The mask was a rank 5 1-D MURA with a pixel size of 6 mm repeated 5 times.

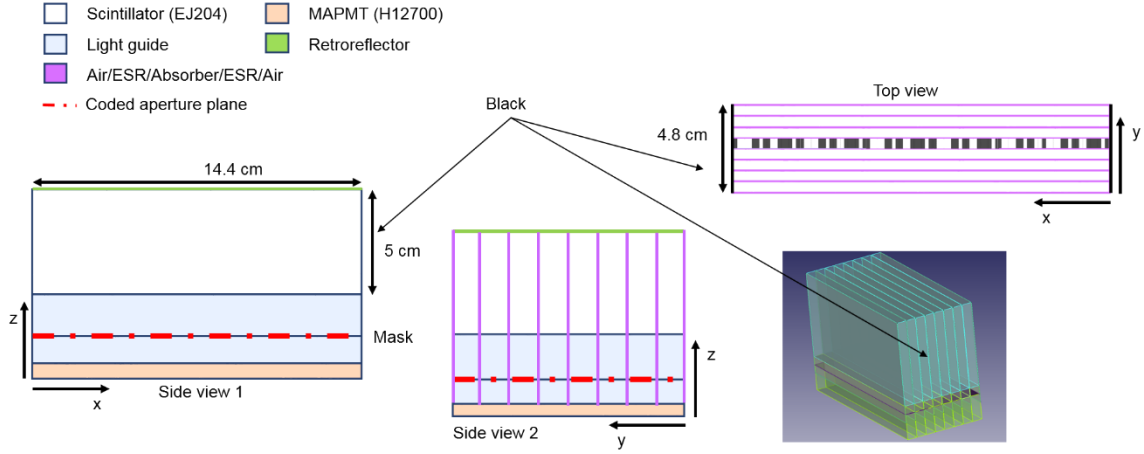


Figure 4.13. Schematic diagrams (not to scale) of the reference detector geometry. Left: side view. Middle: another side view. Top right: top view. Bottom right: CAD drawing, with the scintillator shown as turquoise, the light guides shown as green, and the mask plane shown as purple.

The performance of each parameter was measured by creating the distributions of the difference between reconstructed values and true values. These distributions consist of events where the neutron scattered in at least two separate slabs and resulted in the detection of at least 10 photons in each. The slabs were required to be separated by at least 1 slab to avoid the effects of optical crosstalk, which is discussed in Section 4.4.3. The distributions include events where the neutron scattered in more than two slabs; in these cases, the first two scatters are plotted. Figure 4.14 shows the  $X$  and  $Z$  components of the spatial resolution, as well as the energy ( $E_p$ ) and timing ( $t$ ) resolution when localizing neutron double scatters. The shapes of these distributions were found to be consistent across the different designs. The distributions for  $Y$  resemble a box function since the center of the slab was assumed for the position in that dimension – they will be shown in Section 4.4.

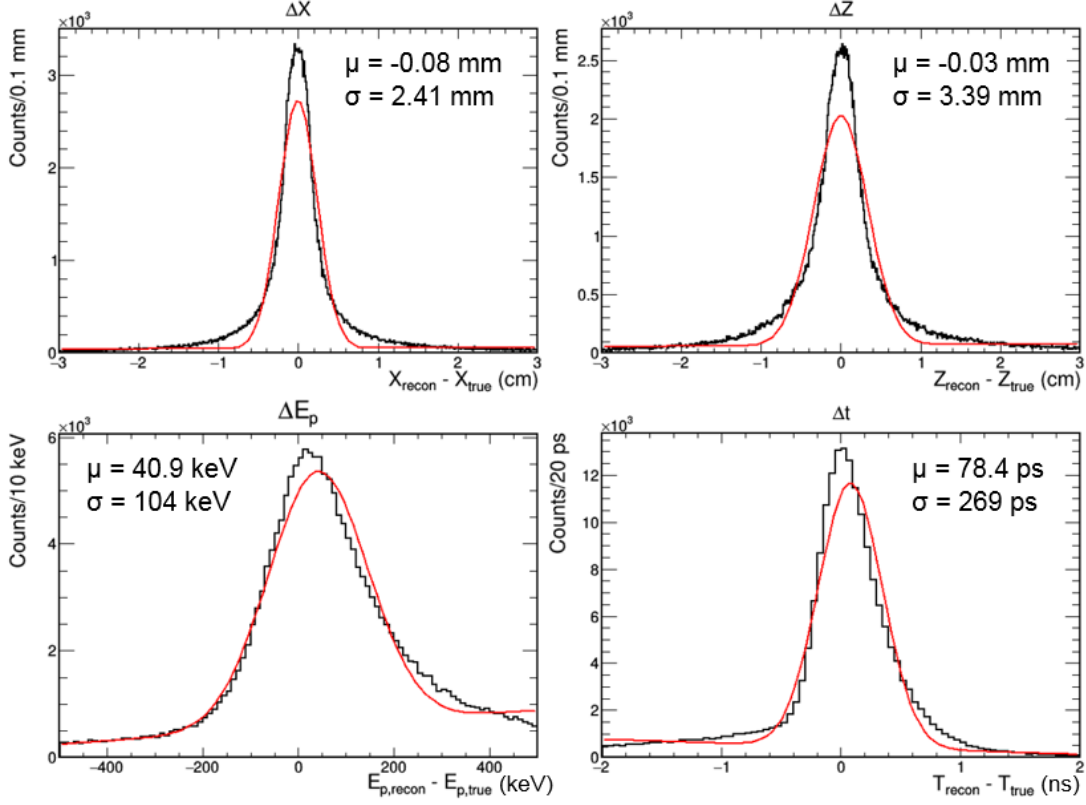


Figure 4.14. Performance of the OCA Slab Reference Design. The distributions are fit with a Gaussian superposed with a linear offset. The means and standard deviations are shown in the top right.

### 4.3.2 No Coded Mask

One of the most basic questions to pose when considering the OCA-based compact NSC is: how much does the coded mask pattern improve spatial performance in this geometry? The pattern had an open fraction of 0.4, so 60% of the light emitted by an energy deposition was lost, along with the information that comes with it. The pattern introduces high-frequency spatial modulations that allow one to make better use of the information that remains for localization purposes. Removing the mask therefore resulted in worse

spatial performance while improving energy and timing resolution due to significantly improved light collection (Table 4.3). The expected increase in energy resolution was  $\sim\sqrt{2}$  based on the higher counting statistics, however some of this gain was negated by the decreased ability to correct for the spatially variant photodetection efficiency due to worse localization performance. While expected, the magnitude of the improved energy resolution lent credibility to the simulation and analysis code as well as the detector concept in general.

Table 4.3. Comparison of performance between the reference design and the same detector with no coded mask pattern.

	$\sigma_{\Delta X}$ (mm)	$\sigma_{\Delta Z}$ (mm)	$\sigma_{\Delta E_p}$ (keV)	$\sigma_{\Delta t}$ (ps)
<b>Reference</b>	2.41	3.39	104	269
<b>No mask</b>	6.54	7.62	86	261

### 4.3.3 *Detector Height*

The detector height ultimately determined the depth FOV for the coded mask system. Fundamentally, the depth resolution necessarily gets worse as the object gets further away, so a taller detector naturally leads to, on average, worse spatial resolution (and vice versa). This is demonstrated by Table 4.4. The energy and timing resolution also diminished with a taller detector due to more opportunities for light to be absorbed. However, the trade-off was overall detector efficiency since taller slabs meant more detected events – so this parameter presents an opportunity for optimization, depending on the desired requirements.

Table 4.4. Comparison of performance for different detector heights. The number of reconstructed events was the number of detected neutron scatters with two or more interactions. Approximately the same number of source particles were emitted.

	$\sigma_{\Delta X}$ (mm)	$\sigma_{\Delta Z}$ (mm)	$\sigma_{\Delta E_p}$ (keV)	$\sigma_{\Delta t}$ (ps)	# reconstructed
<b>Reference</b>	2.41	3.39	104	269	353,000
<b>2.5 cm tall</b>	2.05	2.52	96.2	257	326,000
<b>7.5 cm tall</b>	2.72	4.13	114	274	470,000
<b>10 cm tall</b>	3.00	4.79	119	279	573,000

#### **4.3.4 Inter-slab Air Gaps**

The air gaps between slabs served to help pipe light down the slab to the phototubes via total internal reflection (TIR). When removed, just the ESR and absorber sandwich was left in the gaps, preventing optical crosstalk and piping only some of the light down to the MAPMT. The performance was marginally (~5%, Table 4.5) worse overall.



Table 4.5. Comparison of reference design performance, with and without the inter-slab air gaps.

	$\sigma_{AX}$ (mm)	$\sigma_{AZ}$ (mm)	$\sigma_{AEp}$ (keV)	$\sigma_{At}$ (ps)
<b>Reference</b>	2.41	3.39	104	269
<b>No inter-slab air gaps (just reflector/absorber)</b>	2.57	3.65	109	267

#### **4.3.5 Inter-slab Reflectors**

Like the inter-slab air gaps, the reflector (ESR) existed to guide the light down to the MAPMTs. Similarly, removing of the reflector while keeping the air gap and absorber made the overall performance slightly worse, as shown below in Table 4.6. However, the loss was smaller than removing the air gap, suggesting that the air gap was more effective in reflecting the light to the MAPMT.

Table 4.6. Comparison of reference design performance, with and without the inter-slab reflectors.

	$\sigma_{AX}$ (mm)	$\sigma_{AZ}$ (mm)	$\sigma_{AEp}$ (keV)	$\sigma_{At}$ (ps)
<b>Reference</b>	2.41	3.39	104	269
<b>No inter-slab reflector (just air gap/absorber)</b>	2.50	3.55	105	267

#### 4.3.6 *Retroreflector*

The retroreflector on the slab face opposite from the MAPMTs was turned off, turning that surface black and reducing the overall photodetection efficiency. This was expected to decrease spatial and energy resolution due to the overall reduced number of detected photons (Table 4.7). Coincidentally, it had a similar magnitude of impact as removing either of the inter-slab reflectors. Note that the retroreflector in this case had perfect efficiency and introduced no angular deviations, so this is a best-case estimate.

Table 4.7. Comparison of the reference design performance with and without the retroreflector.

	$\sigma_{AX}$ (mm)	$\sigma_{AZ}$ (mm)	$\sigma_{AEp}$ (keV)	$\sigma_{At}$ (ps)
<b>Reference</b>	2.41	3.39	104	269
<b>No retroreflector</b>	2.54	3.50	130	254

#### 4.3.7 *Narrow-edge Air Gap*

The narrow side walls, normally black, were instead exposed to air, causing incident light of an acceptable angle to undergo TIR. As mentioned previously, the procedure used to construct the response LUT incorporated the effects of the change in reflectivity at these edges. This was expected to improve energy performance while potentially degrading spatial performance, since reflections off the edge may work against the encoding introduced by the mask pattern. While this was true in the  $X$  dimension, the  $Z$  dimension improved, shown in Table 4.8. Further work is needed to understand what other potential impacts this change to the geometry could have, and what types of scatter events were affected.

Table 4.8. Comparison of the reference design performance with and without an air gap at the narrow edges.

	$\sigma_{\Delta X}$ (mm)	$\sigma_{\Delta Z}$ (mm)	$\sigma_{\Delta E_p}$ (keV)	$\sigma_{\Delta t}$ (ps)
<b>Reference</b>	2.41	3.39	104	269
<b>Narrow-edge air gap</b>	2.47	2.96	87.9	268

#### 4.3.8 *Narrow-edge Reflector*

Similar to the narrow-edge air gap, reflections off the narrow side walls lead to a better photodetection efficiency, but possibly at the cost of some spatial performance. Again, those ended up being true in the  $X$  dimension, but false in the  $Z$  dimension, shown in Table 4.9.

Table 4.9. Comparison of the reference design performance with and without a reflector at the narrow edges.

	$\sigma_{\Delta X}$ (mm)	$\sigma_{\Delta Z}$ (mm)	$\sigma_{\Delta E_p}$ (keV)	$\sigma_{\Delta t}$ (ps)
<b>Reference</b>	2.41	3.39	104	269
<b>Narrow-edge reflector</b>	2.50	2.78	84.7	269

#### 4.3.9 Gap Light Guide Thickness

The gap light guide provides space for the light spot to spread out before encountering the mask. If the interaction is close to the mask, it is possible for the light to be completely blocked, or for only a partial pattern to be encoded, resulting in diminished performance. Without the gap light guide, there is effectively a less sensitive region adjacent to the mask, with sharp discontinuities in the light distributions as a function of lateral position. This distance should be large enough to allow light to spread, but otherwise minimal in thickness to reduce the opportunities for light to be lost. This trend is confirmed by Table 4.10; the thinner gap guide performs better. Smaller thicknesses may result in even better localization performance, but there would be a loss in detection efficiency, since interactions very close to the mask would be difficult or impossible to reconstruct.

Table 4.10. Comparison of the reference design performance for different thicknesses of gap light guide.

	$\sigma_{AX}$ (mm)	$\sigma_{AZ}$ (mm)	$\sigma_{AEp}$ (keV)	$\sigma_{At}$ (ps)
<b>Reference (2 cm)</b>	2.41	3.39	104	269
<b>0.5 cm gap light guide</b>	1.96	2.51	100	263
<b>1 cm gap light guide</b>	2.09	2.77	101	263
<b>1.5 cm gap light guide</b>	2.26	3.07	103	267

#### ***4.3.10 Focal Length***

The focal length determines the range of magnifications in the coded-aperture system, where a longer length increases the magnification and a shorter length does the opposite. For this reason, in general, a longer focal length was desired; however, at some point the focal length was too long, and many detected hit patterns (depending on the interaction location) were overmagnified and not usable. Overmagnification occurs when the magnification factor results in the mask pattern that no longer fits within the boundaries of the photodetector array when the shadow is cast. On the opposite end, a very short focal length led to every event appearing to occur at the same distance (far away). There was also some connection to the gap light guide thickness, since the distance between the mask and scintillator determined the minimum magnification. Overall, the parameter study confirmed that for spatial performance, a longer focal length was desired (Table

4.11). However, this came at a small penalty in the timing and energy performance, since the added distance to the phototubes presented more opportunity for light to be lost.

Table 4.11. Comparison of the reference design performance for different focal lengths.

	$\sigma_{\Delta X}$ (mm)	$\sigma_{\Delta Z}$ (mm)	$\sigma_{\Delta E_p}$ (keV)	$\sigma_{\Delta t}$ (ps)
<b>Reference (1 cm)</b>	2.41	3.39	104	269
<b>0.5 cm focal length</b>	3.19	4.07	102	267
<b>1.5 cm focal length</b>	2.04	3.02	106	270

#### ***4.3.11 EJ-232Q Scintillator Material***

The monolithic, compact NSC design described in Section 2.2.2 proposed to use EJ-232Q [26] because of its ultra-fast timing properties, listed in Table 1.1. The potential gain in timing resolution was unlikely to be worth the dramatic reduction in light output, but it was still a point of interest. Not only did the overall localization and energy performance get worse (Table 4.12), but there was a dramatic reduction in efficiency ( $\sim 10\times$ ). This was caused by the diminished light output, roughly a third of EJ-204, which means the 10-photon threshold tripled in minimum detectable deposited energy. Since one of the key goals of building this system was to reconstruct lower-energy events with short scatter separations, this was deemed an unacceptable trade-off.

Table 4.12. Comparison of the reference design performance to the same design using EJ-232Q.

	$\sigma_{AX}$ (mm)	$\sigma_{AZ}$ (mm)	$\sigma_{AEp}$ (keV)	$\sigma_{At}$ (ps)
<b>Reference</b>	2.41	3.39	104	269
<b>EJ232-Q</b>	2.86	4.27	338	178

#### 4.3.12 Detector Pixel Size

A detector pixel size of 3 mm was tested, reflecting another common pixel size for MAPMTs, such as the Hamamatsu H9500 and H13700. With 3 mm detector pixels, the slab widths and mask pixel sizes were also changed to 3 mm. During the initial simulation studies, the decision whether to use 3- or 6-mm pixels was not yet made. The trade-off was that small pixels would yield better resolution, but the higher channel count meant fewer slabs could be fully instrumented, as shown below in Table 4.13. It was also observed, while conducting the optical crosstalk studies detailed in Section 4.4.3, that optical crosstalk was worse with smaller pixel sizes – 15% for 3 mm pixels, vs. about 10% for 6 mm pixels.

Table 4.13. Performance of an OCA compact NSC with a 3 mm element size.

	$\sigma_{AX}$ (mm)	$\sigma_{AZ}$ (mm)	$\sigma_{AEp}$ (keV)	$\sigma_{At}$ (ps)
<b>Reference</b>	2.41	3.39	104	269
<b>3 mm Detector Pixel Size</b>	1.71	2.75	98.0	257

#### 4.3.13 Parameter Study Summary

Table 4.14 summarizes all of the results from the parameter study. It includes the results from the prototype design, which will be discussed in more detail in the next section. Overall, the results indicated that a system with a shorter gap length and a longer focal length than the reference configuration would yield the best spatial resolution. Various parameters, such as the edge gap reflectors, traded some amount of position sensitivity for better energy resolution, and the choice was made to prioritize the spatial component. For all data points, more than 100,000 events were included, so the statistical errors were less than 0.5%.

Table 4.14. Full summary of parameter study results based on simulated data.

	$\sigma_{AX}$ (mm)	$\sigma_{AZ}$ (mm)	$\sigma_{\Delta E_p}$ (keV)	$\sigma_{\Delta t}$ (ps)
<b>Reference</b>	2.41	3.39	104	269
<b>No mask</b>	6.54	7.62	86	261
<b>3 mm Detector Pixel Size</b>	1.71	2.75	98.0	257
<b>2.5 cm tall</b>	2.05	2.52	96.2	257
<b>7.5 cm tall</b>	2.72	4.13	114	274
<b>10 cm tall</b>	3.00	4.79	119	279
<b>No inter-slab air gaps (just reflector/absorber)</b>	2.57	3.65	109	267



Table 4.14 Continued

<b>No inter-slab reflector (just air gap/absorber)</b>	2.50	3.55	105	267
<b>No retroreflector</b>	2.54	3.50	130	254
<b>Narrow-edge air gap</b>	2.47	2.96	87.9	268
<b>Narrow-edge reflector</b>	2.50	2.78	84.7	269
<b>0.5 cm gap light guide</b>	1.96	2.51	100	263
<b>1 cm gap light guide</b>	2.09	2.77	101	263
<b>1.5 cm gap light guide</b>	2.26	3.07	103	267
<b>0.5 cm focal length</b>	3.19	4.07	102	267
<b>1.5 cm focal length</b>	2.04	3.02	106	270
<b>EJ232-Q</b>	2.86	4.27	338	178
<b>Prototype</b>	1.71	2.34	103	264

## 4.4 OCA Slab Prototype Simulation

Based on the results from the preceding section, the following prototype design was selected and modeled to determine the optimum performance that the experimental prototype might achieve. The prototype detector height was 5 cm, the gap length was 0.5 cm, the focal length was 1.5 cm, the narrow edges were black, the retroreflector and gap reflectors were kept in place, and EJ-204 was used as the active material. These parameters were a compromise between spatial resolution, energy resolution, and overall detection efficiency. The need to use the same MAPMTs as the monolithic prototype meant that 6 mm detector pixels were chosen.

### 4.4.1 Overall Performance

Figure 4.15 shows the different measures of the prototype detector's performance. The spatial resolution was 1.7 mm in the X dimension and 2.3 mm in the Z dimension. The individual interaction energy and timing resolutions were 102 keV and 264 ps, respectively.

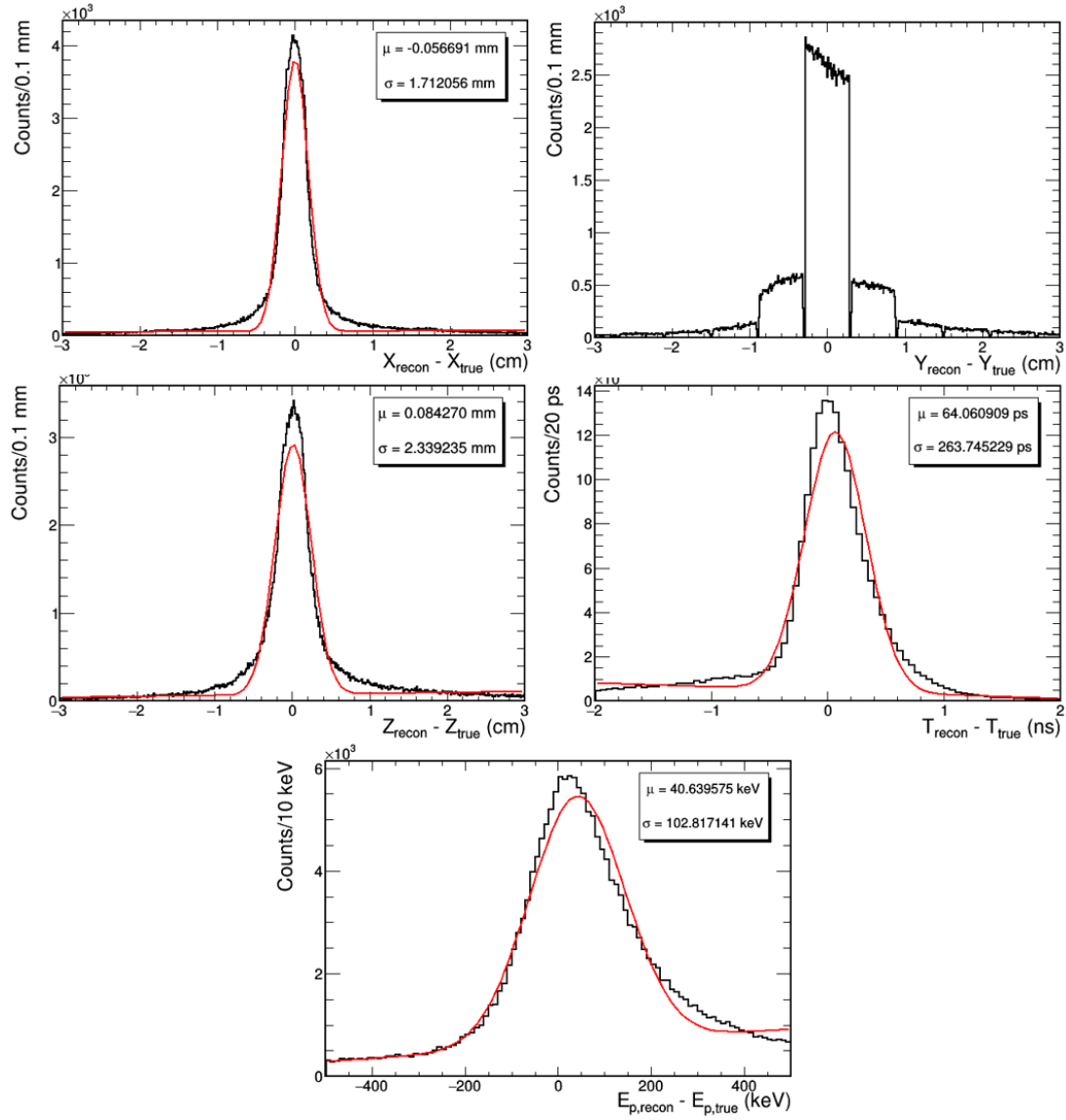


Figure 4.15. Simulated spatial, timing, and energy performance of the OCA Slab Prototype Design. These are comparisons of reconstructed and true values for neutron scatter interactions in which at least two slabs triggered (at least 10 photons detected).

As noted previously, the simulation was ideal in a number of ways, resulting in better performance than can be expected from an experimental prototype. However, these performance numbers were promising and achieved the performance goals of sub-cm localization and sub-ns timing.

#### ***4.4.2 Neutron Backprojection***

The final step in measuring the detector system's performance was to backproject the neutron double scatters and produce an image. For this, events were selected that scattered at least twice, deposited at least 100 keVee in each slab, had one slab separating the first two scatters (no nearest neighbor double scatters were allowed), and were separated by at least 500 ps in time. In theory, this permitted some events that had undetected (below threshold) scatters in other slabs, which caused the backprojection for those events to point in the wrong direction. However, these were determined to be a small fraction of events, because the energy threshold meant that the proton needed to deposit approximately 500 keV. The mean neutron kinetic energy of a fission source is around 1.4 MeV, and the scatter thresholds added up to 1 MeV, so most of the energy was captured by the two scatters.

Figure 4.16 shows a comparison of the backprojected neutron image between the event information reconstructed with the prototype and the truth information. This gives a sense for how the sum of the different parameter resolutions impact the overall performance and it shows clearly where the source was located in the images. The image on the left has a standard deviation of about  $37^\circ$  in the polar dimension and  $51^\circ$  in the azimuthal dimension. While this is larger than the experimental performance reported by, e.g., MINER ( $25^\circ$  standard deviation in the azimuthal dimension) [14], that system used a maximum likelihood expectation maximization algorithm to perform the neutron backprojection, so it is not a 1:1 comparison.

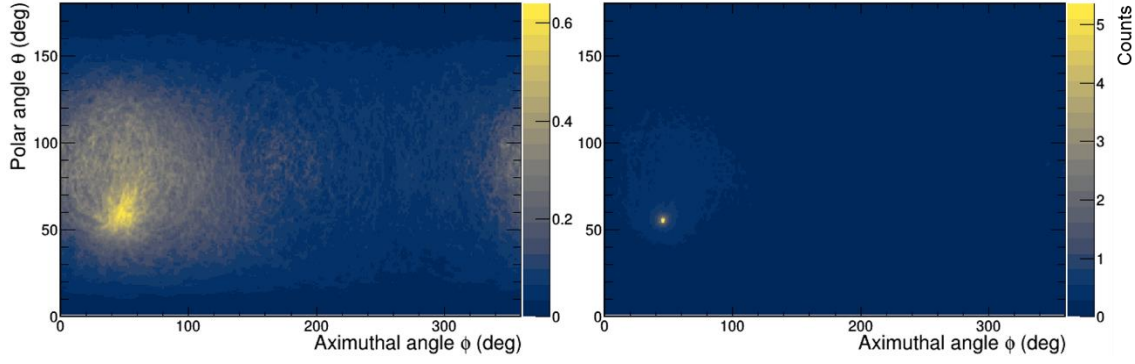


Figure 4.16. Left: backprojected image using reconstructed neutron scatter information. Right: backprojected image using the truth information. There are 6086 events in the images.

#### 4.4.3 Optical Crosstalk

For the results shown so far, optical crosstalk was included in the simulation and analysis. The crosstalk is caused by light spreading across slab boundaries as it traverses the 1.5-mm thick MAPMT entrance window. The impact was largely mitigated by requiring separation between coincident slabs; however, it was still important to understand how much optical crosstalk to expect in the experimental prototype system. This proved useful when creating the experimental event selection cuts, discussed later in Section 5.6.1.

To this end, a simulation similar to the response table configuration was run: 10 million optical photons were released from random locations in a central slab in the prototype geometry and the observations of the MAPMTs were recorded. First, it was confirmed that the amount of optical crosstalk was independent of the interaction location within the slab. For comparison, the same distribution was constructed using the photon arrival positions as they entered the window (rather than when they exited, which accounted for the light spread). Figure 4.17 shows the relative light detected by pixels underneath the different slabs.

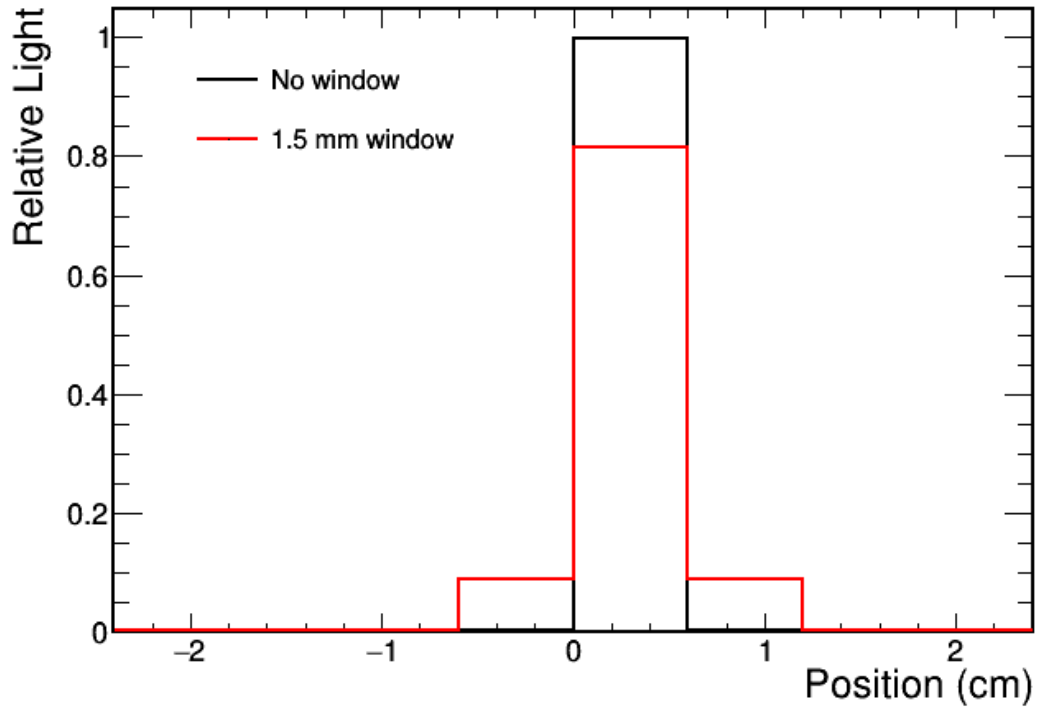


Figure 4.17. Simulation of optical crosstalk in the prototype detector. Roughly 10% of the light goes to each neighbor.

With optical crosstalk, roughly 10% of the light leaked from the primary slab into its nearest neighbors. This resulted in a small loss of spatial and energy resolution; however, at least some of this degradation is recoverable with more sophisticated event processing. One could, for example, identify slabs that likely only saw optical crosstalk and add them back to the neighbor with the appropriate normalizations.

## 5 EXPERIMENTAL WORK

The experimental prototype reflected the parameters used in the simulation, described briefly in Section 4.4, and described in more detail below. Overall, the experimental detector system consisted of eight slab modules that were coupled to three MAPMTs and housed in a 3-D printed enclosure to ensure the components stayed in place. A breakout board was used for the MAPMT anodes and the last dynodes. Only 128 digitizer channels were available, so three slabs were summed in hardware, then those three signals were digitized, along with 120 anodes (5 slabs, 24 anodes per slab). The assembly was placed in a dark box with feedthroughs for the signal cables, which were connected to the NIM electronics and digitizers. A powerful desktop computer was used to collect and store the raw waveforms and perform data processing and analysis. Sections 5.1, 5.2, 5.3 discuss the details of each of these components, and the rest of this chapter details their experimental characterization and the measurements demonstrating their performance.

### 5.1 Prototype Mechanical Design

#### 5.1.1 *Slab Fabrication*

A number of options were considered for fabricating the slabs for the OCA Slab Prototype. Due to a variety of practical factors, we ultimately tasked Eljen Corporation with fabricating the eight slabs from three individual pieces: the scintillator, the focal length, and the standoff parts. Each slab was made by taking a piece of EJ-204 ( $\sim 15.6 \times 0.57 \times 5 \text{ cm}^3$ , with margin) and affixing it to a piece of polyvinyltoluene (PVT) with the same length and width but 0.5 cm tall (the gap light guide) with EJ-500 optical cement. Another piece of PVT, this time 1.5 cm tall (the focal length), was similarly glued to the opposing side of the gap guide after painting the mask pattern on either face with black paint. Once dry, the entire slab was machined to size and diamond milled. Figure 5.1 shows a picture of a single bare slab shortly after receipt.



Figure 5.1. Picture of a single bare slab. The closest end in the image is the side viewed by the MAPMT. Small, thin lines appear at the edges where slab pieces were joined together. The mask pattern seen on the side closest to the viewer is an optical illusion of the mask projected through the light guide.

While some diamond mill lines were visible on the surface, careful visual inspection showed that the finish was comparable to the polished pieces of plastic scintillator we had in the lab. The joints between layers were visible at the edges (thin black lines) and there were some small regions where air bubbles caused a white or hazy appearance (not visible in the image). Overall, these defects were relatively small and infrequent.

### ***5.1.2 3-D Printed Enclosure***

A plastic enclosure was designed to mechanically contain the slabs, reflectors, MAPMTs, and electronics. For this design, it was critical to maintain alignment between the slabs and the anode rows of the phototubes for the encoding to work. Additionally, three 64-anode phototubes required 192 cables to instrument, and these could provide significant



mechanical stress on the assembly, so it was desirable for the detector assembly to be sturdy and mountable. The enclosure featured a compartment large enough for the eight slabs plus interlaid reflectors and absorbers (Figure 5.2).



Figure 5.2. Pictures of the 3-D printed enclosure with a single slab placed inside, showing how the slabs sit when placed.

On one side was an opening for inserting and viewing the slabs. It could be closed with a rigid plastic plate that also applied some mechanical pressure to the slabs as it was secured in place with screws around its perimeter. The opposing side was recessed, and the wall was made thin ( $\sim 1$  mm) to act as an entrance window (shown later). Above the slabs was space for the MAPMTs, which were plugged into a custom breakout board with 195 (192 anodes and 3 dynodes) MCX connectors on the other side. The board was screwed into a rigid frame with feedthroughs for the high voltage cables. While not light tight, the enclosure was pretty dark, and the overall assembly was mounted in a dark box. Figure 5.3 shows the enclosure and Figure 5.4 shows pictures of the breakout board.



Figure 5.3. 3-D printed enclosure for the slab modules and MAPMTs. The breakout board sits in place on top and the side plate is below.



Figure 5.4. Breakout board to provide MCX connectors for 192 anodes and 3 dynodes from the MAPMTs.  
The bottom hosts rows of pins for the MAPMTs to plug into.

### ***5.1.3 Slab Assembly***

Slab assembly was one of the more challenging components of bringing this work to completion for a variety of reasons. There were many considerations when planning the assembly procedure; specific tolerances of the geometry were absolutely necessary in order for the system to function properly. Alignment of the components was critical, so large tolerances could quickly stack up to become a problem. Surface finishes and optical

coupling needed to be as high of quality as possible to achieve the best performance. Figure 5.5 shows a picture of the detector components with inter-slab layers in place.

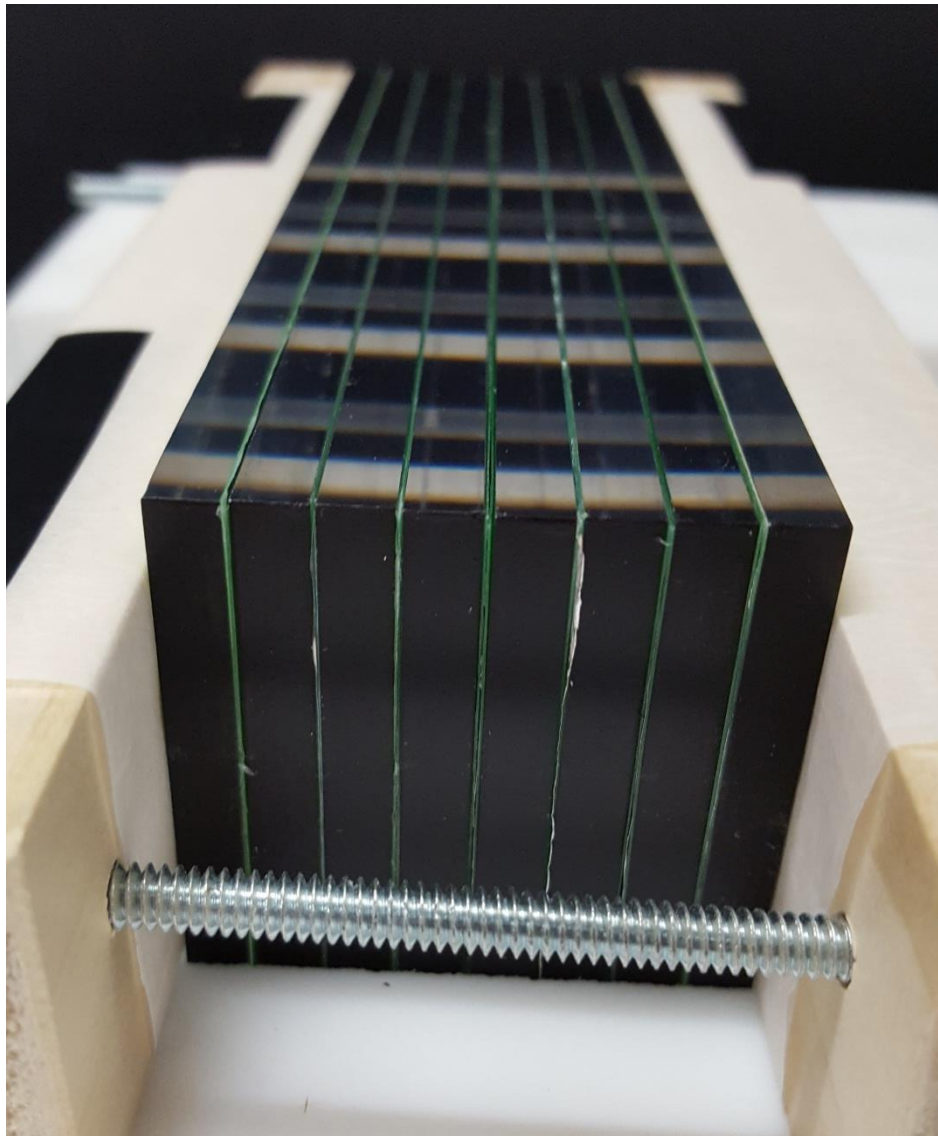


Figure 5.5. Image of the slab assembly, clamped, with inter-gap layers in place.

Simulations indicated that the air gap was responsible for the majority of the work in piping the light down to the phototubes, so it was important to maintain it. Of concern was anything that could wick up and create an optical link across the air gap, such as optical grease.

An attempt was made to use EJ-560, a 1 mm thick silicone rubber pad, as a dry optical interface instead of grease. Experimentation quickly revealed that it was impossible to couple both sides of the slab assembly (phototube side and retroreflector side) using pads without large numbers of air bubbles. A compromise was made; since a wet solution seemingly had to be used, optical cement (EJ-500) was employed as a seal to close the gaps, meaning that the system could then be coupled to the MAPMT with optical grease. While a small amount of EJ-500 would wick up into the air gaps, it would dry and therefore block the grease when coupled to the phototubes. This small, stable compromise of the air gaps greatly simplified that portion of the assembly. The EJ-500 was also used to optically glue the retroreflector to the other side of the slab assembly. In both cases, the sealed side was placed on an inspection plate – a large, heavy, super flat stone – as the EJ-500 dried, to achieve a flat optical surface.

Parchment paper was used to protect the stone surface from the EJ-500. Unfortunately, once it was peeled away, the resulting multi-slab surface was of poor optical quality (Figure 5.6) with residual material from the paper coating the surface. After attempting to remove it gently, first with alcohol and then with 300 nm wet polish, the surface was sanded using 2000 grit sandpaper and polished until it was smooth.

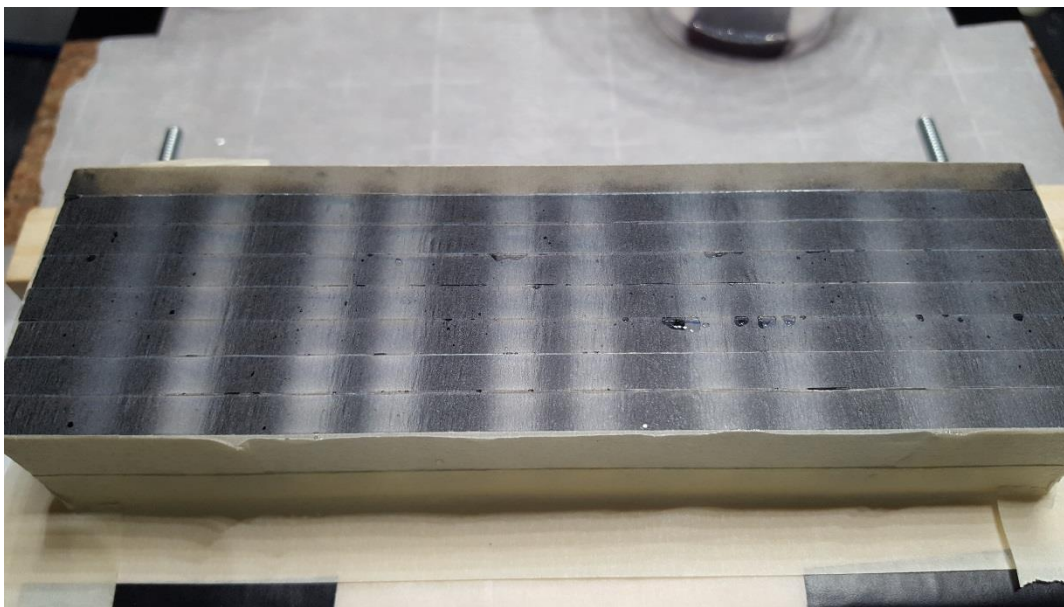


Figure 5.6. Glued surface after allowing it to dry and peeling off the parchment paper.

While most of the gaps remained sealed by the dried glue, some regions had a thinner layer that was breached during the sanding, allowing debris and polish into some of the gaps. There were also sections where air bubbles in the cement created thin layers of glue that became exposed regions of plastic once it was sanded. Careful inspection reveals smooth, curved lines in the gaps, indicating the transition between air and glue that wicked into them. Figure 5.7 shows a picture of the slab assembly phototube window side after treatment.



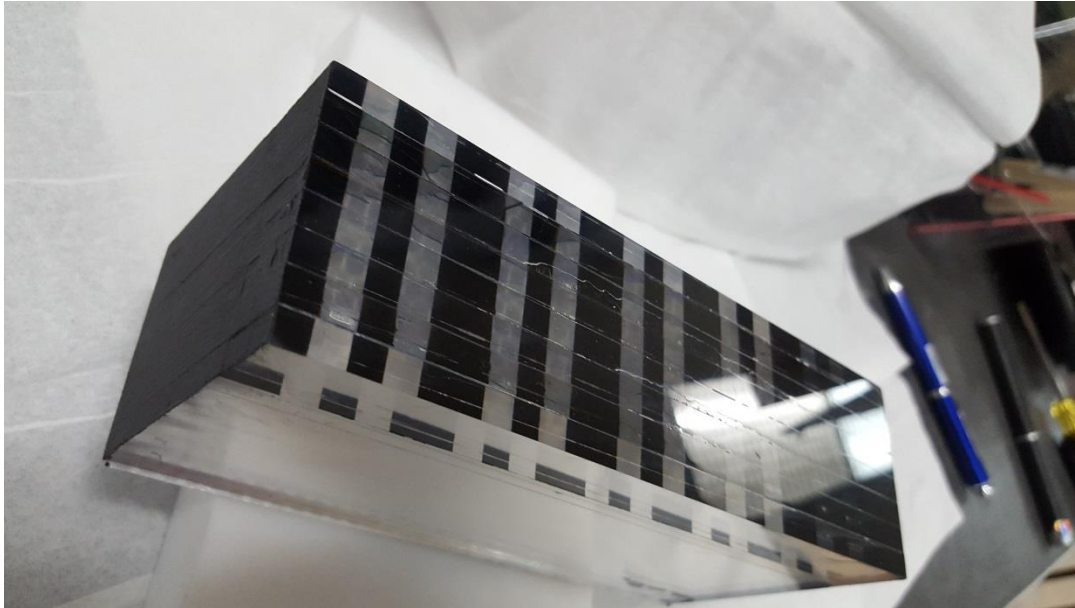


Figure 5.7. Picture of the finished slab assembly. Minor defects are visible due to bubbles in the glue, along with some wicking into the gaps.

With the MAPMT and retroreflector sides finished, the last step was to flatten and shorten the two narrow black side walls. The ESR and aluminum foil stuck out slightly, and combined with minor differences in the slab lengths, meant that it was necessary to sand them down slightly. After sanding with 2000 grit they were again painted black. Figure 5.8 shows the four pictures of the completed slab assembly before, while, and after being placed into the enclosure.



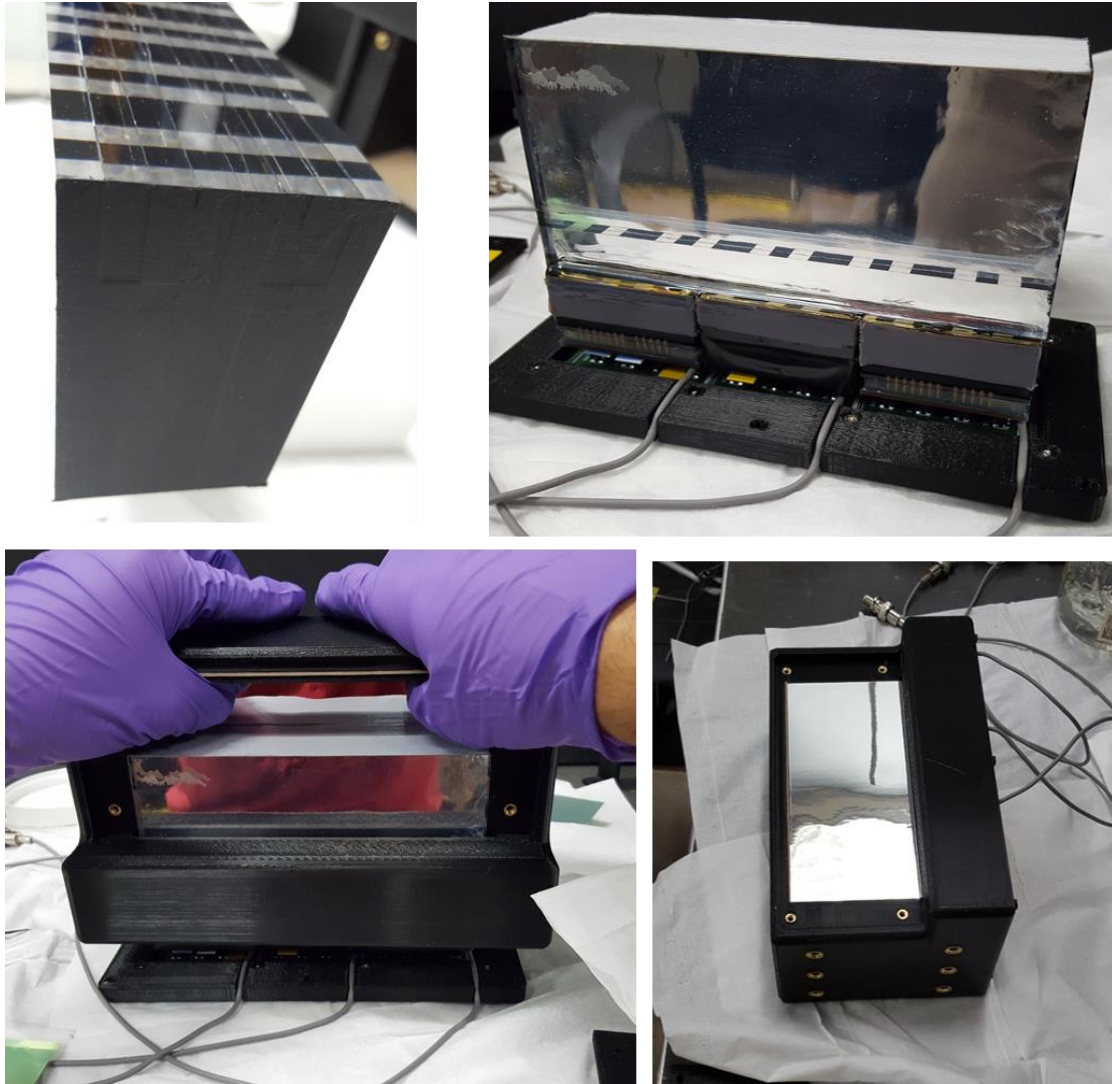


Figure 5.8. Top left: finished slab assembly. Top right: slab assembly coupled to the phototubes with grease. Bottom left: the enclosure as it was slipped over the assembly. Bottom right: assembly fully in the enclosure with two sheets of ESR covering the side, with the side plate removed.

Figure 5.9 shows the final, closed prototype detector from the front and back. The top image shows the thin entrance window in the inset region.



Figure 5.9. Front and back views of the completed prototype detector assembly. The three high voltage cables from the three H12700s are visible, along with 192 MCX anode outputs and 3 dynode outputs.

#### ***5.1.4 MAPMT Breakout Board and 3-Slab Signal Summation***

The breakout board took the signals from the rows of pins on the back of the MAPMTs and output them via an  $8 \times 8$  array of MCX connectors per phototube. For fully

instrumented slabs, six-foot cables with MCX connectors on both ends ran through the dark box wire feedthroughs to the CAEN V1742 digitizers. The digitizer inputs included a 50-ohm termination. Five slabs were fully instrumented and the anodes for the other three were summed using a custom circuit board designed by a colleague. The three sum signals were digitized along with the 120 anodes from five slabs. Figure 5.10 shows a picture of the detector fully wired along with the summing circuit board and a dark box feedthrough.



Figure 5.10. Picture of the fully wired prototype mounted inside the dark box before the box was extended. 192 anode cables are connected to the prototype, with 72 connected to the summation board. High voltage cables are gray and connected to a common source.

During initial testing, it was discovered that one anode did not produce a signal. The phototube, cable, and digitizer were eliminated as culprits, so the most likely explanation was a bad solder joint on the breakout board's MCX connector. The wiring was rearranged so that this slab was not one of those fully instrumented, changing it instead to one of the three summed slabs. Aside from a reduction in the sum signal amplitude, the inactive pixel did not appear to have any other deleterious effects.

## 5.2 Photodetector

The photodetectors used for this work are Hamamatsu H12700 MAPMTs. These feature 64 anodes in an  $8 \times 8$  arrangement. The anodes along the outer edge are slightly larger than the inner anodes (6.25 vs 6 mm), making the active array  $48.5 \times 48.5 \text{ mm}^2$  in area. The entrance window is 1.5 mm thick and made of borosilicate glass. According to the datasheet, this MAPMT has a rise time (defined as the 10-90% time) of 520 ps, a transit time of 4.9 ns, a transit time spread of 350 ps FWHM, and a typical quantum efficiency (QE) of 33%. The MAPMT was biased with -1000 V, producing negative anode pulses and positive last dynode pulses, the latter of which was used to trigger the system.

### 5.2.1 Photodetector Calibration

Each anode had a different gain and quantum efficiency and the amplitude of the observed signal was influenced by the product of the two. If the gain and QE are known, one can use them to correct the anode pulse amplitudes and obtain a more uniform response. This information was also necessary for the likelihood-based reconstruction employed by the monolithic detector system, so an experiment was devised to extract these quantities for the three MAPMTs that were used with the OCA Slab Prototype. For convenience, these phototubes will be denoted as MAPMT A, MAPMT B, and MAPMT C.

The gain calibration procedure was developed and conducted for two MAPMTs by a colleague. The last MAPMT was characterized by the author. The procedure used a Photech LPG-405 pulsed laser (45 ps pulse width) shining through a diffuser into an optical fiber. The fiber was routed into a 3-D printed pegboard with holes that held the optical fiber to the center of each MAPMT pixel. The apparatus fit snugly over the face of the MAPMT, so the opening was as close to the MAPMT entrance window as possible. The laser output was set so that, on average, between one half and one photoelectron were detected per laser shot. The laser sync pulse was used to trigger the digitizers (Section 5.3), which recorded 200 ns long waveforms. Between each



acquisition, the dark box was opened, and the optical fiber was manually moved to the next location. Figure 5.11 shows a picture of the 3-D printed pegboard and Figure 5.12 shows the experimental setup.



Figure 5.11. Picture of the pegboard used to hold the optical fiber up to the MAPMT anodes.

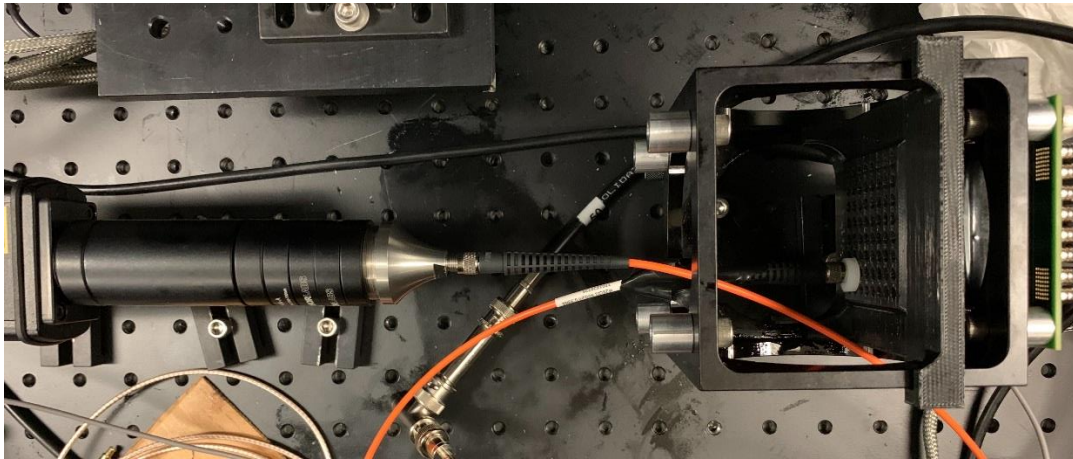


Figure 5.12. Image of the gain calibration setup inside the dark box. The MAPMT was mounted in an aluminum chassis. The laser fired from the left, was diffused, then was piped into the optical fiber, which plugged into the pegboard.

To extract the relative gains and QEs, an expression was derived by a colleague that describes the expected distribution of photoelectrons detected by an anode based on summing the results from multiple pulses from the laser:

$$S(x) = N \sum_n^5 \frac{\lambda^n e^{-\lambda}}{n!} \cdot \frac{\Delta x}{\sqrt{2\pi(w_0^2 + nw_1^2)}} \exp\left(-\frac{1}{2} \frac{(x - (x_0 + nx_1))^2}{(w_0^2 + nw_1^2)}\right) \quad (5.1)$$

In this expression,  $S(x)$  is the expected intensity,  $x$  is the measured integral (arbitrary units),  $\Delta x$  is the bin width,  $x_0$  is the mean integral of 0 photoelectrons (PE),  $x_1$  is the mean integral of 1 PE,  $w_0$  and  $w_1$  are their respective widths,  $\lambda$  is the mean number of detected PE per pulse, and  $N$  is the total number of PE detected in the data set. While not absolute, the relative  $\lambda$  values between anodes were used as a relative QE. The spectra were built by integrating the pulse for 25 ns and were fit with this expression, shown in Figure 5.13, to extract  $x_1$ , and  $\lambda$ .

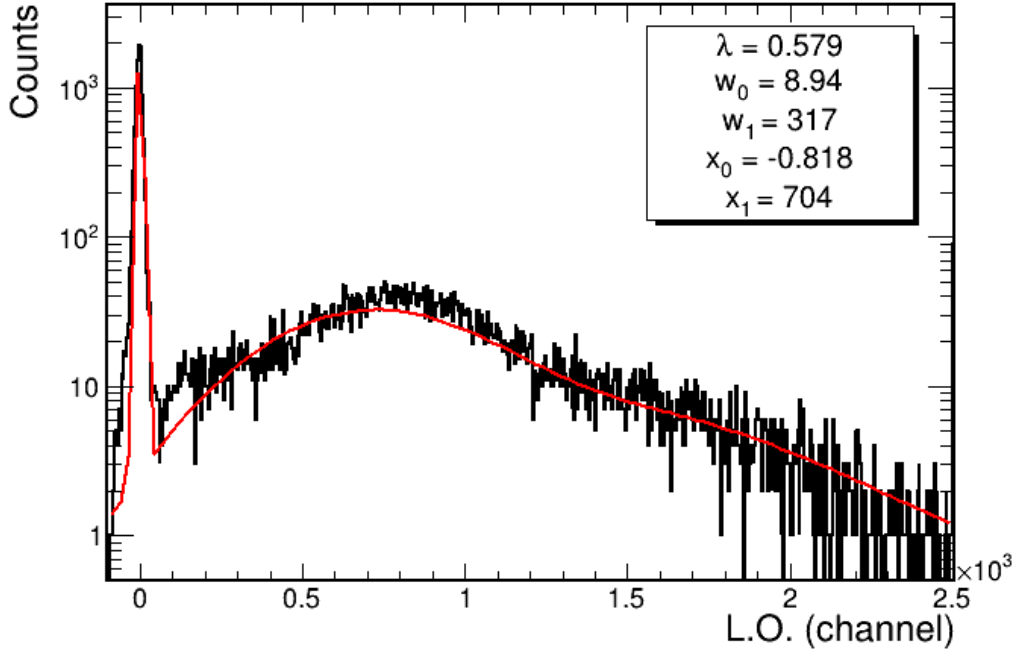


Figure 5.13. Pulse integral spectrum for a representative anode, fit with Eq. 5.1.

From the fit parameters reported in Figure 5.13, one PE was determined to have an average integral of 704, and a Poisson-distributed mean of 0.58 PE were detected per trigger for this anode.

Heat maps of the products of the gain and QE for each MAPMT are shown in Figure 5.14, self-normalized to the highest gain-QE anode. These plots are shown from the perspective of someone looking at the phototubes from behind, down into the slab assembly when mounted. In terms of the terminology that will be used for the remainder of the experimental work, the vertical dimension (across slabs) is  $Y$ , the horizontal dimension (along a slab) is  $X$ , and the observer is looking into the  $-Z$  direction (distance



from the MAPMT). Figure 5.15 shows all three gain-QE maps, normalized to the highest gain anode of the entire array. Note the significant difference in values between the MAPMT B in the center and MAPMT C.

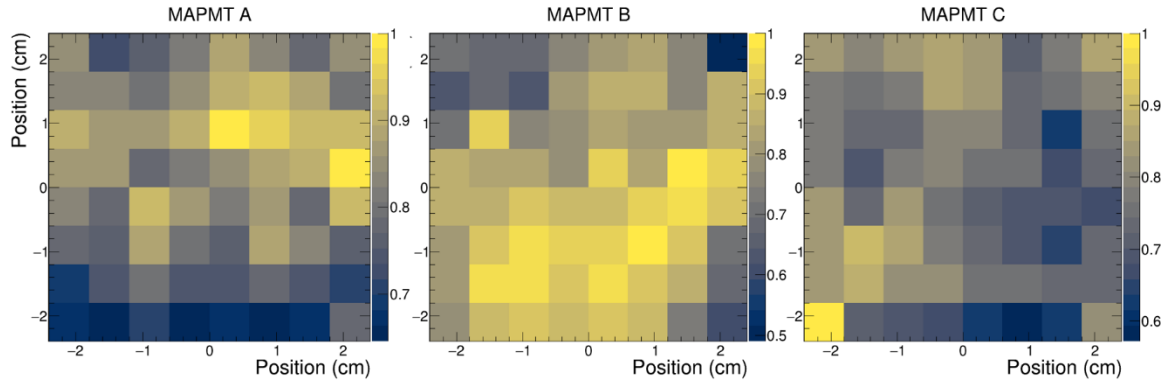


Figure 5.14. Individually normalized gain-QE heat maps measured using the optical fiber experiment.

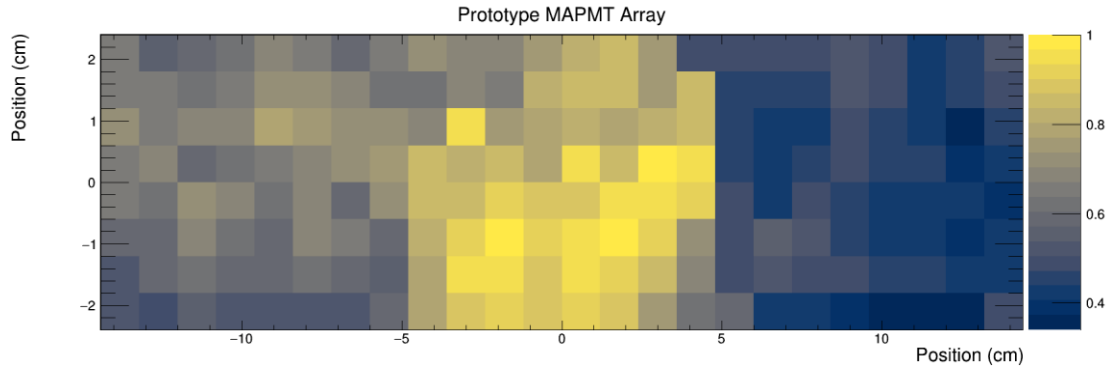


Figure 5.15. Measured gain-QE heat maps normalized to the highest-gain anode out of all three.

Unless otherwise noted, when constructing hit patterns and energy spectra, the gain-QE calibrations were applied to every anode for all of the results that follow. This was not technically necessary for the log-likelihood localization algorithm, since that used a

normalized response. However, it was needed for the energy calibration, since spectral features were not visible without the gain calibration.

### 5.3 Data Acquisition System

Figure 5.16 shows a schematic of the readout and data acquisition system. All connections were made with cables that had either MCX or LEMO connectors on the ends. An optical link connected the CAEN V1742 digitizers to the desktop computer, which recorded the raw waveforms to a 10 TB disk array in a RAID configuration. These digitizers were selected because of their high sampling rate, sufficient bandwidth, and relatively high channel count (32) per board.

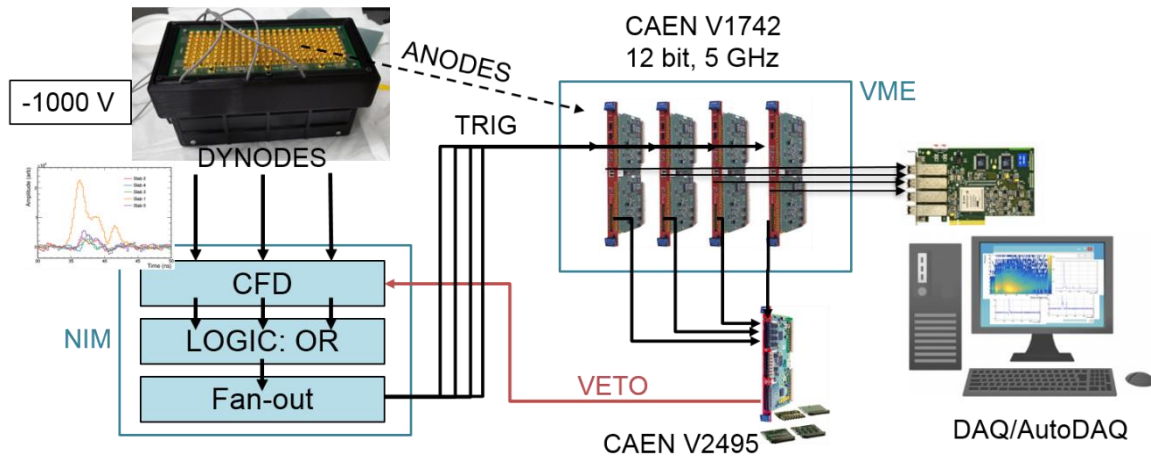


Figure 5.16. Schematic of the readout and data acquisition system for the experimental prototype.

A software engineer was contracted to develop the data acquisition (DAQ) software, which communicated with four CAEN V1742. The digitizers were housed in a VME crate and the software provided a simple command-line interface to configure them, set save paths, start, and stop acquisition. Waveform data from all 32 anode channels, plus the two trigger signals for each board, were digitized for 200 ns at 200 ps intervals (5 GHz). The trigger signals were used to correct the timing of the anode pulses, accounting

for time jitter between boards and DRS4 chips. A software correction, provided by the manufacturer, was applied to the waveforms to account for non-uniform times between DRS4 samples.

Triggers were generated by connecting the last dynodes of the MAPMTs to an ORTEC 935 NIM CFD, then sending that signal to a Phillips Scientific 756 NIM quad four-fold logic unit, which was connected to a Phillips Scientific 757 NIM mixed logic fan-in/fan-out module, duplicating the trigger signal for the eight digitizer trigger inputs. The CFD had a threshold of 40 mV for all three MAPMT dynode signals. No coincidence was required between MAPMTs; triggers were generated when any one tube went over threshold.

## 5.4 Retroreflector Characterization

### 5.4.1 Introduction

Recent development work on a compact neutron scatter camera (NSC) employing fast but relatively dim plastic scintillators [26], [53] has motivated investigation of surface treatments that not only maximize light collection efficiency but also preserve its spatial information content. Commonly, specular (e.g. Enhanced Specular Reflector (ESR)) or Lambertian (e.g. white paint, Teflon) reflectors are used to maximize light collection [66], but in most geometries the spatial information is lost as the light is redirected to the photosensor. Retroreflective materials, or retroreflectors, can be used with scintillator-based detectors to improve the light collection efficiency while retaining spatial information; incident light originally directed away from the readout is instead backscattered  $180^\circ$  through its vertex (Figure 5.17). These types of materials are most frequently used for markings on roads and signs since they reflect light from headlights back to the driver. Light is typically redirected by one of two methods (Figure 5.18), both involving one or more specular reflections that ultimately result in photons going back the direction from which they came. However, there is an offset that depends on the feature size of the retroreflecting microstructure.

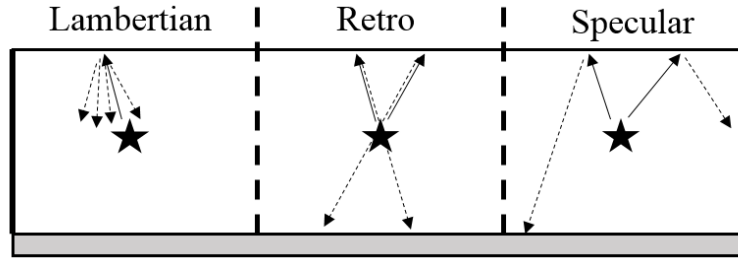


Figure 5.17. Diagram of a block of scintillator with black side walls, a photosensor on the bottom, and a reflector on top. Three different types of reflections are shown, with solid lines indicating emitted photons and dashed lines indicating reflected photons.

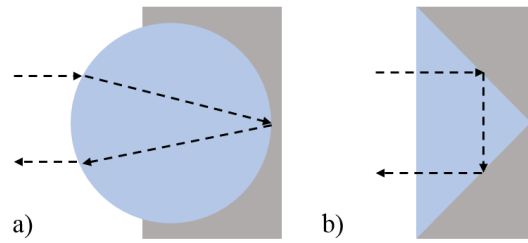


Figure 5.18. Schematic diagrams of a) microsphere retroreflectors and b) microprism retroreflectors. Reflective material is shown in gray. Retroreflective sheets are made by closely arraying these microstructures on a flat surface.

Prior work [51], [48], [52], [49] has shown that for crystalline scintillators, retroreflective tapes may improve spatial performance; the authors of [52] improved performance by embedding the microstructures directly into the scintillator crystal, and [49] successfully employed retroreflective tape by 3M Industries. Unfortunately, there is limited quantitative information on the reflectivities (which depend on incidence angle) and spatial distributions of reflected light for the commercial offerings available today. Further, we could not find any information on using them with plastic scintillators. This information is required to accurately model the impact of these tapes and to understand

the effect they might have on the system performance of the NSC designs under development. This article investigates the performance of retroreflective tapes compared to Teflon, black paint, and air-coupling when used as reflective surface treatments for plastic scintillators. A simple theoretical model of the effect on the light distributions observed by the photodetectors is presented and validated experimentally. The relative reflectivities by angle for a selection of five commercially available retroreflective tapes are also reported.

#### 5.4.2 Theory

Fundamentally, the ability to centroid the energy deposited by incident radiation (denoted  $\delta x$ ) in a bulk scintillator is dependent on the width  $w$  of the light distribution observed by the photosensor and the number of counts  $N$  in that distribution (see [67] for a more detailed explanation) according to:

$$\delta x \propto \frac{w}{\sqrt{N}} \quad (5.1)$$

Based on this equation, a reflector that introduces some additional width may result in better performance if  $N$  is sufficiently improved. For the detector geometry shown in Figure 5.17 that has a slab of scintillator with all sides but the one connected to the phototransducer painted black, the width of the light spot  $w_d$  observed (containing  $N=N_d$  detected counts) at the open face is solely due to light that travels directly from the emission point to the readout device. If one were to replace the black paint with a reflector on the scintillator side opposing the phototransducer, then  $w$  becomes the weighted in-quadrature sum of the original width  $w_d$  and the width of the reflected light,  $w_r$  given by:

$$w = \sqrt{\frac{N_d}{N_d + N_r} w_d^2 + \frac{N_r}{N_d + N_r} w_r^2} \quad (5.2)$$

where  $N_r$  is the magnitude of the reflected light. The weights are the relative fractions of light associated with the respective widths, and  $N$  in Eq. 5.1 becomes  $N_d + N_r$ . For an

ideal retroreflector  $N_r = N_d$ , which, when combined with Eq. 5.1, implies that the resolution would improve by  $\sqrt{2}$ . In reality the width will increase based on the reflector properties, including specular and Lambertian reflections or imperfect retroreflections. In this case one can accept an additional spread of  $w_r = w_d\sqrt{2}$  (about  $1.19w_d$ ) and still obtain equal or better spatial resolution when centroiding. Following a similar argument, a 90% efficient retroreflector limits the acceptable blurring to a factor of  $1.17w_d$ .

Confirmation of Eq. 5.2 would make it possible to estimate whether retroreflectors might benefit a specific detector system based on the anticipated width of the light spot arriving at the photodetector and the expected amount of reflector blurring. Using collimated beam data, Eq. 5.2 is validated, and values are estimated for the net reflectivity and effective blurring of the retroreflectors, air, Teflon, and black paint.

### 5.4.3 *Methods*

Five commercial reflective tapes were obtained from a variety of manufacturers, summarized in Table 5.1 and shown in Figure 5.19. Some of these tapes were explicitly marketed as retroreflective materials and consequently conform to the ASTM D4956-19 [68] standards for retroreflectors used for traffic control. These standards were designed specifically for white light (headlights) reflecting off of far-away surfaces and are therefore not directly relatable to the scintillator use case. Others were advertised as reflectors to be used for the same purpose as the retroreflective tapes, but it was not clear whether they were retroreflective or merely reflective. Four of the tapes had shiny, repeating, triangle, square, or hexagonal features that are presumed to be the retroreflective regions, with interceding areas appearing white. Conversely, instead of having regular polygons, the 3M Industries tape had a more uniform, fine-grained, matte topology. All of the tapes came as 2-inch-wide rolls or sheets, which could be peeled and adhered to a smooth surface.

Two experiments were conducted to assess the retroreflective properties of the selected tapes. The first directly measured the relative retroreflectivity of each tape and Teflon when interrogated with a blue laser beam at different incident angles relative to normal,



described fully in Section 5.4.4. The second experiment employed a fully polished block of fast plastic scintillator coupled on one broad side (referred to as the bottom) to a multi-anode photomultiplier tube (MAPMT), described in Section 5.4.5. The top side was either optically coupled to a retroreflective tape, or it had another surface treatment for comparison. The detector was interrogated with a pencil beam of gamma radiation from an isotropic source so that the intrinsic spatial resolution and relative light collection efficiency with each top surface treatment could be measured.

Table 5.1. List of manufacturers and part names for the tapes investigated in this study.

<b>Manufacturer</b>	<b>Part Name</b>
Oralite	5900 HIP Reflective Tape
3M Industries	Scotchlite™ Silver Reflective Tape
Michel Production	High Intensity Reflective Tape
Reflexite	Retroreflective V92 Daybright Tape
Telemecanique Sensors	Reflector Tape

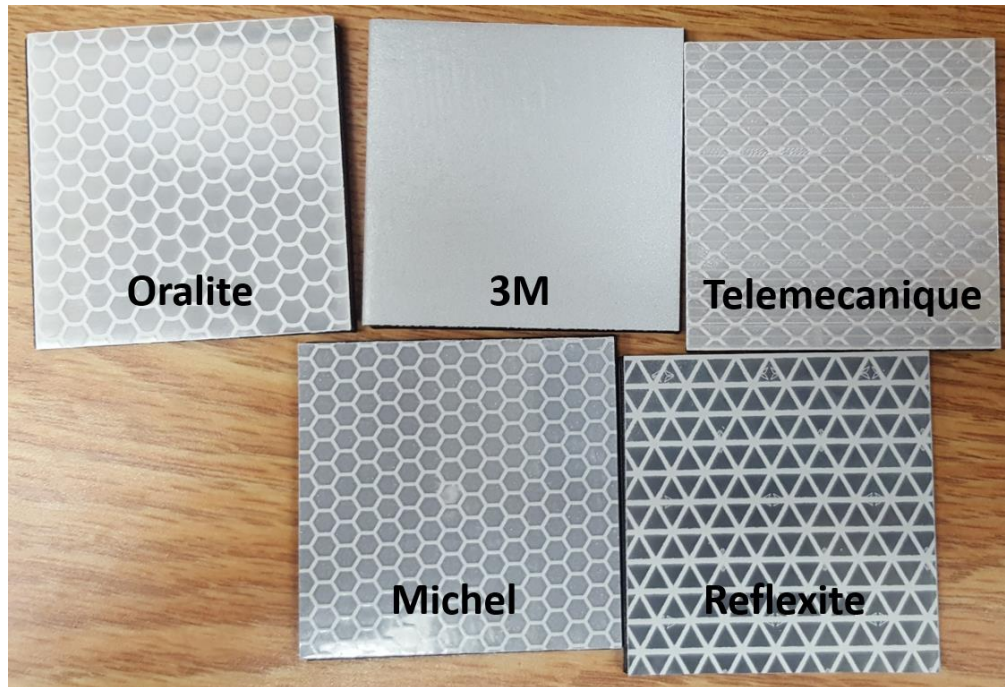


Figure 5.19. Photo of the five tapes studied. The polygonal features are 3-4 mm and the tapes are attached to 3-D-printed slides.

The laser experiment allowed control of the incident angle of the retroreflected light and its subsequent capture using a color camera. The result is a direct comparison of the retroreflectivity angular dependence of each tape. The scintillator measurement complements this data by demonstrating the performance in an example radiation detector system. By doing so, systematic factors such as the wavelength distribution of the scintillation light, its spatial distribution as it arrives at the tape surface (which will depend on the interaction location), and local variations in retroreflectivity (e.g. due to surface features and scuffs) were incorporated into the results.

Images of the retroreflective tapes at 4x magnification are shown in Figure 5.20. Figure 5.21 shows the same images zoomed in on the central 500×500 pixels to highlight the repeating microprism and microsphere structures, each on the order of 100  $\mu\text{m}$  in size.

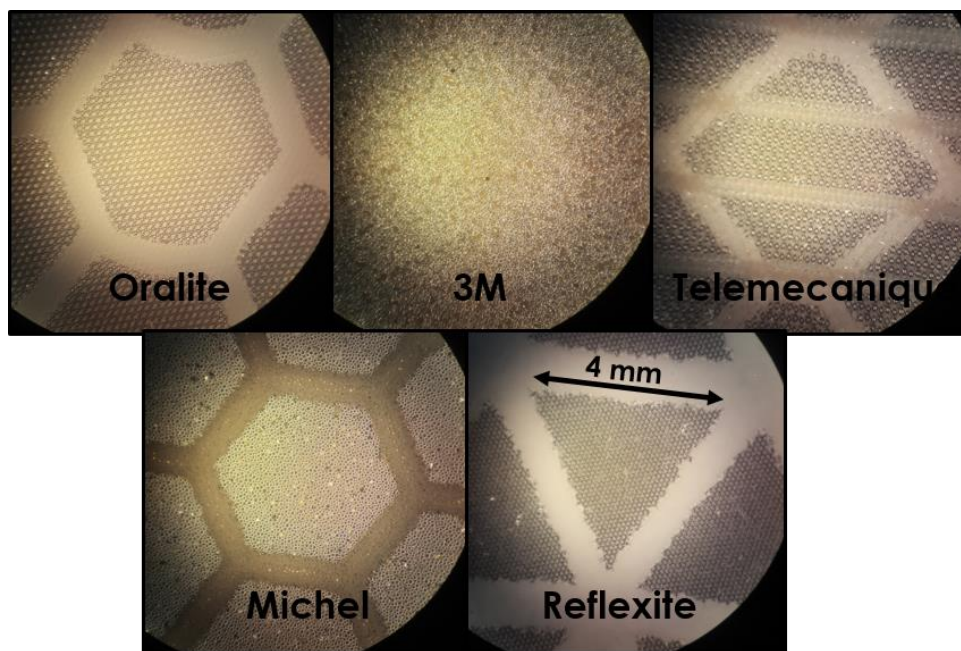


Figure 5.20. Microscope images of the reflective tapes. All five images are the same scale.

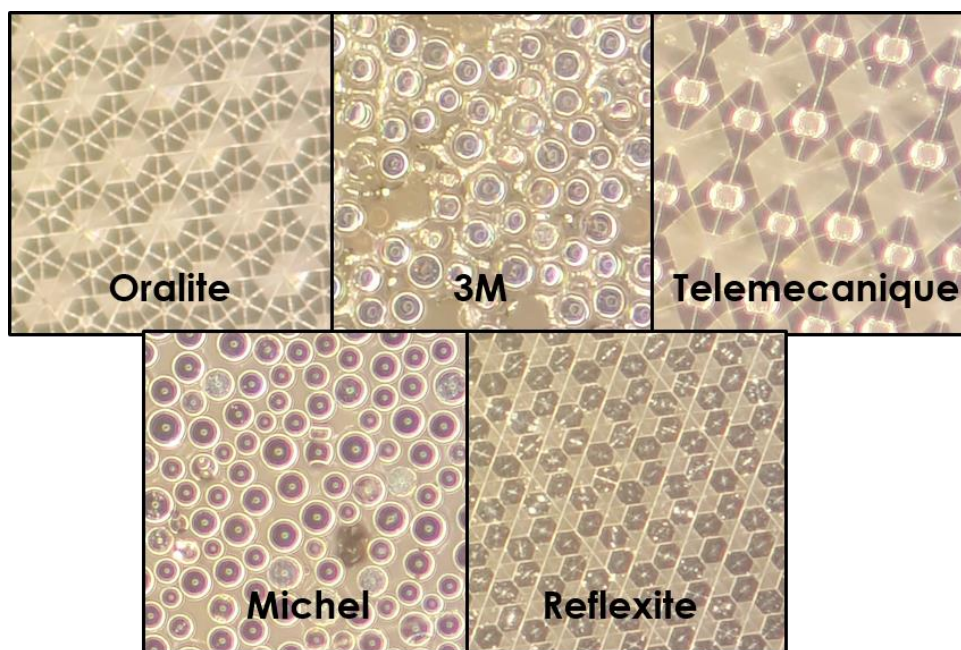


Figure 5.21. Zoomed-in optical microscope images, taking the central 500×500 pixels region of the pictures in Fig. 4. Microprisms are evident in the top left, top right, and bottom right images, whereas microspheres are shown on the other two: top middle and bottom left.

Note that the microscope light had a golden tint which is evidenced in the images. Two of the tapes, the Michel and 3M offerings, employ microspheres while the other three tapes use microprisms. The exact details – how the periodic structures are repeated, what is used to fill the space in between, etc. – vary depending on each manufacturer’s process. The feature sizes of all the tapes are comparable, and the areas between microstructures all appear similar, suggesting that a similar material may have been used.

#### ***5.4.4 Laser Measurement***

The laser experiment directed a narrow (3.5 mm diameter) beam of blue light from a 0.97 mW, Edmund Optics 37023 laser to the surface of the retroreflective tape. The reflected light was captured with a QImaging Retiga 6000 color camera, as shown in Figure 5.22. Since the light was back-reflected parallel to its incident trajectory, a Thorlabs, Inc. CCM1-BS013 50/50 400-700 nm optical beamsplitter cube was used to redirect the light. The laser aperture was coupled to a Thorlabs, Inc. SM1D12C ring-actuated iris set to an opening-diameter of 1 mm. This iris was aligned with a second iris 69 cm away, also fixed to a 1 mm opening, resulting in a beam spot size of 1.3 mm at the tape surface. Immediately past the second iris was the beamsplitter. Figure 5.22 shows a closeup of the retroreflector, beamsplitter assembly. During data acquisition black cloth was draped over the entire assembly to keep out ambient light.

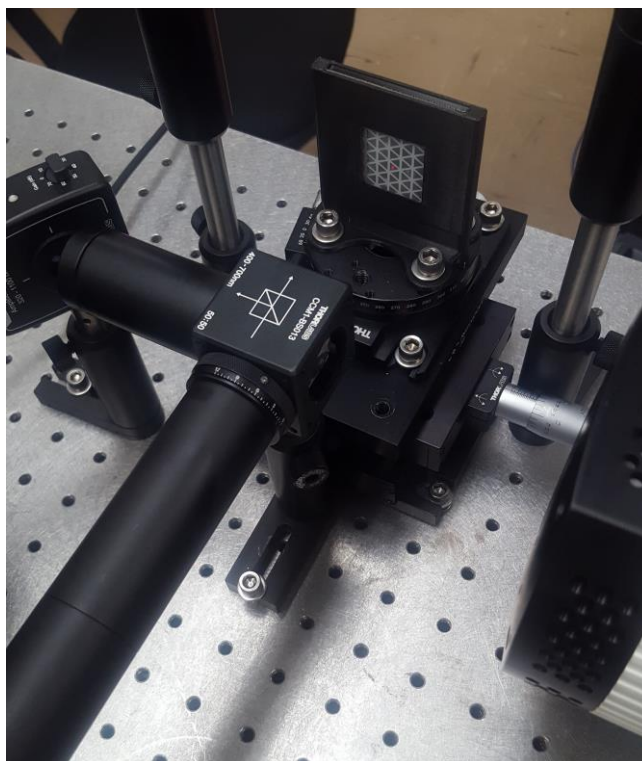


Figure 5.22. Closeup of the beamsplitter, photodiode, rotation stage, sample holder, and camera. A beam spot produced by a red laser during alignment is also visible at the center of the sample.

The beamsplitter passes half of the incident light and the other half is deflected  $90^\circ$ . The deflected light from the first pass through the beamsplitter is sent to a Thorlabs, Inc. PDA100A2 switchable gain silicon photodiode (PD), offset by 7.9 cm and angled by approximately  $45^\circ$  relative to the plane of the beamsplitter face to prevent the back-reflection from re-entering the beamsplitter. The PD was used as a reference to monitor the stability of the laser light intensity. The transmitted light shone onto the retroreflector sample which was affixed to a sample slide. The  $51 \times 51 \times 2.8 \text{ mm}^3$  slides could be repeatedly inserted into a sample holder that held the front face of the tape as close as

possible to the rotation axis of a Thorlabs, Inc. PR01 high-precision rotation stage. Laser light that came out of the beamsplitter was retroreflected by the sample back into the beamsplitter, where it was once again split, with the redirected beam sent to the color camera, which had its lens removed. This charge-coupled device (CCD) has  $2750 \times 2200$ ,  $4.54 \mu\text{m}$  pixels and was set to its highest gain (3x), with an exposure time of  $150 \mu\text{s}$ . The central  $2000 \times 2000$  pixels in the field of view (FOV) of each exposure were saved to disk, with 100 exposures comprising a single measurement.

The laser was aligned by placing a mirrored sample slide in the holder and adjusting the components until the back-reflected beam returned through the pinhole created by the iris closest to the laser. Therefore, light had to pass through both irises, the beamsplitter, be reflected off the mirror, and then pass back through the beamsplitter and second iris to be visible on the periphery of the first iris. Alignment was further confirmed by observing the specular reflection of the laser off of the mirror with the camera, which was only present when the beam was incident within a few degrees of normal. Using the mirror slide and rotation stage, the angular width of the camera CCD was empirically determined to be about  $3.5^\circ$ , which agrees with the value derived from the geometry shown in Figure 5.22. The rotation axis of the stage was not perfectly aligned with the front of the sample slides, so there was a small beam spot translation of approximately 1 mm over the range of tape angles measured. To counter this, the sample tapes were aligned so that this translation was completely confined to a single visible “shiny” feature (square, hexagon, etc., shown in Figure 5.19 and Figure 5.20) on the tape surface, where applicable.

Data were collected for sample angles with respect to the beam axis of  $-45^\circ$  to  $+45^\circ$ . Between acquisitions, the black cloth was raised, and the stage was manually rotated by  $5^\circ$ . The camera uses a Bayer color format. To obtain the relative reflected intensity at each measurement angle, the blue channel of the central region of each image was integrated after passing it through MATLAB's *demosiac()* function. The final result at each angle was the average value from all the images collected at that angle.



#### 5.4.5 *Scintillator Measurement*

To complement the blue laser measurements, scintillator experiments were conducted to quantify and compare how retroreflector and common scintillator surface treatments impacted light collection and spatial localization performance. Previous work [49] showed that the presence and magnitude of improvement depends principally on the scintillator geometry, so it is impossible for a single experiment to comprehensively represent all cases. However, a detector geometry was chosen that was expected to result in an improvement in both the light collection efficiency and the spatial resolution when a retroreflector is present. Assuming a retroreflector is applied to the scintillator surface opposite from the MAPMT, the theoretical improvement diminishes as the distance between the two surfaces increases. This is because, as the interaction moves away from the phototube, the width of the light spot is dominated by light that travels directly from the emission point to the photosensor.

The experiment used a 600  $\mu\text{Ci}$   $^{133}\text{Ba}$  source mounted in a custom tungsten collimator that was 3.81 cm thick, had a 1 mm diameter hole and was placed 3 cm from the front face of the scintillator. This resulted in a beam spot size of 1.6 mm full width at half maximum (FWHM) at the face of the scintillator. The collimator/source was mounted on a Velmex linear translation stage driven by a 2-phase stepping motor, with a rotary shaft encoder read out by a Measurement Computing USB-QUAD08.

The block of plastic scintillator was  $52 \times 52 \times 13 \text{ mm}^3$  and coupled to a  $51 \times 51 \text{ mm}^2$  H12700 MAPMT, using Saint-Gobain BC-630 silicone grease. The four narrow “side” walls were painted black and the entire block was affixed to the MAPMT using black tape, leaving the “top” face of the block exposed for the various surface treatments. The  $8 \times 8$  array of  $6 \times 6 \text{ mm}^2$  anodes from the H12700 were plugged into a custom breakout board, which had connectors for each anode and the last dynode. The detector and board assembly were held fixed by an adjustable, 3-D printed stand inside a dark box, and the anode signals were digitized using a CAEN V1742 digitizer at 5 GHz with 12-bit resolution.



The system was triggered by the signal from the MAPMT last dynode, which was fed into an ORTEC 935 constant fraction discriminator. The CAEN unit also digitizes the trigger signal, and this was used to time-align all of the data. Anode amplitudes were determined by integrating a fixed 25 ns window, and then applying response calibration factors for each channel (detailed below). At each source location, 100,000 events were recorded at a rate of about 300 Hz.

#### ***5.4.6 Spatial Alignment***

The detector assembly was removed from the dark box in which the measurements were collected to apply each of the surface treatments studied. To facilitate realignment so the same scintillator locations could be measured for each treatment, one of the linear stage's motion limit switches was used as a repeatable origin. This was measured to be repeatable to better than 10  $\mu\text{m}$ , which was the limit when using digital calipers. To find the physical edges of the detector, the collimator was scanned in 5 mm steps across the detector face in the approximate vertical center of the assembly. The horizontal center location was estimated by taking the midpoint between the edges where the count rate quickly diminishes.

#### ***5.4.7 Gain Calibration***

The response of the H12700 MAPMT varies as a function of location and this must be corrected to obtain consistent values at different locations across the face of the detector. Unfortunately, the manufacturer-provided gain uniformity maps were found to be insufficient to achieve the desired uniformity in the MAPMT response. To address this issue, the relative anode gains and quantum efficiencies (QE) were measured using a Photech LPG-405 pulsed laser (~45 ps pulse width) which was attenuated, diffused, and piped into an optical fiber, so that on average, between half and one photoelectron was detected per laser shot. A 3-D printed grid structure attached to the MAPMT was used to hold the output end of the fiber very close to the entrance window and at the center of each respective anode. The digitizer was triggered off the laser sync signal, and the sets of waveforms acquired contained a mix of 0, 1, 2, etc., photoelectrons. The amplitude

distributions (as determined by a fixed-window integral) were then fit to determine both the mean amplitude for a single photoelectron (the relative gain) and the ratio of 1's to 0's (the relative QE) for every anode.

The relative gains and QEs were normalized to the maximum anode for the phototube and applied to each respective anode's integrated pulse amplitude for the analysis performed in this study. The approach of using the measured gain and QE products was found to give both a better spatial response -- narrower beam profiles -- and energy response -- less variation across beam locations, with the expected fall-off at the edges (details to be published separately as part of the compact NSC work).

#### **5.4.8 Event Localization**

Spatial localization of interactions was only performed in one dimension (denoted  $X$ ), corresponding to the dimension of the collimated beam translation. It is assumed the orthogonal  $Y$  dimension in the MAPMT plane behaves similarly. To find the interaction position, the  $X$ -projection of the anode hit map was created, integrated across the full  $Y$  dimension, and the center of mass (weighted average) was found. The distributions of the reconstructed  $X$  positions for each beam position were then fit with a Gaussian function that included a linear baseline and the mean values extracted. The means were plotted versus the true position from the motor stage encoder and fit to a line, the slope of which was used as the plate scale: the conversion factor from the calculated position to spatial units. This approach was then applied to all of the reconstructed event locations.

#### **5.4.9 Laser Measurement Results**

Figure 5.23 through Figure 5.26 show the progression of images captured by the camera at different incident laser angles for four of the selected tapes. The fifth, the Telemecanique tape, was omitted due to being very similar to the Oralite and Reflexite images. In the pictures taken with the beam normally incident on the Oralite and Michel tapes (Figure 5.23, top left, bottom right), a partial reflection is visible (dashed circle). This is the specular reflection due to the refractive index change at the front surface of the tape, which is typically made of acrylic, and thus has a significantly higher index of

refraction than air. In the image for the 3M and Michel tapes at the same beam angle (bottom left and bottom right), the spot in the center (solid circle) is caused by a fraction of the beam that is transmitted through the beamsplitter and bounces off of its flat faces. This spot is therefore present in every image, but it is weak enough to be hidden by the retroreflected light from the better tapes.

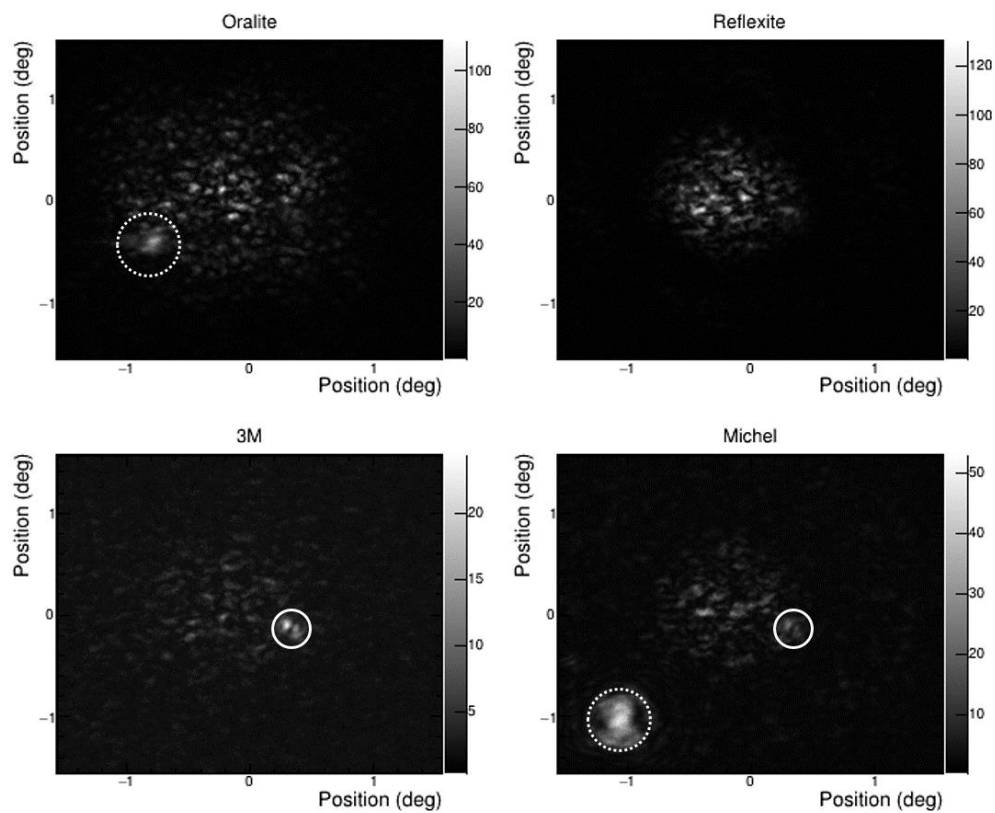


Figure 5.23. Camera images with the beam incident normal to the tapes. The directly transmitted beam spot is seen in the bottom images (solid circle), while the partial reflection off the tape (dashed circle) is visible in two of the images.

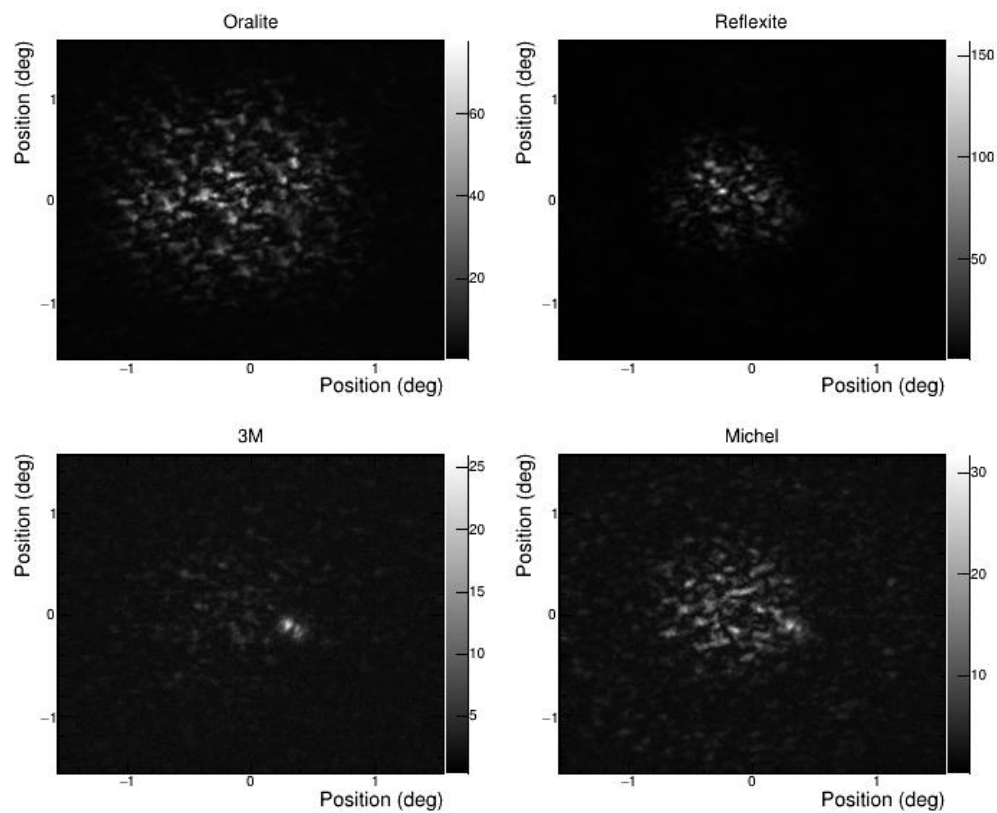


Figure 5.24. Camera images with the beam incident  $5^\circ$  relative to normal.

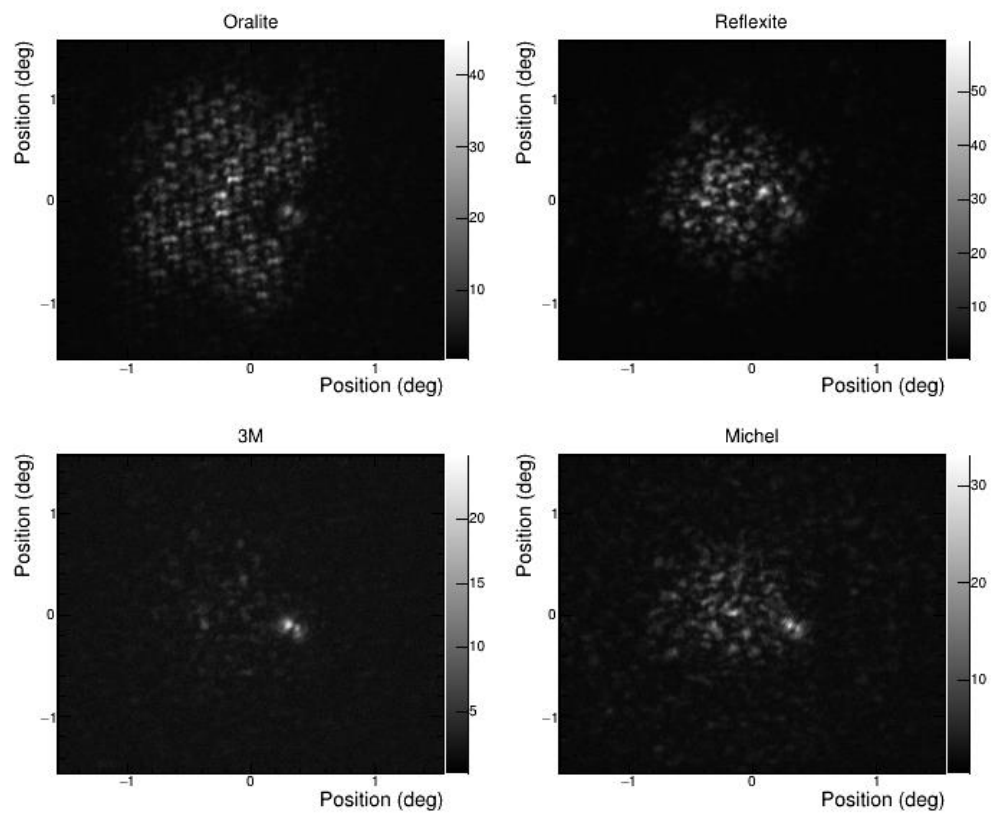


Figure 5.25. Camera images with the beam incident  $25^\circ$  relative to normal.

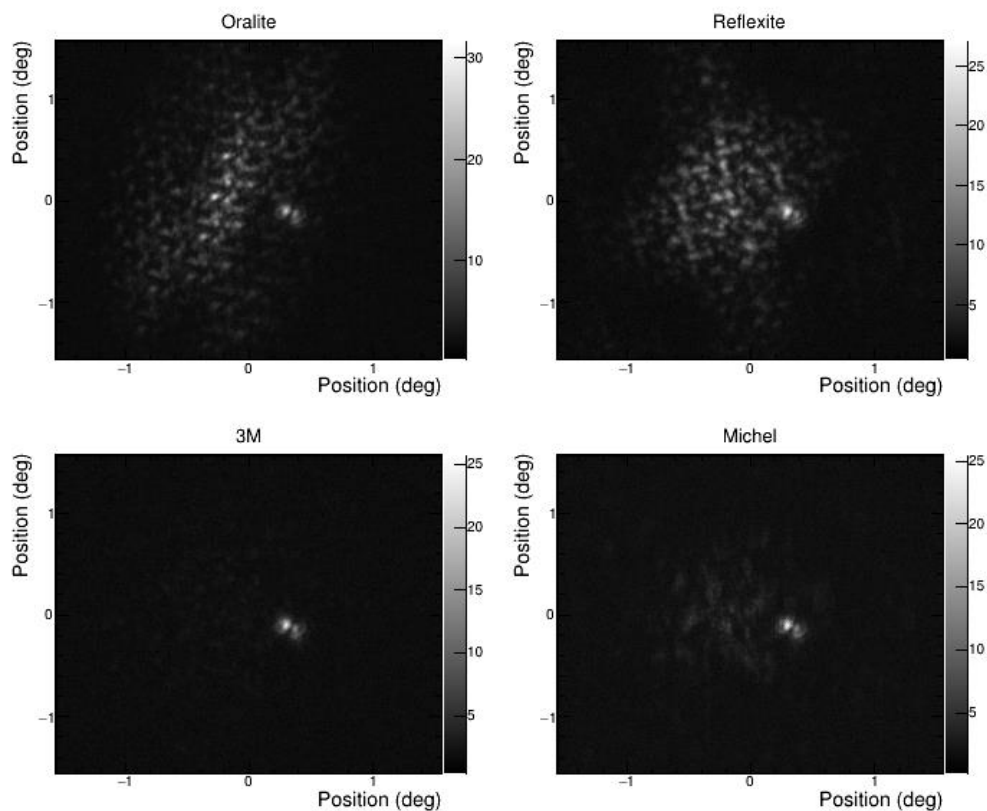


Figure 5.26. Camera images with the beam incident  $40^\circ$  relative to normal.

Repeating structures in the images are a byproduct of the microstructures used to create retroreflection, as shown earlier in Figure 5.18. In general, as the incident beam angle moves away from normal, the reflected beam spots become broader and dimmer. The retroreflected intensity, which was measured by taking the average blue-channel integral of 100 images, is shown in Figure 5.27 as a function of the incident beam angle for all of the tapes as well as Teflon.

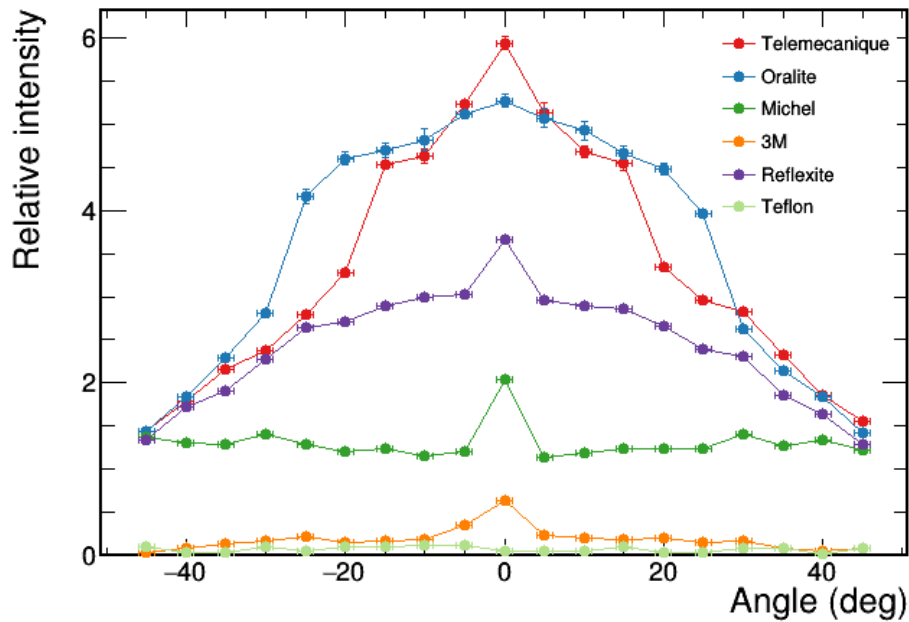


Figure 5.27. Relative retroreflected intensity as a function of incident beam angle.

For all cases except Teflon, there is a small peak in intensity when the beam is normally incident, which is due to the circled partial reflections visible on the right side of Figure 5.23. The retroreflective tapes vary in how consistently they respond as a function of beam angle; at one extreme is the Telemecanique tape, which responds strongly within  $\pm 20^\circ$  of normal with a sharp falloff, and at the other is the Michel tape, which responds almost uniformly. The falloff with angle is primarily due to the fact that the microstructures are imperfect – microprism corner cubes are not always  $90^\circ$  angles and microspheres are not perfectly spherical. As the incident angle becomes less normal, these imperfections result in larger displacements of the reflected light, or in the case of the microprisms, may result in only a single reflection. Imagine, in Figure 5.18, that the microprism corner is  $95^\circ$ , and note that a normally incident ray would be displaced less



than one incident at e.g.  $45^\circ$ . Depending on how deep into the structure it reflects, it may only reflect once.

Due to the significant differences in optics between the laser measurement and a real detector system, the relative retroreflected intensities between tapes presented in Figure 5.27 do not directly correlate with the expected performances when coupled to a scintillator. Additionally, it was not possible to extract the absolute reflected intensities since the number of incident photons, the characteristics of the beamsplitter, and several other factors were unknown. However, the relative intensities are self-consistent for each tape individually and across the tapes.

#### ***5.4.10 Scintillator Measurement Results***

The first performance metric applied to the scintillator measurements compares the total amount of light detected. However, because photoelectric depositions were far less likely than Compton scatters, and the light output of the fast plastic scintillator was poor compared to inorganic scintillators like NaI or LSO, there were no observable photopeaks. To obtain the relative light collection efficiencies for the different surface treatments, the 207-keV Compton edges (Figure 5.28 and Figure 5.29, from 356-keV gammas) from the data collected at the scintillator center location were used. The edge locations were determined by fitting the data to the error function convolved with a Gaussian and are reported in Table 5.2 for every surface treatment. This shows that two of the tapes perform slightly better than Teflon, and all of the tapes are within a few percent of Teflon with respect to overall reflectivity. The Michel tape performs the worst but is still significantly better than either air or black paint.

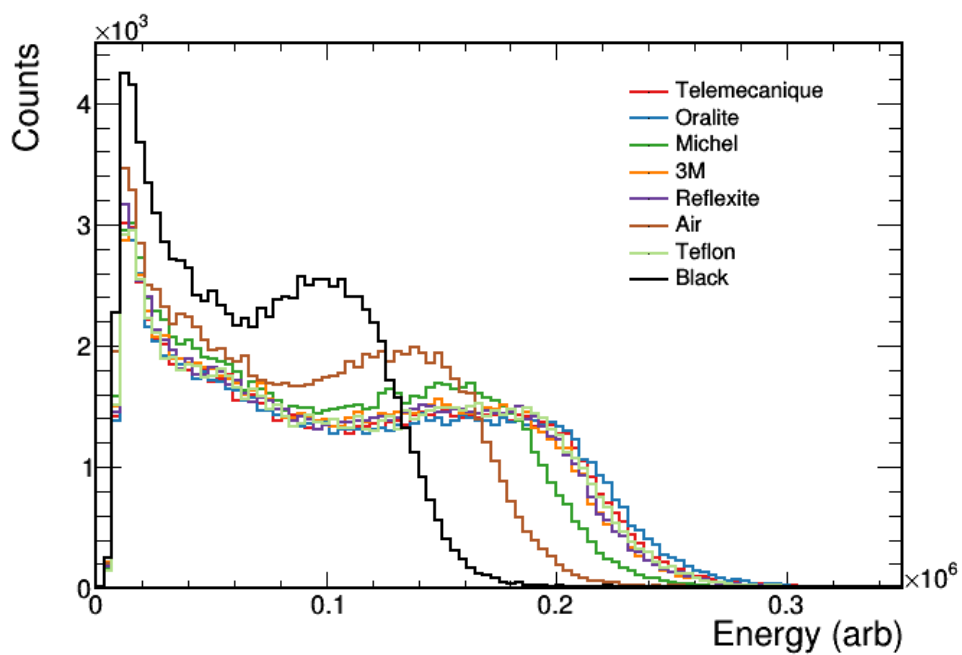


Figure 5.28.  $^{133}\text{Ba}$  spectra from the central beam location for every surface treatment. All eight distributions have the same number of counts.

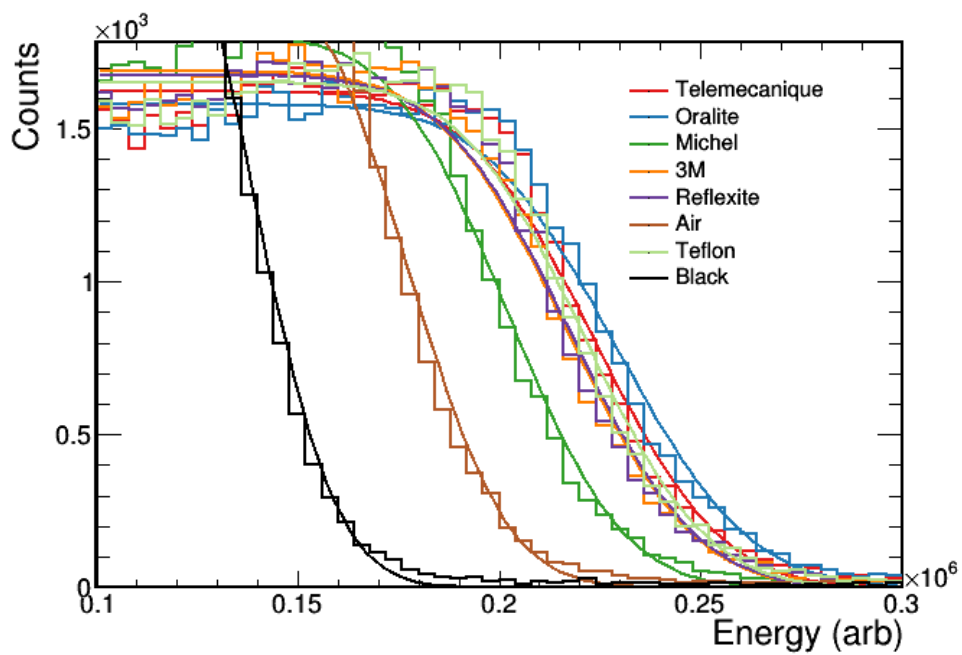


Figure 5.29.  $^{133}\text{Ba}$  spectra, zoomed-in on the Compton edge. Fits with the error function are shown.

Table 5.2. Light collection efficiency, relative to the best performer, as a function of the surface treatment.

Data are from the central beam position shown in Figure 5.28 and Figure 5.29.

<b>Surface Treatment</b>	<b>Relative Light Collection Efficiency (center)</b>
Oralite tape	100%
3M tape	94.6%
Michel tape	88.2%
Reflexite tape	95.0%
Telemecanique tape	97.6%
Teflon	96.5%
Air	77.3%
Black paint	60.0%

The difference in spatial response between the treatments can be seen in Figure 5.30, which overlays the energy-selected beam profiles from two locations for the Oralite tape, Teflon, air, and black paint. Events were selected from the Compton edges in Figure 5.28, to the right of the local minimum around  $1 \times 10^5$ . In the center, the beam profile for air is clearly wider than the others. At the edge beam location, the differences are more apparent due to signal crosstalk between anodes in these MAPMTs. There are two primary modes of crosstalk: nearest neighbor (caused by charges crossing pixel boundaries or AC coupling) and capacitively coupled through the voltage divider [27]. The former has a small impact because the net charge is conserved and stays near the pixel that truly observed the photon. The latter manifests as a bipolar signal with a non-zero integral introduced into every anode. The amplitude depends on the total number of photons that strike the MAPMT for a given trigger: every anode effectively sees a 1-2% integral contribution from every other anode. These additional fluctuations in the signal amplitude negatively impact the centroiding algorithm because pixels that detect few to

no photons have amplitudes dominated by this capacitive crosstalk and can potentially be negative. When centroiding, the weights are not defined for negative values, which biased the results.

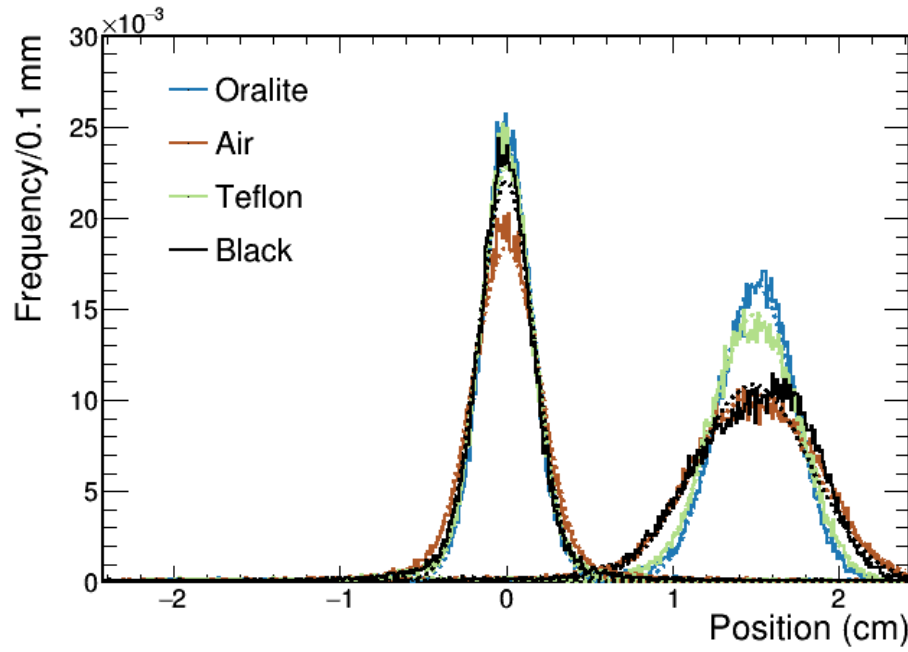


Figure 5.30. Solid: reconstructed X positions for two beam locations and four surface treatments: Oralite tape (blue), air (brown), Teflon (green), and black paint (black). Dashed lines show fits using a Gaussian with a linear baseline.

To estimate the localization performance, the FWHM was estimated at each beam position using energy-selected Compton edge events. The distribution of X positions of

the events was fit using a Gaussian with a linear baseline, and the standard deviation from the fit was multiplied by 2.35 to obtain the FWHM. The results are given in Table 5.3 and Figure 5.31 after quadrature subtraction of the 1.6 mm FWHM beam spot size.

Table 5.3. Intrinsic  $X$  spatial resolution versus top surface treatment. A beam spot size of 1.6 mm was subtracted in quadrature.

<b>Surface Treatment</b>	<b>Best FWHM (mm)</b>	<b>Average FWHM (mm)</b>
Oralite tape	2.81	3.40
3M tape	3.00	3.55
Michel tape	3.54	4.20
Reflexite tape	2.83	3.35
Telemecanique tape	2.88	3.44
Teflon	3.17	3.77
Air	4.31	5.17
Black paint	3.12	3.91

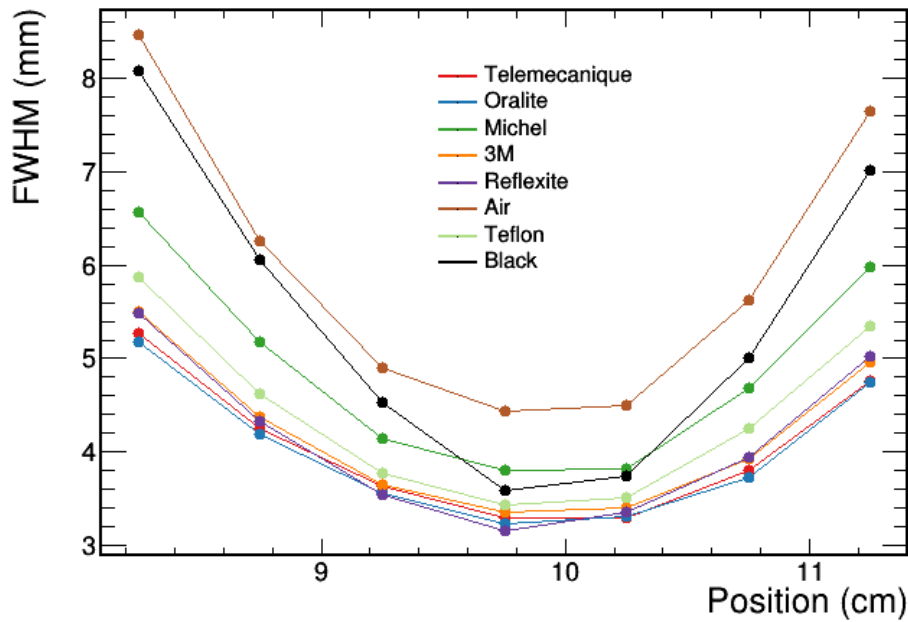


Figure 5.31. Measured intrinsic spatial resolution as a function of lateral position in the detector. A beam spot size of 1.6 mm FWHM was subtracted in quadrature.

As expected, the best intrinsic spatial resolution was universally obtained at the center of the volume, where light collection is the best and edge reflections are the smallest. The resolution falls off toward the edges due to a combination of truncation of the light spot, resulting in less detected photoelectrons and an increased impact of crosstalk as counting statistics decline. The former was verified by comparing the energy spectra at the edges and observing the shift of the Compton edge towards slightly lower values. The latter was confirmed by observing that the relative variation on each anode's amplitude in the black paint data set was significantly higher than would be expected due to counting statistics alone. Relative to the higher reflectivity surface treatments, there were also more events with anodes with negative amplitudes due to crosstalk.

As mentioned previously, the observed size of the light spot is expected to be the weighted in-quadrature sum of the direct width and the reflected width, respective of their contribution to the counting statistics. These values can be approximated directly from the scintillator data, by subtracting the black paint beam data from the other sets and studying the remaining distributions. In this case, instead of integrating the entire Y range to obtain the X projection of the anode hit maps, only the central two rows were integrated. This minimized the impact of edge reflections and increasing specular reflections that occur off the top face with the shallower angles at greater Y values. An energy cut was applied to select events in the Compton edge in the same way as described previously. Figure 5.32 shows the X-projected hit maps from all surface treatments, and Figure 5.33 shows the result when the black beam data are subtracted.

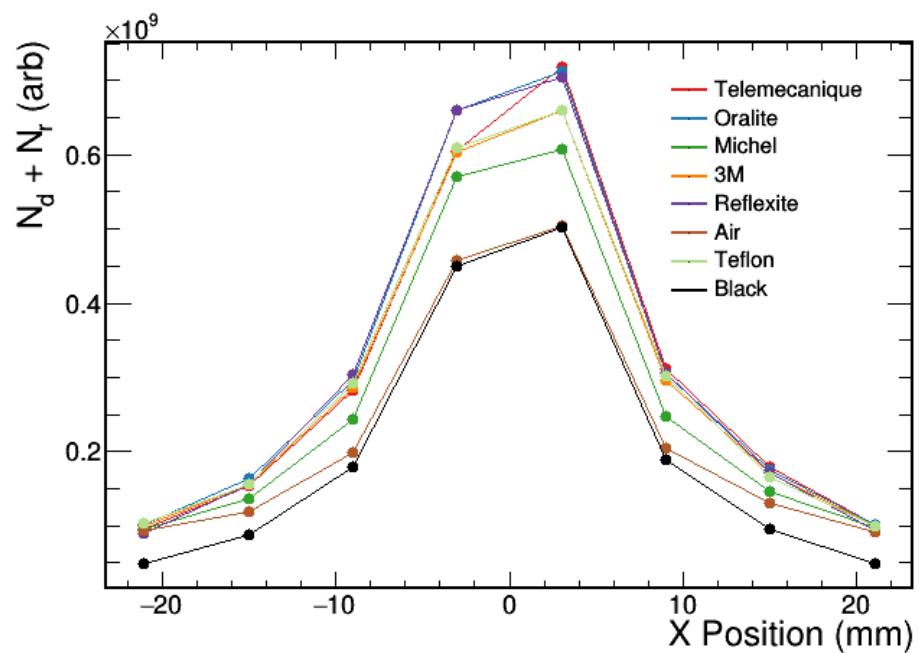


Figure 5.32. X-projection of 30,000 anode hit maps from the middle beam location, integrated across the two central  $Y$  rows of anodes. Events are selected from the Compton edge region.

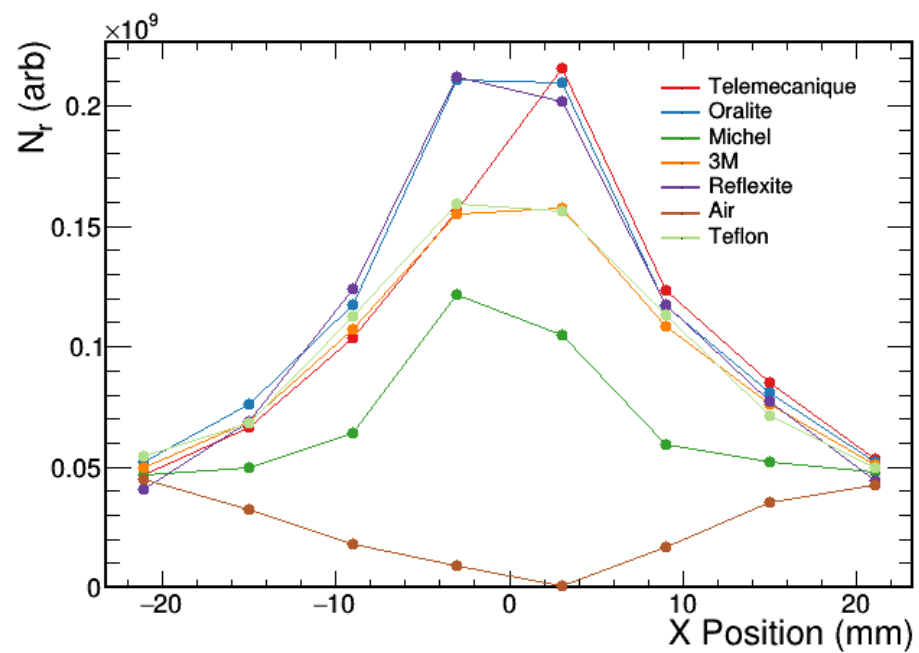


Figure 5.33. Hit maps from Figure 5.32 with the black paint hit map subtracted from the others.



Figure 5.33 shows that, when the direct contribution to the hit map is removed, the Teflon (a Lambertian reflector) and retroreflectors retain a peaked distribution, indicating that they are largely reflecting light near normal incidence back downwards. The light reflected by Teflon is broader than the retroreflectors, since it is diffuse at steep angles and behaves like a specular reflector at shallow angles [44]. The bowl-shaped distribution for air is a consequence of its reflection mechanism, only a few percent of the light normally incident on the surface will be reflected due to the index mismatch. This increases as the angle increases until total internal reflection (TIR) occurs at the greatest angles.

The widths (standard deviations) and integrals of the distributions from Figure 5.32 and Figure 5.33 were used to confirm that the independent contributions to the width added in quadrature by comparing the measured width of the light spot to the calculated width using the widths of the component distributions. The black beam data were assumed to be entirely constituted by direct light, which is not completely true due to imperfections in the paint coverage and the fact that the paint itself has a refractive index and will thus result in TIR at some incident angles (one of the reasons for only using the central Y data). The beam data also represents an effective width, which varies and was integrated across the 13 mm height of the scintillator slab. Table 5.4 lists the measured contributions to the widths  $w_d$  and  $w_r$  for the black paint and reflectors, respectively, as well as the relative reflectivities. The reflectivities have the same meaning as those presented in Table 5.2 but were instead determined using the measured  $N_d$  and  $N_r$  from Eq. 5.2.

Table 5.4. Contributions to the overall width and relative light collection efficiencies for each surface treatment. Data are from the center beam location. The beam spot width was subtracted in quadrature.

<b>Surface Treatment</b>	<b><math>w_r</math> (<math>w_d</math> for black paint) (mm)</b>	<b>Relative Light Collection Efficiency</b>	<b>Relative Light Collection Efficiency (from Table 2)</b>
Oralite tape	10.7	100%	100%
3M tape	11.2	94.4%	94.6%
Michel tape	11.9	85.3%	88.2%
Reflexite tape	10.3	98.9%	95.0%
Telemecanique tape	10.8	97.4%	97.6%
Teflon	11.2	94.9%	96.5%
Air	16.9	71.6%	77.3%
Black paint	8.75	63.6%	60.0%

#### **5.4.11 Discussion**

The laser data show that for all of the retroreflectors tested except the 3M product, there is a significantly enhanced reflective response within  $\pm 45^\circ$  of normal incidence compared to a non-retroreflective material (Teflon). Figure 5.27 indicates that the Oralite and Telemecanique tapes, both microprism based, yield the best retroreflective response. The Reflexite (microprisms) is next, followed by the Michel and finally the 3M tape (both microspheres); the Michel tape is roughly a quarter as effective at retroreflecting as the Oralite tape and the 3M tape is best described as a Lambertian reflector. Figure 5.27 also shows, for a given tape, the relative reflectivity for a given tape as a function of angle, which could be incorporated into optical simulation codes by assuming an integrated reflectivity extracted from Table 5.2 or Table 5.4. However, care should be taken to

account for the different index of refraction changes between the scintillator and the tape in the radiation measurements and air and the tape in the laser measurements.

According to both measurement methods (Table 5.2 and Table 5.4), the relative light collection efficiencies (indicative of the net reflectivity) are fairly consistent, with black paint performing the worst, as expected; followed by air and then a progression of reflectors. The Oralite and Reflexite retroreflective tapes perform the best in terms of reflectivity and angular dispersion of the reflected light, resulting in the best spatial performance when centroiding. These tapes yielded 3.35 and 3.40 mm FWHM average intrinsic centroiding resolution, compared to 3.70 mm for Teflon, a significant improvement. Conversely, the Michel tape performs the worst of the retroreflectors in these aspects at 4.20 mm FWHM. The Teflon is a good example of a relatively larger spread that is almost completely compensated for by the improved counting statistics, resulting in comparable spatial resolution in the middle of the detector compared to black paint. However, the Teflon significantly improves the energy resolution compared to black paint, and it also helps mitigate the impact of crosstalk, resulting in better spatial performance at the edges. Overall, all of the retroreflective tapes except the Michel tape outperformed the Teflon and black paint in average spatial performance and were comparable to Teflon in light collection improvement.

When measuring the different contributions to the light spot, there is a systematic overestimation of the direct component because the black walls are not perfectly black, so even the black data contain light reflected off of the sides and top of the scintillator. The magnitude of the improvement of the tapes over black paint is therefore correspondingly suppressed. Further, the edge-fitting method is only an estimation of the light output and not a precise measurement. Prior work [44] has shown that three layers of Teflon, as was used here, has a reflectance of over 90%. Based on the results in Table 5.4, the estimated reflectance is closer to 73%, showing that the absolute reflectivities reported above should instead be interpreted as relative to Teflon in this configuration. Regardless of the exact values, the data show conclusively that the retroreflectors have a reflectance comparable to, or slightly better than Teflon.

When using these tapes, there are a few practical matters to consider. One is that there are polygonal patterns on the tape, which were likely placed to aid the human eye. In this system, the MAPMT pixel size was 6 mm, so those 3-4 mm features were too small to observe. However, they would be noticeable in a detector system with a higher resolution readout. Furthermore, some practice was required to determine the appropriate amount of grease to use when coupling the tape to the top of the scintillator to minimize air bubbles. While some small bubbles were impossible to eliminate, the tape could be consistently applied with only a few tiny bubbles visible. Finally, for some of the tapes, the silicone optical grease wicked in through the edges to the layers constituting the tape, causing it to turn white in those regions. While the front faces of the tape are weatherproof, the edges must be handled with care to avoid seepage, which likely degrades the retroreflectivity at the boundaries.

#### ***5.4.12 Conclusions***

While the potential for retroreflective tapes to improve the light collection and localization performance of scintillator-based detector systems was previously demonstrated, this work expands that knowledge by reporting the angular dependence of the retroreflectivity for blue light, by directly comparing a larger range of retroreflectors and surface treatments, and by assessing results in plastic instead of crystalline scintillators. However, the performance effects seen in plastic are expected to hold for crystals as well. The tapes that performed the best were shown to result in light collection efficiency comparable to Teflon while improving the intrinsic spatial performance by about 10% over Teflon (3.35 vs 3.70 mm) and 15% over black paint (3.35 vs 3.91 mm). These tapes are therefore an inexpensive, performance-enhancing alternative to Teflon, black paint, and air coupling for applications in which the best possible spatial resolution is required.

## 5.5 Prototype Characterization

### 5.5.1 Data Acquisition and Response Table

As with the simulated detector, the response of the prototype to incident radiation at every position in the detector had to be empirically determined. This was accomplished using the same collimated (1 mm diameter, 600  $\mu\text{Ci}$ )  $^{133}\text{Ba}$  source used for the retroreflector studies in Section 5.4. The beam was directed along the  $Y$  axis, which was the slab width dimension, so that every slab could be probed simultaneously for an array of  $(X,Z)$  positions. The collimator was mounted to a 2-D motorized stage such that the beam was normally incident on the 1 mm thick entrance window of the enclosure, previously described. The collimator pinhole was 8.45 cm from the entrance window, resulting in a beam spot size of 5.5 mm FWHM at the center of the front slab and 8.1 mm at the center of the furthest slab (Figure 5.34). The gamma-ray beam was scanned in both dimensions to find the detector boundaries, using the count rate, which fell off steeply at the edges (Figure 5.35).

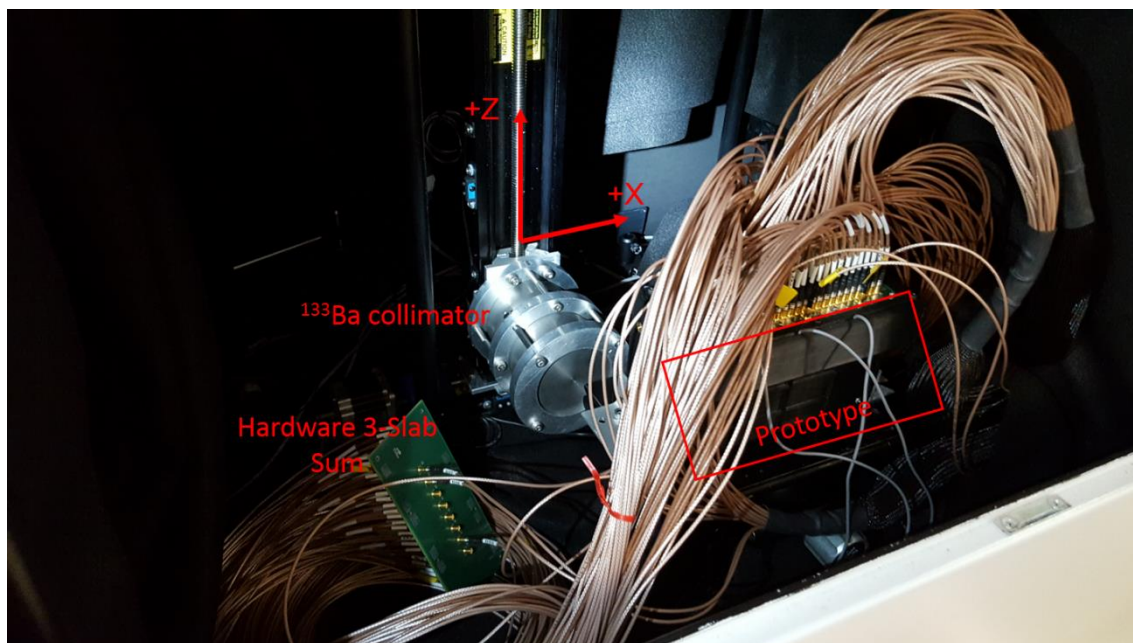


Figure 5.34. Picture of the experimental calibration setup.

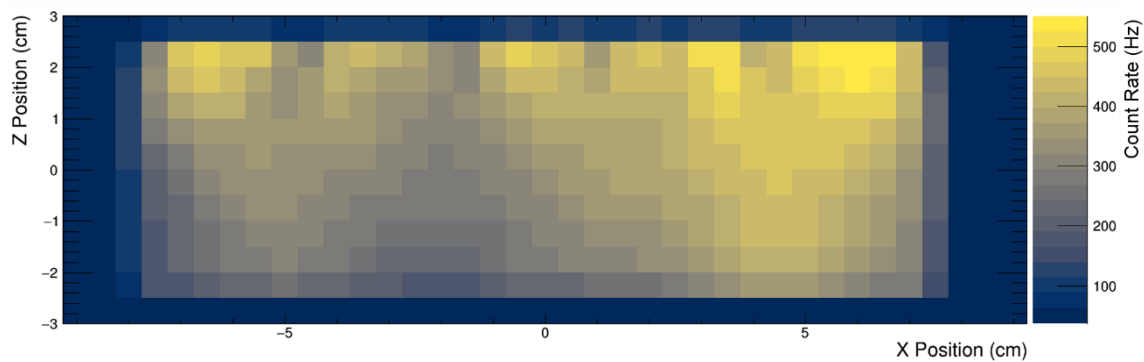


Figure 5.35. Count rate as a function of beam position. The phototubes were at the top of the image. Count rates are shown for 37  $X$  positions and 12  $Z$  positions with 5 mm separation in both dimensions.

For the final table, data were acquired at 31 locations in  $X$  and 10 locations in  $Z$  spaced 5 mm apart for ranges of 15 cm and 4.5 cm, respectively. This covered the full active

volume of the detector. Each position had a dwell time of 500 seconds, resulting in ~150,000 events, which was a compromise between statistics, data rate, and acquisition time. The total measurement time, including re-runs, was about 80 hours. With this setup, the calibration table was comprised of about 8 terabytes of raw binary data.

Figure 5.36 and Figure 5.37 show examples of waveforms from two separate events in which only a single slab triggered. The waveforms were created by summing the 24 anodes comprising each slab. These events were randomly selected for demonstration purposes from a central beam location data set. Figure 5.36 displays waveforms from the five fully instrumented slabs, and Figure 5.37 is the same but for the summed signals of a different event. Negative-going pulse values were caused by electronic crosstalk, described previously in Section 5.4.

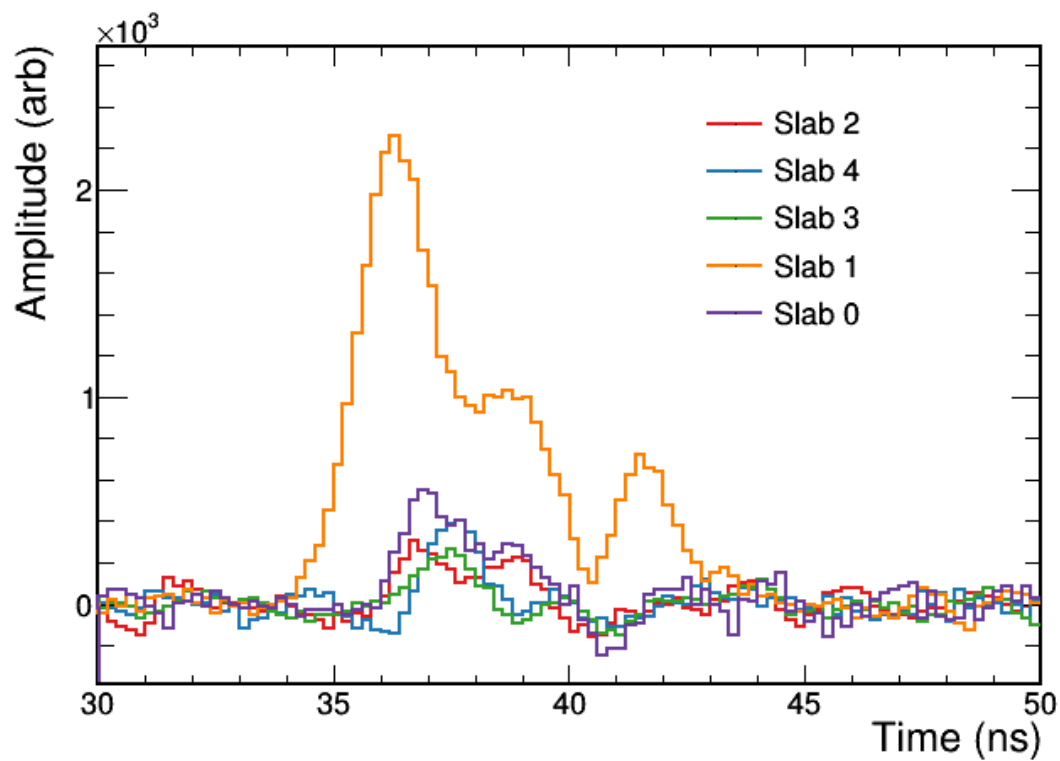


Figure 5.36. Example pulses from a single scatter event. The incident gamma ray deposited about 150 keV into slab 1.

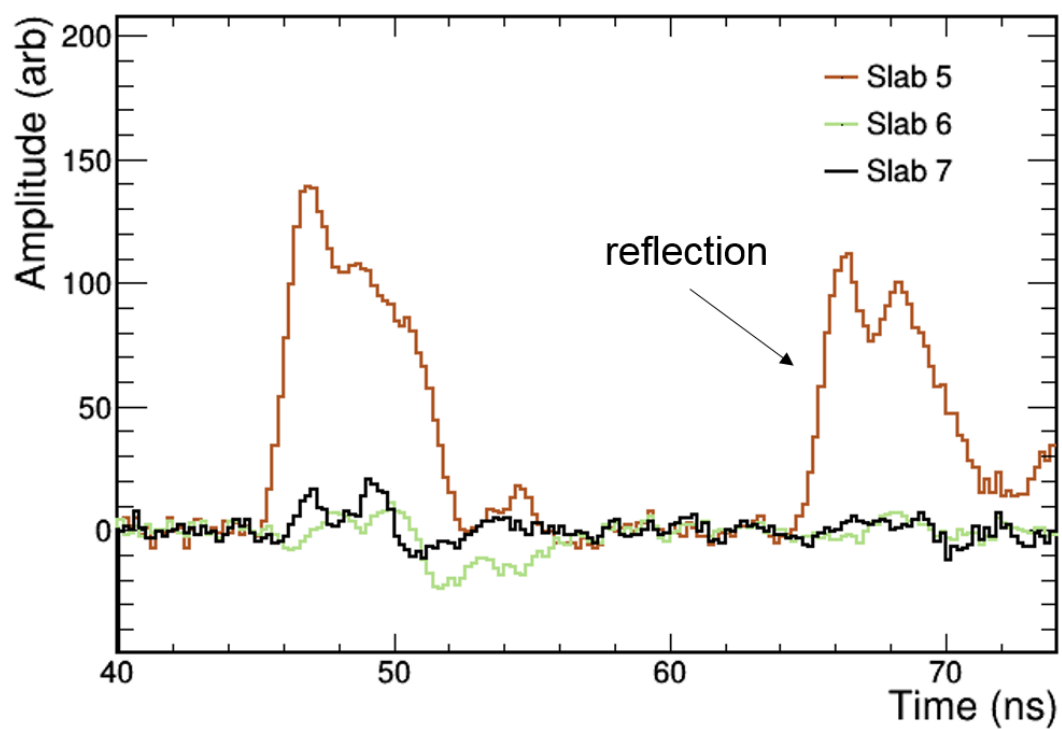




Figure 5.37. Waveforms from a ~300 keV energy deposition in one of the hardware summed slabs. There is an electronic reflection, caused by an impedance mismatch in the summation circuit board, around 20 ns after the real pulse.

Waveforms were integrated for 12 ns starting at a fixed location just before the pulse and gain-corrected using the calibration described in Section 5.1 to produce hit maps (Figure 5.38). This range was chosen to avoid reflections in the pulses, shown in Figure 5.37.

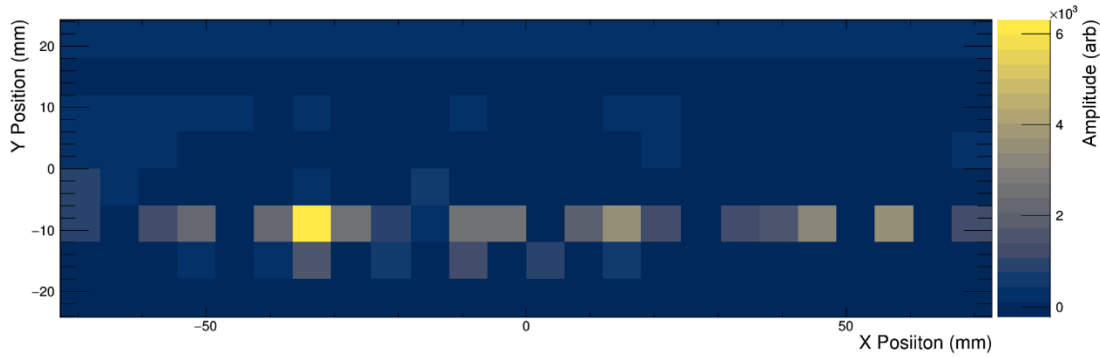


Figure 5.38. Hit map generated from the pulses pictured in Figure 5.36. About 150 keV was deposited in the slab at  $Y = -9$  mm. Light seen in the slab below was likely due to optical crosstalk.

### 5.5.2 Energy Calibration

The eight energy spectra produced by the five fully instrumented slabs and three summed slabs for a beam location near the center are shown in Figure 5.39. The 356 keV Compton edge from  $^{133}\text{Ba}$  is clearly visible at 207 keV.

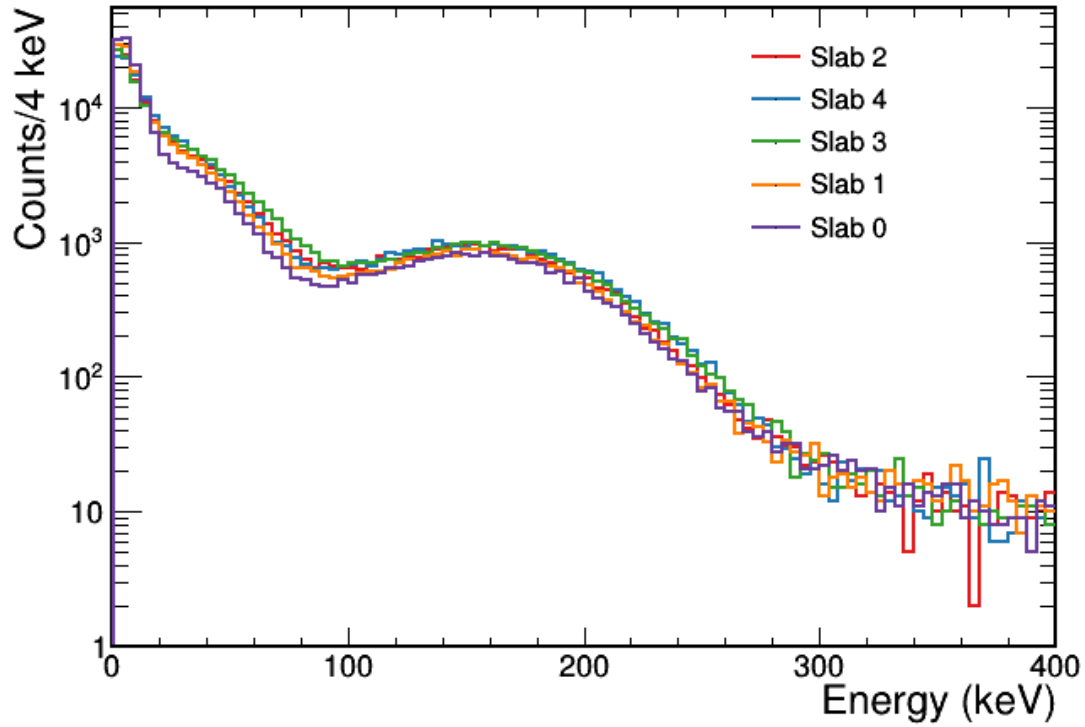


Figure 5.39.  $^{133}\text{Ba}$  energy spectra from all five fully instrumented slabs for a central beam location, after calibration.

The detector response functions simulated in Section 4.2.1 indicated that the photodetection efficiency would vary significantly but smoothly throughout the volume. Additionally, due to the challenges of slab fabrication, the response of each was expected to be slightly different. A total of 2480 spectra ( $8 \text{ slabs} \times 310 \text{ response locations}$ ) needed to be analyzed to determine the energy calibration and doing so manually was not feasible. A number of attempts were made to identify the Compton edge or other spectral features and align the spectra to that feature. While somewhat successful, this did not provide a reliable conversion from pulse integral to energy deposited.

To obtain this conversion factor, a simulation was conducted of a  $^{133}\text{Ba}$  point source inside a single prototype slab. 10,000,000 decays were simulated resulting in around 13,000,000 energy depositions. All of the energies deposited by electrons were recorded, and a spectrum produced, shown in Figure 5.40.

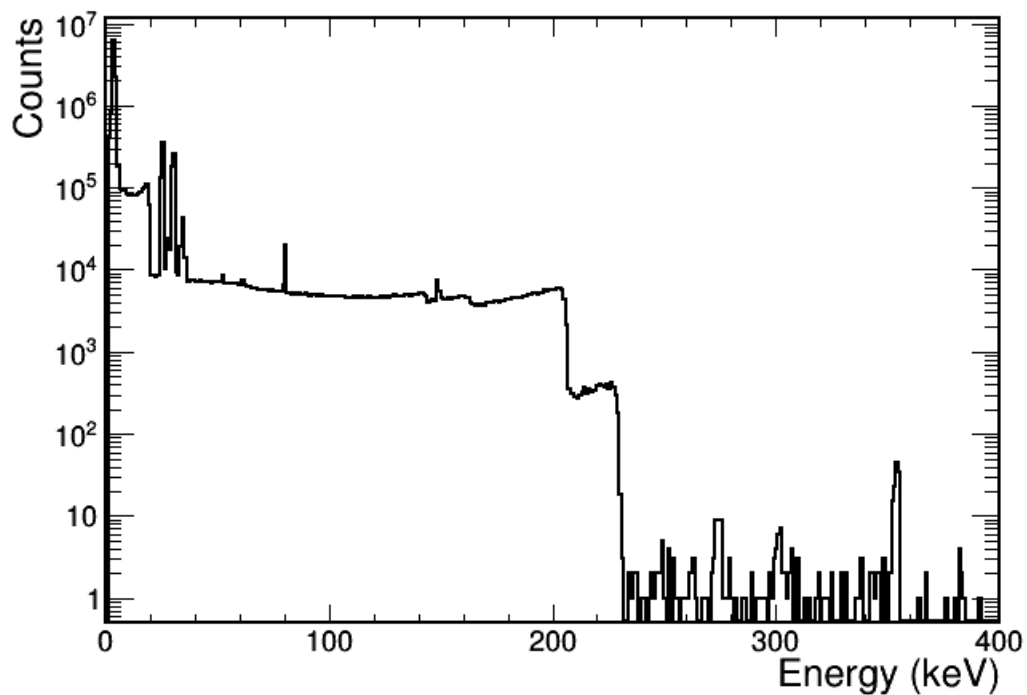


Figure 5.40. Simulated energy spectrum for a  $^{133}\text{Ba}$  point source placed in the center of a slab.

To better match the experimental data, the simulated energy spectra were blurred, accounting for the sum contributions from electronic noise and electronic crosstalk. This

was accomplished by iterating over each bin of the simulated spectrum and randomly resampling those counts from a Gaussian distribution with a mean of  $E$  and a standard deviation of  $\sigma = \frac{\Delta E}{E}$ . Additionally, the experimental spectra were scaled by a factor which was the conversion from arbitrary units to keV (or keVee for neutrons). Therefore, two parameters were used to fit the simulated spectrum to the experimental spectra: the standard deviation of the Gaussian used to blur the simulated spectra, and the scale factor applied to the experimental amplitudes.  $\chi^2$  was used as a goodness-of-fit metric and the ranges of the fit parameters were chosen based on empirical examination of the data. The spectra were only fit over the 100 to 250 keV energy range since the goal was to fit the Compton edge.

Figure 5.41 shows a heat map of the  $\chi^2$  values for an arbitrary, representative spectrum from a central beam location over the 2-D parameter space. The inverse of  $\chi^2$  was plotted to show a peak intensity at the best-fitting set of values. Figure 5.42 shows the blurred, simulated spectrum overlaid with the scaled experimental spectrum using the best-fitting parameters.

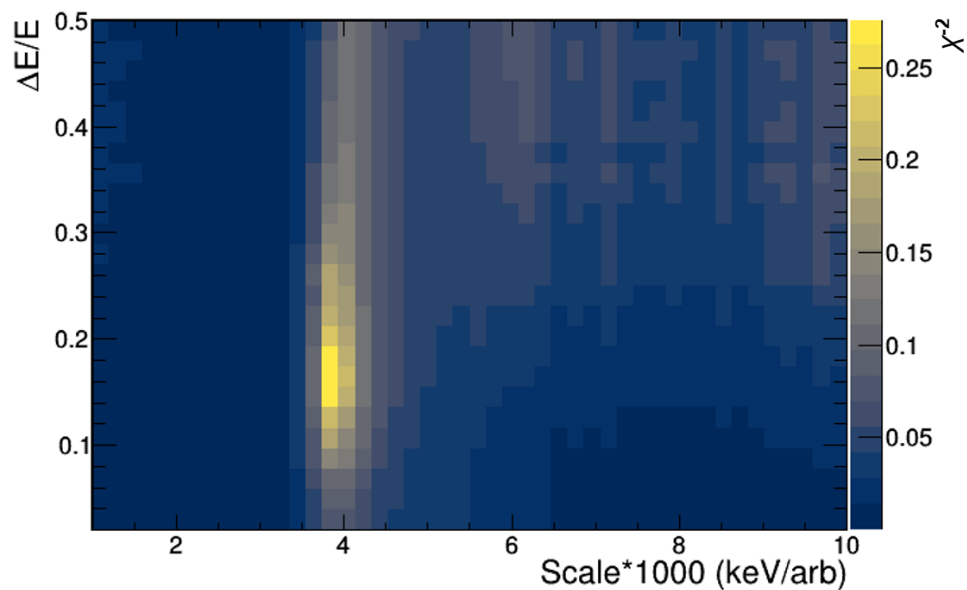


Figure 5.41. Heat map of  $1/\chi^2$  values from fitting the spectrum for a single slab from a central beam location. A maximum (the best fit) is visible at (3.8, 0.16).

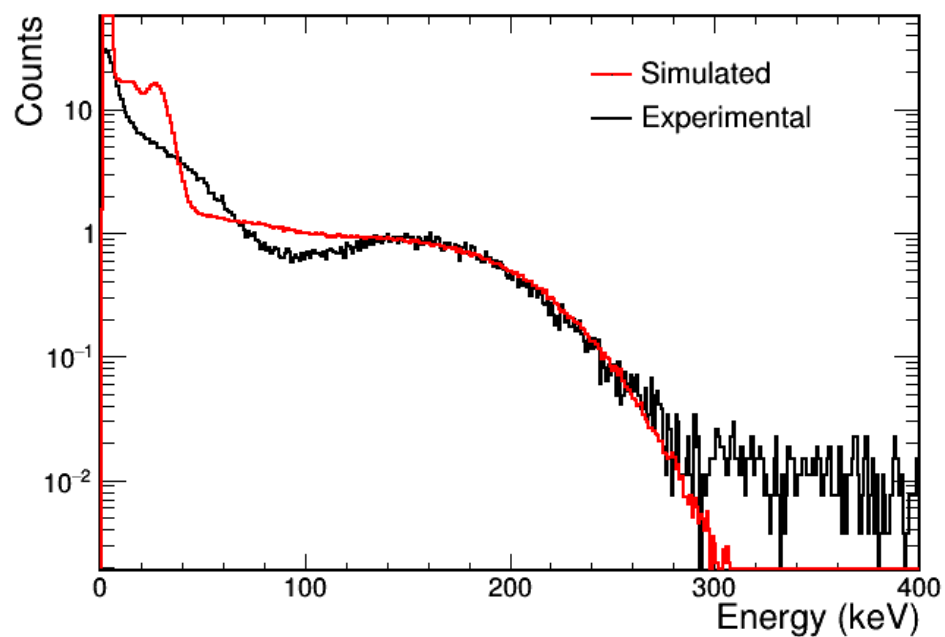


Figure 5.42. Overlaid simulated and experimental spectra for the best-fitting blur and scale factors identified in Figure 5.41.

Overall, this method was effective in determining the energy calibration factors. The value of the scale factor is directly tied to the photodetection efficiency at that beam location; differences in the value represent differences in the number of detected photons for an equivalent energy deposition ( $\sim 207$  keV). Figure 5.43 shows what the relative PDEs were for a single slab, representative of the fully instrumented modules. The shape is consistent with Figure 4.4 shown in Section 4.2.1: in general, the best photodetection efficiency occurs in the middle and nearer to the MAPMTs and falls off towards the black-painted edges. Note that in Figure 4.4, the phototubes are on the bottom ( $-Z$ ), while in Figure 5.43, the phototubes are on top ( $+Z$ ).

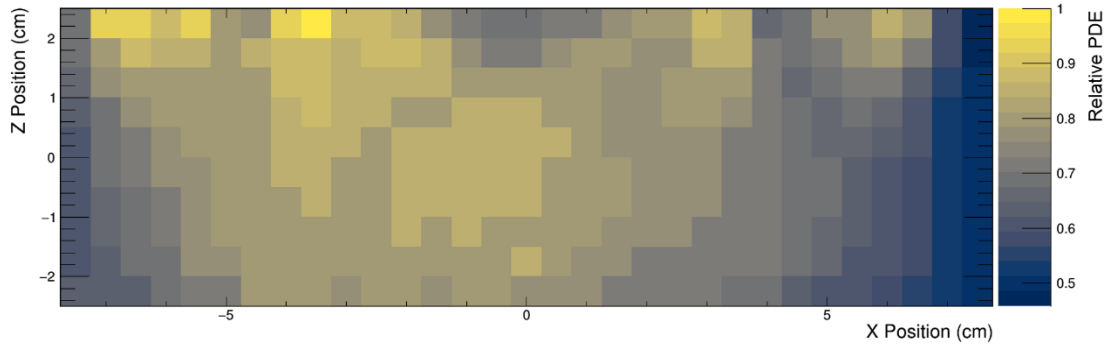


Figure 5.43. Relative PDE as a function of interaction (beam) position.

### 5.5.3 Response Event Selection

To select on events that were likely within the beam trajectory and to minimize the contributions from second interactions following an initial Compton scatter, a set of energy cuts were made. The efficacy of the cuts could be qualitatively seen in the average hit map for a single beam location as the cuts were applied (Figure 5.44). Cuts that eliminated multiple interactions significantly increased the peak-to-valley ratio, which meant a better representation of encoding at that position. Experimentation led to two

energy requirements for selected events that improved the peak-to-valley ratio of the average hit map. One was that only a single slab reported an energy above 180 keV. The second was that every other slab was below 25% (instrumented slabs) or 50% (summed slabs) of the dip (e.g. around 90 keV in Figure 5.42), accounting for optical crosstalk and gamma rays that scattered in another slab.

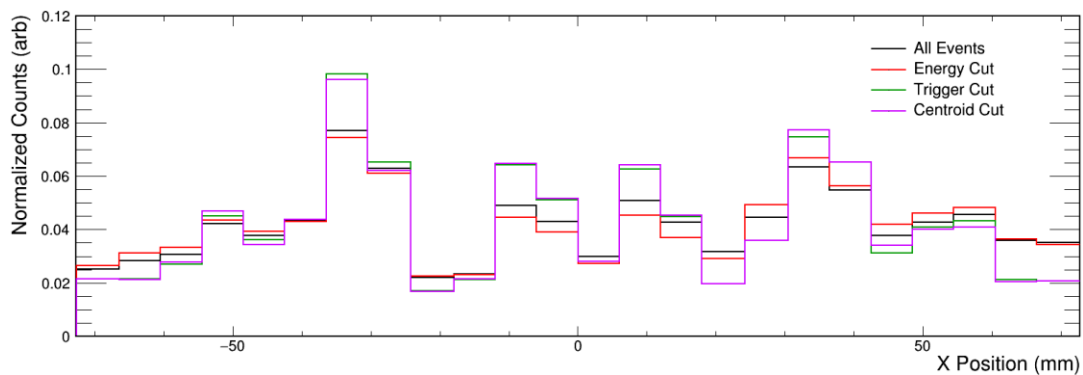


Figure 5.44. Average, normalized hit maps for different levels of event selection cuts for interactions near the center of a slab. In general, better event selection resulted in relatively higher peaks and lower valleys in the distribution.

A set of spatial cuts were also applied. The centroids and standard deviations of the raw hit maps for energy-selected events were calculated for every beam location. When building the response, it was required that the event have a centroid within half a standard deviation of the mean value for that beam position. These cuts resulted in an event selection rate of about 1% per slab per data set: between about 500 and a few thousand events per slab per beam location. Figure 5.45 shows measured the response hit maps at

three different beam positions: one in a corner far from the MAPMTs, one near the middle of the slab, and one in a corner near the MAPMTs.

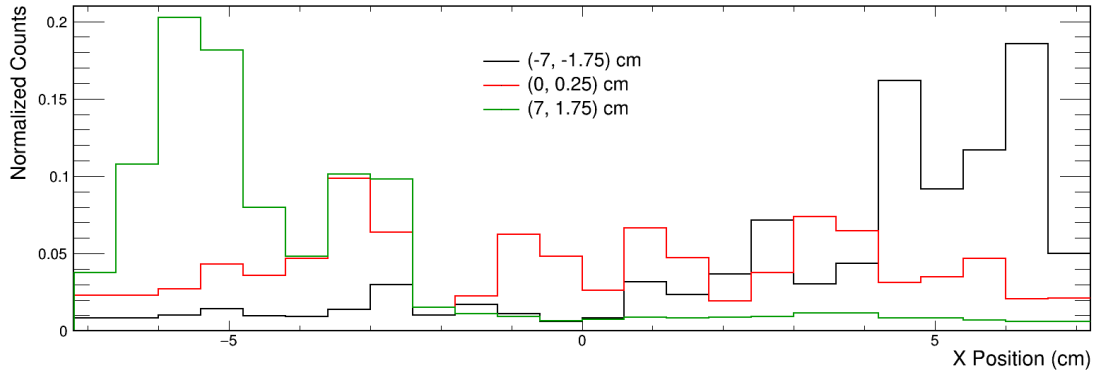


Figure 5.45. Normalized, average hit maps at three different beam positions. The green data are from the beam location closest to the MAPMTs, the red data are from the middle, and black data are from a far corner.

In the middle, the counts are distributed across most of the phototube pixels. The mask pattern was symmetric, and one can see approximately the same pattern on in the green and black plots, except the green distribution is more magnified (1.2 for green vs. 1.07 for black). The black pattern is also more broadly distributed (more of the mask pattern is projected) since the light was generated further away from the MAPMTs.

#### 5.5.4 Response Validation

Before trying to reconstruct interaction locations, it was necessary to verify the consistency of the calibration data. To do so, the data were analyzed with a simple, well-



understood algorithm: finding the centers of mass (COM, also referred to as the centroid) and standard deviations, which are related to the  $X$  and  $Z$  positions, respectively. Calculating these values for each beam location using single trigger, above-threshold events showed consistent results that matched expectations (Figure 5.46 and Figure 5.47). Note the inversion of the sign for the  $X$  positions, which holds no physical meaning. The COM values monotonically change as the beam progresses across the  $X$  dimension, while in general, the width increases as the beam moves away from the MAPMTs.

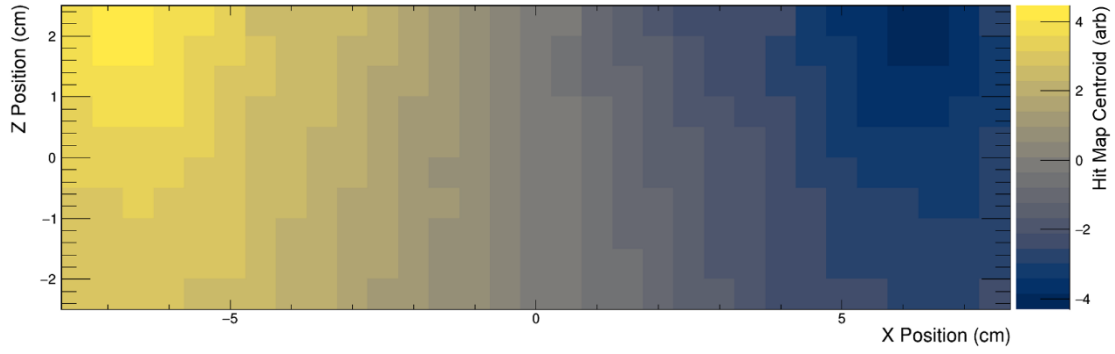


Figure 5.46. Hit map COM values as a function of beam position for a single slab. Each data point has between 500 and 5000 events, depending on location.

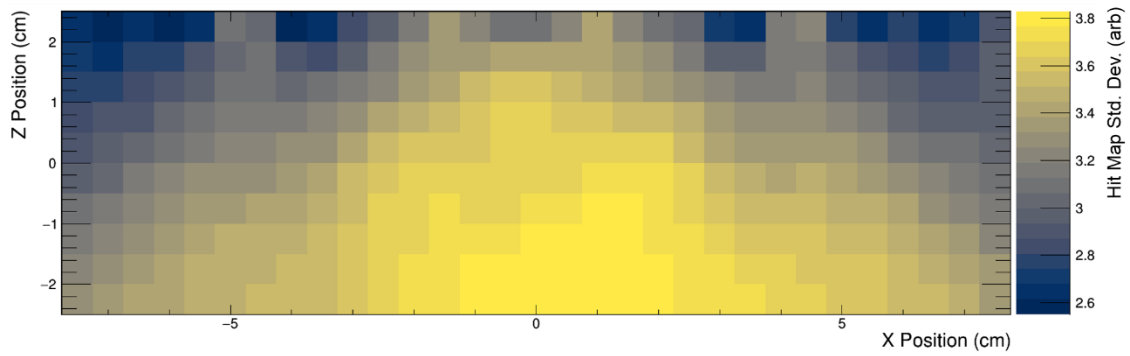


Figure 5.47. Hit map widths (standard deviations) as a function of beam position for a single slab. Each data point has between 500 and 5000 events, depending on location.

Another way the beam data was validated was by reconstructing the calibration data itself. This represented an ideal case for the reconstruction algorithm: the table entries were the average of the data that was being compared against it. For the slab closest to the beam, events were reconstructed, and the means and standard deviations of Gaussian fits to the resulting  $X$  and  $Z$  projections were calculated, shown in Figure 5.48 through Figure 5.51. A beam width of 5.5 mm FWHM was subtracted in quadrature from the

standard deviations of the beam spot distributions in both dimensions. The edge locations were omitted since they were difficult to fit reliably. There were also a few outliers with exceptionally high or low values, e.g. at (-5, 1.75) cm in Figure 5.48 due to bad fits. In Figure 5.51, beam locations far from the phototubes (e.g. the bottom row at -1.75 cm), where the depth resolution is poor, tended to reconstruct at that edge, causing the Gaussian fit to fail (the anomalous white and bright yellow pixels in Figure 5.48, Figure 5.49, and Figure 5.50). As the beam scanned the  $XZ$  plane, the reconstruction algorithm tended to recreate the position correctly, with a standard deviation of 1-5 mm in  $X$  and 5-10 mm in  $Z$ .

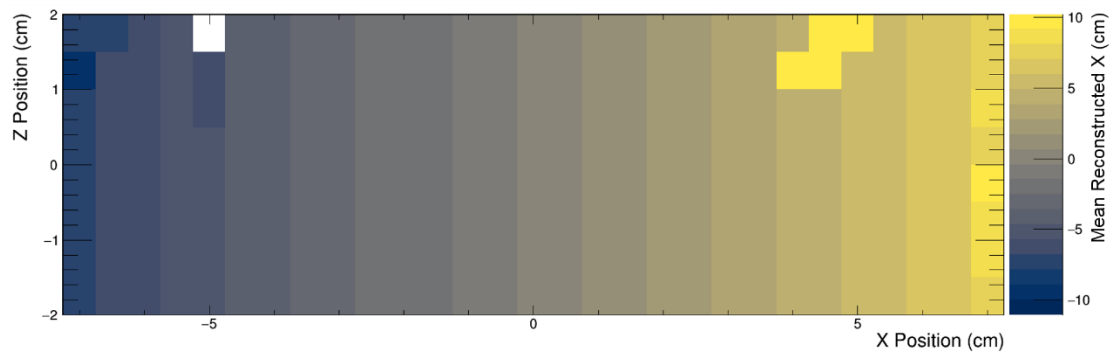


Figure 5.48. Means of Gaussian fits of reconstructed  $X$  positions at each beam location. The anomalous values were caused by poor fits.

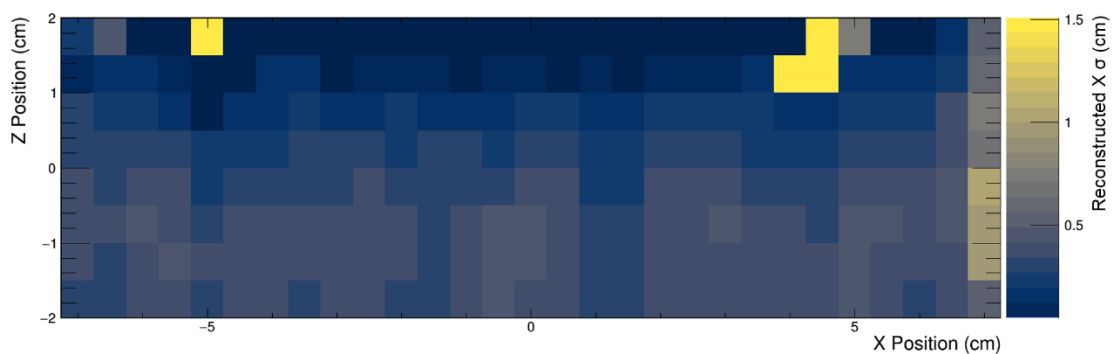


Figure 5.49. Standard deviations of Gaussian fits of reconstructed  $X$  positions at each beam location. The anomalous values were caused by poor fits.

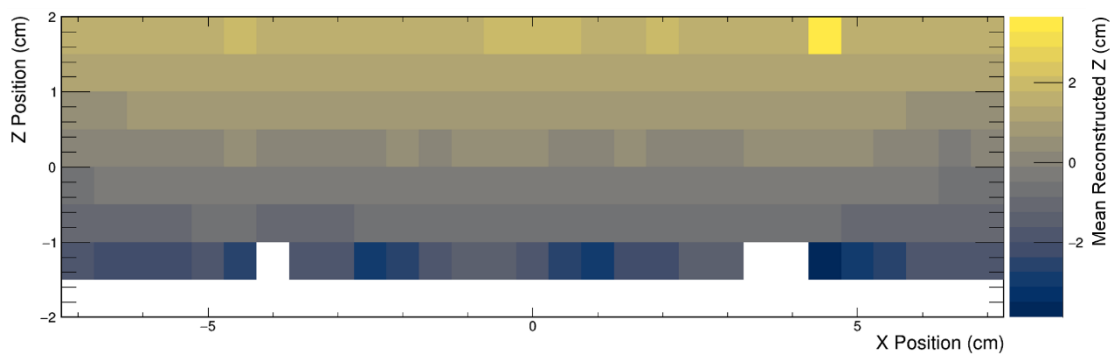


Figure 5.50. Means of Gaussian fits of reconstructed  $Z$  positions at each beam location. The anomalous values were caused by failed or poor fits.

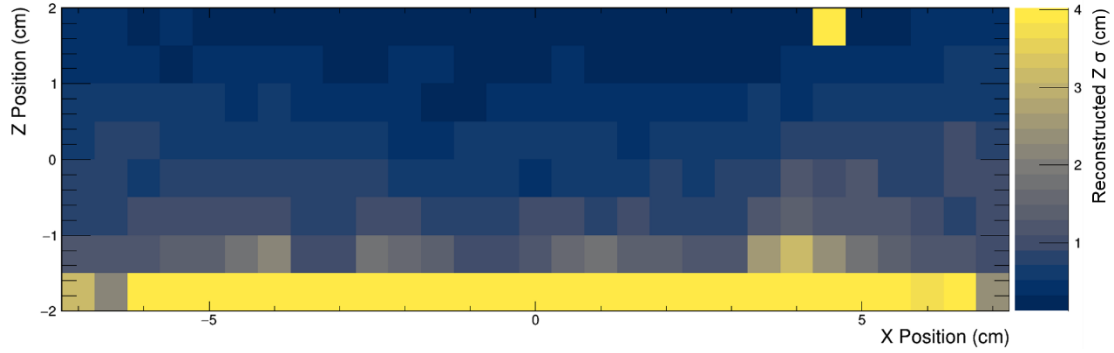


Figure 5.51. Standard deviations of Gaussian fits of reconstructed  $Z$  positions at each beam location. The anomalous values were caused by poor fits. Interactions furthest from the phototubes (bottom row) tended to bunch up against the edge, causing the fit to fail.

The beam was moved to three off-grid locations to demonstrate that the localization algorithm was able to reconstruct interactions that were less ideally placed. The true beam positions were at  $(-6.25, -1.25)$  cm,  $(0.25, 0.25)$  cm, and  $(6.25, 1.25)$  cm. The same event selection cuts were used on this data as were used to build the response table. Figure 5.52 shows the projection of the reconstructed  $X$  positions and Figure 5.53 shows the projection of the  $Z$  positions. The standard deviations on these plots do not have the beam width subtracted. Figure 5.54 shows a 3-D plot of the reconstructed positions for the middle beam location for every fully instrumented slab.

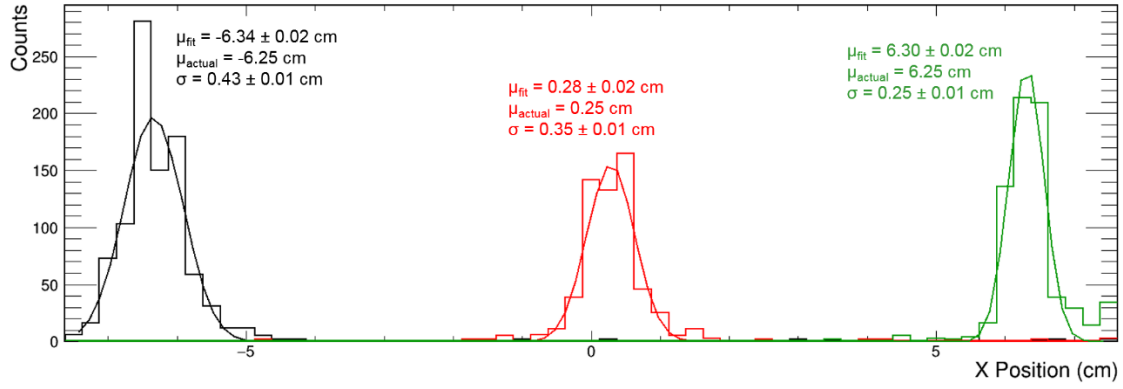


Figure 5.52. Reconstructed X positions for the three off-grid beam locations. Gaussian fits of each are overlaid. The means of the fits were in good agreement with the true beam location, extracted from the 2-D stage encoder.

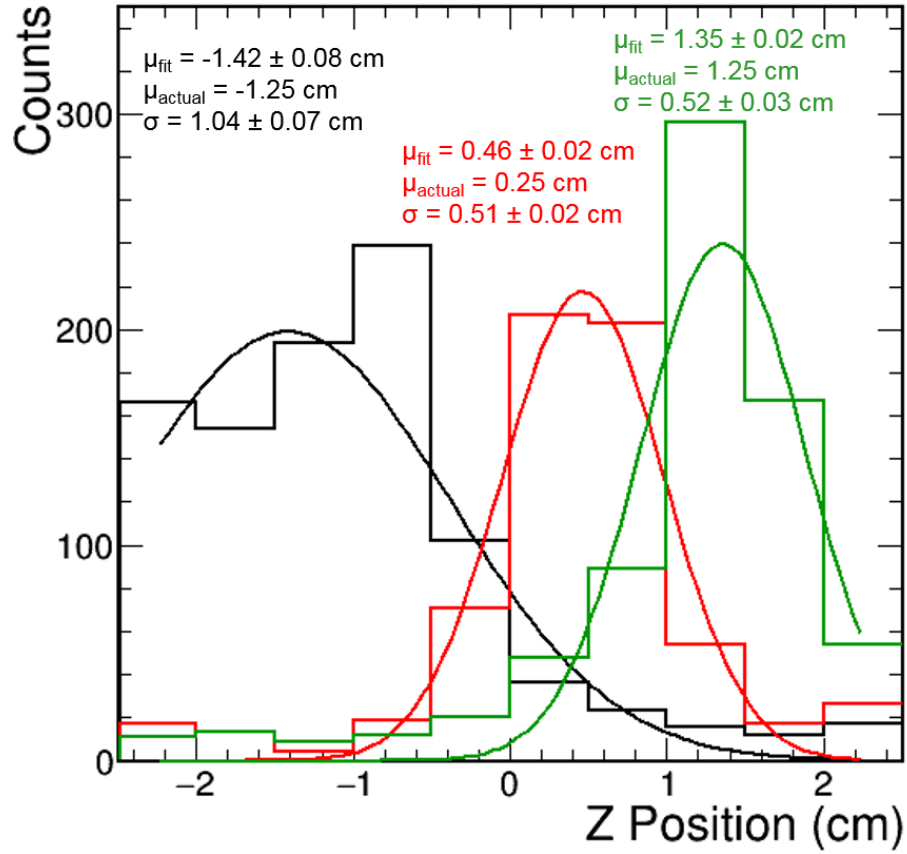


Figure 5.53. Reconstructed Z positions for the three off-grid beam locations. Gaussian fits of each are overlaid. The actual beam locations were extracted from the 2-D stage encoder.

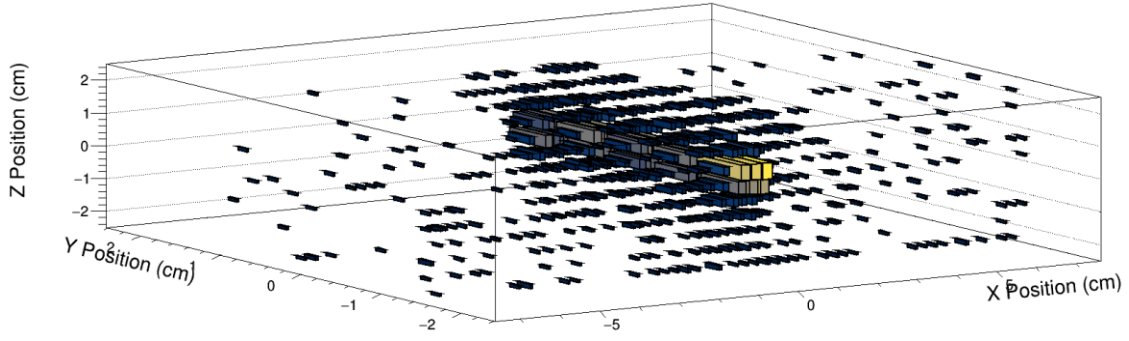


Figure 5.54. Reconstructed interaction positions for the data set where the beam was pointed at the middle of the slabs.

In general, the performance was better the closer the interactions were to the phototubes, as expected. In  $Z$ , there is a systematic bias away from the phototubes. The localization performance was better in  $X$  than in  $Z$  as predicted by simulation (Section 4.3). Table 5.5 summarizes the measured means and standard deviations and the actual beam locations, measured by the 2-D translation stage encoder. An estimated beam width of 5.5 mm FWHM was subtracted in quadrature for the last column of the table.

Table 5.5. Summary of off-grid beam reconstruction performance. The assumed beam spot size was 5.5 mm FWHM.

<b>Location, Dimension</b>	<b><math>\mu_{\text{meas}}</math> (cm)</b>	<b><math>\mu_{\text{actual}}</math> (cm)</b>	<b><math>\sigma</math> (cm)</b>	<b><math>\sigma</math> (cm), beam width subtracted</b>
<b>1, X</b>	$-6.34 \pm 0.02$	-6.25	$0.43 \pm 0.01$	$0.36 \pm 0.01$
<b>1, Z</b>	$-1.42 \pm 0.08$	-1.25	$1.04 \pm 0.07$	$1.01 \pm 0.07$
<b>2, X</b>	$0.28 \pm 0.02$	0.25	$0.35 \pm 0.01$	$0.26 \pm 0.01$
<b>2, Z</b>	$0.46 \pm 0.02$	0.25	$0.51 \pm 0.02$	$0.45 \pm 0.02$
<b>3, X</b>	$6.30 \pm 0.02$	6.25	$0.25 \pm 0.01$	$0.09 \pm 0.01$
<b>3, Z</b>	$1.35 \pm 0.02$	1.25	$0.52 \pm 0.03$	$0.46 \pm 0.03$

To confirm that the energy calibration was effective, the prototype was exposed to an 827 nCi  $^{137}\text{Cs}$  button source placed next to the detector, about 2 inches away. Interactions were reconstructed using the response table, and the energy spectrum was created. Figure 5.55 shows that the 662 keV Compton edge at 477 keV is clearly visible, validating the energy calibration. Unlike the beam data, the interaction locations were dispersed throughout the entire detector volume. Figure 5.55 therefore suggests that both the localization and energy calibration were functioning as desired, since the energy is corrected based on the inferred interaction location.



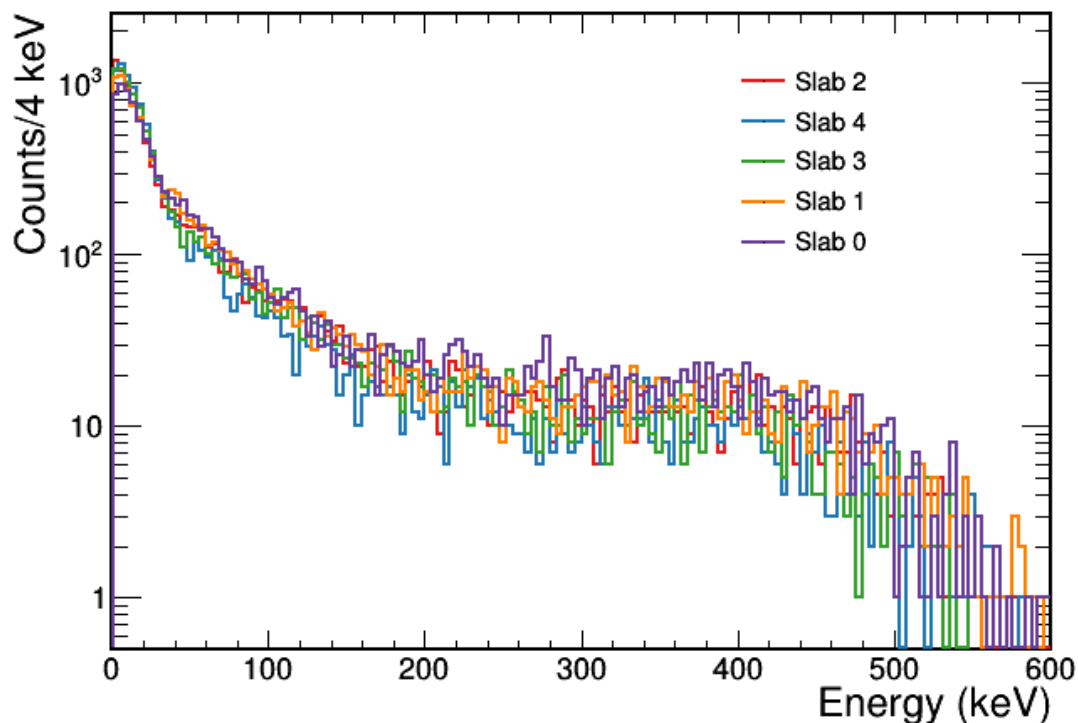


Figure 5.55. Reconstructed energy spectra for all five fully instrumented slabs when a  $^{137}\text{Cs}$  source was placed next to the detector.

### 5.5.5 Timing Performance

Using the  $^{252}\text{Cf}$  fission chamber measurement data, described in the next section, the timing performance was estimated. This was done by employing the cuts described below in Section 5.6.4 to select gamma ray double scatter events. The time difference between the first scatter (using a CFD on the slab signal), assumed to be the one closest to the source, and the fission chamber CFD time (using an LED on the digitized CFD logic pulse), is plotted in Figure 5.56. The peak of the distribution is largely composed of the desired events, while the tail contains events where the gamma ray scattered off of an item in the lab before reaching the detector. The standard deviation of a Gaussian

function fit to the distribution was 528 ps, suggesting that the device achieved the desired timing resolution. It is important to keep in mind that the chamber pulse rise time was a few nanoseconds, limiting the resolution that could be achieved. Also note that the absolute offset of about 57 ns in Figure 5.56 was primarily a product of the triggering configuration and should not be interpreted to have physical meaning with regard to the gamma ray transit time.

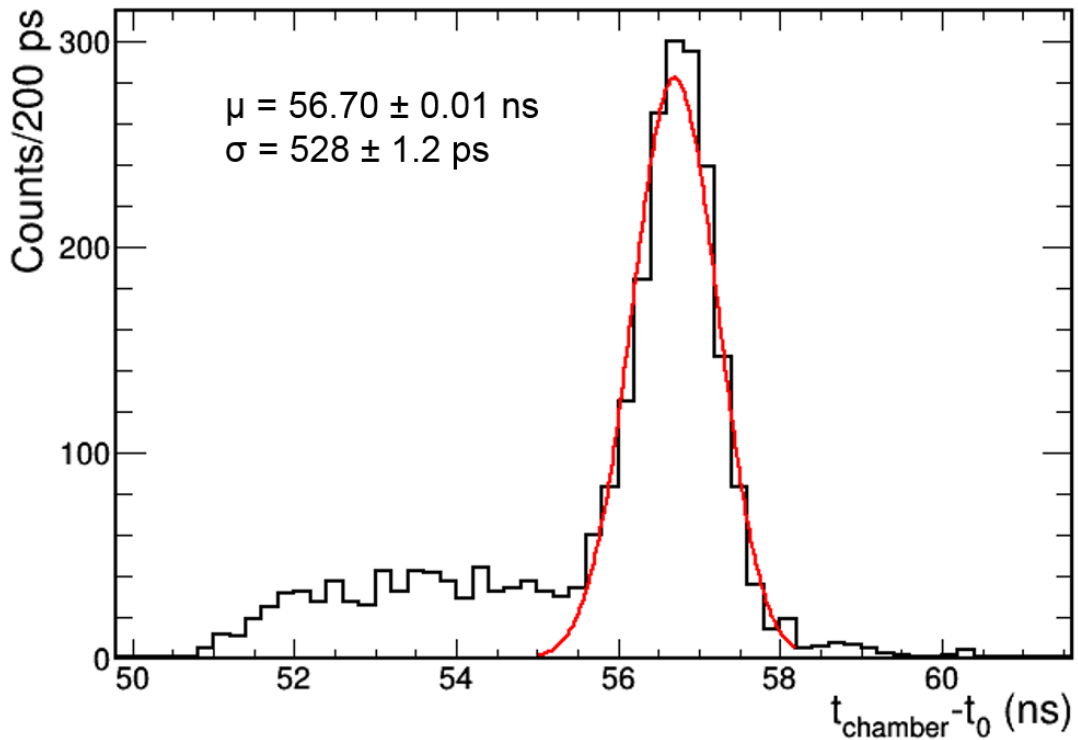


Figure 5.56. Time difference between the fission chamber, extracted from the digitized CFD signal, and the assumed first gamma ray scatter, determined from a 50% CFD on the slab pulse.

## 5.6 Prototype Measurements

### 5.6.1 Experimental Setup and Event Selection Cuts

With the localization capability demonstrated, the prototype was exposed to a 9.2  $\mu\text{Ci}$   $^{252}\text{Cf}$  fission chamber to acquire neutron double-scatter data at two source locations. The fission chamber is an ionization chamber that contains  $^{252}\text{Cf}$ , generating an electrical signal when a fission occurs. This start pulse can be used to tag the neutron and gamma-ray emissions and trigger the data acquisition system (in coincidence with the prototype) to record the event. To reduce the gamma-ray flux from the chamber, it was shielded by a lead enclosure outside of the dark box in both cases. A trigger was generated by providing the signal from the chamber to a NIM CFD with a 100-mV threshold. This was added to the data acquisition logic shown earlier in Figure 5.16, with the updated logic shown in Figure 5.57.

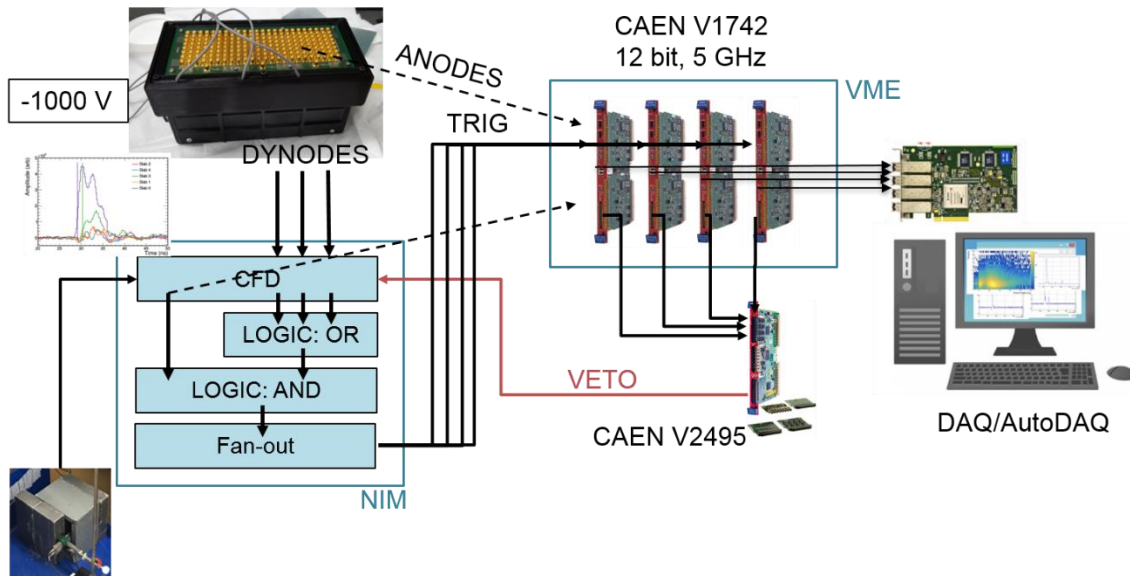


Figure 5.57. Schematic of the data acquisition setup for the  $^{252}\text{Cf}$  fission chamber measurement.

The logic unit was configured so that there was a logical OR between the MAPMTs, which was then compared to the chamber signal via a logical AND. A second output of the CFD for the fission chamber was digitized to record a start time, from which the time of flight could be obtained. The resulting trigger rate was about 30 Hz, about 90% of which were neutrons. Figure 5.58 shows a picture of the experimental setup with the fission chamber at the first location.

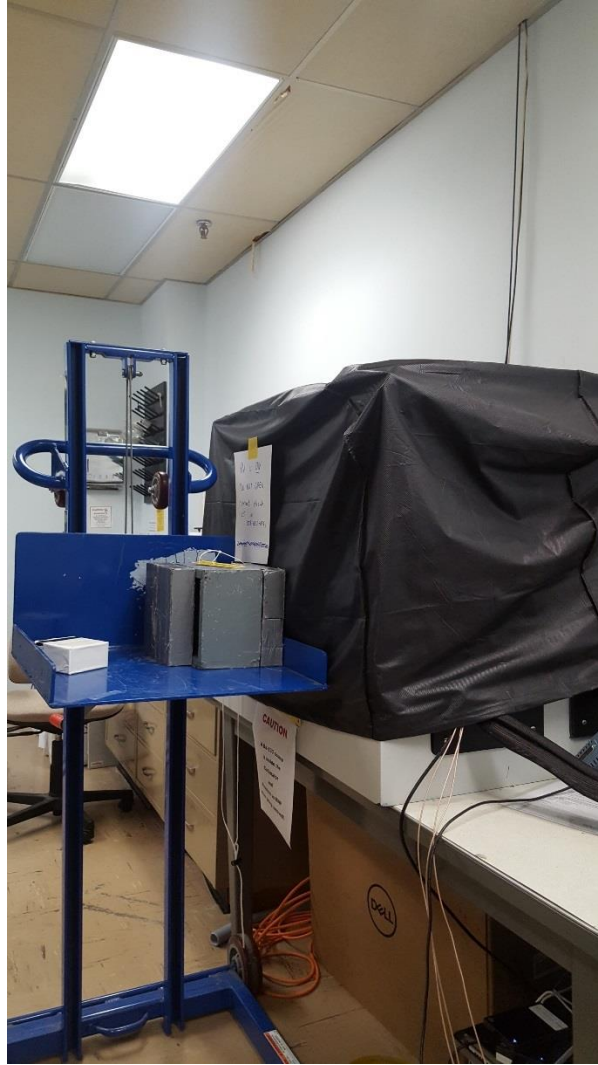


Figure 5.58. Picture of the experimental setup. The prototype detector was inside the dark box on the right while the chamber was mounted outside the box and shielded with lead bricks. The chamber was not installed in this picture.

Using the necessary delays at various points in the trigger chain, the CFD logic pulse from the fission chamber was timed to be fully captured by the digitizer. Waveforms for

500 events are shown overlaid in Figure 5.59a. Around 85 ns, a thin band is visible, corresponding to gamma rays. The neutron continuum begins around 80 ns, extending to the left; events closer to 80 ns correspond to faster (higher energy) neutrons and vice versa. Note that the system trigger time is related to the output from the detector, with the chamber delayed to occur after this. Hence, there is a reversal in time where “longer” flight times trend to lower chamber times (earlier in the waveform). In software, a leading-edge discriminator with a threshold of 1000 was applied to these waveforms to estimate the fission chamber trigger time. Figure 5.59b shows the trigger time spectrum, which is a 1-D slice through Figure 5.59a at an amplitude of 1000. Gamma rays and neutrons are clearly distinguishable by the particle time of flight.

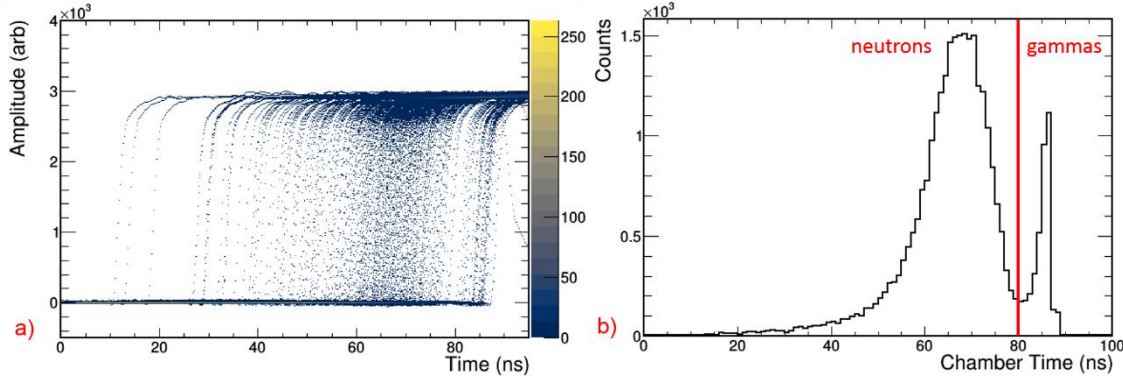


Figure 5.59. a) 500 overlaid waveforms of the leading edge of the fission chamber CFD signal. b) Spectrum of chamber trigger times, corresponding to the particle's time of flight.

A series of selection cuts were required to identify events that were likely to be neutron double scatters. First, the mean gamma-ray time of flight was determined, and it was required that interactions come at least 3 ns after that time. This cut (Figure 5.59) eliminated almost all gamma rays that traveled directly from the chamber to the prototype detector. Further, it was required that two and only two fully instrumented slabs triggered with at least 100 keVee, and that these depositions were separated in time by at least 500 ps.

To eliminate scatters in the hardware-summed slabs, it was required that any energy deposition be under a ceiling of approximately 100 keVee. A ceiling was required to allow for optical crosstalk. If a fully instrumented, neighboring slab (whose signal was generated by summing the anodes in software) also triggered, then the upper limit of allowed energy linearly depended on the primary slab's amplitude. Figure 5.60 shows, for the first source location, the correlations between energy depositions in 1) one slab and another with two slabs in between (left), 2) one slab and another with one slab in between (middle), and 3) neighboring slabs (right).

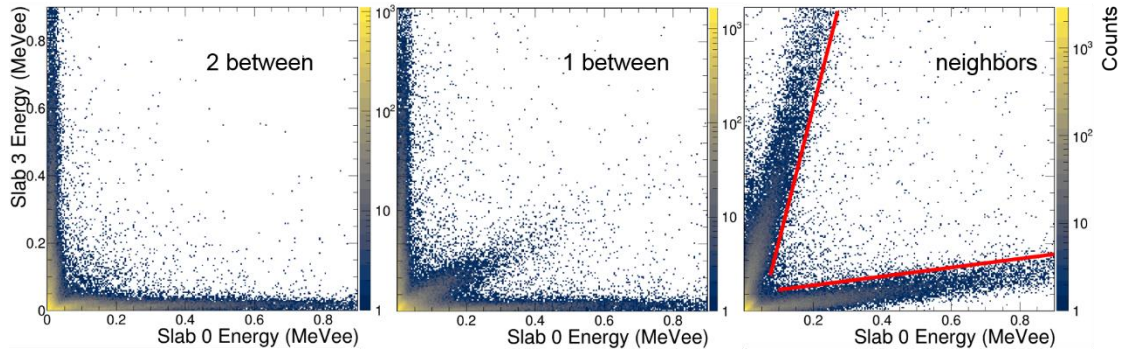


Figure 5.60. Deposited energy correlations between slabs with different levels of separation. 110,000 events from the first fission chamber location are shown. The left image shows the correlation for well separated slabs. The middle shows two slabs separated by a single slab. On the right is the energy correlation between two neighboring slabs, with the lines for threshold ceilings depicted in red.

In the first case (left), the individual spectra are visible along the  $X$  and  $Y$  axes, with no apparent correlations. When there is only one slab separating the two (middle), there is an approximately linear correlation between the two, representing a significant fraction of reconstructable events. These were likely scatters where a large energy deposition was made in one slab, resulting in significant optical crosstalk seen in the other. Finally, Figure 5.60 (right) shows the linear correlation between neighboring energy depositions going both ways, caused by optical crosstalk. As discussed previously in Section 4.4.3, optical crosstalk on the order of 10% per side was expected. Based on Figure 5.60 (right) and examination of other slab combinations, it was actually somewhat larger, between 15-25%. This is likely due to imperfections in the fabrication process providing unanticipated pathways for the light to reach the phototubes. The additional thickness of the EJ-500 seal, as well as the coupling between the retroreflector and the top of the slab assembly, also provided optical crosstalk pathways that were not included in the simulation. Additionally, reflections off of the photocathode meant that photons from one



slab could be reflected back into another, then reflected again by the retroreflector and eventually detected. The linear dependence of the threshold ceiling used for neighboring slabs was extracted by manually drawing a line above (or to the right) of the crosstalk bands in Figure 5.60 (right), then using the equation for this line to calculate the ceiling on a per-event basis.

The last cut required that the slabs that triggered have at least one slab between them, e.g. nearest neighbor triggers were not allowed. This was done for two reasons: one was to minimize the impact of optical crosstalk, which would cause both scatters to be localized at the wrong location due to overlapping hit patterns. The second reason was because scatters in adjacent slabs have a small lever arm (the line connecting the two scatter locations) in the backprojection, so small errors in the spatial localization can result in dramatic errors in the reconstructed cone. In general, these are scatters that are separated by distances within or near the estimated detector resolution ( $\sim 0.5$ -1 cm) and therefore do not image well. This resulted in a significant reduction in imaging efficiency, but greatly improved the performance.

### ***5.6.2 Example Double Scatter Event***

A likely neutron double scatter event was selected from the set that was used to produce the final image at the first source location, shown below in Section 5.6.3. Reconstructing this event, the first scatter deposited 414 keV<sub>ee</sub> (1659 keV<sub>proton</sub>) at (30, -15, -17.5) mm. This was the closest fully instrumented slab to the source. The second scatter was detected at (52.5, 3, -21.3) mm, 3 slabs away, where it deposited 162 keV<sub>ee</sub> (915 keV<sub>proton</sub>) 1.2 ns later. Figure 5.61 shows the signals read out from each slab for this event with vertical lines indicating the extracted trigger times, determined using a 50% CFD. Based on the time of flight from the fission chamber trigger signal, the estimated incident neutron energy was 5.3 MeV.

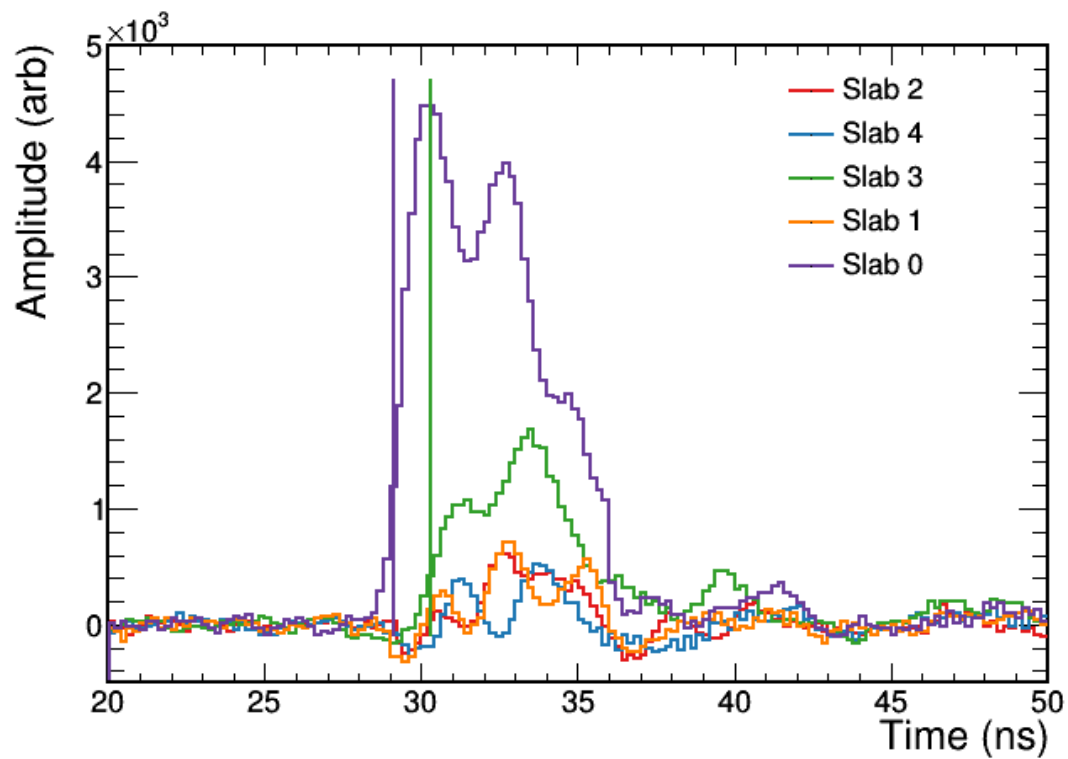


Figure 5.61. Slab pulses for the demonstration neutron double scatter event. Vertical lines highlight the trigger times for the two slabs that triggered. Slab 0 was the closest fully instrumented slab to the source, while slab 4 was the furthest from the source.

The hit maps for all the slabs are shown in Figure 5.62. All 24 pixels of the summed slabs in the image were set to the average value for that slab.



Figure 5.62. Hit patterns for the example event. The very bottom and top two slabs ( $Y=-21$ ,  $15$ , and  $21$  mm) were summed in hardware. The fission chamber was in the  $-Y$  direction.

### 5.6.3 Backprojected Neutron Images

Before showing the experimental, backprojected neutron image, it is instructive to see what was predicted by simulation – the location and approximate shape of the source distribution. An isotropic  $^{252}\text{Cf}$  point source was simulated at the estimated experimental source locations (30 cm and 76 cm from the detector), reconstructed using the log-likelihood method described in Section 4.2.9, and backprojected. Only the systematic effects described in Section 4.1 were included to produce Figure 5.63, so the image is sharper than the one expected from the experimental system. The figure also shows the image produced when using the truth information so that the source is clearly visible. Figure 5.64 shows the backprojected image for the second source location. Analogous selection cuts were applied to the simulated data as the experimental data, except the optical crosstalk restriction. Again, the intent was to get a rough idea of what to expect, rather than do a detailed performance comparison.

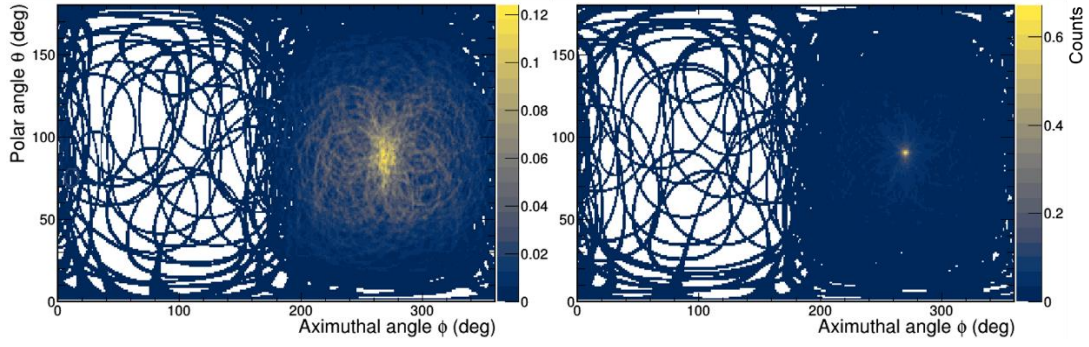


Figure 5.63. Backprojected images of neutron double scatters events for a source mimicking the experimental setup at the first source location. Left: reconstructed using realistic detector parameters, detailed in Section 4.1. Right: reconstructed using the scatter truth information (e.g. a perfect detector). The images contain 493 events.

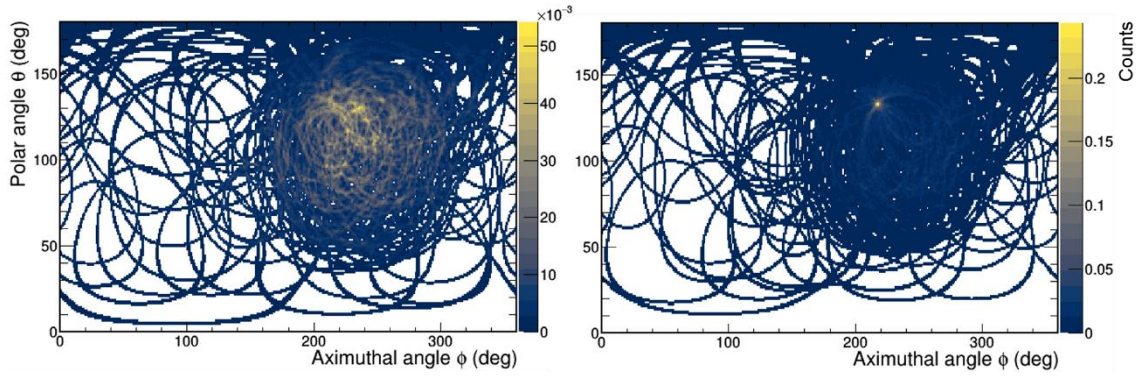


Figure 5.64. Backprojected images of neutron double scatters events for a source mimicking the experimental setup at the second source location. Left: reconstructed using realistic detector parameters. Right: reconstructed using the scatter truth information (e.g. a perfect detector). The images contain 195 events.

While it was clear that there is a source in each of the images, it was distributed over a fairly large range of angles. Based on these plots, the source was expected to be at about  $(270^\circ, 90^\circ)$  for the first measurement and  $(220^\circ, 135^\circ)$  for the second measurement.

Returning to the experimental data: at the first source location, with the source at a distance of 30 cm, 6,000,000 events were recorded. After the cuts described above were applied, about 28,500 double scatter interactions remained. An additional requirement was placed that neutrons come from the known source side, in this case, the  $-Y$  direction. This reduced the number of imaged events to 20,759 for an overall imaging efficiency (fraction of total triggers successfully backprojected) of 0.3%. Figure 5.65 shows the backprojected image produced by these neutron double-scatter events, and Figure 5.66 shows the reconstructed energy spectrum.

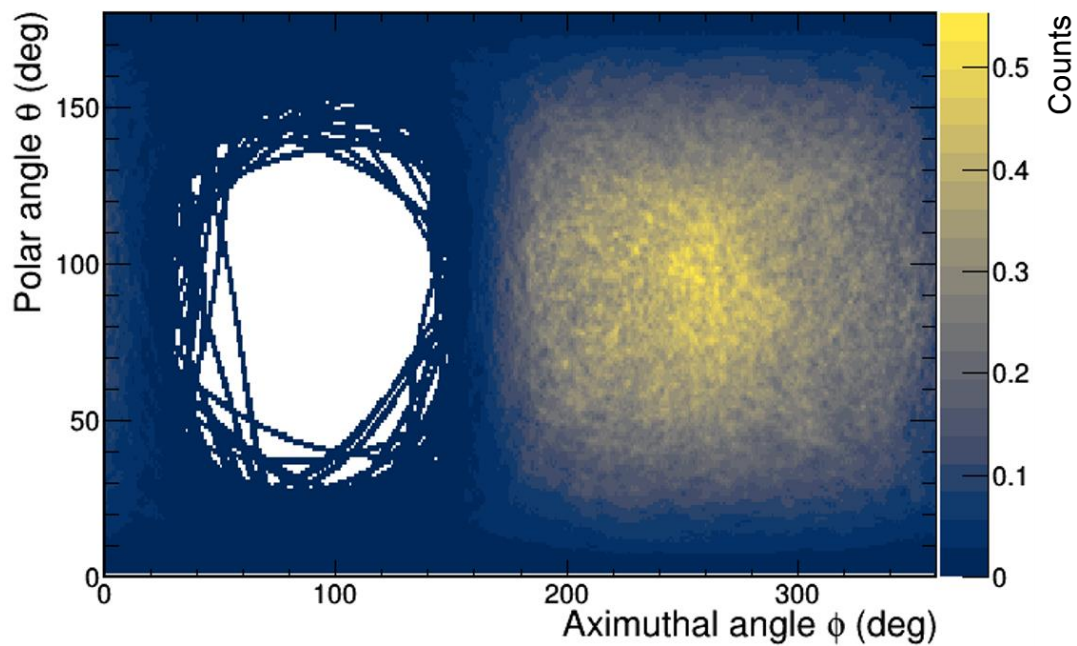


Figure 5.65. Backprojected image of neutron double-scatter events at the first source location, 35 cm away.  
The true source location was approximately  $(270^\circ, 90^\circ)$ .

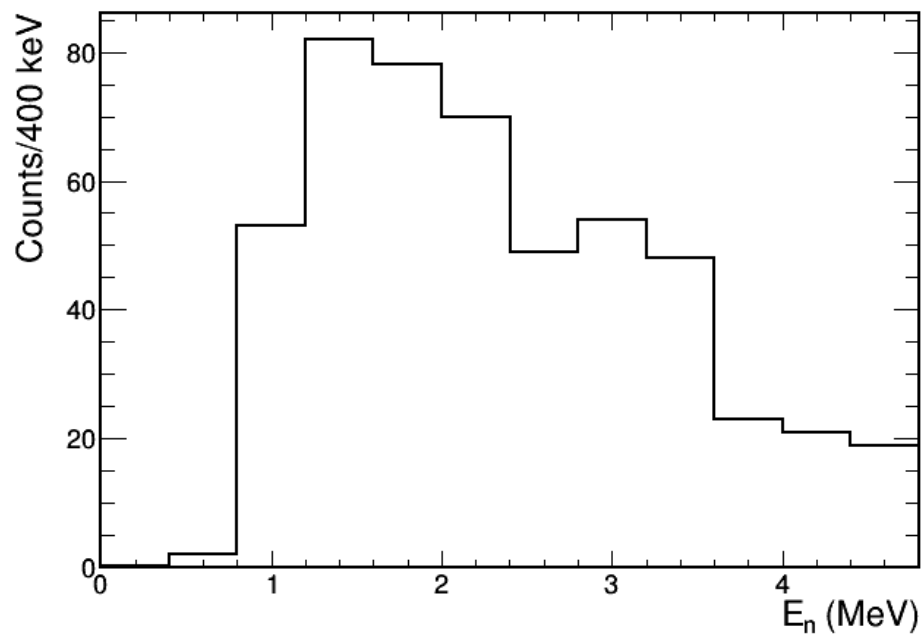


Figure 5.66. Reconstructed incident neutron energy spectrum from the first source position.

The fission chamber was moved to the second location, about 52.7 cm down (-Z, towards the floor) and 22.9 cm horizontally (-X, towards the photographer in Figure 5.58, shown in Figure 5.67). This source geometry was less ideal than the first position because scatters tend to be forward-directed, resulting in more double scatters within a single slab. These are not currently identified and thus add background to the backprojected image. In comparison, for the head-on source configuration of the other chamber location, forward scatters were more likely to end up in a separate slab.

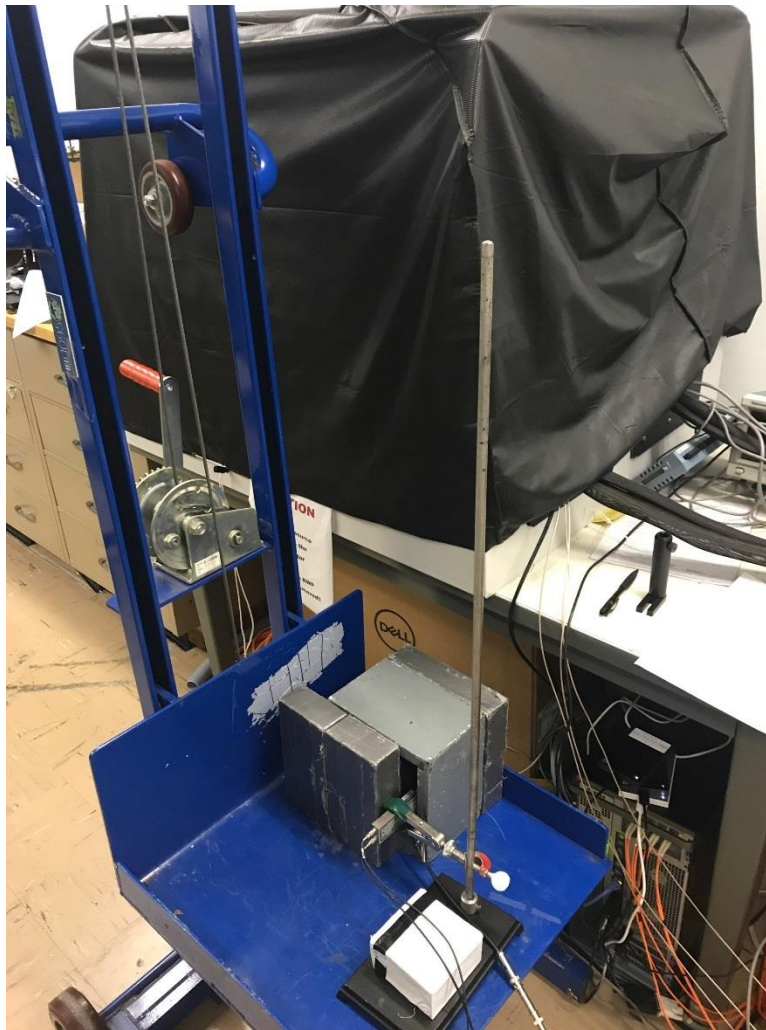


Figure 5.67. Picture of the fission chamber at the second source position, which was closer to the floor.



The source to detector distance at this location was about 76 cm. 998,000 triggers were acquired, and the same selection cuts and processing were applied to the data as above. Additionally, it was required that incident neutrons come from below the detector ( $z_0 < z_I$ ). Figure 5.68 shows the resulting backprojected image, which contains 1947 events, corresponding to an overall imaging efficiency of 0.2%. The efficiency was notably worse than the other source location (0.3%), primarily as a result of the less favorable source configuration.

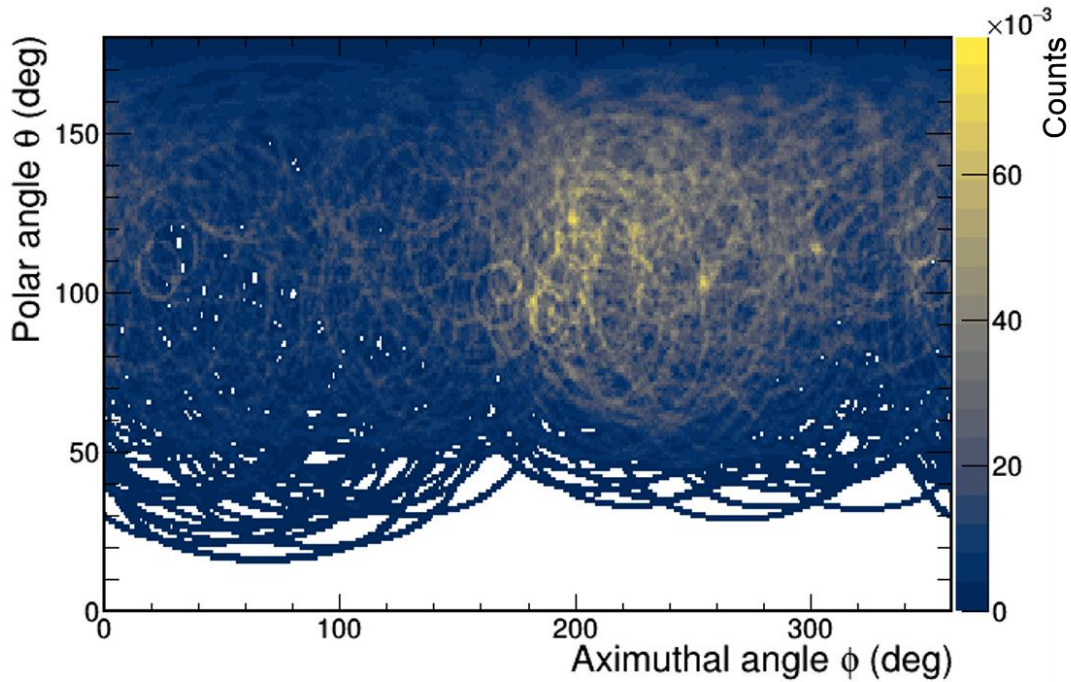


Figure 5.68. Backprojected image of the fission chamber at the second source location, 76 cm away.

The incident neutron energy spectrum is plotted in Figure 5.69. The shape of the underlying Watt spectrum is apparent, however there is a bias towards higher energy due to the energy thresholds. Recall that 100 keVee was required in each of two slabs, which



meant a neutron had to deposit  $\sim 500$  keV into each slab. The spectrum was therefore biased towards neutrons with more than 1 MeV of kinetic energy.

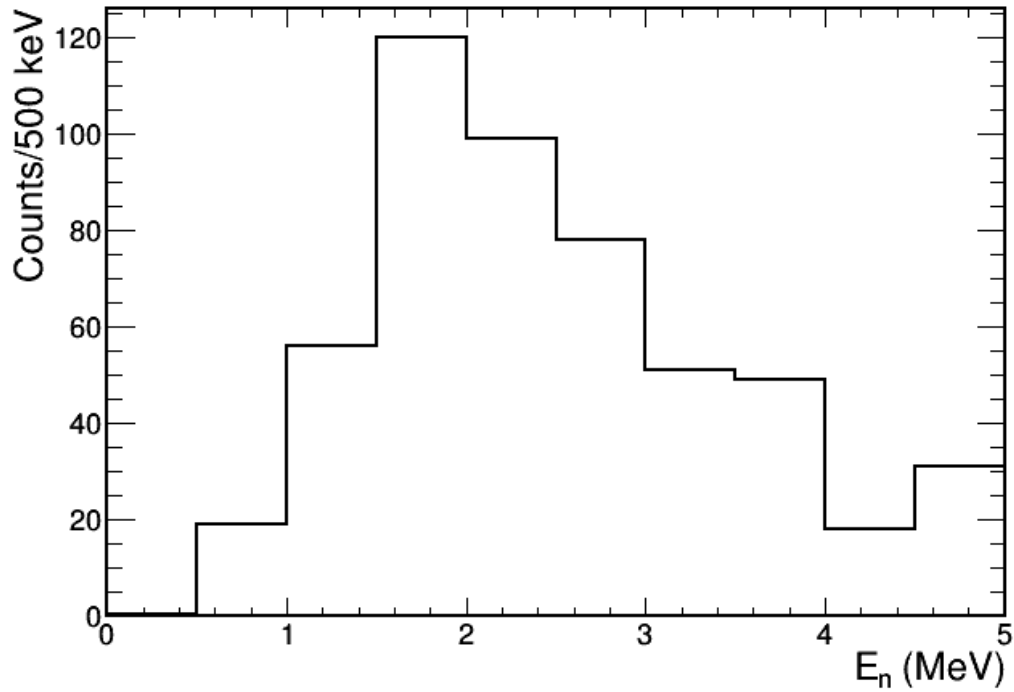


Figure 5.69. Incident neutron energy spectrum at the second source location.

#### 5.6.4 Backprojected Compton Images

Compton imaging works very similarly to the neutron double scatter imaging, utilizing the conservation of energy and momentum to constrain the incident gamma-ray direction to the surface of a cone. Since gamma rays travel at the speed of light and scatter

separations are short, the detector system does not have sufficient time resolution to determine which interaction happened first. Instead of using the timestamps, the locations and energies of both interactions are used. Additionally, in plastic scintillator, the second interaction is unlikely to deposit its full energy, so a correction factor must be used, described below.

The same event selection cuts from the neutron backprojection were used for the Compton images, with a few changes. The energy threshold was lowered to 75 keV, and the comparison with the fission chamber time was changed to select gamma-ray instead of neutron events (Figure 5.59b). Since the timing resolution was insufficient to know which scatter came first, it was assumed to be the one occurring in the slab closest to the chamber. The second interaction had its energy scaled by a factor of two to account for the fact that it was unlikely to deposit all of its energy in the plastic [13]. This was used as a very rough estimate, and detailed simulations are required to obtain a better scaling factor.

Figure 5.70 shows the result of backprojecting the Compton scatters from the first source position. Like with the neutron image (Figure 5.65), there is a hot spot around  $(270^\circ, 90^\circ)$ .

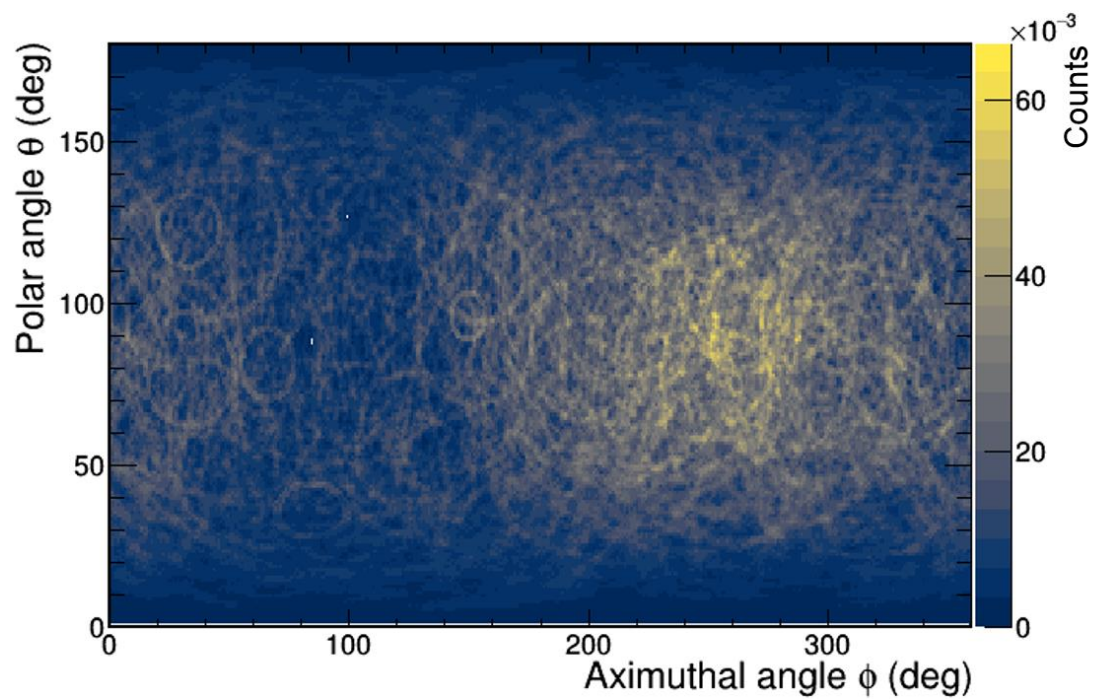


Figure 5.70. Compton image of the  $^{252}\text{Cf}$  source at the first source position. The image contains 2659 reconstructed events out of a total of 6 million triggers.

Applying the same cuts to the second source location data did not produce a convincing image of the source.

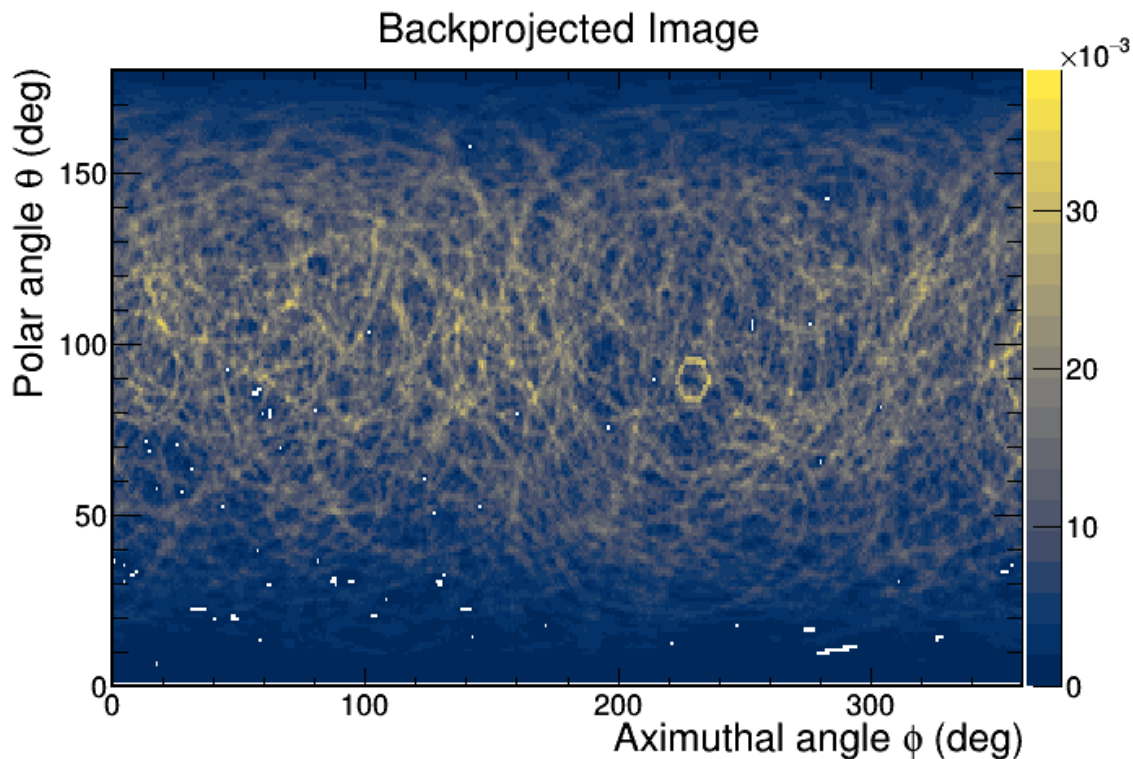


Figure 5.71. Compton image of the  $^{252}\text{Cf}$  source at the second source position. The image contains 1621 reconstructed events out of a total of 998,000 triggers.

Due to unforeseen circumstances, data acquisition for the second location was limited to about  $1/7^{\text{th}}$  of the number of events compared to the first position. Combined with the scatter kinematics being less favorable for imaging in this position for reasons stated previously, it was difficult to obtain a sufficient number of quality events after applying selection cuts. Finally, as evident in Figure 5.59b (compare the areas of the neutron and gamma ray regions) and as intended with the application of the lead shield, both data sets contained more neutrons than gamma rays. It was therefore not surprising that counting statistics were limited.

## 6 SUMMARY AND CONCLUSIONS

Fission-energy neutrons serve as a useful signature of fissionable material. The desire to directionally localize sources of these neutrons is partly motivated by the evolving demands of emergency response, arms control treaty verification, and other nuclear security applications. While neutron kinematic imaging is not new, the present challenge pertains to the miniaturization of the neutron scatter camera with minimal loss in angular resolution, and potentially, an improvement in efficiency. Multiple potential solutions to this challenge were briefly discussed and this thesis focused on the possibility of employing optical coded aperture imaging to this end. Compared to the other designs, this approach offers a compromise in terms of localization performance, physical complexity, and reconstruction complexity.

The OCA concept was previously demonstrated with 662 keV gamma rays that deposited all of their energy in a single location; however, there were still open questions about how it would perform with neutrons and plastic scintillators, and how multiple-site interactions would be reconstructed. The question about whether coded-aperture imaging was viable at such low counting statistics was addressed by the study in Section 3.1. We showed that the number of counts required to accurately reconstruct a source depended principally on the number of mask elements. This motivated the use of 1-D mask patterns in Designs B and D. The study also showed that, with a low rank 1-D pattern, a very small number of counts could be reconstructed correctly with spatial resolution on the order of a few millimeters.

The multiple-site localization question proved much more challenging to answer. Development of both the optical transport and full physics simulation codes, along with the analysis algorithms to process and reconstruct the data, built invaluable intuition regarding coded-aperture imaging systems. A large amount of time and effort were spent conceiving and testing methods to simultaneously image two interactions, with no success. Finally, the multiple site problem simplified into multiple single-site problems when the detector volume was optically segmented, and this led to the slab design.

Once the basic concept was demonstrated with the optical transport Geant4 code, a full physics simulation was developed, and a parameter study was conducted (Chapter 4) to understand the performance mechanics of the detector system. The simulation included most of the major physical effects that were expected to significantly impact the performance. Different approaches to the event localization were developed and tested, including the cross-correlation, and a set of response-based fits, detailed in Section 4.2. Through this study, the detector response localization methods not only were expected to perform better but were necessary in certain geometries. Ultimately, resolutions on the order of 5-10 mm FWHM were demonstrated, suggesting the OCA approach was potentially viable and was worth pursuing experimentally.

The MAPMTs used in the prototype and retroreflector study were characterized to normalize the response of each pixel. This was accomplished by directing a constant-amplitude, 405-nm light pulse from a 45 ps laser into each pixel individually. The relative responses of each anode were measured and used to extract a normalization factor, which was the product of the relative gains and QEs for that anode. These calibrations were shown to improve the performance and were critical to the experimental data analysis.

In the simulations, it was proposed to use a retroreflector to maximize photodetection efficiency. Since there was insufficient information on the detailed performance of commercially available retroreflective tapes, two experiments were designed (Section 5.4). The first used a 405 nm laser to probe the retroreflectors at different angles, then captured the retroreflected light with a color camera. This gave a relative measurement of the retroreflectivity at this wavelength between the tapes and between angles. Secondly, the tapes were affixed to a block of EJ-212, which was then hit with a collimated gamma-ray beam from  $^{133}\text{Ba}$ . The light detection efficiency and spatial localization performance were measured, showing that some of the retroreflectors performed better than Teflon and black paint in both categories. This information was not incorporated into the simulations, however it justified the experimental use of the retroreflectors, since it showed they were working as expected.

Based on the simulation results, the OCA Prototype Design was constructed. In part because of my limited experience, this proved to be one of the most challenging components of this work. The 3-piece slab assemblies were built and sent to us, glued together and diamond milled by Eljen Corporation. Multiple efforts were made to assemble the detector while minimizing wicking of grease or other material in the detector gaps. The final process, described in Section 5.1, was the result of many trials, errors, and mock tests with small acrylic pieces in the lab. It was very far from perfect and I believe the detector assembly provides the largest opportunity for hardware-based detector performance improvement. Refinement of the fabrication process would result in more uniform slab modules, better slab-MAPMT coupling, and improved light transport, among other benefits.

Using a collimated gamma-ray beam from  $^{133}\text{Ba}$ , the performance of the experimental prototype was measured and reported in Section 5.5. The energy spectrum was simulated and fit to obtain the experimental energy scale. The localization performance was reasonable in the slab dimension, but significantly worse in the depth dimension than what was predicted by simulation, for a number of reasons discussed throughout this document. Further studies are needed to be sure, but reflections off the photocathode (used to achieve a higher QE) were probably the biggest culprit in degrading the depth spatial resolution. Imperfect optical surfaces likely played a significant role in the discrepancy, since in this geometry, photons were liable to bounce dozens of times before reaching the phototubes. In this scenario, even a small angular deviation could result in a large displacement at the MAPMT. Additionally, this created optical pathways in the experimental prototype that did not exist in the simulation. The net effect was a general blurring of the coded pattern projected onto the MAPMT, somewhat diminishing the localization benefits provided by the coded aperture. As seen in the experimental hit maps (Figure 5.44 and Figure 5.45), there was a positive offset in the baseline even with stringent cuts. Compare that to a simulated hit map (Figure 4.6, red), where many pixels were exactly zero in value. This discrepancy suggests that the optical transport was less

than ideal, and also perhaps that more selective event cuts were needed when building the response table.

Finally, in Section 5.6, the prototype was used to localize a  $^{252}\text{Cf}$  fission chamber in the lab at two locations, 30 and 76 cm away, using the neutron backprojection. The chamber was encased in  $\sim 2''$  lead bricks to maximize the neutron to gamma ratio and the prototype was triggered in coincidence. While the images that were produced did not contain sharp peaks, simulation was leveraged to show that the neutron source appeared in the experimental image where expected. Compton imaging was also demonstrated, however due to the lead shielding, the gamma to neutron ratio in the data was poor. Still, we achieved the goal of demonstrating the multiple-site localization and imaging capability of the OCA-based compact NSC detector system. The imaging performance was worse than current systems, such as MINER, but this can definitely be improved, and the active volume of the prototype system has a significantly smaller footprint.

## 6.1 Future Work

Since the detector concept was experimentally demonstrated, future work primarily pertains to improving the performance. Further simulation studies should be performed and compared to the experimental results to gain a better understanding of which parameters were most important to match to the simulated model. A high priority performance improvement is rejection and/or recovery of intra-slab scatters based on the pulse shape, which significantly distort the backprojected image. The design itself could be optimized to minimize these events by modifying the slab module geometry, such as by making the slabs thinner. This change would result in more optical crosstalk, however this information is potentially partially recoverable, as previously discussed. Another priority is improving the imaging efficiency by recovering next-neighbor scatters, since the mean free path of a fission neutron is on the order of the width of two slabs.

The H12700 MAPMTs were effective, but suffer from electronic crosstalk, described previously. As a result, there will likely be significant performance benefits to instead using SiPMs, assuming the amplification and instrumentation of nearly 200 channels can



be resolved for this form factor. While the electronic crosstalk is expected to be improved or eliminated with SiPMs, other possible issues, such as dark counts, would need to be considered. In general, SiPMs also have a higher QE, which would result in better performance in every aspect – localization, energy, and timing.

As discussed, the detector assembly process was very challenging and delicate. As with any product, serious effort would need to be invested in understanding the best method for building the detector that results in a consistent, high-performing device. A better solution is needed for keeping grease out of the air gaps, or perhaps the air gaps should be sacrificed. According to the simulation, the performance would take a small hit, but fabrication may be dramatically easier.

The system needs a lot of development work to be fieldable or commercially ready. While the detector volume was small ( $5 \times 5 \times 15.6 \text{ cm}^3$ ), dozens of kilograms of cables, a VME crate with four digitizer boards, a full NIM bin, and a powerful desktop computer were needed to readout and process the data. ASICs would need to be designed to implement the trigger logic and signal processing methods employed in this dissertation. Data loads and processing requirements can be dramatically reduced once the detector system is better understood. It is very likely, for example, that a lower sampling frequency than 5 GHz can be used, instead performing analog pulse integrals and time-over-threshold calculations to generate photon hit maps and identify multiple scatters within a single slab.

Finally, with the basic concept demonstrated, other applications of this technology can be explored, such as medical imaging. For example, positron emission tomography (with a different scintillator, e.g. LSO) may benefit from the ability to localize multiple interactions in the detector module, allowing for Compton scatters to be rejected or reconstructed. This would come at the cost of spatial and energy resolution, so studies would need to be performed to understand whether or not this tradeoff is worthwhile.

## LIST OF REFERENCES

- [1] F. H. Ruddy, R. Gold, J. H. Roberts, B. J. Kaiser, and C. C. Preson, "Imaging of fast neutron sources using solid state track recorder pinhole radiography," *Nucl. Tracks Radiat. Meas.*, 1984.
- [2] P. A. Hausladen, M. A. Blackston, E. Brubaker, D. L. Chichester, P. Marleau, and R. J. Newby, "Fast neutron coded-aperture imaging of special nuclear material configurations," in *53rd Annual Meeting of the INMM*, 2012.
- [3] R. T. Grannan, R. Koga, W. A. Millard, A. M. Preszler, G. M. Simnett, and R. S. White, "A large area detector for neutrons between 2 and 100 MeV," *Nucl. Instruments Methods Phys. Res. Sect. A Accel. Spectrometers, Detect. Assoc. Equip.*, vol. 103, pp. 99–108, 1972.
- [4] L. Forman and P. E. Varnier, "Fast neutron source detection at long distances using double-scatter spectrometry," *Brookhaven Natl. Lab*, 2003.
- [5] S. E. Walker, A. M. Preszler, and W. A. Millard, "Double scatter neutron time-of-flight spectrometer as a plasma diagnostic," *Rev. Sci. Instrum.*, 1986.
- [6] U. Bravar *et al.*, "Calibration of the fast neutron imaging telescope (FNIT) prototype detector," *IEEE Trans. Nucl. Sci.*, vol. 56, no. 5, pp. 2947–2954, 2009.
- [7] P. Marleau, J. Brennan, K. Krenz, N. Mascarenhas, and S. Mrowka, "Advances in imaging fission neutrons with a neutron scatter camera," in *IEEE Nuclear Science Symposium Conference Record*, 2007, pp. 170–172.
- [8] S. Agostinelli *et al.*, "Geant4 - a simulation toolkit," *Nucl. Instruments Methods Phys. Res. Sect. A Accel. Spectrometers, Detect. Assoc. Equip.*, vol. 506, pp. 250–303, 2003.
- [9] D. J. Forrest and E. L. Chupp, "Upper limit for the solar neutron flux in the energy interval 20–120 MeV," 1969.
- [10] G. . Frye, T. L. Jenkins, and A. Owens, "SONTRAC: A solar neutron track chamber detector system," *Work. Scintill. Fiber Dev.*, 1985.
- [11] R. S. Miller, J. R. Macri, M. L. McConnell, J. M. Ryan, E. Flückiger, and L. Desorgher, "SONTRAC: An imaging spectrometer for MeV neutrons," *Nucl. Instruments Methods Phys. Res. Sect. A Accel. Spectrometers, Detect. Assoc. Equip.*, 2003.

- [12] S. Mukhopadhyay, R. Maurer, P. Guss, and C. Kruschwitz, "Review of current neutron detection systems for emergency response," *Hard X-Ray, Gamma-Ray, Neutron Detect. Phys. XVI*, vol. 9213, no. September 2014, 2014.
- [13] M. D. Gerling, J. E. M. Goldsmith, and J. S. Brennan, "MINER - A mobile imager of neutrons for emergency responders," *2014 IEEE Nucl. Sci. Symp. Med. Imaging Conf. NSS/MIC 2014*, pp. 1–4, 2016.
- [14] J. E. M. Goldsmith, M. D. Gerling, and J. S. Brennan, "A compact neutron scatter camera for field deployment," *Rev. Sci. Instrum.*, no. 87, 2016.
- [15] C. Dujardin *et al.*, "Needs, trends, and advances in inorganic scintillators," *IEEE Trans. Nucl. Sci.*, 2018.
- [16] J. P. Islamian, M. Khoshakhlagh, B. Mahmoudian, and S. M. Abedi, "Development of Scintillators in Nuclear Medicine," *World J. Nucl. Med.*, 2015.
- [17] J. Glodo *et al.*, "New Developments in Scintillators for Security Applications," *Phys. Procedia*, 2017.
- [18] C. Cuesta *et al.*, "Slow scintillation time constants in NaI(Tl) for different interacting particles," *Opt. Mater. (Amst)*, vol. 36, no. 2, pp. 316–320, 2013.
- [19] Eljen Technology, "EJ-20x Datasheet." [Online]. Available: <https://eljentechnology.com/products/plastic-scintillators/ej-200-ej-204-ej-208-ej-212>. [Accessed: 11-Nov-2019].
- [20] Eljen Technology, "EJ-23x Datasheet." [Online]. Available: <https://eljentechnology.com/products/plastic-scintillators/ej-232-ej-232q>. [Accessed: 11-Nov-2019].
- [21] Eljen Technology, "EJ-30x Datasheet." [Online]. Available: <https://eljentechnology.com/products/liquid-scintillators/ej-301-ej-309>.
- [22] G. F. Knoll, *Radiation Detection and Measurement*, 3rd ed. John Wiley & Sons, Inc.
- [23] M. L. Roush, M. A. Wilson, and W. F. Hornyak, "Pulse shape discrimination," *Nucl. Instruments Methods*, vol. 31, no. 1, pp. 112–124, 1964.
- [24] S. A. Pozzi, J. A. Mullens, and J. T. Mihalczo, "Analysis of neutron and photon detection position for the calibration of plastic (BC-420) and liquid (BC-501) scintillators," *Nucl. Instruments Methods Phys. Res. Sect. A Accel. Spectrometers, Detect. Assoc. Equip.*, vol. 524, no. 1–3, pp. 92–101, 2004.

- [25] T. A. Laplace *et al.*, “Low energy light yield of fast plastic scintillators,” *Nucl. Instruments Methods Phys. Res. Sect. A Accel. Spectrometers, Detect. Assoc. Equip.*, 2018.
- [26] J. Braverman *et al.*, “Single-volume neutron scatter camera for high-efficiency neutron imaging and spectroscopy,” 2018.
- [27] M. Calvi *et al.*, “Characterization of the Hamamatsu H12700A-03 and R12699-03 multi-anode photomultiplier tubes,” *J. Instrum.*, 2015.
- [28] C. Jackson, K. O’Neill, L. Wall, and B. McGarvey, “High-volume silicon photomultiplier production, performance, and reliability,” *Opt. Eng.*, 2014.
- [29] F. Acerbi and S. Gundacker, “Understanding and simulating SiPMs,” *Nucl. Instruments Methods Phys. Res. Sect. A Accel. Spectrometers, Detect. Assoc. Equip.*, 2019.
- [30] A. Lehmann, A. Britting, W. Eyrich, and F. Uhlig, “Studies of MCP properties,” *J. Instrum.*, 2009.
- [31] S. Ritt, R. Dinapoli, and U. Hartmann, “Application of the DRS chip for fast waveform digitizing,” *Nucl. Instruments Methods Phys. Res. Sect. A Accel. Spectrometers, Detect. Assoc. Equip.*, vol. 623, pp. 486–488, 2010.
- [32] W. W. Moses, “Fundamental limits of spatial resolution in PET,” *Nucl. Instruments Methods Phys. Res. Sect. A Accel. Spectrometers, Detect. Assoc. Equip.*, 2011.
- [33] J. B. Braverman, L. Fabris, J. Newby, D. Hornback, and K. P. Ziock, “Three-dimensional event localization in bulk scintillator crystals using optical coded apertures,” *IEEE Trans. Nucl. Sci.*, vol. 62, pp. 1405–1412, 2015.
- [34] K. P. Ziock, M. A. Blackston, and T. Van Vuure, “3D millimeter event localization in bulk scintillator crystals,” *IEEE Trans. Nucl. Sci.*, 2013.
- [35] J. G. Ables, “Fourier transform photography: a new method for x-ray astronomy,” *Astron. Soc. Aust.*, 1968.
- [36] R. H. Dicke, “Scatter-hole cameras for x-rays and gamma rays,” *Astrophys. J.*, 1968.
- [37] K. Mcmillan, P. Marleau, E. Brubaker, S. N. Laboratories, and L. Angeles, “Random mask optimization for fast neutron coded aperture imaging,” 2015.
- [38] M. J. Cieřlak, K. A. A. Gamage, and R. Glover, “Coded-aperture imaging systems: Past, present and future development – A review,” *Radiat. Meas.*, 2016.

- [39] E. E. Fenimore and T. M. Cannon, "Coded aperture imaging with uniformly redundant arrays," *Appl. Opt.*, vol. 17, no. 3, pp. 337–347, 1978.
- [40] S. R. Gottesman and E. E. Fenimore, "New family of binary arrays for coded aperture imaging," *Appl. Opt.*, vol. 28, no. 20, pp. 4344–4352, 1989.
- [41] R. Accorsi, "Design of near-field coded aperture cameras for high-resolution medical and industrial gamma-ray imaging," Massachusetts Institute of Technology, 1971.
- [42] J. Gregory and J. Lander, *Game Engine Architecture*. 2009.
- [43] P. Hausladen, J. Newby, F. Liang, and M. Blackston, "The deployable fast-neutron coded- aperture imager: demonstration of locating one or more sources in three Dimensions," 2013.
- [44] M. Janecek and W. W. Moses, "Optical reflectance measurements for commonly used reflectors," *IEEE Trans. Nucl. Sci.*, pp. 2432–2437, 2008.
- [45] P. L. Bender *et al.*, "The lunar laser ranging experiment," *Science* (80-. ), 1973.
- [46] F. Ankel-Simons, *Primate Anatomy*, 3rd ed. 2007.
- [47] H. O. Anger, "Use of a gamma ray pinhole camera for in-vivo studies," 1952.
- [48] A. A. R. Fremout, R. Chen, P. Bruyndonckx, and S. P. K. Tavernier, "Spatial resolution and depth-of-interaction studies with a PET detector module composed of LSO and an APD array," *IEEE Trans. Nucl. Sci.*, pp. 131–138, 2002.
- [49] D. P. McElroy, S. C. Huang, and E. J. Hoffman, "The use of retro-reflective tape for improving spatial resolution of scintillation detectors," *IEEE Trans. Nucl. Sci.*, pp. 165–171, 2002.
- [50] J. S. Karp and G. Muehllehner, "Performance of a position-sensitive scintillation detector," *Phys. Med. Biol.*, pp. 643–655, 1985.
- [51] J. G. Rogers, D. P. Saylor, R. Harrop, X. G. Yao, C. V. M. Leitao, and B. D. Pate, "Design of an efficient position sensitive gamma ray detector for nuclear medicine," *Phys. Med. Biol.*, pp. 1061–1090, 1986.
- [52] F. A. Harrison, S. M. Kahn, C. J. Hailey, and K. Zioc, "Performance optimization for hard x-ray/soft  $\gamma$ -ray detectors," *SPIE Proc.*, pp. 47–52, 1990.

- [53] K. Weinfurter, J. Mattingly, E. Brubaker, and J. Steele, “Model-based design evaluation of a compact, high-efficiency neutron scatter camera,” *Nucl. Instruments Methods Phys. Res. Sect. A Accel. Spectrometers, Detect. Assoc. Equip.*, vol. 883, pp. 115–135, 2018.
- [54] M. Sweany *et al.*, “Interaction position, time, and energy resolution in organic scintillator bars with dual-ended readout,” *Nucl. Instruments Methods Phys. Res. Sect. A Accel. Spectrometers, Detect. Assoc. Equip.*, vol. 927, pp. 451–462, 2019.
- [55] K. P. Ziock, J. B. Braverman, L. Fabris, M. J. Harrison, D. Hornback, and J. Newby, “Event localization in bulk scintillator crystals using coded apertures,” *Nucl. Instruments Methods Phys. Res. Sect. A Accel. Spectrometers, Detect. Assoc. Equip.*, vol. 784, pp. 382–389, 2015.
- [56] M. L. Ruch, “Silicon Photomultipliers for Compact Neutron Scatter Cameras,” University of Michigan, 2017.
- [57] N. Mascarenhas, J. Brennan, K. Krenz, P. Marleau, and S. Mrowka, “Results with the neutron scatter camera,” *IEEE Nucl. Sci. Symp. Conf. Rec.*, 2009.
- [58] S. D. Barthelmy *et al.*, “The burst alert telescope (BAT) on the SWIFT midex mission,” in *Proceedings of SPIE*, 2004.
- [59] K. P. Ziock *et al.*, “Source-search sensitivity of a large-area, coded-aperture, gamma-ray imager,” *IEEE Trans. Nucl. Sci.*, 2006.
- [60] E. E. Fenimore, “Coded aperture imaging: predicted performance of uniformly redundant arrays,” *Appl. Opt.*, vol. 17, no. 22, pp. 3562–3570, 1978.
- [61] R. Brun and F. Rademakers, “ROOT - An object oriented data analysis framework,” *Nucl. Instruments Methods Phys. Res. Sect. A Accel. Spectrometers, Detect. Assoc. Equip.*, 1997.
- [62] R. Batchelor, W. B. Gilboy, J. B. Parker, and J. H. Towle, “The response function of organic scintillators to fast neutrons,” *Nucl. Instruments Methods*, 1961.
- [63] C. E. Shannon, “Communication in the Presence of Noise,” *Proc. IRE*, vol. 37, no. 1, pp. 10–21, 1949.
- [64] J. Braverman, M. Harrison, and K. P. Ziock, “An approximate analytic expression for the flux density of scintillation light at the photocathode,” *IEEE Nucl. Sci. Symp. Conf. Rec.*, no. 3, pp. 335–338, 2012.
- [65] M. et al (Particle D. G. Tanabashi, “2019 Review of Particle Physics,” *Phys. Rev. D*, 2019.

- [66] M. Janecek, “Reflectivity spectra for commonly used reflectors – Janecek Background,” *IEEE Trans. Nucl. Sci.*, 2012.
- [67] C. J. Hailey, F. Harrison, J. H. Lupton, and K. P. Ziock, “An inexpensive, hard x-ray imaging spectrometer for use in x-ray astronomy and atomic physics,” *Nucl. Instruments Methods Phys. Res. Sect. A Accel. Spectrometers, Detect. Assoc. Equip.*, 1989.
- [68] “Standard Specification for Retroreflective Sheeting for Traffic Control,” *ASTM D4956-19*. 2009.

## **VITA**

Micah Folsom was born in San Diego, California to Joseph and Rachel Folsom. After completing high school in 2007, he attended the University of California, Berkeley, obtaining a Bachelor of Science in Nuclear Engineering in 2012. He spent the next two years conducting radiation detector research at Lawrence Berkeley National Lab, and in the fall of 2014, began his graduate education at the University of Tennessee, Knoxville. In 2017, he earned a Master of Science in Nuclear Engineering, then promptly began work on his dissertation research, which concluded in the spring of 2020.